FEDERAL UNIVERSITY OF ALFENAS – UNIFAL- MG

GISLENE BATISTA

NIOBIUM AND TANTALUM-BASED PHOSPHATE GLASSES AND GLASS-CERAMICS FOR PHOTONIC APPLICATIONS

ALFENAS/ MG

2024

GISLENE BATISTA

NIOBIUM AND TANTALUM-BASED PHOSPHATE GLASSES AND GLASS-CERAMICS FOR PHOTONIC APPLICATIONS

Thesis presented as part of the requirements for the title of PhD in Chemistry from Federal University of Alfenas – UNIFAL-MG.
Field area: Inorganic Chemistry
Line of research: Materials Chemistry
Advisor: Prof. Dr. Gaël Yves Poirier

ALFENAS/ MG

2024

Sistema de Bibliotecas da Universidade Federal de Alfenas
Biblioteca Central

Batista, Gislene.
Niobium and Tantalum-based Phosphate Glasses and Glass-ceramics for Photonic Applications / Gislene Batista. - Alfenas, MG, 2024.
218 f. : il. -

Orientador(a): Gael Yves Poirier.
Tese (Doutorado em Química) - Universidade Federal de Alfenas, Alfenas, MG, 2024.
Bibliografia.

1. Thermal Poling. 2. Second Harmonic Generation. 3. Glasses. 4. Tantalum. 5. Niobium. I. Poirier, Gael Yves, orient. II. Título.

Ficha gerada automaticamente com dados fornecidos pelo autor.

Gislene Batista

Title: Niobium and tantalum-based phosphate glasses and glass-ceramics for photonic applications

The president of the examination committee signs the approval of the PhD thesis presented as part of the requirements for the title of PhD in Chemistry from Federal University of Alfenas - UNIFAL.

Field area: Inorganic Chemistry

Approved in: 30th of January 2024.

Prof. Dr. Gael Yves Poirier

President of the Examination Committee

Institution: Fedral University of Alfenas

Dr. Thierry Cardinal

Institution: University of Bordeaux

Dr. Marc Dussauze

Institution: University of Bordeaux

Prof. Dr. Marcelo Nalin

Institution: State University of São Paulo - UNESP

Prof. Dr. Lauro June Queiroz Maia

Institution: Federal University of Goias

ACKNOWLEDGMENT

First, I would like to thank God, for having blessed every day of my life, for lighting my path and giving me strength to always move forward. To my parents, Elaine and Gamaliel; and to my brothers, Marcelo and Gabriel, for all the trust and support they have always given me; and especially to my (twin) sister Gisele, for all her support and patience, and especially for always being by my side at all times.

To my advisor, Prof. Gaël Poirier, for the guidance and discussing the development of the research, and for being an "inspire person" to all of us of the Unifal glass research group and for encouraging me to my sandwich PhD in France. Also, to my supervisors during the period I was in Bordeaux, Dr. Thierry Cardinal and Dr. Marc Dussauze for welcoming me and providing the opportunity to further expand my knowledge.

To the glass research group at Unifal, Prof. Fábia, Prof. Tânia, Valentina, Roni, Rodrigo, Cristiano, Ana Júlia, Ana Flávia, Raphael, Yago, for all the partnership, discussions, and meetings that allowed us to discuss science especially in the period of the pandemic when we were away from the laboratory. To everyone in Group 3 of the ICMCB in Bordeaux, who contributed directly or indirectly to the research and mainly for the reception within the group. To Léo, both for the help inside the laboratory, but mainly for the friendship that was essential during my stay in Bordeaux. And to William who joined us and made this period much more special.

To everyone who collaborated in my research, accompanying me and teaching me how to perform various analyses, Alexandre Fargues, Frédéric Adamietz, Vincent Rodriguez, Christian Aupetit, Lara Karam, Julien Hunel, Nithavong Cam. Also, for some analysis, crystallography laboratory in UNIFAL (*Santa Clara*) - Alfenas, crystallography laboratory in UNIFEI, Roni A. Silva, C-Labmu in UEPG, UEM and LaMaV in UFSCAR; and CAQI in USP-São Carlos.

To Prof. Dr. Italo Mazali and to Prof. Dr. Marcelo Vivas for discussion and contributions during Qualification. To Prof. Dr. Marcelo Nalin, Prof. Dr. Lauro Maia, Dr. Thierry Cardinal and Prof. Dr. Marc Dussauze to participate as the committee members of my defense.

UNIFAL-MG (PIB-POS) and CAPES for the scholarship granted in Brazil, and CAPES for the scholarship granted during the sandwich PhD.

The present work was carried out with the support of the Coordination for the Improvement of Higher Education Personnel - Brazil (CAPES) - Financing Code 001.

This work was carried out with financial support from the "Minas Gerais Research Funding Foundation (FAPEMIG)" and that of the "PRPPG (*Pró-reitoria de Pesquisa e Pós-graduação*) at UNIFAL-MG".

“Divide each difficulty into as many parts as is feasible and necessary to resolve it.”

(René Descartes, 1637)

ABSTRACT

Tantalum and Niobium-containing alkaline phosphate glasses are relevant materials for photonic applications due to several properties such as high thermal, chemical and mechanical stability, wide optical window, low phonon energy and high quantum efficiency of luminescent ions. The highest amount of their respective oxides reported in a phosphate glass is 50 mol%, with tantalum or niobium-rich regions that can induce precipitation of crystalline phase of type $M_2N_8O_{21}$ (M = Na or K and N = Nb or Ta). In addition to these relevant properties, tantalum/niobium phosphate glasses have a low production cost due to the abundance of starting materials and national strategic relevance, since they are considered strategic elements for technology development. Therefore, these glass and glass-ceramic materials are promising as luminescent matrices, non-linear optical materials for second harmonic generation and substrates for microstructuration of optical properties. Thus, this work may be separated in three main parts: i) study of sodium phosphate glasses with the addition of tantalum oxide from 40 to 50 mol%, as well as the Eu^{3+}-doped glasses and their behavior under Thermal Poling and Micropoling. These glasses were analyzed by Differential Scanning Calorimetry, X-ray Diffraction, Raman and Infrared spectroscopies, Refractive Index, transparency in the UV-Vis region and luminescence. Based on these data, it was verified that the addition of tantalum increases the glass transition temperature, i.e., increasing the connectivity of the glass network; the band-gap shift to longer wavelengths with high transparency (~80%); relatively high refractive index (~1.9 at 532 nm); and strongly modifies the $^7F_2/^7F_1$ asymmetry ratio in Eu^{3+}-doped glasses. Some of these glasses were thermally poled using a microstructured electrode, under 250°C and voltage from 600 to 900V depending on the glass composition. Maker Fringes measurements confirmed Second Harmonic Generation (SHG) in the poled glasses attributed to Electric Field Induced Second Harmonic (EFISH) model, as well as by the correlative measurements of micro-SHG/Raman/Luminescence in one of them. The microstructured electrode allowed the microprinting of patterns on the glasses, according to micrographs and Atomic Force Microscopy measurements, with changes in the topology, in refractive index and an edge effect of SHG, suggesting a microscale control of the optical properties. ii) study of phosphate glass-ceramics (GC) containing 47.5 mol% of tantalum oxide doped with europium and its behavior under Thermal Poling. Translucent glass-ceramics containing $Na_2Ta_8O_{21}$ crystalline phase were obtained with the degree of crystallinity and transparency controlled as a function of the heat treatment time. By photoluminescence it was verified that the europium ions are present in the crystalline phase; since, among others, the ratio of [$^5D_0 \rightarrow$] $^7F_2/\ ^7F_1$

transitions decreases with the increase of the degree of crystallinity. Some of these GC were thermally poled. Measurements of electric current during poling, Time of Flight Secondary-Ion Mass Spectrometry, Infrared and Maker Fringes allowed to establish a model for ion migration under electric field: it appears that sodium ions in the crystalline phase do not migrate within the material, but only those that are still within the glassy phase, with the main change occurring in the phosphate structure after sodium depletion. Also, SHG of GC appears to be originated from EFISH effect after thermal poling as in precursor glasses. Calculated values of $\chi^{(2)}$ in GC are one magnitude lower than the respective poled glass. And iii) study of phosphate glasses containing 45 mol% of niobium oxide with increasing amounts of silver and also co-doping with antimony, as well as its preliminary evaluation under Thermal Poling. High silver contents could be incorporated, reaching ~9 mol% in potassium-based glasses and ~5 mol% in sodium-based glasses. Silver increment in these glasses decreases Tg, that is, network connectivity; as well as thermal stability against crystallization with silver acting as a nucleating center. Silver addition also red-shifts the band-gap and increases refractive index. Sodium silver/antimony co-doped glasses present different colors, and consequently, absorption spectra when varying annealing temperature. The glass annealed at Tg exhibits a band related to plasmon resonance not appearing for lower annealing temperatures. One of these glasses - with sodium and 5 mol% of silver - was submitted to Thermal Poling at 300°C/1kV and investigated by Energy Dispersive Spectroscopy. It was verified that not only sodium ions but also silver ions are depleted beneath the anode surface and accumulate below the poled layer.

Keywords: phosphate glasses; glass-ceramics; tantalum; niobium; silver; second harmonic generation; thermal poling.

RESUMO

Vidros fosfatos alcalinos contendo tântalo e nióbio são materiais relevantes para aplicações fotônicas devido a diversas propriedades como alta estabilidade térmica, química e mecânica, ampla janela de transparência, baixa energia de fônons e alta eficiência quântica de íons luminescentes. A maior quantidade de seus respectivos óxidos relatada em um vidro fosfato é de 50% em mol, com regiões ricas em tântalo ou nióbio que podem induzir precipitação de fases cristalinas do tipo $M_2N_8O_{21}$ (M = Na ou K e N = Nb ou Ta). Além dessas propriedades relevantes, os vidros fosfatos de tântalo/nióbio apresentam baixo custo de produção devido à abundância de matérias-primas e à relevância estratégica nacional, uma vez que são considerados elementos de interesse estratégico para o desenvolvimento tecnológico. Portanto, esses materiais vítreos são promissores como matrizes luminescentes, em óptica não linear para geração de segundo harmônico e substratos para microestruturação de propriedades ópticas. Assim, o presente trabalho pode ser dividido em três partes principais: i) estudo de vidros fosfatos de sódio com adição de óxido de tântalo de 40 a 50% em mol, bem como dos vidros dopados com európio e sua avaliação quando submetidos a Polarização e Micropolarização Térmica. Esses vidros foram analisados por Calorimetria Exploratória Diferencial, Difração de Raios-X, espectroscopias Raman e Infravermelho, Índice de Refração, transparência na região UV-Vis e luminescência. Pelas medidas verificou-se que a adição de tântalo aumenta a temperatura de transição vítrea, ou seja, aumentando a conectividade da rede vítrea; a mudança do band-gap para comprimentos de onda mais longos com alta transparência (~80%); índice de refração relativamente alto (~1.9 em 532 nm); e modifica fortemente a razão de assimetria $^7F_2/^7F_1$ nos vidros dopados com Eu^{3+}. Alguns desses vidros foram polarizados termicamente utilizando eletrodo microestruturado, sob temperatura de 250°C e tensão de 600 a 900V dependendo da composição do vidro. As medidas de Franjas de Maker confirmaram a Geração de Segundo Harmônico (GSH) nos vidros polarizados atribuídos ao modelo de Segundo Harmônico Induzido por Campo Elétrico (EFISH), bem como pelas medidas correlativas de micro-GSH/Raman/Luminescência em um deles. O eletrodo microestruturado permitiu a microimpressão de padrões nos vidros, conforme micrografias e medidas de Microscopia de Força Atômica, com alterações na topologia, variação no índice e efeitos de borda nas medidas de GSH, sugerindo um controle em microescala das propriedades ópticas. ii) estudo de vitrocerâmicas (VC) de fosfato contendo 47,5% molar de óxido de tântalo dopado com európio e seu comportamento quando submetidas a Polarização Térmica. Foi possível obter VC translúcidas com apenas uma fase cristalina, $Na_2Ta_8O_{21}$, com grau de cristalinidade e

transparência controlado em função do tempo de tratamento térmico. Por fotoluminescência verificou-se que o íon európio está presente na fase cristalina; já que, entre outros, a razão das transições [$^5D_0 \rightarrow$] $^7F_2/^7F_1$ diminui com o aumento do grau de cristalinidade. Algumas dessas VC foram polarizadas termicamente e através das medidas de corrente elétrica durante a polarização, Espectrometria de Massa de Íons Secundários por Tempo de Voo, Infravermelho e Franjas de Maker foi possível estabelecer um modelo do comportamento destas VC à polarização: os íons de sódio na fase cristalina não migram dentro do material, mas apenas aqueles que ainda estão dentro da fase vítrea, com a principal alteração ocorrendo na estrutura do fosfato após a saída do sódio. Além disso, a GSH das VC é atribuída apenas devido à polarização térmica e é originada pelo EFISH, como ocorre nos vidros. O valor calculado de $\chi^{(2)}$ das VC mostra uma magnitude menor que o respectivo vidro polarizado. E iii) estudo de vidros fosfatos contendo 45 % em mol de óxido de nióbio aumentando a quantidade de prata e também co-dopados com antimônio, assim como um estudo preliminar de seu comportamento quando submetido a Polarização Térmica. Foi possível incorporar grande quantidade de prata nesses vidros, alcançando ~9% molar em vidros com potássio e ~5% molar com sódio. O incremento de prata nesses vidros diminui o valor da Tg, ou seja, a conectividade da rede; bem como diminui a estabilidade frente à cristalização com a prata atuando como centro de nucleação. A adição de prata também desloca o band-gap para maiores comprimentos de onda e aumenta o índice de refração. Os vidros co-dopados (prata/antimônio) com sódio apresentaram colorações diferentes e, consequentemente, espectros de absorção ao variar a temperatura de recozimento. O vidro recozido na Tg apresenta uma banda relacionada à ressonância de plasmon que não aparece nos vidros recozidos em temperaturas mais baixas. Um destes vidros - com sódio e 5% em mol de prata - foi submetido à Polarização Térmica a 300°C/1kV e avaliado por Espectroscopia de Energia Dispersiva. Verificou-se que, além dos íons de sódio, também ocorre depleção dos íons de prata sob o ânodo que se acumula após a camada de depleção.

Palavras-Chave: vidros fosfatos; vitrocerâmicas; tântalo; nióbio; prata; geração de segundo harmônico; polarização térmica.

LIST OF FIGURES

LIST OF TABLES

LIST OF SYMBOLS

α	Absorption coefficient
ψ	Angle that varies the polarization of light in the measure of Maker Fringes
θ	Angle that varies the position of the sample in the measure of Maker Fringes
θ_B	Brewster's angle
Lc	Coherence length
cc	Complex conjugate
Tc	Crystallization peak temperature
χ_{eff}	Effective susceptibility
i	Electric current
E	Electric field
ν	Frequency
Tg	Glass transition temperature
[Tg]	Glass transition temperature range
k	Imaginary part of the refraction index
B	Magnetic field
Tm	Melting temperature
β	Microscopy hyperpolarizability
n_2	Non-linear refractive index
tn	Nose time
Tn	Nose temperature
N	Number of dipoles per unit volume
Tx	Onset crystallization temperature
$\chi^{(n)}$	Optical susceptibility of order *n*
L	Orbital Angular Momentum Quantum Number
$P^{(n)}$	Polarization of order *n*
n	Refractive index (linear)/ real part
$\chi^{(2)}_{EFISH}$	Second-order susceptibility due to EFISH
$\chi^{(2)}_{reor.}$	Second-order susceptibility due to reorientation
S	Spin Angular Momentum Quantum Number
$C_{\infty v}$	Symmetry with infinite rotation axis
J	Total Angular Momentum Quantum Number
ε_0	Vacuum permittivity

k	Wave vector
λ	Wavelength
$\tilde{\upsilon}$	Wavenumber

LIST OF ABBREVIATIONS AND ACRONYMS

ASTM	American Society for Testing Materials
AFM	Atomic Force Microscopy
BBO	Beta-Barium Borate
BLF	Bottom Loading Furnace
BO	Bridging Oxygen
CBMM	*Companhia Brasileira de Metalurgia e Mineração*
CCD	Charge-Coupled Device
C-Labmu	*Complexo de Laboratórios multiusuários*
C	Crystal growth rate
DTGS	Deuterated Triglycine Sulfate Detector
DFG	Difference Frequency Generation
DSC	Differential Scanning Calorimetry
DBO	Double Bonded Oxygen
EFISH	Electric Field Induced Second Harmonic
ED	Electric Dipole
EDS	Energy Dispersive Spectroscopy
EPR	Electron Paramagnetic Resonance
E_2	Energy of excited state
E_1	Energy of ground state
E_2’	Energy of intermediary state
FCC	Face Centered Cubic
FTIR	Fourier-Transform InfraRed spectroscopy
GB	Gaussian-Bessel
GC	Glass-ceramic
HT	Heat Treatment
IR	InfraRed
ICMCB	*Institut de Chimie de la Matiére Condensée de Bordeaux*
ISM	*Institut de Sciences Moléculaires*
ITO	Indium Tin Oxide
KPFM	Kelvin Probe Force Microscopy
LABMAT	*Laboratório de Pesquisa em Materiais*
LaMaV	*Laboratório de Materiais Vítreos*

LO	Linear Optics
MD	Magnetic Dipole
NC	Nanocluster
NP	Nanoparticle
NBO	Non-Bridging Oxygen
NLO	Non-Linear Optics
NR	Non-Radiative Decay
N	Nucleation rate
OR	Optical Rectification
OPD	Optical Path Difference
PTR	Photo-Thermo-Refractive
PLACAMAT	*PLataforme Aquitaine de CAractérisation des MATériaux*
S	Polarization of light perpendicular to the plane (*Senkrecht*)
P	Polarization of light parallel to the plane (*Parallel*)
KDP	Potassium Di-hydrogen Phosphate
R	Radiative Decay
RE	Rare-Earth
QPM	Quasi Phase Matching
SCL	Supercooled Liquid
SHG	Second Harmonic Generation
SFG	Sum Frequency Generation
TTT	Temperature - Time - Transformation
ToF-SIMS	Time of Flight Secondary-Ion Mass Spectrometry
T	Transmittance
RE^{3+}	Trivalent Rare-Earth Ions
UV-Vis-Nir	Ultraviolet-Visible-Near infrared
XRD	X-ray Diffraction
WDS	Wavelength-Dispersive X-Ray Spectroscopy

SUMMARY

1 INTRODUCTION AND MOTIVATIONS

One of the most important research lines from an academic and technological point of view is the study and development of materials. Among these are glasses and glass-ceramics, and glass can be defined as "a solid, non-crystalline, which presents the phenomenon of glass transition" (ZARZYCKI, 1991[1]), and is distinguished from other materials by characteristics such as lack of porosity, excellent insulating properties (dielectric) and low rate of expansion and thermal conductivity, and especially the ease of preparation. Glass-ceramics consist of materials in which there is simultaneously a glass phase and one or more crystalline phases, and which are commonly obtained by the growth of crystals by heat treatment performed on glasses. Research with vitreous materials has aroused a lot of interest in recent years, since, for the most part, it constitutes the main element in devices for photonics. The range of applications of photonics is wide and includes optical communication, modulation, amplification, information and computation, biochemical detection, image processing (FIGURE 1). This list is not exhaustive and other application domains are possible.

Figure 1 - Examples of glasses in photonic applications.

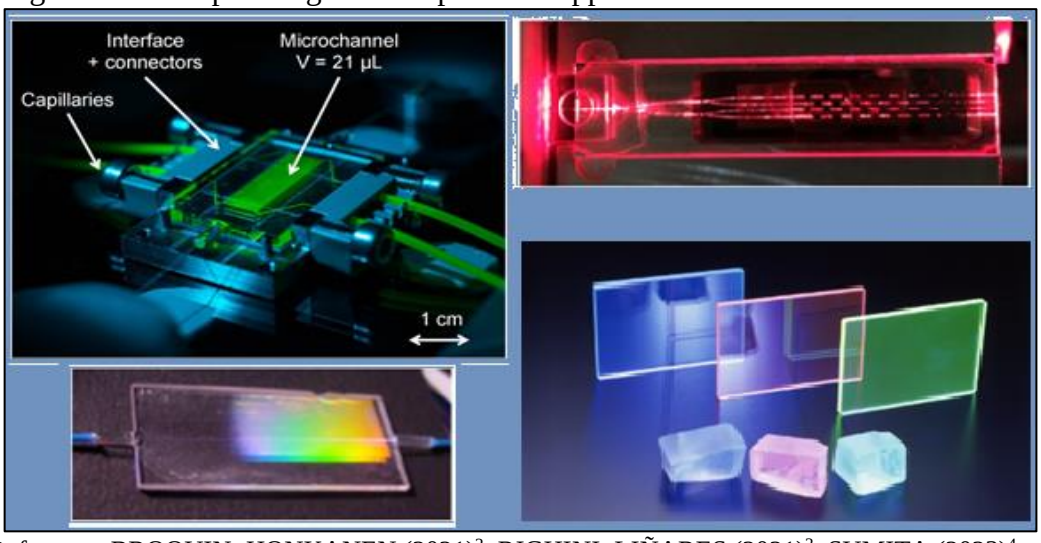

Reference: BROQUIN; HONKANEN (2021)[2]; RIGHINI; LIÑARES (2021)[3]; SUMITA (2023)[4].
Note: Optofluidic sensor realized on BF33 glass wafer for the measurement of radioactive elements diluted in highly concentrated nitric acid. Distribute Bragg Reflectors laser pigtailed to HI1060 single mode fibers. Light propagation along a waveguide chip. UV to Visible light converter fluorescent glasses.

[1] ZARZYCKI, J. **Glasses and the vitreous state**. New York: University Press, 1991.
[2] BROQUIN, J-E; HONKANEN, S. Integrated photonics on glass: a review of the ion-exchange technology achievements. **Applied Sciences**, Switzerland, v.11, p.4472, 2021.
[3] RHIGINI, G.C.; LIÑARES, J. Active and quantum integrated photonic elements by ion exchange in glass. **Applied Sciences**, Switzerland, v.11, p.5222, 2021.
[4] SUMITA new glass & fiber optics. Available in: https://www.sumita-opt.co.jp/en/products/lumilass.html. Access: 25 oct. 2023.

Among classical oxide glass formers, phosphate glasses, in general, are relatively cheap, easy to prepare and have higher solubility of rare-earth and transition metal ions compared to traditional silica glasses. Furthermore, the addition of heavy metallic oxides to these glasses, such as Nb_2O_5, WO_3 and Ta_2O_5, tend, for example, to increase the transparency in the infrared, with a decrease in phonon energy, which allows improvement of rare-earth ion luminescence for photonic applications. Also, both, niobium and tantalum are abundant in Brazil, which make them national strategic elements for emerging technologies.

The addition of tantalum oxide in high concentrations has already been studied by the glass research group at UNIFAL-MG in recent years, reaching a content of around 50 mol% of Ta_2O_5. Phosphate glasses containing high amounts of niobium have also been studied by the group and, in general, are much more studied materials over the world comparing to tantalum-based glasses since the latter requires higher melting temperatures which makes their preparation harder. However, tantalum present higher polarizability than niobium, which, among others characteristics, justify its investigation. They present similar behavior, with relatively high refractive indices, increased quantum efficiency when doped with rare earth, and are suitable for the preparation of glass-ceramics with the bronze-like perovskite phase $Na_2Ta_8O_{21}$ / $Na_2Nb_8O_{21}$, which is an interesting phase in non-linear optical applications. Thus, the interest in working with these glass compositions comes from both the technological part, in photonic applications; and also, the low cost for glass preparation.

Moreover, glasses containing silver have several applications depending on the silver nature, as ions, clusters or metallic nanoparticles (NP). AgNP-containing glasses are promising materials for non-linear optical devices, photoluminescence and optical amplifiers. Plasmonic metallic nanoparticles have attracted significant interest due to their unique optical properties. Potential applications of metallic nanoparticles include but are not limited to biosensing, surface-enhanced Raman spectroscopy, solar cells, photocatalysis. Also, it is known that silver molecular clusters (SMC) formed in glasses of different compositions are characterized by intense broadband luminescence in the visible spectral range. For example, it has been proposed to use the luminescence of SMC in glass to design phosphors white LEDs, down-converters for solar cells, and data recording and storage devices. Glasses containing silver can also be used for direct laser writing with formation of NP and color centers (FIGURE 2A).

Figure 2 - A) Glass containing silver for direct laser writing (optical image, overlay of optical image and SEM image, SEM image of NP and EDX signa of Ag); B) SHG signals of the cross-section of a multi-hole array thermally poled; C/D) Optical image of the grating imprinted by thermal poling on a glass and its SHG periodical structuring.

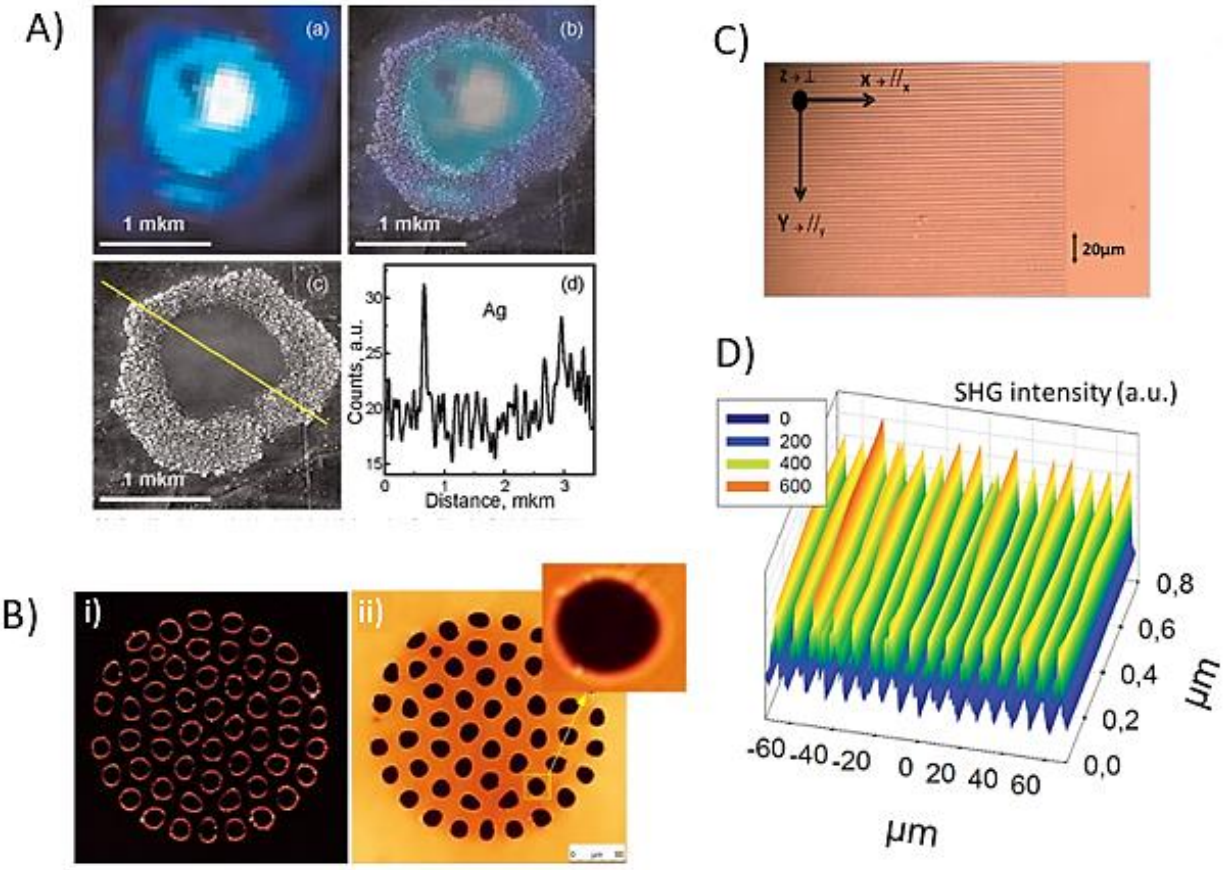

Reference: A) VASILEVA *et al.* (2015)[5]; B) HUANG *et al.* (2018)[6]; C/D) DUSSAUZE *et al.* (2016)[7].

Furthermore, devices such as optical switches, electro-optical modulators, frequency converters, etc., require a material exhibiting1 non-linear optical properties, such as Second Harmonic Generation (SHG) (FIGURE 3). The materials that have been used for non-linear optics are inorganic crystals that have a strong non-linear response. However, these materials may have certain disadvantages, as they are difficult to manufacture and induce significant intensity losses as light propagates. Optical glasses are a good alternative to crystal because they are easy to manufacture and have good light transmission with low losses. However, because they are isotropic, the glasses are macroscopically considered centrosymmetric and do not present second-order nonlinearity, which can be acquired using the Thermal Poling

[5] VASILEVA, A.A. *et al.* Structural features of silver-doped phosphate glasses in zone of femtosecond laser-induced modification. **Journal of Solid-State Chemistry**, [S.l.], v.230, p.56-60, 2015.
[6] HUANG, L. *et al.* Thermal poling of multi-wire array optical fiber. **Optics Express**, [S,l.], v.26, p.674-679, 2018.
[7] DUSSAUZE, M. *et al.* Accurate Second Harmonic Generation microimprinting in glassy oxide materials. **Advanced Optical Materials**, Weinheim, v.4, p.929-935, 2016.

technique. Thermal Poling consists of applying an electric field to the material at the same time that the glass is heated below Tg inducing some mobile cations present in the material, such as Na^+, to migrate, resulting in a depletion layer. The field is removed after cooling and the final material presents non-linear properties due to the implanted permanent static electric field.

Figure 3 - Second Harmonic Generation.

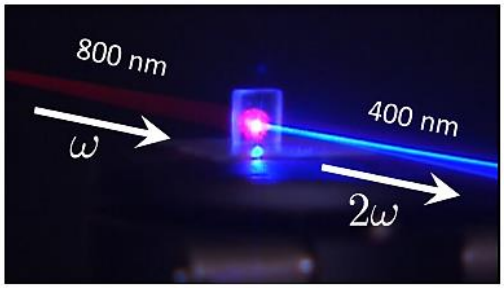

Reference: REIS, 2017 [8].

The number of article publications containing these terms is presented in Figure 4A, and it is observed that the use of this technique has been increased in the last decades and its use for glasses too, but it still not that much pronounced. Additionally in Figure 4B is a comparison of articles containing terms SHG and SHG/glasses, from which it is clearly seen that SHG preferentially investigated in other materials.

Figure 4 - Evolution of publications of thermal poling and SHG in glasses along the years.

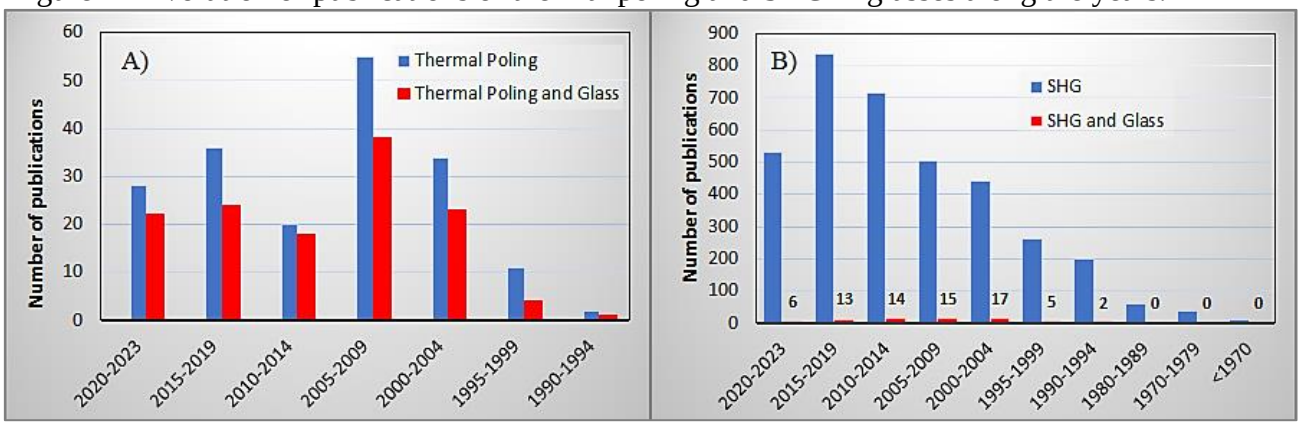

Reference: AUTHOR.
Note: Data collected from *Periódicos Capes* for only articles published, words appearing in title or subject.

The use of the Thermal Poling technique in phosphate glasses, especially niobium borophosphate glasses, is already well established by several studies carried out mainly by research groups at the Institutes in Bordeaux in France (ICMCB and ISM); showing excellent

[8] REIS, G.B. **Interpreting the absorption spectrum of two photons in semiconductor nanocrystals $CuInS_2$.** 2017. 81p. Thesis (Master in Physics) - Universidade Federal de Alfenas, Poços de Caldas, 2017.

results. It is also known that the highest SHG responses were obtained for poled glasses with compositions in which niobium-rich regions formation occurs that lead to phase crystallization of sodium niobate. Thus, due to the similarity between niobium and tantalum, using phosphate glasses with high tantalum contents is interesting to verify their potentiality in non-linear optical applications. Also, Thermal Poling can be an important instrument for luminescence studies by inserting rare-earth ions into the strong electric field, and this type of study is still poorly performed, as well as the unreported thermal poling in tantalum phosphate glasses. Besides, although thermal poling in niobium phosphate/borophosphate glasses was already investigated, thermal poling in silver doped niobium phosphate glasses (and silver-doped glasses in general) are not much studied.

In addition, the development of materials whose properties can be controlled and modified at a micrometer scale is increasingly being sought. Thermal Micropoling can then be an instrument for controlling different properties, such as the refractive index, variation in the reactivity of the glasses (acid attacks, attack of reactive ions, etc.), controlling the second harmonic response on a microscopic scale. Thermal Poling may even be applied on multi-wire array fibers (FIGURE 2B) or for Second Harmonic diffraction grating (FIGURE 2C/D). In this case, the Poling experiment occurs using microstructured electrodes in order to imprint different patterns on the material.

Finally, the Second Harmonic Generation in glass-ceramics generally occurs due to the presence of non-centrosymmetric crystalline phases. However, it may also be of interest to verify the behavior of glass-ceramics when using Thermal Poling, and how mobile ions behave when there is a crystalline phase in the glass. Furthermore, whether or not there is a change in luminescence with the presence of rare earth ions in the crystalline phase instead of the glass phase.

Therefore, the research work presented in this thesis was centered on the behavior of alkaline phosphate glasses and glass-ceramics containing high tantalum or niobium contents under thermal poling and micropoling for photonic applications. Thus, the thesis is organized as follows:

Chapter I - Theoretical references presenting concepts about glasses and glass-ceramics, phosphate glass materials and the effect of tantalum or niobium oxide addition; glasses containing silver, luminescence; and non-linear optics, Second Harmonic Generation, Thermal Poling and Micropoling of glasses;

Chapter II – This chapter presents the theoretical principles and experimental details of characterization techniques used in this work, mainly Differential Scanning Calorimetry, X-ray

diffraction, Raman/ Infrared/ Uv-vis spectroscopies, refractive index, Luminescence, Atomic Force Microscopy, Time of Flight Secondary-Ion Mass Spectrometry, Wavelength-Dispersive X-Ray Spectroscopy, Energy Dispersive Spectroscopy, Maker Fringe, micro-SHG/Raman/luminescence, Index variation;

Chapter III focuses on the preparation and characterization of sodium phosphate glasses with high tantalum oxide contents (40 to 50% in mol) both undoped and doped with europium;

Chapter IV is related to both Thermal Poling and Micropoling on these sodium tantalum phosphate glasses studied in Chapter III, followed by the respective structural, topological and optical characterizations;

Chapter V presents a study for the preparation of Eu^{3+}-doped glass-ceramics by heat treatment of a sodium tantalum phosphate glass composition containing 47.5 mol% of Ta_2O_5;

Chapter VI focuses on thermal poling performed of these glass-ceramic and subsequent characterizations;

Chapter VII presents the preparation and characterization of sodium/potassium phosphate glasses containing niobium oxide contents (45 mol%) doped with silver and a preliminary thermal poling study;

Finally, it is presented the General Conclusions.

CHAPTER I - THEORETICAL REFERENCES

CHAPTER I – THEORETICAL REFERENCES

This chapter presents a theoretical review of the subjects discussed in this Thesis, including concepts such as glasses and glass-ceramics, glasses containing silver, luminescence, and Second Harmonic Generation in glasses and glass-ceramics by Thermal Poling.

I-1 GENERAL CONCEPTS OF GLASSES

Glass is one of the oldest materials and it exists also in a natural form, as example, obsidian, which is a natural volcanic glass. The first report of obtaining glass is attributed to the Phoenicians, who used sodium nitrate (which served to hold their cauldrons) placed on sand and observed the flow of a transparent liquid that rapidly solidified after some time in fire, that considered the origin of glasses. Since then, glasses have been developed and used in different ways. In the 15th century, glass was used mainly as decoration for cathedrals, churches and palaces. The 18th, 19th and 20th centuries marked important advances in the manufacture and applications of glass (CARTER; NORTON, 2013; CHOPINET, 2019; MATOS, 2012; THOMAS, 2013).

The great interest in glasses is due, among other characteristics, that they are suitable for been used in almost all aspects of activities: at home, in industry, in art, in science, etc. They are present in microscopes, cameras, waveguides, chemical and clinical analyses, civil construction, etc. (HALIMAH *et al*., 2010). Applications such as optical fibers, which are capable of transmitting more information than copper, laser tubes for CO_2 in microsurgery, and solar cells can also be mentioned (KHADAR; SEBASTIAN, 2004). More recently, it is possible to mention “smart glass”, such as photochromic, electrochromic or thermochromic glass, which, among others, are electronically controlled to change from transparent to colored or opaque, which windows in houses or automobiles reduce heat transmission and reduce noise, which can be used to display images or serve as an interactive touchscreen (CORNING, 2022). According to the latest report by Report Ocean (2022) the global market for advanced glass is expected to reach around US$95 billion by 2026.

Over the years, glass has received various definitions. Zachariasen (1932 *apud* SIDEL, 2011, p. 19) defined that glasses are: “essentially non-crystalline solids obtained by quenching liquids”. This definition does not accurately characterize a glass, as it does not take into account those obtained by means other than melt/quenching. Other methods to prepare glasses are sol-

gel and sol-gel/emulsion (AHMADI *et al.*, 2022), chemical vapor deposition (MOCHALOV *et al.*, 2015), etc.

However, it is correct that glasses are non-crystalline materials, which indicates that they do not present regularity in their long-range atomic order. In his article, "The Atomic Arrangement in Glass", Zachariasen proposed that regardless of whether the material has a crystalline or non-crystalline structure, it should have similar chemical bonds, but with different structures. Figure I-1A/B presents a two-dimensional scheme for a crystal arrangement and for a silica glass - SiO_2, respectively. These representations suggested by Zachariasen were theoretical at the time, however, 80 years later, Huang *et al.* (2012) confirmed the glass structure through the analysis of High-Resolution Scanning Electron Microscopy, shown in Figure I-1C.

Figure I-1 - Two-dimensional representation: (A) of the crystalline arrangement of a crystal of composition SiO_2, (B) of the lattice of the glass of the same composition and (C) High Resolution Scanning Electron Microscopy of a two-dimensional silica glass on a graphene film.

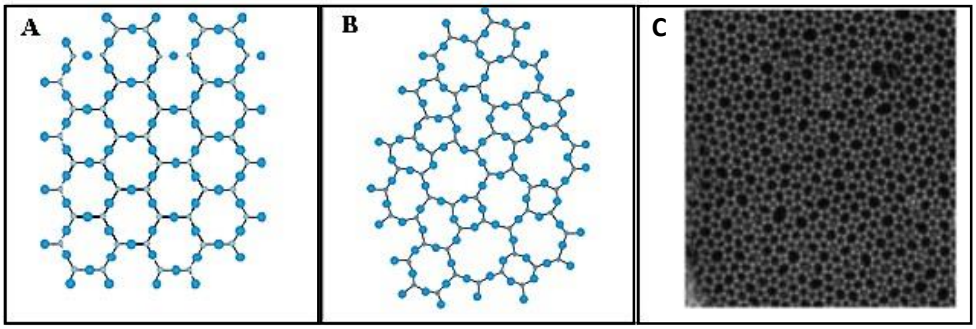

Reference: A/B) GONÇALVES (2014, p.25) and C) HUANG *et al.* (2012, p.1083).

Materials with a crystalline arrangement, in general, as in Figure I-1A, are considered anisotropic, which means that their properties are dependent on crystallographic orientation. On the other hand, non-crystalline materials, as in Figure I-1B, are isotropic, that is, the properties are independent of the direction (CALLISTER, 2007).

Usually, the term non-crystalline is taken as a synonym for amorphous, and therefore glass is often called an amorphous material. For Gupta (1996) these cannot be considered synonyms, because for the author, from the point of view of thermodynamics, non-crystalline solids can be divided into: glasses and amorphous solids. Non-crystalline solids would be those that do not show long-range order in the three-dimensional arrangement. When there is the presence of a glass transition, this is then considered a glass; otherwise, it is considered amorphous.

In 1949, the American Society for Testing Materials (ASTM) defined glass as: “the inorganic, amorphous, product of a rapidly cooled melt”. This is also a restricted concept, as it does not consider, for example, metallic and organic glasses (KHADAR; SEBASTIAN, 2004).

Thus, a definition of glass proposed by Zarzycki (1991), which does not present the mentioned restrictions and basically is in agreement with the distinction signalize by Gupta, consists of: “**a non-crystalline solid that presents glass transition**”. The glass transition temperature (T_g) can be considered as the temperature at which the entire liquid passes to the glassy state - a property that differentiates glass from crystal. As well, T_g is also arbitrarily considered as the temperature at which the material has a viscosity of 10^{13} P[9], and thus, at this viscosity it would be too thick to flow (CASSAR, 2014; FOTHERINGHAM, 2019; MASSERA, 2009).

A recent definition of glasses was proposed by Zanotto and Mauro (2017):

> [...] Glass is a nonequilibrium, **noncrystalline** condensed state of matter that exhibits a **glass transition**. The structure of glasses is similar to that of their parent supercooled liquids (SCL), and they spontaneously relax toward the SCL state. Their ultimate fate, in the limit of infinite time, is to crystallize (ZANOTTO; MAURO, 2017, p. 494, emphasis added).

The most traditional method for obtaining glass is the melt/quenching. Starting the cooling of the molten material at a high temperature, a contraction occurs in the material until the melting temperature (T_m). From this point, depending on the cooling rate, one of two phenomena occurs (FIGURE I-2):

a) Low cooling rate - the atoms have enough time to rearrange themselves into an organized structure and the material reaches crystallization, then forming crystals and significantly reducing its specific volume (A→B→C→D);

b) High cooling rate - the material become more and more viscous, until the mobility at the atomic level practically ceases and the atoms fix spatially in a random and disordered arrange (maintaining the liquid structure), i.e., in a metastable state of supercooled liquid. The supercooled liquid then passes to the glassy state, through the glass transition temperature (T_g). In this case, there is a low reduction in the specific volume, and the material does not crystallize, but vitrifies (A→B→E→F).

[9] For comparison, the viscosity of water at room temperature is about 0.01P.

Figure I-2 - Melt-quenching for glasses and crystals - specific volume versus temperature.

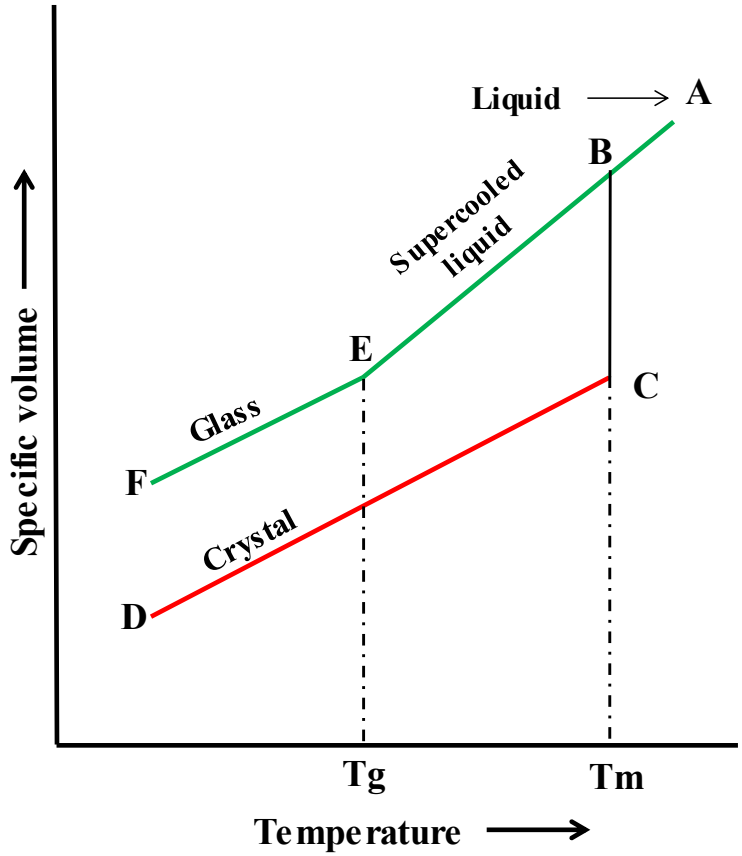

Reference: Translated from BATISTA; VIANNA (2022, p.269).

At constant pressure, T_g is not fixed like T_m, and varies with the rate of cooling (faster cooling shifts T_g to higher temperatures). Due to this condition, a glass transition range ([T_g]) is sometimes used, where the lower and upper limits are defined, respectively, by the lowest and highest cooling rates. In addition, observing the Figure I-2, it is possible to notice that the volume of the material is also affected by the cooling. In the case of crystals, the specific volume is smaller when compared to glass of the same mass. Glasses of the same composition may present different volumes depending on the colling rate; those with higher rates will present higher specific volumes, and therefore lower density.

After obtaining the glass, it is usually made a thermal treatment called “annealing” so that the internal tensions resulting from the cooling are relieved. And, by relieving these tensions, this process increases the mechanical strength of the glass (THOMAS, 2013).

In theory it is possible to obtain glass from any materials, since the liquid is quenching in an adequate cooling rate; but in practice this is not so simple, as the cooling rate for some materials has to be very high. Also, in addition to the cooling rate, the thickness must be taken into account, because together these variables indicate the ease or not of obtained a glass from

some compositions. Table I-1 presents the values for the cooling rate and critical thickness (smallest possible thickness to obtain the glass in the cooling rate) for some materials for the glass formation. Silica and germanium dioxide form glasses easily, unlike of water and silver, which have a high value of cooling rate (RIAÑO, 2006; VARSHNEYA, 2006).

Table I-1 - Cooling rate and critical thickness values for glass formation of some materials.

Material	**Cooling rate (Ks^{-1})**	**Critical thickness (cm)**
Silica	$2x10^{-4}$	400
Germanium dioxide	$7x10^{-2}$	07
Water	10^{7}	10^{-4}
Silver	10^{10}	10^{-5}

Reference: RIAÑO (2006, p. 22).

Thus, for preparing a glass, it is important that the precursor material is a good glass former. Some criteria have been proposed to establish the required conditions to obtain glasses from simple oxides from a structural point of view. One of the first criteria to verify the vitrification of simple oxides (stoichiometric formula A_mO_n) was proposed by Goldschimidt (1926), which was based on the ratio between the ionic radius of the cation (A) and the ionic radius of oxygen: r_A/r_O. For a glass-forming oxide, this ratio would be directly related to the coordination number of the central cation, considering a tetrahedral coordination (common characteristic to all glasses known at that time); being between 0.2 and 0.4. This criterion includes most of the forming oxides, but is incomplete, as, for example, BeO satisfies this criterion (r_A/r_O = 0.31Å/ 1.4Å = 0.221) but cannot be vitrified.

Zachariasen extended this concept of Goldschimidt's study and established a set of rules about the structural arrangements that could produce a glass from oxides (CARTER; NORTON, 2013; THOMAS, 2013):

1. The coordination number of the cation must be small;

2. None of the oxygens can be shared by more than two cations, as higher-order coordination would prevent variations in the angles of cation-oxygen bonds;

3. The oxygen polyhedron shares vertices but not edges or faces; in order to distance the cations as much as possible;

4. At least three vertices in each polyhedron must be shared with other polyhedron, resulting in a three-dimensional network.

Considering rules 2, 3 and 4, for oxides of formula A_2O_3 the oxygens form triangles around the A atoms. For the oxides AO_2 and A_2O_5, the oxygens form a tetrahedron. Finally, for the oxides AO_3 and A_2O_7, when the oxygens are arranged in an octahedral form. Therefore, it was Zachariasen who first used the term "**formers**" to indicate oxides that can vitrify pure. Among the main formers are: SiO_2, GeO_2, Be_2O_3, P_2O_5 and V_2O_5 (MATOS, 2012; THOMAS, 2013).

"**Modifiers**" oxides are those that do not participate directly in the main structure; so, they do not form the polyhedra in the structure like the formers, and instead tend to break the continuity of the network. The cations of the modifiers in general occupy the vacancies that form in the glassy structure and they are randomly distributed[10]. These cations bind to "Non-Bridging Oxygen" (NBO), that is, oxygens that do not give continuity to the glass network. The "Bridging Oxygen" (BO) bind to the cations of the former and increase the connectivity of the vitreous network. Modifiers generally make glass easier to form at a certain temperature and decrease the melting temperature but increase its chemical reactivity. Among the main modifiers are alkaline and alkaline earth oxides, such as: Li_2O, Na_2O, K_2O, CaO and BaO. Figure I-3 presents a schematic representation of the bonds in a glass between oxygen and cations of the formers and modifiers (FERENCZ, 2013; THOMAS, 2013).

Figure I-3 - Two-dimensional schematic representation of bonds in a glass.

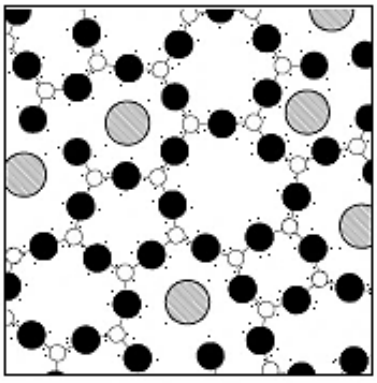

Reference: CASSAR (2014, p. 08).

Note: The spheres represent atoms and the lines represent bonds. The white atoms are network formers, the black ones represent oxygens and the hatched ones the modifiers. Atom and bond sizes are for illustrative purposes only.

[10] Although this is the main theory that describes the structure of the glasses, there are theories that some oxides added to the former oxides are not randomly distributed, but that they occupy different sites forming a "sub-net" with a certain degree of ordering at a short distance. This was pointed out by Fragoso (2003) who states that the distribution of niobate groups in the La_2O_3-Nb_2O_5-B_2O_3 vitreous matrix does not occur randomly, contrary to the random aperiodic network model that is the most commonly accepted for glass systems.

Some oxides that do not easily form glasses pure, but when mixed with the former oxides may occupy the vitreous network in the position of the former or in the position of the modifier (generally conferring improvements in the properties of the glass) were given the name of "**intermediates**". Among the main intermediates are: Al_2O_3, PbO, ZnO, CdO and TiO_2 (MATOS, 2012; THOMAS, 2013).

I-2 GENERAL CONCEPTS OF GLASS-CERAMICS

From glass it is possible to obtain glass-ceramic (GC) materials. The researcher Stanley D. Stookey, in the 50's, was the first one to use the term "glass-ceramics", when he "accidentally" noticed an uncontrolled crystallization process while working with photosensitive glasses containing silver and cerium. He started to study this material by controlling crystallization, thus obtaining the first patent for this type of material. Stookey defined glass-ceramics based on the process used: "[...] made by first melting and forming special glasses containing nucleating agents and then causing controlled crystallization of the glass particles" (DEUBENER *et al.*, 2018, p.03).

Since then, similar definitions have been used to identify materials with this same preparation - controlled crystallization of glasses. Thus, glass-ceramics are mostly defined as: "polycrystalline materials, which contain a residual glassy phase, produced from the controlled crystallization of glasses through heat treatments" (MATOS, 2012, p. 15, translated by the author). Still, some authors, such as Dabnun (2004) restrict this definition further, considering that glass-ceramic materials would be those that, in addition to being obtained by crystallization by heat treatment, must present between 90 and 98% of crystalline phase, whose crystal size is between 0.1 to 1.0 μm. Boccaccini *et al.* (2006) consider a range of 50 to 90% of crystals and Pascual (2015) from 30 to 70%.

These definitions are based on the initial definition given to glass-ceramics, which was in agreement with the material that was obtained at that time. However, they do not take into account only the final material, restricting the obtaining method. Furthermore, although originally the term "glass-ceramics" only described materials with a high percentage of crystals, glass-ceramics with significantly lower percentages have also been developed over the last few years (DEUBENER *et al.*, 2018).

Deubener *et al.* (2018) published an article entitled "Update definition of glass-ceramic" in which the researches review the definition of glass-ceramic to cover different methods and

the percentage of crystalline phase in the final material. According to the authors, glass-ceramics are:

> [...] inorganic, non-metallic materials prepared by controlled crystallization of glasses via different processing methods. They contain at least one type of functional crystalline phase and a residual glass. The volume fraction crystallized may vary from ppm to almost 100% (DEUBENER *et al.*, 2018, p. 09).

This definition still considers obtaining glass-ceramics by growing crystals in glasses, but the method is not limited to conventional heat treatments. In addition, it does not restrict the percentage of crystalline phase in the material, which may even be in *ppm*. Despite this, it is point out that, in their conception, materials are not considered glass-ceramics if the non-crystalline precursors are not glasses (lack of T_g), those in which only metallic particles are precipitated after crystallization (they are not ceramics) and if they contain only nucleants (desired functionality is not achieved). They also exclude materials that show uncontrolled crystallization, since they are unwanted microstructures and, consequently, unwanted properties (DEUBENER *et al.*, 2018). In this work, glass-ceramics will be considered simply as: "**materials that present a crystalline phase in a glass matrix**".

Some of the characteristics and advantages of glass-ceramics are: processing efficiency in the glassy state, dimensional control in the final product and good mechanical properties. Also, in most cases, the crystal has greater hardness than the glass phase, so the appearance of defects less likely during its use, increasing the useful life of the material. Also, resistance to thermal shock, since the coefficient of thermal expansion may be close to zero, allowing the volume of the material not to vary over a wide temperature range (DABNUN, 2004; LO, 2016; MASSERA, 2009).

Regarding the technological characteristics for glass-ceramics, there is the possibility of obtaining them with porosity very close to zero and; within certain limits, the control of optical, mechanical, thermal and electrical properties. Furthermore, they can exhibit quantum crystal properties if optically active ions are isolated in the crystals. Still, with the ions present in the crystal, energy transfer processes can be optimized depending on the frequency of phonons in the medium, the distance between the ions and the local order around them (MASSERA, 2009; RIAÑO, 2006).

There are applications of glass-ceramics in the mechanical, electronic, chemical, medical and scientific equipment industries, biological and domestic applications, etc. For example, in electronics, it has been used in microelectronics packaging; in odontology and medicine, bioactive glass-ceramics are used as dental implants and bone prostheses. In optical

fibers, they have applications in the most different fields: telecommunications (Internet, data transmission), diagnostic medicine (endoscopy), microscopy and precision lighting, study of cracks in structural components (airplane wings), remote detection and sensing, etc. (LO, 2016; VARSHNEYA, 2006).

There are several researches involving glass-ceramics in different fields, such as: crystallization and luminescence properties of Eu^{3+}-doped ZrF_4-BaF_2-$NaPO_3$ glass and glass-ceramics (GONCHARUK *et al.*, 2018); enhanced bioactive glass-ceramic coating on Ti_6Al_4V substrate by microwave processing technique for biomedical applications (GHOSH *et al.*, 2018), a one-step synthesis of rare-earth phosphate-borosilicate glass composites (DONATO *et al.*, 2018), combination of Na-Ca-phosphate and fluorapatite in wollastonite-diopside glass-ceramic: degradation and biocompatibility (MAHDY; AHMED; FARAG, 2021), effect of microstructure on up-conversion luminescent of $Tb^{3+/}Yb^{3+}$ co-doped phosphate glass and glass-ceramic (ZHAO *et al.*, 2019), structural, electrical and energy storage properties of BaO-Na_2O-Nb_2O_5-WO_3-P_2O_5 glass-ceramics system (IHYADIN *et al.*, 2019), controlled surface crystallization of lithium-zinc-alumosilicate glass-ceramics using Thermal Poling (SANDER *et al.*, 2021), high tantalum oxide content in Eu^{3+}-doped phosphate glass and glass-ceramics for photonic applications (MARCONDES *et al.*, 2020), etc.

In general, crystallization decreases transparency in the glass; however, it is possible to obtain transparent glass-ceramics (transparency is an important factor for observing electro-optical phenomena). Transparency (or opacity) will depend, among other factors, on the difference between the refractive index of the glass and crystalline phases, so that light dispersion is minimal at the glass/crystal interface; in addition to the size of the crystals (influences optical dispersion). According to Malakho (2006), to obtain transparent glass-ceramics, the crystal size should not be greater than 100 nm. Also, according to Marcondes (2019), the attenuation that occurs due to scattering can be insignificant if the particle size is smaller than 15 nm and the difference between the refractive index of the glass phase and the crystalline phase is 0.1. However, it still indicates that particles with sizes smaller than 30 nm and with differences in refractive index of up to 0.3 are acceptable if the particles are scattered.

Some different methods are used to prepare glass-ceramics, such as the petrurgic method[11] (CHEN *et al.*, 2018), sintering (PARTYKA *et al.*, 2016), laser-induced nucleation followed by crystallization (SENN *et al.*, 2018), incorporation of crystalline nanoparticles in

[11] Method in which the nucleation and crystal growth steps take place during the cooling step (slow). Usually used when the material contains a high percentage of transition metals and tends to crystallize, and mainly as a recovery of residues (BOCCACINI *et al.*, 2006).

glass (BATISTA *et al.*, 2023; ZHAO; EBENDORFF-HEIDEPRIEM, 2016), and more commonly through crystal growth performing conventional heat treatments on glass. As glass is in a metastable state, it can be crystallized under favorable conditions. Since the properties of glasses are influenced by crystallization processes, it is important to know the conditions under which it occurs and what effect it has on the material.

I-2.1 Traditional method of heat treatment for preparing glass-ceramics

The traditional method for preparing glass-ceramics is initially preparing a glass, i.e., in the case of the melt/quenching method - through the fast cooling of the molten material to a temperature lower than that of the nucleation and growth regions to avoid any type of uncontrolled crystallization. Then an annealing (below the T_g) is performed to eliminate any residual stresses that may have formed (LO, 2016; MATOS, 2012).

To obtain the crystalline phase, a heat treatment is performed at the glass above the T_g (above this temperature the viscosity decreases allowing the atoms to move), so crystals are grown inside. This heat treatment must be controlled (time and temperature) and can be done using two steps or one step (LO, 2016; MARCONDES, 2019; MATOS, 2012).

In crystallization process, **nucleation** occurs first, with the formation of small nuclei in the glass, being superficial or volumetric (internal). In superficial nucleation (heterogeneous), nuclei form on the surface of the material in a volume direction, while in volumetric nucleation (heterogeneous or homogeneous), they form in volume. In homogeneous nucleation, the formation of nuclei is random and uniform, and occurs when the entire volume of the material is chemically homogeneous and without imperfections. In practice, this hardly occurs alone, since the surface itself is an inevitable imperfection and impurities are also imperfections, which can cause the nucleus to form in favorable regions and with lower energy. When this occurs, then there is heterogeneous nucleation. Figure I-4 shows Scanning Electron Microscopy images of glasses with homogeneous and heterogeneous nucleation (ACÁCIO, 2006; CAETANO, 2013; LO, 2016; MARCONDES, 2019).

When the nuclei are stable, **crystallization** occurs, with the growth of the crystalline phase(s) from these nuclei. This is an important step because, even if the nuclei are formed, without grain growth it will not be possible to detect the phase, given the extremely small size. Although they can be simultaneous, these steps have different rates. The number of nuclei produced in a volume in a given time is called the Nucleation rate (N) and the rate at which the nuclei grow is called the Crystal growth rate (C) (ACÁCIO, 2006; LO, 2016; MAESTRI, 2018).

Figure I-4 - Scanning Electron Microscopy images: (a) homogeneous nucleation of a SiO_2-Al_2O_3-MgO-K_2O-F glass and (b) heterogeneous nucleation of a GeO_2-BaO-MnO glass.

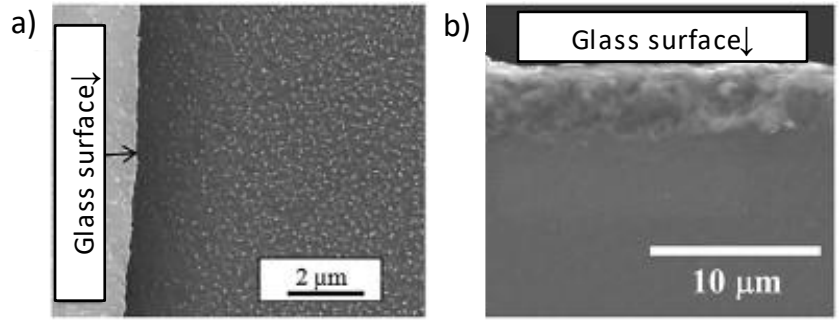

Reference: Translated from MARCONDES (2019, p.28).

The simplified diagram TTT - Temperature - Time - Transformation (FIGURE I-5) is commonly used to understand crystallization process. If a material is at a temperature equal to or above its melting temperature (T_m) it will be a liquid, therefore, only for temperatures below T_m the crystallization time starts to decrease until reaching the nose time (t_n)[12] and, only then, one can expect the formation of a crystalline material. However, as this temperature decreases, inversely, the viscosity increases and, as a consequence, the crystallization time increases again for temperatures below nose temperature (T_n). It can be seen that the gray area then represents the region where the crystallization of a material could occur (EVANGELISTA, 2021; RUPP, 2010; VOGEL, 1985).

Figure I-5 - TTT diagram.

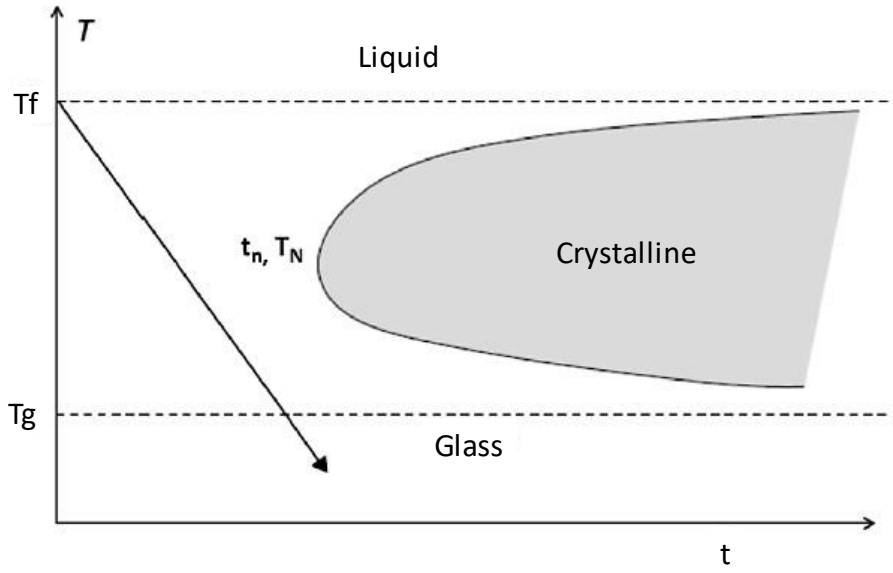

Reference: RUPP (2010, p.2810).

[12] Shorter time required for growth at any temperature (EVANGELISTA, 2021).

It is important that the glass-ceramic has an adequate number of nuclei in which the crystals can grow to obtain the crystalline phase. The shape of the crystals will depend on the type of growth that occurs in the vitreous matrix and on the chemistry of the crystal; and the size of the crystals will depend on how the nucleation and growth steps are carried out. Experimentally, the separation of the nucleation and growth is not trivial and involves the proper synthesis procedure and the choice of the correct matrix. The control of these processes can be even more complex due to the formation of several simultaneous crystalline phases within the glass. In general, the crystal composition is different from the glass matrix composition, indicating that the composition of the crystal-glass interface is constantly changing (LO, 2016; MASSERA, 2009).

I-3 CONCEPTS OF PHOSPHATE GLASSY MATERIALS

Phosphorus pentoxide, P_2O_5[13], is a glass former oxide, i.e., it forms the main network of the glass structure (covalently bonded) and also glass is obtained without the addition of other elements. This glass former oxide is according to the criteria in topic I-2, both by Goldschmidt (r_A/r_O = 0.34Å/ 1.4Å = 0.25) and by Zachariasen. Also, according to the last one, in the case of A_2O_5 oxide, the criteria are accomplished when the oxygens form a tetrahedron, which is therefore the basic unit of phosphate glasses - PO_4.

Phosphate glasses may have properties that cannot be obtained from traditional silicate glasses, since one of the differences between SiO_2 and P_2O_5 glass formers is based on the cation-oxygen ratio. In pure silica, the number of cations (silicon) is half the number of oxygens (ratio of 1:2), then each oxygen necessarily bonds to two silicon; in other words, tetrahedrons have all their vertices shared, which creates a rigid structure. This type of structure gives silica great stability and a high melting point. In the same way, phosphate glasses are formed by tetrahedra connected at their vertices; however, phosphorus is pentavalent, that is, in P_2O_5 the P:O ratio is 1:2.5; causing a double bond between phosphorus and one of the oxygens, consequently obstructing the continuation of the network through this vertex. Thus, the chain of phosphate glasses is more flexible, and its melting point is lower than that of silicates (ATTALLAH *et al.*, 2017; MUÑOZ *et al.*, 2019; ROMÃO, 2011).

So, the structure of phosphate glasses is described by a three-dimensional network with PO_4 tetrahedra covalently bonded by the vertices, in which each tetrahedron has three “BO”

[13] In Brazil, the primary source of phosphate is concentrated in deposits of igneous origin and is considered one of the strategic minerals by federal government (ALMEIDA *et al.*, 2015).

and a Double Bond Oxygen (DBO). The formation of the three-dimensional network is often called polymerization, due to the fact that, like polymers, they form repeating units of a mere, in this case, of the tetrahedron as a repeating unit (DIAS, 2010; HIRAO; TODOROKI; SOGA, 1994; VICENTE, 2004).

Despite being a good glass former, one of the characteristics of pure phosphate glass is its hygroscopicity, which can make it limited for many applications. Thus, to improve the chemical stability of the material, modifiers/intermediates are usually added to the glass. By adding the network modifiers to the phosphate glass structure, they break the bonds between the PO_4 chain and the three-dimensional network transforms into a one-dimensional, chain-like structure, "depolymerizing" the glass. The oxygens that form the O-M^+ bond, with M being any cation that acts as a modifier, are considered NBO. Figure I-6 presents a representation of the PO_4 structure with the classification of the oxygens in the glassy structure (a) and a two-dimensional scheme of the structure after addition of a modifier (b) (ALMEIDA, 2006; DIAS, 2010; MUÑOZ *et al.*, 2019).

Figure I-6 - (a) Representation of a PO_4 tetrahedron and oxygens classification and (b) Two-dimensional structure scheme for a phosphate glass with added modifier (Na^+).

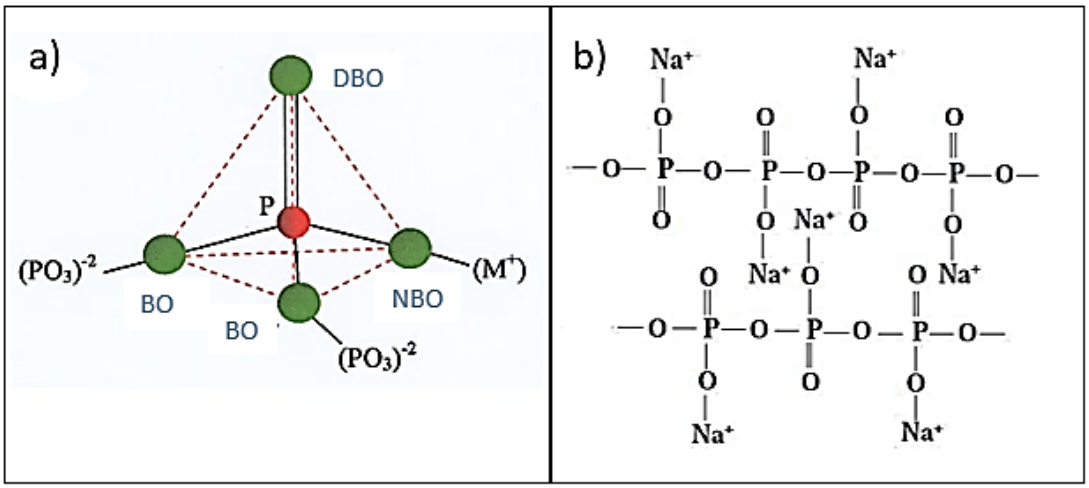

Reference: (a) Translated from VICENTE (2004, p.10) and (b) ALMEIDA (2006, p.08).

Therefore, the addition of modifiers induces a change in the structure - depolymerization, and depending on how many BO are present in the tetrahedron, the phosphates receive a different classification, according to the terminology Q^n (n = 0 to 3) – Figure I-7. When there is three BO, it is considered as a Q^3 and is nominated ultraphosphate (corresponds to pure glass with P_2O_5). When it starts to form chains of polyphosphates due to depolymerization, it is Q^2, nominated as metaphosphate. The Q^1 is based on anions with pyrophosphate composition, that

is, the pyrophosphates, and when the phosphate is isolated, and does not have any BO - Q^0, nominated as orthophosphate (HIRAO, TODOROKI; SOGA, 1994; MAHFOUDHI, 2019; VICENTE, 2004).

Figure I-7 - Q^n terminology for phosphates.

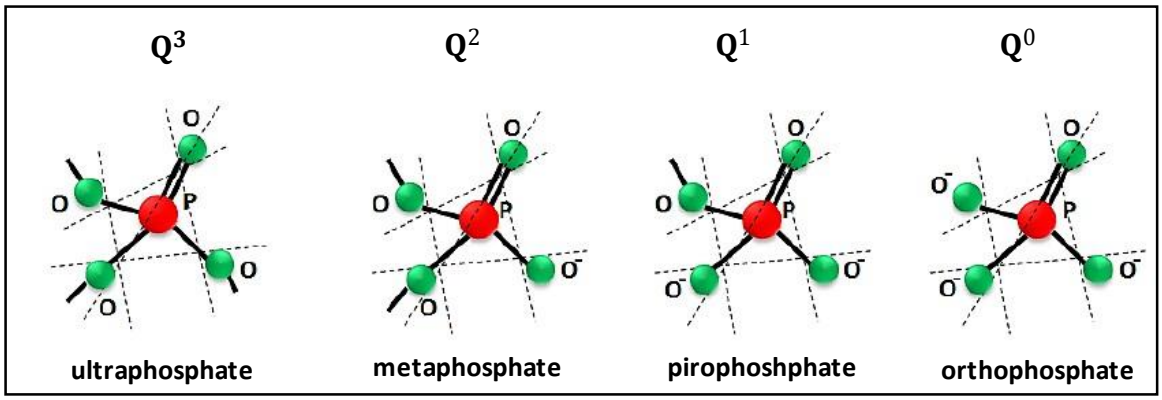

Reference: Modified from FARACO (2015, p.36).

With modifiers in the phosphate glass structure, the P = DBO bond becomes delocalized due to the polarization effect of electron clouds, generated by the positive charge of the modifier cation. This delocalization causes variations in the length of such bonds, affecting glass properties such as refractive index and non-linear optical properties (MAHFOUDHI, 2019; MUÑOZ *et al.*, 2019; VICENTE, 2004).

The most practical known use of phosphate glass is as a water softener when washing glassware in the form of sodium hexametaphosphate ($NaPO_3$) or Calgon® that helps avoid deposits of calcium. It is worth mentioning that there have been two fields of application where phosphates have made extraordinary achievements: as bioglasses and as laser host materials (MUÑOZ *et al.*, 2019). Additionally, several phosphate glass systems have been studied over the years. For example, Braz (2014) studied the preparation of glasses and glass-ceramics in the system $NaPO_3$-WO_3-PbF_2 undoped and doped with Eu^{3+}, and co-doped with Er^{3+}/Yb^{3+}, in which the crystalline phase obtained consists of $Pb_5F(PO_4)_3$, and also it was observed the decrease in phonon energy in the doped samples and the process of energy transfer between these ions more efficient in the co-doped samples. Caetano (2013) studied non-doped and Er^{3+}-doped aluminum phosphate glasses (P_2O_5-Al_2O_3-Na_2O), aiming at applications in optical fibers and amplifiers. Dias (2010) worked with PbO and Cr_2O_3 doped antimony phosphate glasses with possible application in diffraction gratings. Mahfoudhi (2019) used metaphosphate and polyphosphate glasses with a mixture of alkali-doped Eu^{3+} in order to modify the environment around the rare-earth ion by laser irradiation. The KPO_3-Nb_2O_5 system was studied by Lima

(2014), in which niobium was added in order to improve optical, mechanical, thermal and chemical stability[14].

I-3.1 Tantalum phosphate glassy materials

The chemical element tantalum - Ta (Z = 73) was discovered in 1802 in Sweden and is found mainly in the mineral tantalite[15], which in addition to tantalum also has niobium (Nb) - [(Fe,Mn)(Ta,Nb)$_2$O$_6$]. Due to the similarities, until the 19th century it was believed that both elements were the same, but it was confirmed in 1844 that they were different chemical elements. It is considered a relatively rare element, present in the earth's crust in the order of 0.000017% (CUNHA, 2018; MAESTRI, 2018).

In the oxide form, Ta_2O_5, has a melting temperature of 1800°C and an orthorhombic crystal structure, with polymorphism, in which the L-Ta_2O_5 phase is at low temperature and the H-Ta_2O_5 phase is at high temperature. The addition of Ta_2O_5 in phosphate glasses aims to improve thermal and chemical stability, mechanical properties, and especially linear and non-linear optical properties. The change of several of these properties is related to the structure of the vitreous network after the addition of Ta. Unlike alkalines that break the glass network and connect by ionic bonds, Ta bonds covalently replacing phosphorus, as an intermediate (CORDEIRO *et al.*, 2014; CUNHA, 2018; MARCONDES *et al.*, 2019; SOUSA *et al.*, 2020).

High amount of Ta_2O_5 in phosphate glasses have already been reported by the glass research group at UNIFAL-MG (Brazil), with 40 mol% in the KPO_3-Ta_2O_5 glass system (SOUSA *et al.*, 2020) and 50 mol% in the $NaPO_3$-Ta_2O_5 glass system (MARCONDES *et al.*, 2019). According to these studies, with the high concentration of tantalum, the glass structure is formed by chains of metaphosphates with a “first group of Ta atoms” connected to this network, forming Ta-O-P bonds. An “other group of atoms of Ta” consists of clusters [TaO_6] that are inserted in the middle of the main chain. These [TaO_6] units are octahedral and act within the glass as nuclei promoting crystallization, especially of tantalates crystalline phases.

Through studies of crystallization and preparation of transparent glass-ceramics from these phosphate glasses rich in tantalum, it is known that these clusters [TaO_6] lead to crystallization of bronze-like perovskite crystalline phase $Na_2Ta_8O_{21}$, which appears only with

[14] More information about phosphate glasses can be found in Muñoz *et al.* (2019).
[15] The largest reserves of this mineral are found in the states of Roraima (with a predominance in the south of the state) and Amapá in Brazil, with almost 52.1% of the world's reserves.

high concentrations of tantalum oxide. The perovskite crystal structure[16] has the general formula ABO_3, in which the A cation and the anions form a face-centered cubic (FCC) matrix with an octahedron at the center of the cell.

Furthermore, the addition of tantalum to phosphate glasses increased the glass transition temperature, the refractive index (1.97 in the potassium glasses with 40 mol% Ta_2O_5, and 1.94 in the sodium with 50 mol% Ta_2O_5), extended the transparency window (0.4 to 4 µm - $60KPO_3$-$40Ta_2O_5$), reduced phonon energy, and are promising for rare-earth ion incorporation and luminescent applications. Both glasses and glass-ceramics doped with Eu^{3+} were studied, showing high quantum efficiency due to the proximity of these ions to regions rich in [TaO_6] (MARCONDES *et al.*, 2020; SOUSA *et al.*, 2020). Figure I-8 presents the proposed structure of the europium-doped sodium phosphate glass with a high concentration of tantalum.

Figure I-8 - Proposed structure for europium-doped high tantalum sodium phosphate glass.

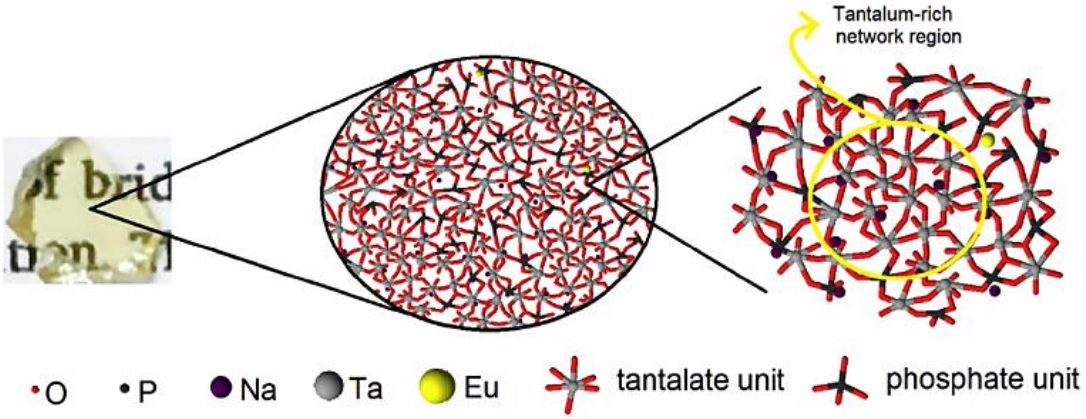

Reference: MARCONDES *et al.* (2020, p.09).

I-3.2 Niobium phosphate glassy materials

The chemical element niobium - Nb (Z = 41) was discovered by the chemist Charles Hatchett, who at first named it Columbium. However, it was only recognized in 1949 after the distinction between niobium and tantalum through the studies of the chemist Heinrich Rose; because until then, as previously mentioned, it was believed that they were the same element (SEER; MORAES, 2018). Niobium is mostly found in Brazil, being a strategic national element. According to Szczesniak (2021) the country has around 90% of the reserves of this metal on the planet and Lopes *et al.* (2014) mentions Brazil as the largest producer and exporter.

[16] The name of the **perovskite** structure is due to the perovskite **mineral** $CaTiO_3$ discovered by Lev Perovski in 1839. This mineral is actually orthorhombic at room temperature, becoming cubic only at temperatures above 900°C (CARTER; NORTON, 2013).

In the form of oxide, Nb_2O_5, has a melting temperature of 1512°C and crystalline structure with T or γ phase, orthorhombic, which crystallizes at 500°C and the H or α phase, monoclinic, which crystallizes at 1100°C (NOWAK; ZIOLEK, 1999). In general, the addition of Nb_2O_5 in phosphate glasses is very similar to the addition of Ta_2O_5, but the use of niobium oxide in glasses is much more developed.

Like tantalum, niobium in phosphate glasses behaves as a network intermediate; performing covalent bonds, and increasing the Tg value - increasing network connectivity. So, at high concentrations occurs the formation of octahedral clusters [NbO_6], which act within the glass as nuclei promoting crystallization, especially of niobate phases. This structural behavior for phosphate glasses with addition of niobium has been extensively studied over the years[17].

The modification in the structure of phosphate glasses with the addition of niobium leads to changes in several properties, such as improvement in chemical properties, for example, resistance to corrosion in acidic, basic and neutral media; and as biomaterial, increasing the resistance in Simulated Body Fluid (GHUSSN; MARTINELLI, 2004; MA, 2014; SILVA, 2022; ZERLIM, 2008). In mechanical properties, the addition of niobium in phosphate glasses increases density, atomic packing density, modulus of elasticity, indentation fracture toughness and hardness; and reduces the coefficient of linear thermal expansion. Electrical measurements also showed that the activation energy for ionic conduction increases from 0.46eV to 0.59eV for glasses containing 19-32 mol% of Nb_2O_5 (GOMES, 2004; SENE; MARTINELLI; SILVA, 2022).

Changes are observed as well in optical properties, such as increase in refractive index (KARAM *et al.*, 2020; OL'SHIN *et al.*, 2017; SILVA, 2022) and glass window of transparency shifts to higher values due to the addition of niobium (CASSANI, 2022; OL'SHIN *et al.*, 2017). Additionally, phosphate and borophosphate glasses with niobium have been widely used for second harmonic generation studies using Thermal Poling (DUSSAUZE *et al.*, 2005; FERREIRA *et al.*, 2004; KARAM *et al.*, 2020; MALAKHO *et al.*, 2005). He *et al.* (2021) studied SHG microstructured patterns in niobium borophosphate glasses doped with Sm_2O_3 by laser-induced Thermal Poling, and the authors pointed out that the Poling process used may be a potential method to design second-order optical properties or even to manufacture microstructures. Lepicard (2016) also used microstructured electrode for Thermal Poling using

[17] ANDRADE *et al.* (1999); FLAMBARD *et al.* (2004); GHUSSN *et al.* (2006); HOPPE *et al.* (2013); HOLUBOVÁ; ČERNOŠEK; HEJDA (2018); KOUDELKA, *et al.* (2008); LIMA *et al.* (2015); MALAKHO *et al.* (2005); RACHKOVSKAYA; BOBKOVA (1987); SIMON; CACAINA; BALASZ (2006).

niobium borophosphate glasses, in which the results indicated that is possible to pattern large areas using the technique and to induce sodium cations displacement in two directions.

It is also possible to obtain glass-ceramics containing different niobate phases, depending on the composition of the original glass. For example, glass-ceramics containing the phases Nb_2O_5 - monoclinic, and $K_2Nb_6P_4O_{26}$ from glasses in the KPO_3-Nb_2O_5 system were obtained by Lima *et al.* (2014). The perovskite phase $Na_2Nb_8O_{21}$ - sodium niobate - was obtained from niobium borophosphate glass by Malakho *et al.* (2005); as well as the $Na_4Nb_8P_4O_{32}$ phase. Same phases, and others niobophosphate were obtained by Stunda-Zujefa *et al.* (2017), e.g., $NbOPO_4$, $Na_2Nb_6P_4O_{26}$ and $Na_2Ca_2Nb(PO_4)_3$ working with the P_2O_5-Nb_2O_5-CaO-Na_2O system. Cassani (2022) obtained Nb_2O_5, $NaNbO_3$ and $Na_2Nb_8O_{21}$ crystalline phases by studying the sodium phosphate glass-ceramics.

I-4 GLASSES CONTAINING SILVER

Silver has several applications, for example, in the photographic/radiographic material industry, in the electronics industry, in coining and jewelry, in energy production (as in the case of dry batteries), in the manufacture of mirrors, in dental amalgam, in pharmaceuticals, in water purification. The use of silver and its compounds in medicine and water purification is due to the antibacterial and antifungal activity of Ag^+ ions (FITERMAN, 2001; SOUZA *et al.*, 2013). During the COVID-19 pandemic, the use of silver nanoparticles to combat the coronavirus has been extensively studied (ARJUN *et al.*, 2022; HE *et al.*, 2022; PILAQUINGA *et al.*, 2021).

When added into glasses, the different applications of silver are related, among others, to its form in the material: atoms (Ag^0), ions (Ag^+), Nanoclusters (NC) neutral Ag_n or charged Ag_n^{m+} or metallic nanoparticles (NP). The insertion of silver into glass can be done either by melt/quenching process of glass preparation adding a precursor (AgCl, $AgNO_3$, Ag_2O) or by immersing the glass in a bath rich in silver salts, so that Ag^+ ions can be replaced by, for example, Na^+ ions through an ion exchange reaction. In general, when silver is added to glasses, it is in the form of an ion (Ag^+). Subsequently, silver ions can be reduced to form the other species (DUBIEL *et al.*, 2005; MARCONDES *et al.*, 2022; SANTOS, 2021).

Both isolated and NC ions show Ultraviolet (UV) absorption and visible emission, which is why their luminescent properties are adjustable through different techniques, such as irradiation with UV light or direct engraving with high-intensity laser in nano and femtosecond regimes (CHEN *et al.*, 2018; SANTOS, 2021).

The glass matrix containing NP can be defined as a metal-dielectric nanocomposite, and silver (as well as other noble metals), can present the plasmon resonance phenomenon - Figure I-9 - that corresponds to the coherent oscillation of the electrons in the conduction band of the NP in response to the electric field of light and its magnitude and spectral position depend on the metal that composes the NP, the dielectric matrix and the NP size and shape. These effects cause a change in the electrical, magnetic and optical properties of glasses, and it is widely used in the development of sensors and optical amplifiers (GOUVÊA JUNIOR, 2016; OLIVEIRA, 2014).

Figure I-9 - Plasmon Resonance.

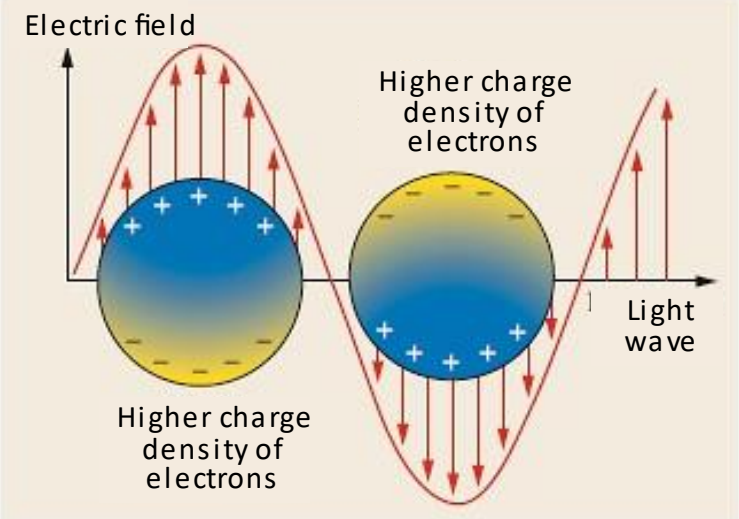

Reference: LIGNY; MÖNCKE (2019, p. 312).

Plasmon resonance can be identified through the absorption spectrum in the visible region, which appears as a band that varies, among others, with the size and shape of the NP. For example, Baia *et al.* (2007) observed this band around 400 to 500 nm for the sodo-calcium phosphate glass varying the amount of silver, Gouvêa Junior (2016) observed at 520 nm for a potassium phosphate glass after thermal treatment and Lino (2013) at 570 nm for a sodium tungsten glass after thermal treatment. Santos (2021) observed the band centered at 535 nm for a tungsten phosphate glass containing 4 mol% of silver, being attributed to particles of different sizes as evidenced by the bandwidth in the spectrum. Since the NP are in nanometric size, in general, they do not affect the transparency of the material, although they may influence its color.

Therefore, several species of silver can be present in the glass, depending not only on the treatments, but also, silver concentration. According to Ma *et al.* (2017):

> […] the formation of different silver species and the luminescent behaviors of Ag doped glasses are largely controlled by the Ag doping concentration. Generally, isolated Ag^+ is the dominant silver species at low concentration doping, while with increasing doping level a number of Ag^+ are easily reduced into Ag^0 atoms and the aggregation of Ag^0 and Ag^+ would generate a large amount of [NC]-Ag. As the reduction of Ag^+ and the aggregation proceeding, silver nanoparticles are formed and [NP] becomes dominant. The strong reduction tendency of Ag^+ makes it hard to further improve the luminescence performance since heavy doping of Ag^+ or subsequent heat treatment usually leads to formation of [NP]-Ag without any luminescent performances (MA *et al.*, 2017, p.22638).

Among the different classes of glasses containing silver, it can be mentioned the photosensitive glasses, that show difference of structural or electronic order after exposure to gamma-ray, X-ray, ultraviolet, visible and infra-red; and one of its variations, the photo-thermo-refractive glass (PTR). PTR glass is obtained by a sequence of steps, which include: exposure to radiation (photo), a controlled thermal treatment (thermo), and which will show periodic difference in the refractive index due to the presence of crystals (refractive). In recent years the interest in this type of material has been increasing mainly due to its non-linear optical properties, since these properties are important in photonics and plasmonics devices, being one of the main applications in the manufacture of optical elements holographically engraved in the volume (LUMEAU; ZANOTTO, 2017; NALIN *et al.*, 2016; SOUZA, 2019).

Regarding phosphate glasses containing silver, some examples can be cited, as Hsu *et al.* (2010) that studied $30Na_2O$-$10Al_2O_3$-$60P_2O_5$ glass system increasing the content of silver, and according to the authors, a maximum in the radiation sensitivity occurs with the addition of 0.05 mol% Ag_2O. Further additions of Ag_2O reduce the relative sensitivity to radiation and glasses with more than 2.5 mol% Ag_2O are impractical for use in a typical radiophotoluminescence glass dosimeter. Konidakis *et al.* (2018a) reported the fabrication of high regularity, erasable and rewritable periodic surface patterns on silver metaphosphate glass by means of ultrashort pulsed laser processing. The effect of composition and temperature on the second harmonic generation of silver iodide phosphate glasses of the series $xAgI$-$(1-x)AgPO_3$ ($0 < x \leq 0.5$) were studied by Konidakis *et al.* (2018b), in which SHG signal intensity is enhanced upon increasing silver content due to the random formation of silver microstructures within the glass network and the heating towards the Tg improves the SHG (Second Harmonic Generation) efficiency, whereas above Tg, the capacity of glasses to generate second harmonic radiation is drastically suppressed.

By adding silver into a sodium-niobium phosphate or borophosphate glasses with 42 mol% of niobium oxide, the rate of crystallization is affected while keeping same crystalline phase precipitation. For 0.5 molar percent of silver added, no effect on the glass transition temperature

is evidenced but significant shortening of the thermal stability against crystallization is demonstrated. Silver addition in the glasses favors the phase separation leading to sodium phosphate and sodium niobate rich regions (SMOGOR *et al.*, 2009). Using the same composition of the sodium-niobium phosphate glass with 0.5 mol% of silver, Fargin *et al.* (2009) performed a Thermal Poling on the glass comparing to the undoped one. The authors reported that the sodium depletion zone thickness for both is identical, and for the doped one the silver depletion is not as large as the sodium. A bathochromic increase in the cutoff wavelength was observed after Poling in the silver doped glass that leads to the increase in the linear and nonlinear susceptibilities that is at the origin of the enhancement of the quadratic susceptibility. Vasileva *et al.* (2015) studied the structural features of silver phosphate glasses (high concentration of silver oxide - 55 mol%) in zone of femtosecond laser-induced modification, in which the fs laser writing of two-dimensional microstructures (waveguides) was demonstrated in bulk glasses. It was found that the direct laser writing process enables not only reorganization of glass network, but also formation of color centers and silver nanoparticles that are revealed in appearance of luminescence signal and plasmon absorption. The process of NP formation is more efficient for Nb-phosphate glass, while color centers are preferably formed in phosphate glass.

I-5 LUMINESCENCE AND RARE-EARTHS

I-5.1 Luminescence

Luminescence can be defined as the emission of electromagnetic radiation by a material when excited by an energy source. The luminescent properties can be obtained when an “activator ion” is incorporated into a host matrix in small amounts. So, when the material is excited by an energy source, the activator ion absorbs this energy and converts it into electromagnetic radiation (CASSANJES, 2003). This excitation energy can be provided by several sources: thermal (thermoluminescence), pressure (triboluminescence), chemical reactions (chemiluminescence), electric field (electroluminescence), ultrasound (sonoluminescence), electromagnetic radiation (photoluminescence), etc.

The excitation energy absorbed by the activator ion allows the electron to pass from the ground level (E_1) to an excited level (E_2). With the return of the electron from the excited level (E_2) to the fundamental level (E_1), an emission by luminescence and heat dissipation occurs. It

may be that a non-radiative decay (NR) to an intermediate state (E_2') occurs before the electron radiatively decays (R) to the ground state, decreasing the efficiency of the radiative emission process (Figure I-10) (CASSANJES, 2003).

The presence of a "sensitizer ion" may also occur, which absorbs the excitation energy and transfers the absorbed energy to the activator ion (also called an acceptor), which will then luminesce. The sensitizer ion can be another ion or the matrix itself, which can act as a sensitizer, transferring the absorbed energy to the activator ion. The different combinations between the sensitizer and/or activator ions are very important in luminescence, since depending on the combination of these ions it is possible to obtain higher intensities, different emission profiles, etc. (CASSANJES, 2003; FRAGOSO, 2003). Due to their optical characteristics, rare-earth ions are considered a class of activator ions, with increasing technological application and therefore are widely used for luminescence.

Figure I-10 - Luminescence process: (a) excitation, (b) non-radiative decay and (c) radiative decay.

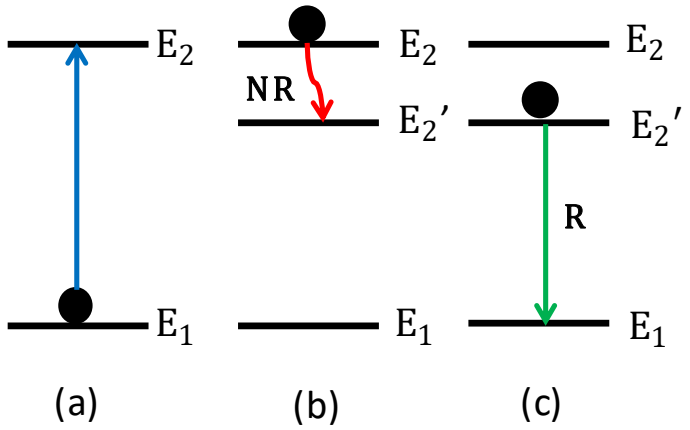

Reference: BATISTA (2018, p.40).

I-5.2 Rare-earth ions

Rare-earth elements (RE) are those that belong to the lanthanide series, plus Scandium and Yttrium, with an electronic configuration in neutral state of [Xe] $4f^n5s^25p^65d^{0-1}6s^2$ (n = 1 a 14). The most common oxidation state of rare-earths is trivalent (RE^{3+}) (although some can also present divalent and tetravalent oxidation states) and when ionizing they lose their electrons from the outermost orbitals shell. The valence electrons that remain bound participate in the optical excitation process and are called "optically active electrons" (AMARAL, 2010; BINNEMANS, 2015; REMONTE, 2008).

RE^{3+} have the contraction effect, which consists of significantly and constantly decreasing the size of atoms and ions as the atomic number and ionization increase. Also, since the 4f orbitals are internal, the electrons present in them are "shielded" from interactions with external forces by the electrons present in the 5s and 5p orbitals. Because of this, the optical properties of RE^{3+} are almost not affected by the environment and remain practically constant when incorporated into solids. This characteristic is the main difference between these ions and transition metals, in which the 3d electrons are located in an outermost shell and are therefore greatly affected by the environment in which they are inserted (LO, 2016; REMONTE, 2008).

The luminescence of RE^{3+} is due to the fact that the 4f orbitals are not completely filled, i.e., there is a certain number of unoccupied levels; so, the electrons by absorption of the excitation energy pass to these empty levels, that luminesce when decay. Thus, the RE^{3+} that do not have 4f electrons or that the 4f orbitals are complete do not have electronic energy levels that can promote the processes of excitation and luminescence emission, for example, lanthanum (La), which does not have any electrons f in its ground state (BURTAN *et al.*, 2011; REMONTE, 2008).

RE^{3+} ions exhibit different behaviors when doped into glasses and crystals. In crystals, the spectra normally present a more resolved spectra than in glasses, which present a non-homogeneous broadening - in glasses each ion feels the disturbance of the environment in which it is inserted in a different way from one another, and when added together they expand the width of the line (Figure I-11) (ALMEIDA, 2009; AMARAL, 2010).

Figure I-11 - Luminescence intensity peak for a set of ions: (a) in a crystal (homogeneous line width) and (b) in a glass (non-homogeneous line width due to the sum of the different sites).

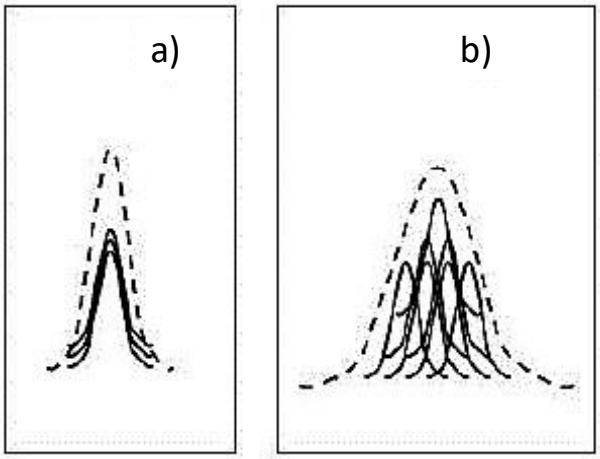

Reference: AMARAL (2010, p.07).

I-4.2.1 Transition mechanisms of rare-earth ions

The RE^{3+} ions sublevels depend on the number of electrons involved in the system and the local symmetry; and according to this symmetry the degeneracy is removed, that is, the levels do not remain with the same energy. That is caused by three main effects, the first two being present in the free ion and corresponding to the Coulomb interaction (electron-electron) and the spin-orbit coupling. When the rare-earth ion is incorporated in a matrix, the third effect appears, which corresponds to the interaction with the crystal field (or ligand field in the case of glasses). Figure I-12 presents the three effects on the 4f configuration of a RE^{3+} ion (CASSANJES, 2003; THIEL, 2003).

Figure I-12 - Schematic diagram of energy levels of a rare-earth ion due to Coulomb interaction, spin-orbit interaction and crystal field.

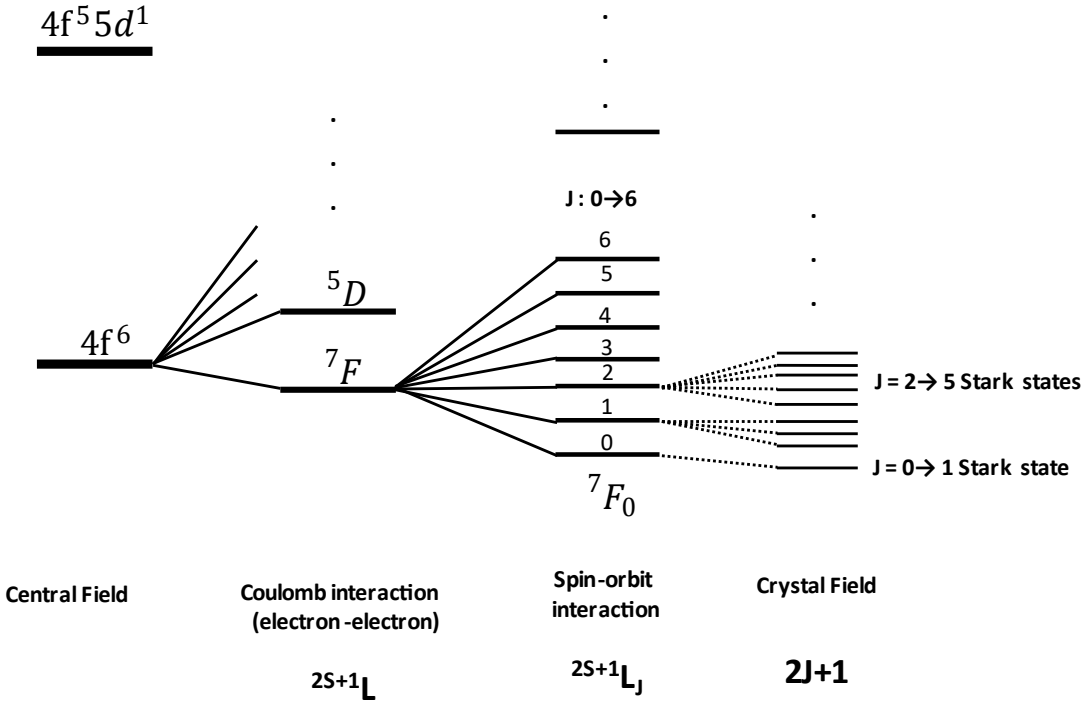

Reference: Translated from BATISTA (2018, p.43).

The first effect, the Coulomb interaction (electron-electron), refers to the interaction between electrons of the same shell and results in ^{2S+1}L spectroscopic terms separated by energies of the order of 10^4 cm^{-1}, which L represents the 'orbital angular momentum quantum number' (whose values can be 0,1,2,3,4,...corresponding respectively to the letters S, P, D, F, G), S represents the 'spin angular momentum quantum number', which is a number positive or multiple of ½, and 2S+1 represents the multiplicity of the term. The spin-orbit interaction

corresponds to the second effect, which then splits the 2S+1L terms into the $^{2S+1}L_J$ levels, separated by energies of the order of 10^3 cm^{-1}, with J corresponding to the 'total angular momentum quantum number', which is a combination between S and L. For rare-earth ions - Ce^{3+} to Eu^{3+}: J = L – S, which is the case when the number of 4f electrons is less than 7; and Tb^{3+} to Yb^{3+}: J = L + S, which is when the number of 4f electrons is greater than 7. The third effect is the crystal field (or ligand), which when present removes the degeneracy of the J states, resulting in, at most 2J+1 (if J is integer) or J + ½ (if J is half-integer) Stark states, depending on the symmetry of the field. The separation of these states is of the order of ≈100 cm^{-1} (AMARAL, 2010; BINNEMANS, 2015; CASSANJES, 2003; LO, 2016).

The main transitions mechanisms of 4f level of RE^{3+} are electric and magnetic dipole. The Magnetic Dipole (MD) transition operator possesses even transformation properties under inversion and allows transitions between states with even parity, i.e., the same ***l*** value (MATOS, 2012; THIEL, 2003). On the other hand, Electric Dipole (ED) transition operator has odd transformation properties under inversion with respect to an inversion center. Intraconfigurational electric dipole transitions are forbidden by the Laporte selection rule. Thus, transitions between even (g - *gerade*) and odd (u - *ungerade*) orbitals are allowed, but not between same parity (g-g or u-u). As the f-f transitions have the same value of ***l***, they have the same parity and, therefore, by Laporte selection rule they are forbidden. However, the Laporte selection rule strictly applies to a lanthanide ion in the gas phase (i.e., a centrosymmetric environment); so, it is relaxed for lanthanide ions embedded in a medium, since the transitions can be partly allowed by vibronic coupling or via mixing of higher configurations into the 4f wavefunctions by the crystal-field effect. The observed transitions are much weaker than ordinary electric dipole transitions. Therefore, they are often called "induced" electric dipole transitions (or "forced" electric dipole transitions), rather than just electric dipole transitions, and are described by the Judd-Ofelt theory (FRAGOSO, 2003; MATOS, 2003; MATOS, 2003). 2012; THIEL, 2003).

I-5.3 Europium

The rare-earth element europium (Eu) has atomic number 63, atomic mass 152u, and electronic distribution [Xe] $4f^76s^2$, as a trivalent ion (Eu^{3+}) the distribution becomes [Xe] $4f^6$. In the oxide form (Eu_2O_3) it is used mainly as a neutron absorber in the control of nuclear reactors, in trichromatic lamps, high-definition TV screens, X-ray films, biomedicine, etc. One

of the most important applications of europium is the red phosphor Y_2O_3: Eu^{3+} (YOX) in fluorescent lamps (BINNEMANS, 2015; THIEL, 2003).

Regarding the doping of Eu^{3+} in glasses, there are plenty of studies, such as: Eu^{3+}- doped alumino-phosphate glass for ratiometric thermometer based on the excited state absorption (MORASSUTI *et al.*, 2018); development of phosphate glass - $(63\text{-}x)P_2O_5\text{-}32Li_2O\text{-}5Al_2O_3\text{-}xEu_2O_3$ - doped with Eu^{3+} for red luminescent solid state optical devices (ARYAL *et al.*, 2020); Eu^{3+} doped alkaline earth zinc phosphate glasses - $39ZnO\text{-}35P_2O_5\text{-}20RO\text{-}5TiO_2\text{-}1Eu_2O_3$ (R=Mg, Ca, Sr e Ba) - for white LED applications (JHA; JAYASIMHADRI, 2017); and transparent glass-ceramic with ferroelectric bismuth titanate doped with Eu^{3+} (MOLLA *et al.*, 2012).

Compounds that have the Eu^{3+} ion present emission bands in a range that goes from visible to infrared. When excited with ultraviolet light, emit red light (FIGURE I-13) (MAHFOUDHI, 2019; SILVA, 2010).

Figure I-13 - Compounds with Eu^{3+}: a) solid under visible light, b) solid under ultraviolet light, and c) solution under ultraviolet light.

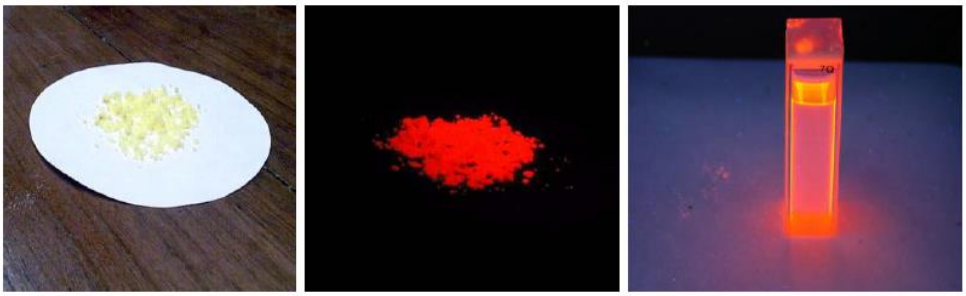

a b c

Reference: SILVA (2010, p. 01).

Furthermore, the europium ion is widely used as a structural probe through its spectra. These allow exploring the environment around the ion when embedded in glasses and crystals to study its symmetries. In general, broad bands in the Eu^{3+} emission spectrum indicates inhomogeneous sites (BINNEMANS, 2015; SILVA, 2010). The energy diagram of Eu^{3+} is presented in Figure I-14, in which the main emitting state of this ion is the $^5D_0$ level. Table I-2 presents the characteristics of the transitions $^5D_0 \rightarrow {}^7F_J$ (J=0→6) of the Eu^{3+} (MAHFOUDHI, 2019; REIS, 2012; SILVA, 2010).

Figure I-14 - Energy Level Diagram of Eu^{3+}.

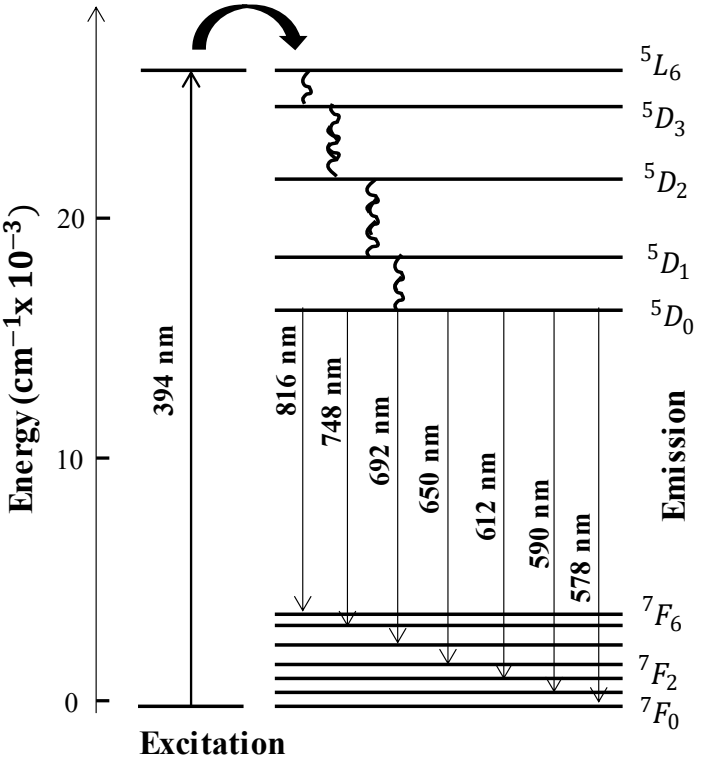

Reference: Modified from SILVA (2010, p.05).

Table I-2 - Characteristics of Eu^{3+} transitions $^5D_0 \rightarrow {}^7F_J$ (J=0→6).

Transition	Mechanism	Range and (barycenter) (nm)	Intensity	Information
$^5D_0 \rightarrow {}^7F_0$	ED	577-581 (578)	Very weak	Only observed in C_n, C_{nv} and C_s symmetry
$^5D_0 \rightarrow {}^7F_1$	MD	585-600 (590)	Strong	Largely independent of environment
$^5D_0 \rightarrow {}^7F_2$	ED	610-625 (612)	Very strong	Hypersensitive; strongly dependent on environment
$^5D_0 \rightarrow {}^7F_3$	ED	640-655 (650)	Very weak	Forbidden transition
$^5D_0 \rightarrow {}^7F_4$	ED	680-710 (692)	Medium	Dependent on environment, but no hypersensitivity
$^5D_0 \rightarrow {}^7F_5$	ED	740-770 (748)	Very weak	Forbidden transition
$^5D_0 \rightarrow {}^7F_6$	ED	810-840 (816)	Very weak	Rarely measured and observed

Reference: BINNEMANS (2015, p.07).

As Eu^{3+} ions are used as a structural probe, its spectra must show differences according to the different chemical environment around them. The $^5D_0 \rightarrow {}^7F_1$ transition is MD and its intensity is almost not affected by the environment of the ion. That is, this transition does not depend on the structure in its surroundings and is considered a reference transition. The

$^5D_0 \rightarrow {}^7F_2$ transition is an ED and hypersensitive to the environment in which the ion is inserted and its intensity varies when the symmetry around the ion changes (BINNEMANS, 2015; SILVA, 2010). Thus, the intensity ratio of these two transitions (or asymmetry ratio), defined as "[...] measure of the degree of inversion symmetry distortion of the environment where the ion is inserted […]" (AMARAL, 2010, p. 64, translated by the author), can be used as an indication of the Eu^{3+} symmetry site (BINNEMANS, 2015).

Additionally, the presence of the $^5D_0 \rightarrow {}^7F_0$ transition indicates that the ion is in a low symmetry environment, as this transition is prohibited for environments with a center of inversion. If the intensity of this transition is very low, the symmetry must be relatively high. Another characteristic of this transition is that as both levels ($^5D_0$ and $^7F_0$) are non-degenerate (J=0), if the spectrum presents more than one peak in this region, it is concluded that the ion is inserted in more than one emitting site (BINNEMANS, 2015; MAHFOUDHI, 2019; SILVA, 2010).

I-6 SECOND HARMONIC GENERATION IN GLASSES AND THERMAL POLING

I-6.1 Non-Linear Optics

Linear Optics (LO) and Non-Linear Optics (NLO) are related to the phenomena that occur when electromagnetic radiation interacts with matter. Electromagnetic radiation corresponds to the product of electric (E) and magnetic (B) fields (perpendicular to each other) that vary with time in wave motion and cross the vacuum at $3x10^8$ $m.s^{-1}$. In the present work it will be discussed this interaction in dielectric and non-magnetic materials, which is the case of glasses, and, therefore, the part of the magnetic field not considered (LEPICARD, 2016; VERBIEST; CLAYS; RODRIGUEZ, 2009)[18].

Matter can be described as a group of charged particles: electrons - negative; and nuclei (protons + neutrons) - positive. The electric field ($\vec{E}$) carried by the light interacts with these particles: the positive ones will tend to move in the direction of the field, while the negative ones in the opposite direction. The movement of electrons is usually more significant, as their considerably lower mass leads to a faster response. This interaction will cause a separation of charges with deformation of the electronic cloud that induces, on a molecular scale, a dipole

[18] In this work it will not be presented in details the description and development of the equations. Most detail information about NLO is described in: Boyd (2020); Sauter (1996); Verbiest; Clays; Rodriguez (2009) and Zilio (2009).

moment oscillating at the same frequency as the field. Considering N atoms per unit volume, the polarization of the medium corresponds to the response of the material in the presence of light, that is the sum of contribution of all dipoles. This polarization is related to the electric field according to the equation I-01 (LEPICARD, 2016; MALAKHO *et al.*, 2005; VERBIEST; CLAYS; RODRIGUEZ, 2009; ZILIO, 2009).

$$\vec{P} = \varepsilon_0 \overleftrightarrow{\chi} : \vec{E} \qquad \text{(I-01)}$$

which $\vec{E}$ is the electric field, ε_0 the electrical vacuum permittivity (8.854×10^{-12} F.m^{-1}) and $\overleftrightarrow{\chi}$ is the linear or first order optical susceptibility.

The oscillatory nature of the electric field components can be described in the temporal domain as a propagating electric field, E(r,t), which varies in space and time. Consequently, the material response expressed by its polarization and its linear susceptibility are also temporally and spatially dependent. Alternatively, it can be used the frequency domain representation, where the electric field E(ω,k) is described by its oscillation frequency (ω) and its wave vector k (MENDONÇA, 2000).

Equation I-01 describes Linear Polarization, which is valid when the electromagnetic radiation has low intensity, related to linear optical phenomena: absorption, refraction, reflection, scattering. If the light intensity is too high, the linear approximation is no longer sufficient to describe the electron cloud response; and then the phenomena related to **Non-Linear Optics** are observed.

A high intensity light corresponds to approximately the interatomic field (field that holds the electron to the nucleus), which is around 1×10^8 V.cm^{-1}, e.g., a laser[19]. Usually, lasers used in NLO are pulsed that provides a peak intensity high enough for the optical nonlinearity phenomena occur. In addition, NLO phenomena occur in non-resonant regions (i.e., they do not absorb energy) (EVANGELISTA, 2021; VIVAS, 2021; ZILIO, 2009).

Non-linear Polarization terms can be developed in a Taylor series (I-02) that varies **non-linearly**, in which the higher order terms are added to the linear term ($\vec{P}^{(1)}$), and $\overleftrightarrow{\chi}^{(2)}$ and $\overleftrightarrow{\chi}^{(3)}$ corresponding to second and third order susceptibilities, respectively (KARAM, 2020; LEPICARD, 2016; ZILIO, 2009):

[19] The phenomena related to NLO were only observed after the development of lasers, in the 60's, as they provide a high intensity and coherent light.

$$\vec{P} = \vec{P}^{(1)} + \vec{P}^{(2)} + \vec{P}^{(3)} + \cdots = \varepsilon_0(\overleftrightarrow{\chi}^{(1)}\vec{E} + \overleftrightarrow{\chi}^{(2)}\vec{E}\vec{E} + \overleftrightarrow{\chi}^{(3)}\vec{E}\vec{E}\vec{E} + \cdots) \quad \text{(I-02)}$$

The **Second Harmonic Generation** (SHG) is a non-linear second-order phenomenon and is related to $\overleftrightarrow{\chi}^{(2)}$, that connects the product of two electric fields with the polarization, presenting 27 components, and can be written by (I-03):

$$P_i^{(2)} = \varepsilon_0 \sum_{j,k} \chi_{ijk}{}^{(2)} E_j E_k \quad \text{(I-03)}$$

where ijk referring to the Cartesian components of the field, $P_i^{(2)}$ is a component of the polarization vector and E_j and E_k components from the electric field vector.

Or in matrix form:

$$\begin{bmatrix} P_x{}^{(2)} \\ P_y{}^{(2)} \\ P_z{}^{(2)} \end{bmatrix} = \varepsilon_0 \begin{bmatrix} \chi_{xxx}{}^{(2)} & \chi_{xyy}{}^{(2)} & \chi_{xzz}{}^{(2)} & \chi_{xyz}{}^{(2)} & \chi_{xzy}{}^{(2)} & \chi_{xzx}{}^{(2)} & \chi_{xxz}{}^{(2)} & \chi_{xxy}{}^{(2)} & \chi_{xyx}{}^{(2)} \\ \chi_{yxx}{}^{(2)} & \chi_{yyy}{}^{(2)} & \chi_{yzz}{}^{(2)} & \chi_{yyz}{}^{(2)} & \chi_{yzy}{}^{(2)} & \chi_{yzx}{}^{(2)} & \chi_{yxz}{}^{(2)} & \chi_{yxy}{}^{(2)} & \chi_{yyx}{}^{(2)} \\ \chi_{zxx}{}^{(2)} & \chi_{zyy}{}^{(2)} & \chi_{zzz}{}^{(2)} & \chi_{zyz}{}^{(2)} & \chi_{zzy}{}^{(2)} & \chi_{zzx}{}^{(2)} & \chi_{zxz}{}^{(2)} & \chi_{zxy}{}^{(2)} & \chi_{zyx}{}^{(2)} \end{bmatrix} \begin{bmatrix} E_x{}^2 \\ E_y{}^2 \\ E_z{}^2 \\ E_yE_z \\ E_zE_y \\ E_zE_x \\ E_xE_z \\ E_xE_y \\ E_yE_x \end{bmatrix}$$

Considering the intrinsic permutation symmetry, the susceptibility tensor χ_{ijk} is symmetric in its last two indices, then, $\chi_{ijk}{}^{(2)} = \chi_{ikj}{}^{(2)}$, reducing the matrix terms. More physically, this condition is simply a statement that it cannot matter which is the first field and which is the second field in products such as EjEk (BOYD, 2020; NASR, 2015).

Also, another formalism is frequently used, that is d equals $\chi^{(2)}/2$[20], and the components $\chi_{ijk}{}^{(2)}$ become dil with i = 1, 2, 3 which corresponds respectively to x, y, z and l, according to Table I-3:

Table I-3 - Values of second-order nonlinear susceptibility components.

	xx	**yy**	**zz**	**yz = zy**	**xz = zx**	**xy = yx**
l	1	2	3	4	5	6

Reference: KARAM (2020, p.18)

Thus, the matrix can be rewritten as (I-04):

[20] According to Nasr (2015) and Boyd (2020) the fraction ½ is a historical convention.

$$\begin{bmatrix} P_x^{(2)} \\ P_y^{(2)} \\ P_z^{(2)} \end{bmatrix} = \varepsilon_0 \begin{bmatrix} d_{11} & d_{12} & d_{13} & d_{14} & d_{15} & d_{16} \\ d_{21} & d_{22} & d_{23} & d_{24} & d_{25} & d_{26} \\ d_{31} & d_{32} & d_{33} & d_{34} & d_{35} & d_{36} \end{bmatrix} \begin{bmatrix} E_x^2 \\ E_y^2 \\ E_z^2 \\ 2E_y^2 E_z^2 \\ 2E_x^2 E_z^2 \\ 2E_x^2 E_y^2 \end{bmatrix} \quad \text{(I-04)}$$

The $\overleftrightarrow{\chi}^{(2)}$ tensor has specific properties link to symmetries: permutation symmetry, time reversal symmetry and symmetry in space. The first two types of symmetry are fundamental properties of the susceptibilities while spatial symmetry is linked to the nonlinear medium. Considering the case where the material is centrosymmetric, i.e., it has a center of inversion[21], when there is an incident electric field of light, the polarization $\vec{P}$ it also responds symmetrically in any direction causing a proportional inversion - Figure I-15 (KARAM, 2020; LEPICARD, 2016; VERBIEST; CLAYS; RODRIGUEZ, 2009).

Figure I-15 - Response of polarization to the electric field of electromagnetic wave.

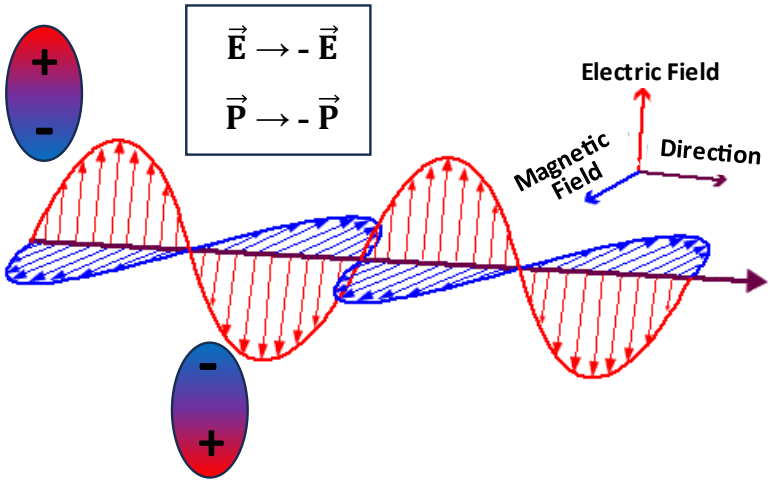

Reference: AUTHOR.

So, (I-04):

$$\vec{P}^{(2)} = \varepsilon_0 \overleftrightarrow{\chi}^{(2)} \vec{E}\vec{E} \quad \text{or} \quad \vec{P}^{(2)} = \varepsilon_0 \overleftrightarrow{\chi}^{(2)} (\vec{E}^2) \rightarrow$$
$$-\vec{P}^{(2)} = \varepsilon_0 \overleftrightarrow{\chi}^{(2)} (-\vec{E})(-\vec{E}) \quad \text{or} \quad -\vec{P}^{(2)} = \varepsilon_0 \overleftrightarrow{\chi}^{(2)} (\vec{E}^2) \quad \text{(I-04)}$$

[21] For every point with coordinates (x, y, z) in the unit cell, there is an indistinguishable point with coordinates (-x, -y, -z).

In this case, the value of $\overleftrightarrow{\chi}^{(2)}$ in I-04 must equal zero. This means that in a centrosymmetric material, the second-order susceptibility is zero; which in general is true for all even terms in a material of such symmetry. Thus, it is noted that the terms of the susceptibility tensor depend on the symmetry of the material.

Considering a material with symmetry $C\infty v$ (or ∞mm in international notation)[22] - which presents an infinite number of rotation axis, transparent (involved fields are considered far from any transition), and SHG, the tensor $\overleftrightarrow{\chi}^{(2)}$ according to Karam (2020) and Lepicard (2016) can then be described by (I-05):

$$\frac{1}{2}\overleftrightarrow{\chi}^{(2)} = \mathrm{d} = \begin{bmatrix} 0 & 0 & 0 & 0 & d_{31} & 0 \\ 0 & 0 & 0 & d_{31} & 0 & 0 \\ d_{31} & d_{31} & d_{33} & 0 & 0 & 0 \end{bmatrix} \tag{I-05}$$

In addition to SHG, there are several optical phenomena related to $\overleftrightarrow{\chi}^{(2)}$, which can result in different applications. The simplest case in which there is only one field involved $[\mathrm{E}(\mathrm{r},\mathrm{t}) = \mathrm{E}_0(\mathrm{e}^{\mathrm{ikr}-\mathrm{i}\omega\mathrm{t}} + \mathrm{cc})]$, the second term of the polarization, $\mathrm{P}^{(2)}$ is described by (I-06):

$$\begin{aligned} \mathrm{P}^{(2)} = \varepsilon_0\chi^{(2)}\mathrm{EE} = \varepsilon_0\chi^{(2)}\mathrm{E}_0\left(\mathrm{e}^{\mathrm{ikr}-\mathrm{i}\omega\mathrm{t}} + \mathrm{cc}\right)\mathrm{E}_0\left(\mathrm{e}^{\mathrm{ikr}-\mathrm{i}\omega\mathrm{t}} + \mathrm{cc}\right) = \\ 2\varepsilon_0\chi^{(2)}{\mathrm{E}_0}^2 + \varepsilon_0\chi^{(2)}{\mathrm{E}_0}^2\left(\mathrm{e}^{\mathrm{i2kr}-\mathrm{i2}\omega\mathrm{t}} + \mathrm{cc}\right) \end{aligned} \tag{I-06}$$

The first term of equation I-06 is independent of frequency and corresponds to Optical Rectification (OR). The second term is related to **SHG** and consisted of "double the frequency (2ω)". In a more general case, the two fields are different, that is, $\mathrm{E}_1(\mathrm{r},\mathrm{t}) = \mathrm{E}_{0,1}(\mathrm{e}^{\mathrm{ik}_1\mathrm{r}-\mathrm{i}\omega_1\mathrm{t}} + \mathrm{cc})$ and $\mathrm{E}_2(\mathrm{r},\mathrm{t}) = \mathrm{E}_{0,2}(\mathrm{e}^{\mathrm{ik}_2\mathrm{r}-\mathrm{i}\omega_2\mathrm{t}} + \mathrm{cc})$, resulting in (I-07):

$$\begin{aligned} \mathrm{P}^{(2)} = \left[2\varepsilon_0\chi^{(2)}{\mathrm{E}_{0,1}}^2 + 2\varepsilon_0\chi^{(2)}{\mathrm{E}_{0,2}}^2\right] + \left[\varepsilon_0\chi^{(2)}{\mathrm{E}_{0,1}}^2\left(\mathrm{e}^{\mathrm{i2k}_1\mathrm{r}-\mathrm{i2}\omega_1\mathrm{t}} + \mathrm{cc}\right)\right. \\ \left. + \varepsilon_0\chi^{(2)}{\mathrm{E}_{0,2}}^2\left(\mathrm{e}^{\mathrm{i2k}_2\mathrm{r}-\mathrm{i2}\omega_2\mathrm{t}} + \mathrm{cc}\right)\right] + 2\varepsilon_0\chi^{(2)}\mathrm{E}_{0,1}\mathrm{E}_{0,2}\left(\mathrm{e}^{\mathrm{i}(k_1+k_2)\mathrm{r}-\mathrm{i}(\omega_1+\omega_2)\mathrm{t}} + \mathrm{cc}\right) \\ + 2\varepsilon_0\chi^{(2)}\mathrm{E}_{0,1}\mathrm{E}_{0,2}\left(\mathrm{e}^{\mathrm{i}(k_1-k_2)\mathrm{r}-\mathrm{i}(\omega_1-\omega_2)\mathrm{t}} + \mathrm{cc}\right) = \\ \mathrm{P}^{(0)} + \mathrm{P}^{(2\omega_1)} + \mathrm{P}^{(2\omega_2)} + \mathrm{P}^{(\omega_1+\omega_2)} + \mathrm{P}^{(\omega_1-\omega_2)} \end{aligned} \tag{I-07}$$

[22] This example is not presented by chance, as it corresponds to the symmetry classically induced by Thermal Poling in glasses, presented later.

The terms related to OR and SHG appear in equation I-07, in addition to these are the terms corresponding to the Sum Frequency Generation (SFG) and the Difference Frequency Generation (DFG). Thus, a material having a non-zero second-order susceptibility makes it possible, from two light waves of given frequencies, to generate new frequencies by SHG, SFG or DFG.

Finally, assuming that one of the fields corresponds to a static field, E(0), if the material has $\chi^{(2)}$, then (I-08):

$$P^{(2)} = \varepsilon_0 \chi^{(2)} E(0) E_0 (e^{ikr-i\omega t} + cc) \quad \text{(I-08)}$$

And the total polarization can be written as (I-09):

$$P = \varepsilon_0 \chi^{(1)} E(\omega) + \varepsilon_0 \chi^{(2)} E(0) E(\omega) = \varepsilon_0 (\chi^{(1)} + \chi^{(2)} E(0))\, E(\omega) = \chi_{eff} E(\omega) \quad \text{(I-09)}$$

with $E(\omega) = E_0 (e^{ikr-i\omega t} + cc)$.

An effective linear susceptibility (χ_{eff}) is obtained that depends on the intensity of the static field. Since linear susceptibility is directly related to the index of refraction ($n^2 = 1 + 4\pi\chi^{(1)}$), then it is possible to modulate the refraction index as quickly as an electric field can be modulated. This principle is called the Pockel effect, an effect that is based on the principle of electro-optical modulators, which can be used to produce optical switches or even Mach-Zehnder-type interferometers[23] (KARAM, 2020).

Similarly, but in a higher order, the third-order susceptibility ($\chi^{(3)}$) interacts with the static field to provide an effective $\chi^{(2)}$ (I-10):

$$\chi^{(2)} = 3\chi^{(3)} E(0) \quad \text{(I-10)}$$

If this static field is perpendicular to the surface of the sample, it induces a symmetry $C\infty v$ whose tensor has already been presented. Thus, this relation indicates a second-order susceptibility from the interaction of a static electric field and a third-order susceptibility. In the case of an isotropic material the terms can be related by (I-11):

$$\chi_{zzz}{}^{(2)} = 3\chi_{zxx}{}^{(2)} \text{ or } d_{33} = 3d_{31} \quad \text{(I-11)}$$

[23] Device built to determine the phase differences relative to two rays of light due to variations in the optical path traversed by them, which are usually caused by a change in the size of the interferometer arms or by the insertion of a phase changer (SOARES-PINTO; NAVES, 2021, p.03, translated by the author).

I-6.2 Second Harmonic Generation

As described in topic I-6.1, **Second Harmonic Generation** is often called as "Frequency Doubling" and it was first observed in a quartz crystal by Peter Franken *et al.* (1961), using a 694.30 nm ruby laser, generating, in addition to the refracted beam at 694.30 nm, a signal at 347.15 nm. Simplifying, SHG occurs when radiation of a certain frequency (ω) is incident on material that has second-order nonlinear susceptibility ($\chi^{(2)}$) and a radiation with a doubled frequency (2ω) is generated. It is worth remembering that doubling the frequency implies decreasing the wavelength by a factor of ½ - Figure I-16 (LEPICARD, 2016; ROJAS, 2005).

Figure I-16 - Simplified scheme of SHG: (A) light incident on the material and (B) energy states.

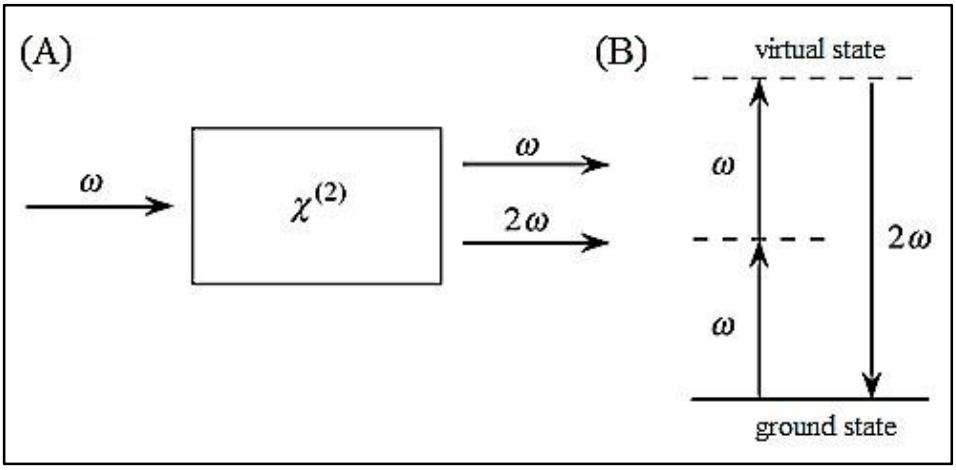

Reference: Modified from BOYD (2020, p.05).

The energy levels related to SHG are represented in Figure I-16B, in which two photons of the same frequency ω combine to produce a new, single photon with twice the frequency 2ω. That is, the phenomenon of SHG does not occur with photon absorption, but an "annihilation" of photons occurs in a "virtual level" of energy (BOYD, 2020; ROJAS, 2005; VIVAS, 2021).

The intensity of this second harmonic wave - 2ω - is described by I-12, and depends on the square of the intensity of ω, the refractive indices and the length of the medium (L):

$$I_{2\omega}(L) = \frac{(2\omega)^2}{8\varepsilon_0 c^3} \frac{\left|\chi^{(2)}\right|^2}{n_\omega{}^2 n_{2\omega}} L^2 \mathrm{sen}^2\left(\frac{\Delta k.L}{2}\right) I_\omega{}^2 \qquad \text{(I-12)}$$

with: $\Delta k = k_{2\omega} - 2k_\omega$ (k corresponds to wave vectors).

When $\Delta k = 0$, $n_\omega = n_{2\omega}$, phase matching occurs, in which the medium is non-dispersive, the interference is constructive, and the energy transfer to the second harmonic is maximum. When $\Delta k \neq 0$, no phase matching occurs, but out-of-phase/imperfect phase matching, and $n_\omega \neq n_{2\omega}$, the medium is dispersive and the speeds of the two waves are different and not constructive. Interferences between the two waves induce oscillations of the amplitude of the second harmonic signal depending on the distance (KARAM, 2020; LEPICARD, 2016).

Phase matching conditions can be obtained in non-linear crystals using crystal birefringence, which allows to eliminate phase mismatch. Another technique can also be used, the quasi-phase matching (QPM), which is used in glasses (but not only), due to not having birefringence. In this case, real phase correspondence does not occur, but it is possible to achieve a high conversion by periodically switching between areas that show a second-order response with those that do not, according to the coherence length (Lc). The coherence length corresponds to the distance over which the phase difference between the two waves (the fundamental wave and the harmonic wave) is equal to π, and given by (I-13):

$$L_c = \left|\frac{\pi}{\Delta k}\right| = \frac{\lambda_\omega}{4[n(2\omega) - n(\omega)]} \quad \text{(I-13)}$$

Thus, although the SHG intensity depends on L, it is useless to use a material much longer than Lc. Figure I-17 presents the evolution of the intensity of the second harmonic as a function of *L/Lc* for the different cases.

The most commonly used materials for SHG are crystals such as KDP (potassium dihydrogen phosphate), BBO (beta-barium borate) and $LiNbO_3$ (lithium niobate). However, these materials may have some drawbacks, such as cost; in addition to presenting losses in interconnections due to differences in refractive index and thermal expansion. Recently, very high values of second-order nonlinear optical susceptibility (29 pm/V at 1.06 μm) were obtained within a thermally micropoled sodo-niobate film (KARAM et al, 2020). Thus, it is interesting to develop new materials that are capable of generating second harmonic, especially with lower costs.

Figure I-17 - Representation of the evolution of the $I_{2\omega}$ intensity as a function of the length of the medium.

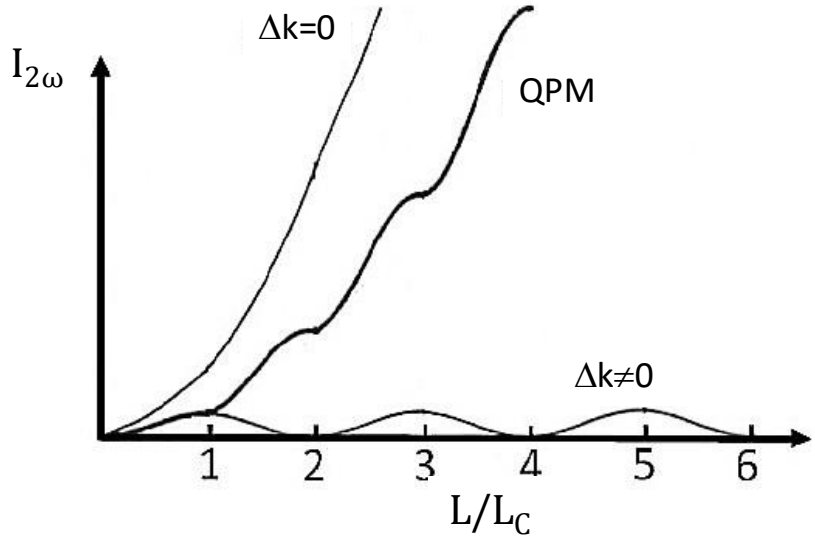

Reference: LEPICARD (2016, p.20).

I-6.3 Second Harmonic Generation in glasses by Thermal Poling

As described, for Second Harmonic Generation, the material must not present a centrosymmetry, since the presence of the inversion center annuls the components related to $\chi^{(2)}$. As the glasses are isotropic, macroscopically it is considered that they are centrosymmetric, and, therefore, do not present Second-order Nonlinear Optics properties, e.g., the SHG.

Due to this characteristic of glasses, it was a surprise that a SHG was observed by Österberg and Margulis (1986) in silica optical fibers doped with germanium and phosphorus, after the incidence of a 1.06 μm Nd:YAG[24] infrared laser radiation. In other words, the authors observed frequency doubling in a material in which the center of symmetry, in principle, prohibits it. Several authors have struggled to understand the origin of this response and it is ultimately the creation of a periodic space charge induced by the incident laser and interacting with the third-order susceptibility of the material that has been used to explain this process.

In 1991, Myers *et al.* observed the SHG in volumetric silica with $\chi^{(2)}$ after the application of an intense electric field at a temperature of 300°C. The experiment, at first, had the objective of Poling a polymer film deposited on a glass substrate, but the authors noticed that the treatment had an effect on the substrate; and so, these researchers were the first ones to observe SHG in glasses using the Thermal Poling technique, which is explained throughout the text (LEPICARD, 2016; NASR, 2015; ROJAS, 2005).

[24] Acronym *neodymium-doped yttrium aluminium garnet.*

Therefore, although at first the glasses do not present Second-order Nonlinear Optics properties, it is possible to change this characteristic of these materials, but it is necessary to break their centrosymmetry. Two techniques can be used: the first is the controlled growth of crystals that are not centrosymmetric, i.e., the preparation of a glass-ceramic containing this type of crystals; the second technique is the application of an electric field, i.e., **Poling**. There are several types of Poling: Corona Poling[25], Optical Poling[26], Thermal Poling. In this work, **Thermal Poling** was used, and only this one will be described (LEPICARD, 2016; NASR, 2015).

Thermal Poling (FIGURE I-18) was first developed in 1960 by Wallis and Pomerantz, and consists of applying a voltage between the two faces of the heated sample (temperature lower than the glass transition temperature), causing the migration of the mobile ions from their original positions. During the process, in the area under the anode, the cations, such as Na^+, Li^+, K^+, are being removed by the action of the applied electric field, forming a depletion layer (Figure I-19). This area becomes increasingly negatively charged, generating a charge space orthogonally to the sample surface. When the sample is slowly cooled keeping the high voltage, the charge configuration is "frozen", and a permanent static electric field embedded under the glass surface is implanted. After the interruption of the voltage, the sample is poled, with the direction of the electric field opposite to that applied during Poling. As there is an electric field recorded in a certain area of the sample, it has its inversion symmetry broken (presenting a C∞v symmetry) and an effective second-order nonlinearity it is then induced in the sample (DUSSAUZE *et al.*, 2013; LEPICARD, 2016; NASR, 2015; ROJAS, 2005).

Figure I-18 - Thermal Poling: (a) Assembly and (b) heat treatment and electric field as a function of time

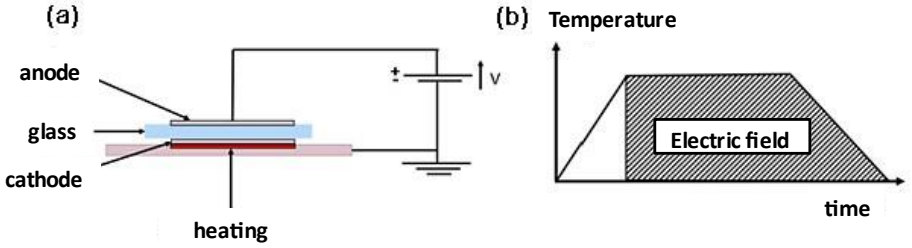

Reference: LEPICARD (2016, p.11).

[25] According to Rojas (2005), corona poling is a technique to orient organic dye molecules in polymeric films, generally called poled polymer films. According to Lepicard (2016) this poling involves the partial breakdown of the air or nitrogen atmosphere. The sample to be poled is placed on a grounded plate that can be used as a heating plate. And for Nasr (2015) it can be performed in glasses in which an electric field is applied through a flat-needle electrode geometry.

[26] A technique that uses intense laser light to irradiate a glass sample. The electric field is then applied without direct contact, but through laser light (LEPICARD, 2016).

Figure I-19 - Depletion layer in a glass generated by cations migration.

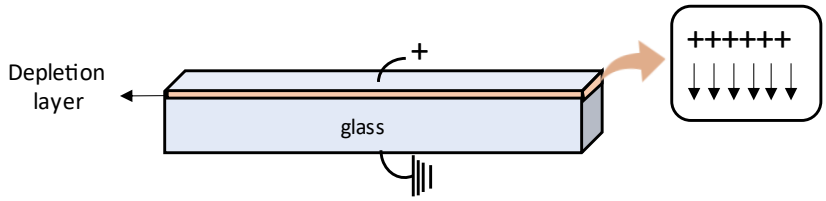

Reference: AUTHOR.

To explain the second-order optical response in glassy materials after Thermal Poling, two phenomena are generally attributed. The first, already described, is from a model originally proposed by Stolen and Tom (1987) in which the second-order susceptibility is related to the interaction between a static/internal electric field induced by the migration of positive charge carriers (Na^+, K^+, etc.) driven by the applied field and the third-order susceptibility ($\chi^{(3)}$). This is called the "Electric Field Induced Second Harmonic" or **EFISH** mechanism (review equation I-10) and described by equation I-14 - (FIGURE I-20) (LEPICARD, 2016; KARAM, 2020; MALAKHO *et al.*, 2005).

$$\chi_{EFISH}{}^{(2)} = 3\chi^{(3)}\mathrm{E_{int}} \tag{I-14}$$

The second phenomenon that can explain the second-order optical response induced by Thermal Poling is due to the reorientation of hyperpolarizable dipoles and entities due to the electric field at high temperatures, which would also break symmetry, and is given by (I-15) (FIGURE I-20):

$$\chi_{reor.}{}^{(2)} = \mathrm{NL(E)}\beta \tag{I-15}$$

where: N is the number of entities per unit volume, β is the microscopic hyperpolarizability and L(E) is the orientation factor.

To validate between these two contributions, Kazanksky and Russel (1994) proposed to study the two components of the $\chi^{(2)}$ tensor - review equation I-11. If the ratio between $\frac{\chi_{zzz}{}^{(2)}}{\chi_{zxx}{}^{(2)}}$ or $\frac{d_{33}}{d_{31}}$ deviates from the value of 3 (that is, from the EFISH), it will be necessary to consider that the non-linearity does not just come from the interaction of a static electric field and $\chi^{(3)}$. However, in general, the second order response in poled glasses is mainly related to

the electric field induced by the migration of charge carriers under the anode (KARAM, 2020; LEPICARD, 2016; NASR, 2015).

Figure I-20 - Mechanisms that described SHG by Thermal Poling.

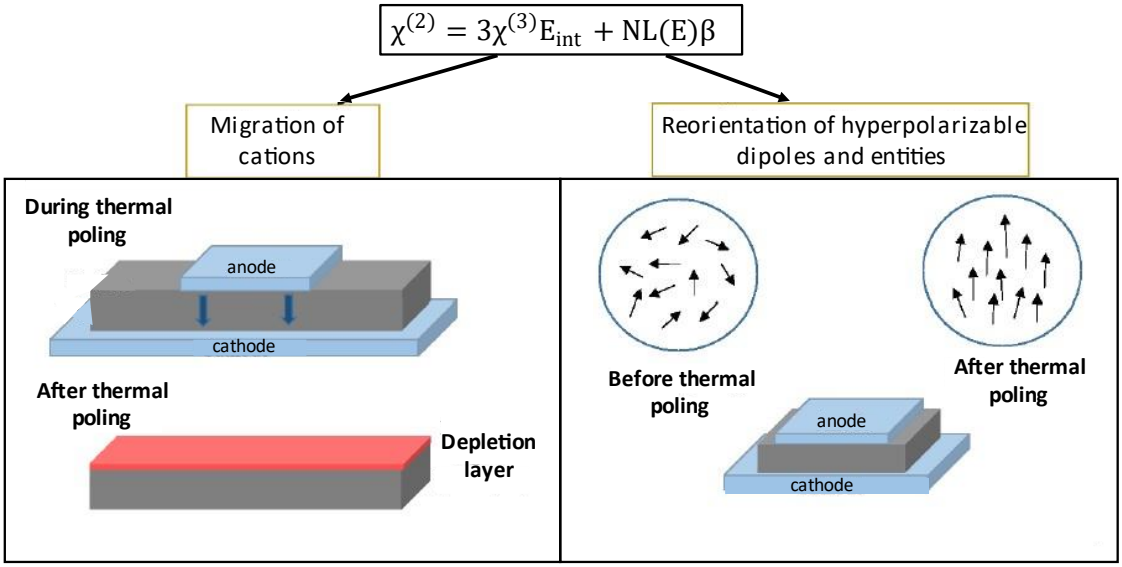

Reference: NASR (2015, p.10).

Several factors can influence the SHG response of the glasses, both related to the sample itself and to the parameters used during the Poling. The sample thickness is one of these factors, as highlighted by Quiquempois, Kudlinski and Martinelli (2005), in the case the total thickness of the poled material is large in comparison to the thickness of the cation-depleted layer, the field will not influence the response of second order since it will be distributed over a large thickness. Or in the case whereupon the total thickness of the poled sample is very thin and comparable to the thickness of the depletion layer, the implementation of a second-order response may be inefficient.

Another factor that influences Thermal Poling is the atmosphere during treatment, as it interferes with charge compensation mechanisms in the depletion layer. In the case of an "open anode", i.e., exchanges between the atmosphere and the surface of the glass are possible, the output of positive charges during Poling is compensated by an injection of "charged species" - usually ions H_3O^+/H^+. When the atmosphere is controlled (vacuum or inert) the injection of positive charges is not possible (blocking anode) and it is necessary to consider the movement in the opposite direction of the negative charges to counterbalance the output of the positive ones. Several studies agree on the presence of molecular oxygen (O_2) in the glass during Poling, in this case due to compensation mechanisms. However, the way in which this occurs is not unanimous, and there are several hypotheses tested under different conditions, such as: the

migration of NBO towards the anode (CARLSON; HANG; STOCKDALE, 1972), the purely electronic process in which electrons of NBO migrate to the anode, while oxygen atoms remain immobile, and recombine to form O_2 (KRIEGER; LANFORD, 1988), mechanisms involving oxygen anions resulting from structural rearrangements induced by the output of cations ($2O^{2-} \rightarrow O_2 + 4e^-$) (GUIMBRETIÈRE *et al.*, 2010), a set of intermediate reactions that explain oxygen diffusion and involve peroxide radicals (REDKOV; MELEHIN; LIPOVSKII, 2015).

The concentration of mobile ions also influences the non-linear response. Dussauze *et al.* (2012) studied Thermal Poling in three types of silica glasses under similar conditions (300°C, 90 min, 5 kV, blocking anode). The authors report very different second harmonic responses depending on the sample, and one of the conclusions of the study is that for a lower charge density, it is necessary for the charges to migrate over a greater distance to compensate for the voltage applied during treatment and, therefore, induce a field comparable to those induced in other glasses.

Furthermore, the composition of the glass influences the NLO response. In addition to the concentration of mobile ions already mentioned, another factor that has some influence is the third-order nonlinear optical susceptibility - $\chi^{(3)}$ - which, as already described, is related to the EFISH mechanism. The $\chi^{(3)}$ is correlated to the n_2 term or nonlinear index, thus, the n_2 value of glass of a certain composition influences the SHG response due to the EFISH mechanism. Several phenomena contribute to n_2, in particular a response of electronic origin and another of nuclear origin. The electronic response is related to the non-linear distortion of the electron cloud. The nuclear response, on the other hand, is related to a slower response induced by the movements of the nuclei, that is, it is a response associated to structural arrangements. In a first approximation, the value of n_2 follows the polarizability of the glass and, in particular, the electronic contribution of the anion ($F^- < O^{2-} < S^{2-} < Se^{2-}$), being low in fluoride glasses, intermediate in oxides and the highest values of non-linear indices are found in chalcogenide glasses (sulfides and selenides) (DUSSAUZE; CARDINAL, 2019).

Within the “same family” of glasses, the evolution of this parameter is quite complex, and the local structure of the material has a great influence. For example, an increase in the amount of NBO generated by the introduction of alkaline will induce an increase in this parameter due to the greater polarizability of these oxygens (negative charge) compared to BO. Also, d^0 ions, such as niobium, titanium or tantalum ions, introduced into oxide glasses (silicates, phosphates, borates) significantly increase n_2. The addition of these ions has an effect on the electronic as well as nuclear response, due to the structural arrangements of these transition

metals; for example, niobium (as well as tantalum) organizes itself as a three-dimensional network of NbO_6 entities and this organization has been shown to increase the non-linear index (CARDINAL, 1997; DUSSAUZE; CARDINAL, 2019).

Table I-4 presents a summary of several studies in which second-order nonlinear susceptibility values were obtained for different type of glasses.

Table I-4 - Examples of second-order nonlinear optical susceptibility values for non-crystalline materials after Thermal Poling.

	Composition or glass type	**$\chi_{zzz}^{(2)}$ ($\lambda_{measure}$)**	**Reference**
Oxide Glasses	Silicate	1 pm/V e 0.004-0.3 pm/V (1.06 µm)	Myers *et al.* (1991)/ Dussauze *et al.* (2012)
	Germanosilicate fiber	0.2 pm/V (1.06 µm)	Kazansky *et al.* (1994)
	$20Na_2O$-$80(0.35Nb_2O_5$-$0.65GeO_2)$	0.6 pm/V (1.06 µm)	Guimbretière *et al.* (2010)
	Sodium Niobium Borophoshphate (BPN)	4-5 pm/V (1.06 µm)	Dussauze *et al.* (2005)/ Dussauze *et al.* (2006)
	BPN (thin film)	3 pm/V (1.06 µm)	Dussauze *et al.* (2006b)
	$70GeO_2$-$10Na_2O$-$20Ta_2O_5$	0.3 pm/V (1.5 µm)	Poirier *et al.* (2019)
	Tellurite	0.2-1.5 pm/V (1.06 µm)	Tanaka *et al.* (1995)/ Tanaka *et al.* (1996)
	Tellurite with tungsten	2.1 pm/V (1.06 µm)	Tanaka *et al.* (2000)
	$0.95Ta_2O_5$-$0.05Na_2O$ (thin film)	0.2 pm/V (1.5 µm)	Tong *et al.* (2019)
Chalcogenide Glasses	$Ge_{25}Sb_{10}S_{65}$	8 pm/V (1.9 µm)	Guignard *et al.* (2007)
	$Ge_{22.5}Sb_{10}S_{67.5}$ + 3 mol.% Na_2S	0.1-0.3 pm/V (1.5 µm)	Lepicard *et al.* (2018)
	$Ga_5Ge_{20}Sb_{10}S_{65}$	4-5 pm/V (1.9 µm)	Zeghlache *et al.* (2007)
	$As_{34}Ge_6Na_2S_{58}$	0.05 pm/V (1.5 µm)	Shoulders *et al.* (2013)
	As_2S_3 (thin film)	0.6 pm/V (1.5µm)	Quiquempois *et al.* (2000)
	$60GeS_2$-$20Ga_2S_3$-20KBr	7 pm/V (? µm)	Jing *et al.* (2006)

Reference: AUTHOR.

Although very useful, a high value of $\chi^{(3)}$ does not necessarily imply a high value of $\chi^{(2)}$. For example, for chalcogenide glasses, the highest values presented are between 7 and 8 pm/V, and this type of glasses, in general, have higher $\chi^{(3)}$ values. However, for other chalcogenide glasses (even with very similar compositions - Table I-4), the reported susceptibilities are one to two orders of magnitude lower.

Time and voltage applied during the Thermal Poling treatment also influence the final result. Quiquempois, Godbout and Lacroix (2002) showed the strong dependence of the SHG intensity on the voltage applied when Poling an Infrasil 301® glass slide, in which they verified the existence of a voltage threshold and also a linear dependence of the square root of the signal

SHG with the voltage intensity. In this particular glass, they found a rather large SHG response and a relatively thin (5 μm) space charge layer.

Another factor that must be considered is the ability of the glass to withstand the implementation of a large electric field for a long time. For example, in sodium niobium borophosphate glasses, which have intermediate nonlinear indices, a response of up to 5 pm/V was induced which is stable (several years). On the other hand, if in these glasses, sodium is replaced by calcium or barium, the response decreases by an order of magnitude (0.2-0.3 pm/V) (KARAM, 2020).

Concerning SHG in glass-ceramics, it is generally related to the presence of non-centrosymmetric crystals present in the material. For example, in the glass-ceramic studied by Evangelista *et al.* (2021) in which SHG was observed in surface spherulites formed by the α-GeO_2 crystalline phase. Vigouroux *et al.* (2011) observed SHG in $LiNbO_3$ crystal in glass-ceramic obtained from lithium niobium silicate glass. Sander *et al.* (2021) investigated the controlled crystallization of the surface of lithium-zinc-alumino-silicate glass-ceramics, in which the thermal treatments to obtain the glass-ceramics were made after performing the Poling on the glass.

Regarding the Thermal Poling of glass-ceramics, there are not many works in this approach. Malakho *et al.* (2005) performed a Thermal Poling test on glass-ceramics obtained from niobium borophosphate glass, in which, for higher concentrations of sodium, two crystalline phases were obtained depending on the type of thermal treatment: $Na_4Nb_8P_4O_{32}$ and another phase in which the authors only identify as a sodium niobate phase, but which is likely to be the $Na_2Nb_8O_{21}$. The researchers verified that before the Thermal Poling, the glass-ceramics (as well as the glasses) did not present a SHG signal, but that these were obtained after the Thermal Poling and would only be related to the samples in which there was the presence of the sodium niobate phase.

I-6.4 Micro-imprinting on glasses by Thermal Poling

In topic I-6.3, it was presented the SHG in glasses through Thermal Poling, and until then the use of electrodes - anode - was considered as being “homogeneous”, i.e., they are conductors in the entire surface. However, for many applications, it is very interesting to structure properties on micrometer scales. The manufacture of compact optical components when the scale of devices continues to decrease will depend on new functional materials. Considering that, Thermal Micropoling of glasses in a micrometric and controlled scale also becomes

promising. Two strategies can then be considered: the first is to uniformly Poling the entire surface and then, in a second step, selectively “depoled” it by laser irradiation; and the second, which is of interest in this work, consists of using the microstructured electrode allowing the structures it presents to be transferred to the surface of the poled sample, that is, “printing” the patterns on the material (KARAM, 2020; SHOULDERS *et al.*, 2013).

Takagi *et al.* (2008) developed a microprinting technique and managed to print reliefs of one hundred nanometers with a precision in the plane of the order of microns. Lipovskii *et al.*, using a metallic grid as an electrode, demonstrated a topological variation of the order of ten nanometers. The authors printed the electrode patterns on the glass surface and associated this variation in topology with the deformation of the glass matrix induced by the migration of alkaline ions and their replacement by H^+ ions. The variation in glass reactivity, e.g., acid attack, was studied by Lepicard *et al.* (2016) in borosilicate glasses, in which the treated sample (Thermal Poling) is exposed to air, and the poled area reacts with ambient water to form boric acid, while the non-poled area remains unchanged. They demonstrate this property on the centimeter scale (with a homogeneous electrode), but they also manage to structure the surface reactivity of their glass on the micrometer scale, as evidenced by the optical image in Figure I-21.

Figure I-21 - Optical image of the surface of a poled borosilicate glass with a microstructured electrode after contact with ambient air.

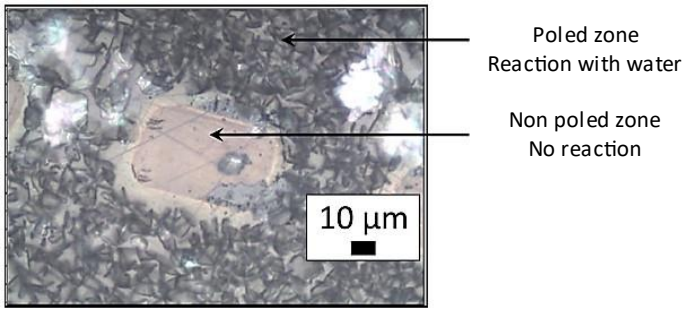

Reference: Modified from LEPICARD *et al.* (2016, p.13).

Thermal Poling is also useful to control optical properties of glasses. Lepicard *et al.* (2018) took advantage of the refractive index variation induced by sodium migration in sodium chalcogenide glasses to manufacture microlens arrays, which makes it possible to consider the design of optical devices for infrared applications. In fact, placed in front of a detector, this set of microlens can make it possible to focus the light intensity on each pixel of the detector. Thus, light information is fully collected.

And, finally, the structured Poling allows to control the response of the Second Harmonic in microscopic scale. Using an electrode with alternating conductive and non-conductive areas, Dussauze *et al.* (2016) demonstrated the accuracy and efficiency of their treatment by producing a second harmonic diffraction grating on the surface of a sodium niobium borophosphate glass. Delestre *et al.* (2010) coated the surface of niobium borophosphate glass with silver, which was then removed locally using a femtosecond laser (microstructuring) and the sample is finally poled.

The SHG response in borosilicate glass after Micropoling was studied by Lepicard *et al.* (2016), in which the SHG mapping is shown in Figure I-22. According to the authors, the SHG response is structured and is correlated to edge effects and a higher density of charges induced on the edge of the patterns. In a classic Thermal Poling treatment, performed without structured electrodes, the electric field is perfectly perpendicular to the surface, giving only a longitudinal and uniform intensity of the SHG along the poled surface. When structuring the electrode, a field increase phenomenon seems to occur, altering the charge density along the glass surface, in addition to promoting charge displacement not only along the z axis (into the sample), but also in the plane x-y of the glass. Over the patterned area, two orders of magnitude increase in charge concentration is observed, resulting in more charges being trapped after Poling and increasing the SHG in these areas.

Figure I-22 - (a) Optical micrograph of a rectangle inscribed on the surface after Poling and (b) corresponding µ-SHG map across the rectangle imprinted on the sample.

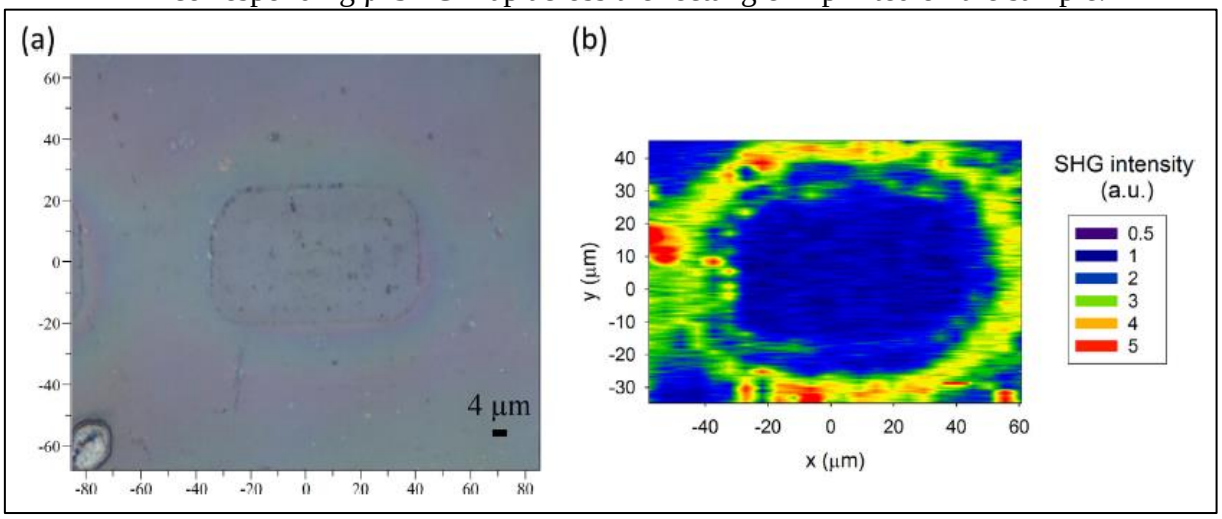

Reference: LEPICARD *et al.* (2016, p.12).

Micropoling was also performed in germanate glasses containing tantalum by Poirier *et al.* (2022), in which topological, structural and optical characterization studies of micro-imprinted structures were performed. A spatial reliefs of 100 nm depth were achieved and, as

the same observed by Lepicard *et al.* (2016), a second harmonic signals originating from both longitudinal and in-plane static electric fields were identified mainly near the borders of imprinted structures and related to a specific charge distribution model. Spatially controlled positive refractive index changes around 7 to 9 x10^{-3} could be induced (Figure I-23).

Figure I-23 - Characterizations of micro-imprinting of a tantalum germanate glass: A) µ-SHG map for azimuthal polarization; B) 3D Atomic Force Microscopy (AFM) image; C) AFM profile along the blue line in B; D) Phase contrast image and E) Optical thickness profile along the poled cross-section shown by the white arrow in D.

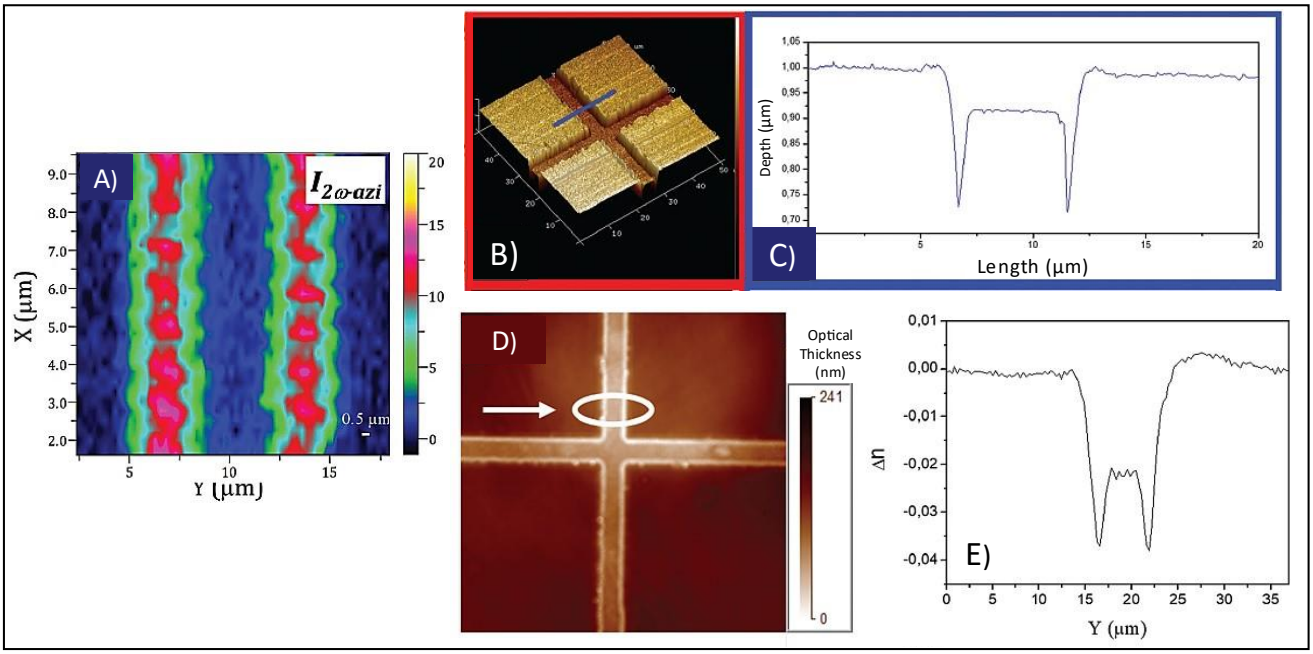

Reference: POIRIER *et al.* (2022, A - p.10314; B/D - p.10316 and D/E - p.10317).

Therefore, Thermal Micropoling, used as an imprinting process, can enable the structuring of a whole range of optical and physical-chemical properties on the surface of glasses. These properties and the resulting potential applications depend mightily on the composition of the glass.

REFERENCES

ACÁCIO, M. A. **Estudo dos processos de nucleação e cristalização em vidros boratos** = Study of nucleation and crystallization processes in borate glasses. 2006. 56p. Thesis (Master in Physics) - Universidade Estadual Paulista, Ilha Solteira, 2006.

AHMADI, S. *et al.* Preparation of monolithic transparent mullite-based glass-ceramics by the sol-gel method. **Journal of Non-Crystalline Solids**, [S.l.], v.575, p.121186, 2022.

ALMEIDA, R. P. **Síntese e caracterização de vidros de telureto dopados com íons de Eu^{3+} e Tb^{3+} com nanopartículas metálicas** = Synthesis and characterization of telluride glasses doped with Eu^{3+} and Tb^{3+} ions with metallic nanoparticles. 2009. 135p. Thesis (PhD in Engineering) - Universidade de São Paulo, São Paulo, 2009.

ALMEIDA, F.J.M. **Obtenção de vidros fosfatos contendo ferro por meio do aquecimento em fornos de microondas** = Obtaining iron-containing phosphate glasses by heating in microwave ovens. 2006. 59p. Thesis (Master in Science in Nuclear-Materials Technology) - Instituto de Pesquisas Energéticas e Nucleares- IPEN, Universidade de São Paulo, São Paulo, 2006.

ALMEIDA, M.E. *et al.* **Diretrizes para avaliação dos minerais estratégicos: fosfato, potássio, terras raras e lítio** = Guidelines for evaluating strategic minerals: phosphate, potassium, rare earths and lithium. Brasília: CPRM, 2015.

AMARAL, D. F. **Uso da luminescência do Eu^{3+} no estudo da vizinhança local e da transferência de energia Yb^{3+}-Eu^{3+} em nanocristais óxidos** = Use of Eu^{3+} luminescence in the study of local environment and Yb^{3+}-Eu^{3+} energy transfer in oxide nanocrystals. 2010. 100p. Thesis (PhD in Physics) - Universidade Federal Fluminense, Niterói, 2010.

ANDRADE, J.S. de. *et al.* Raman and infrared spectra of $KNbO_3$ in niobate glass-ceramics. **Journal of Physics:** Condensed Matter, [S.l.], v.11, p.4451, 1999.

ARJUN, P.N.J *et al.* Silver and silver nanoparticles for the potential treatment of COVID-19: a review. **Coatings,** Basel, v.12, 1679, 2022.

ARYAL, P. *et al.* Development of Eu^{3+}-doped phosphate glass for red luminescent solid-state optical devices. **Journal of Luminescence,** [S.l.], v.227, p.117564, 2020.

ATTALLAH, M. *et al.* Copper doped phosphate glass as an optical bandpass filter. **Silicon**, [S.l.], v.10, p.547-554, 2017.

BAIA, L. *et al.* Structural properties of silver nanoclusters-phosphate glass composites. **Vibrational Spectroscopy,** [S.l.], v.43, p.313-318, 2007.

BATISTA, G. **Incorporação de nanopartículas cristalinas de niobato de lantânio em vidros teluritos para obtenção de vitrocerâmicas funcionais =** Incorporation of crystalline lanthanum niobate nanoparticles in tellurite glasses to obtain functional glass-ceramics. 2018, 134p. Thesis (Master in Material Science and Engineering) - Universidade Federal de Alfenas, Poços de Caldas, 2018.

BATISTA, G.; VIANNA, C.A.F.J. Conhecimentos sobre vidros e abordagem temática: uma proposta pra contextualização do ensino de química em Poços de Caldas, MG = Knowledge about glasses and thematic approach: a proposal for the contextualization of chemistry teaching in Poços de Caldas, MG. **Revista Ciências & Ideias,** Rio de Janeiro, v.13, n.01, p.259-284, 2022.

BATISTA, G. *et al.* Incorporation of as-prepared Eu^{3+}-doped lanthanum niobate nanoparticles in tellurite glasses. **Materials Research**, São Carlos, v.26, e20230376, 2023.

BINNEMANS, K. Interpretation of europium (III) spectra - A review. **Coordination Chemistry Reviews**, [S.l.], v.295, n.01, p.01-45, 2015.

BOCCACCINNI, R. *et al.* Glass-ceramics: their production from wastes - A review. **Journal of Materials Science**, [S.l.], v. 41, n. 03, p. 733-761, 2006.

BOYD, R.W. **Nonlinear Optics**. 4th ed. 634p. London: Academic Press, 2020.

BRAZ, C.E. **Preparação e caracterização de vidros e vitrocerâmicas fluorofosfato s no sistema ternário $NaPO_3$-WO_3-PbF_2** = Preparation and characterization of fluorophosphate glasses and glass-ceramics in the $NaPO_3$-WO_3-PbF_2 ternary system. 2014. 89p. Thesis (Master in Material Science and Engineering) - Universidade Federal de Alfenas, Poços de Caldas, 2014.

BURTAN, B. *et al.* Influence of rare earth ions on the optical properties of tellurite glass. **Acta Physica Polonica A**, Poland, v.140, n.04, p. 579-581, 2011.

CAETANO, M. **Estudos de sistemas vítreos dopados com Er^{3+} visando aplicações em fibras e amplificadores ópticos** = Studies of glassy systems doped with Er^{3+} aiming applications in fibers and optical amplifiers. 2013. 157p. Thesis (Master in Physics) - Universidade Federal de Uberlândia, Uberlândia, 2013.

CALLISTER, W. D. **Ciência e Engenharia de Materiais:** uma introdução = Materials Science and Engineering: na introduction. 7. ed. Rio de Janeiro: LTC Editora S.A, 2007.

CARDINAL, T. **Propriétés optiques non linéaires des verres borophosphatés de titane ou de niobium** = Nonlinear optical properties of titanium or niobium borophosphate glasses. 1997. 241p. Thesis (PhD in Solids Chemistry - Materials Chemistry) - Université de Bordeaux, Bordeaux, France, 1997.

CARLSON, D.E., HANG, K.W., STOCKDALE, G.F. Electrode “polarization” in alkali-containing glasses. **Journal of the American Ceramic Society**, USA, v.55, n.07, p.337-341, 1972.

CARTER, C.B.; NORTON, M.G. **Ceramic Materials**: science and engineering. Nova York: Springer, 2013.

CASSANI, R. **Estudo de cristalização em vidros fosfatos alcalinos contendo óxido de nióbio** = Study of crystallization in alkaline phosphate glasses containing niobium oxide. 2022. 100p. Thesis (Master in Material Science and Engineering) - Universidade Federal de Alfenas, Poços de Caldas, 2022.

CASSANJES, F. C. **Vidros a base de óxido de telúrio para dispositivos fotônicos** = Tellurium oxide-based glasses for photonic devices. 2003. 187p. Thesis (PhD in Chemistry) - Universidade Estadual Paulista, Araraquara, 2003.

CASSAR, D. R. **Nucleação, crescimento de cristais, relaxação e escoamento viscoso em vidros diopsídio e diborato de lítio** = Nucleation, crystal growth, relaxation and viscous flow in diopside and lithium diborate glasses. 2014. 176p. Thesis (PhD in Material Science and Engineering) - Universidade Federal de São Carlos, São Carlos, 2014.

CHEN, K. *et al.* Preparation of glass-ceramic from titanium-bearing blast furnace slag by "Petrurgic" Method. **The Minerals, Metals & Materials Society**: Energy Technology, Pittsburgh, v.07, p. 415-428, 2018.

CHEN, X. *et al.* Evolutionary metal oxide clusters for novel applications: toward high-density data storage in nonvolatile memories. **Advanced Materials**, Weinheim, v.30, p.1-9, 2018.

CHOPINET, M-H. The history of glass. *In:* MUSGRAVES, J.D.; HU, J.; CALVEZ, L. **Springer Handbook of Glass**. [S.l.], Springer International Publishing, 2019. p. 1-47.

CORDEIRO, L. *et al.* Thermal and structural properties of tantalum alkali-phosphate glasses. **Journal of Non-Crystalline Solids,** [S.l.], v.402, p.44-48, 2014.

CORNING, A. **Smart glass opens a window to new applications**. Radiant Vision Systems, 2022. Available in: https://www.radiantvisionsystems.com/blog/smart-glass-opens-window-new-applications. Access: 02 jul. 2022.

CUNHA, C.R. **Vidros e vitrocerâmicas luminescentes de germanato de tântalo** = Tantalum germanate luminescent glasses and glass-ceramics. 2018. 141p. Thesis (PhD in Chemistry) – Universidade Federal de Alfenas, Alfenas, 2018.

DABNUN, M. A. Y. **Machinability studies of machinable glass-ceramic materials: Macor and Boron Nitride.** 2004. 176p. Thesis (Master in Engineering) - Dublin University, Dublin (Ireland), 2004.

DELESTRE, A. *et al.* Towards Second-Harmonic Generation micropatterning of glass surface. **Applied Physics Letter**, [S.l.], v.96, n.09, p.091908, 2010.

DEUBENER, J. *et al.* Update definition of glass-ceramics. **Journal of Non-Crystalline Solids**, [S.l.], v. 501, p.03-10, 2018.

DIAS, S.T. **Efeitos fotoinduzidos em vidros e filmes finos de fosfato de antimônio dopado com chumbo e fosfato de antimônio dopado com cromo** = Photoinduced effects in glasses and thin films of lead-doped antimony phosphate and chromium-doped antimony phosphate. 2010. 87p. Thesis (Master in Material Science and Engineering) - Universidade de São Paulo, São Carlos, 2010.

DONATO, G. *et al.* A one-step synthesis of rare-earth phosphate–borosilicate glass composites. **RSC Advances,** [S.l.], v.68, p.39053-39065, 2018.

DUBIEL, M. *et al.* Structure and properties of nanoparticle glass composites. **Physics and Chemistry of Glasses**, [S.l.], v.46, p.148-152, 2005.

DUSSAUZE, M. *et al.* Large second-harmonic generation of thermally poled sodium borophosphate glasses. **Optics Express**, [S.l.], v.13, n.11, p.4064-4069, 2005.

DUSSAUZE, M. *et al.* Correlation of large SHG responses with structural characterization in borophosphate niobium glasses. **Optical Materials**, [S.l.], v.28, n.12, p.1417-1422, 2006.

DUSSAUZE, M. *et al.* Large second order optical nonlinearity in thermally poled amorphous niobium borophosphate films. **Journal of Applied Physics**, [S.l.], v.100, n.01, 013108, 2006b.

DUSSAUZE, M. *et al.* Thermal Poling of optical glasses: mechanisms and Second-Order Optical properties. **Int Journal of Applied Glass Science**, [S.l.], v.03, n.04, p.309-320, 2012.

DUSSAUZE, M. *et al.* Thermal poling behavior and SHG stability in arsenic-germanium sulfide glasses. **Optical Materials Express**, [S.l.], v.03, n.06, p.700-710, 2013.

DUSSAUZE, M. *et al.* Accurate Second Harmonic Generation microimprinting in glassy oxide materials. **Advanced Optical Materials**, Weinheim, v.04, n.06, p.929-935, 2016.

DUSSAUZE, M.; CARDINAL, T. Nonlinear optical properties of glass. *In:* MUSGRAVES, J.D.; HU, J.; CALVEZ, L. **Springer Handbook of Glass**. [S.l.], Springer International Publishing, 2019. p. 193-225.

EVANGELISTA, R.O. **Alkaline tantalum germanate glasses and glass-ceramics for second harmonic generation.** 2021. 110p. Thesis (Master in Chemistry) - Universidade Federal de Alfenas, Alfenas, 2021.

EVANGELISTA, R.O. *et al.* Spherulitic crystallization of quartz-like GeO_2 and correlated second harmonic generation in sodium tantalum germanate glasses. **Journal of Alloys and Compounds**, [S.l.], v.877, p.160245, 2021.

FARACO, T.A. **Estudo das propriedades térmicas, ópticas e estruturais de vidros fosfato de silício dopados com érbio e prata para aplicação em telecomunicação** = Study of the thermal, optical and structural properties of silicon phosphate glasses doped with erbium and silver for application in telecommunication. 2015. 137p. Thesis (Master in Physics) - Universidade Federal de Juiz de Fora, Juiz de Fora, 2015.

FARGIN, E. *et al.* Second-harmonic generation of thermally poled silver doped sodo-borophosphate glasses. **Journal of Applied Physics,** [S.l.], v.105, p.023105, 2009.

FERENCZ, J. A. P. **Preparação e caracterização de vidros teluritos dopados com cloreto de césio para aplicações ópticas** = Preparation and characterization of tellurite glasses doped with cesium chloride for optical applications. 2013. 61p. Thesis (Master in Physics) - Universidade de Campinas, Campinas, 2013.

FERREIRA, B. *et al.* Second harmonic generation induced by poling in borophosphate bulk and thin film glasses. **Journal of Non-Crystalline Solids**, [S.l.], v.343, p.121-130, 2004.
FITERMAN, I. R. **Balanço Mineral Brasileiro**: Prata = Brazilian Mineral Balance: Silver. Brasília - DF: DNPM, 2001.

FLAMBARD, A. *et al.* Solid-state NMR study of mixed network sodium-niobium phosphate glasses. **Journal of Non-Crystalline Solids**, [S.l.], v.345, p.75-79, 2004.

FOTHERINGHAM, U. Viscosity of glass and glass-forming melts. *In:* MUSGRAVES, J.D.; HU, J.; CALVEZ, L. **Springer Handbook of Glass**. [S.l.], Springer International Publishing, 2019. p. 79-112.

FRAGOSO, W. D. **Espectroscopia e transferência de energia em vidros La_2O_3-Nb_2O_5-B_2O_3** = Spectroscopy and energy transfer in La_2O_3-Nb_2O_5-B_2O_3 glasses. 2003. 102p. Thesis (PhD in Science) - Universidade Federal de Pernambuco, Recife, 2003.

FRANKEN, P.A. *et al.* Generation de optical harmonics. **Physical Review Letters**, USA, v.07, n.04, p.118-119, 1961.

GHOSH, S. *et al.* Enhanced bioactive glass-ceramic coating on Ti_6Al_4V substrate by microwave processing technique for biomedical applications. **Materials Letters**, [S.l.], v.218, p.60-66, 2018.

GHUSSN, L.; MARTINELLI, J.T. A novel method to produce niobium phosphate glasses by microwave heating. **Journal of Materials Science**, [S.l.], v.39, p.1371-1376, 2004.

GHUSSN, L., *et al.* Crystallization of a niobium phosphate glass. **Journal of Non-Crystalline Solids**, [S.l.], v.352, p.3391-3397, 2006.

GONÇALVES, T. S. **Caracterização estrutural e espectroscópica de vidros fluorofosfatos dopados e co-dopados com Er^{3+} Yb^{3+}** = Structural and spectroscopic characterization of Er^{3+} Yb^{3+} doped and co-doped fluorophosphate glasses. 2014. 98p. Thesis (Master in Science) - Universidade de São Paulo, São Carlos, 2014.

GONCHARUK, V. K. *et al.* Crystallization and luminescence properties of Eu^{3+}-doped ZrF_4-BaF_2-$NaPO_3$ glass and glass ceramics. **Journal of Non-Crystalline Solids,** [S.l.], v.480, p.61-69, 2018.

GOUVÊA JUNIOR, J.T. **Propriedades térmicas e ópticas de vidros nanoestruturados dopados com nanopartículas de metais nobres** = Thermal and optical properties of nanostructured glasses doped with noble metal nanoparticles. 2016. 116p. Thesis (Master in Materials Science and Engineering) - Universidade Federal de Alfenas, Poços de Caldas, 2016.

GUIGNARD, M. *et al.* Chalcogenide glasses based on germanium disulfide for second harmonic generation. **Advanced Functional Materials,** Weinheim, v.17, n.16, p.3284-3294, 2007.

GUIMBRETIÉRE, G. *et al.* Correlation between Second-Order Optical response and structure in thermally poled sodium niobium-germanate. **Applied Physics Letters,** [S.l.], v.97, 171103, 2010.

GUPTA, P.K. Non-crystalline solids: glasses and amorphous solids. **Journal of Non-Crystalline Solids**, [S.l.], v.195, p.158-164, 1996.

HALIMAH, M. K. *et al.* Optical properties of ternary tellurite glasses. **Materials Science - Poland**, Poland, v. 28, n. 01, p. 173-180, 2010.

HE, Q. *et al.* Antiviral Properties of Silver Nanoparticles against SARS-CoV-2: Effects of Surface Coating and Particle Size. **Nanomaterials,** Basel, v.12, 990, 2022.

HE, X. *et al.* Microstructured SHG patterns on Sm_2O_3-doped borophosphate niobium glasses by laser-induced thermal poling. **Ceramics International**, United Kingdom, v.47, p.10123-10129, 2021.

HIRAO, K., TODOROKI, S., SOGA, S. Origin of inhomogeneous linewidth of Eu^{3+} fluorescence in phosphate and borophosphate glasses. **Journal of Non-Crystalline Solids**, [S.l.], v.175, p.263-269, 1994.

HOLUBOVÁ, J., ČERNOŠEK, Z., HEJDA, P. The influence of niobium on the structure of Nb_2O_5-ZnO-P_2O_5 glasses. **Journal of Non-Crystalline Solids**, [S.l.], v.502, p.35-43, 2018.

HOPPE, U. *et al.* Structure of Nb_2O_5-$NaPO_3$ glasses by X-ray and neutron diffraction. **Physical Chemistry Chemical Physics,** [S.l.], v.15, p.8520-8528, 2013.

HSU, S.M. *et al.* Effect of silver concentration on the silver-activated phosphate glass. **Materials Chemistry and Physics**, Netherlands, v.123, p.172-176, 2010.

HUANG, P.Y., *et al.* Direct imaging of a two-dimensional silica glass on graphene. **Nano Letters**, USA, v.12, p.1081-1086, 2012.

IHYADN, A. *et al.* Structural, electrical and energy storage properties of BaO-Na_2O-Nb_2O_5-WO_3-P_2O_5 glass-ceramics system. **Materials Research Express**, [S.l.], v.06, p.115203, 2019.

IVANOV, S.A., IGNATIEV, A.I., NIKONOROV, N.V. Advances in photo-thermo-refractive glass composition modifications. **Holography:** Advances Modern Trends IV, Prague, v.9508, 2015.

JHA, K.; JAYASIMHADRI, M. Structural and emission properties of Eu^{3+}-doped alkaline earth zinc-phosphate glasses for white LED applications. **Journal of the American Chemistry Society,** USA, v.100, n.04, p.1402-1411, 2017.

JING, R. *et al.* Second-harmonic generation in thermally poled chalcohalide glass. **Optics Letters,** [S.l.], v.31, n.23, p.3492-3494, 2006.

KARAM, L. **Structuration multi-échelle et multifonctionnelle de nouveaux matériaux vitreux pour la photonique intégrée** = Multiscale and multifunctional structuring of new

glassy materials for integrated photonics. 2020. 275p. Thesis (PhD in Chemistry Science) - Université de Bordeaux, Bordeaux, France, 2020.

KARAM, L. *et al.* Electrically micro-polarized amorphous sodo-niobate film competing with crystalline lithium niobate second-order optical response. **Advanced Optical Materials**, Weinheim, v.08, n.13, p.2000202, 2020.

KAZANSKY, P.G., RUSSEL, P.St.J. Thermally poled glass: frozen-in electric field or oriented dipoles? **Optics Communication,** [S.l.], v.110, n.05-06, p.611-614, 1994.

KHADAR, A. A.; SEBASTIAN, S. Optical properties of $60B_2O_3$–$(40–x)PbO–xMCl_2$ and $50B_2O_3$–$(50–x)$ $PbO–xMCl_2$ (M = Pb, Cd) glasses. **Journal of Material Science - Indian**, United Kingdom, v.27, n.02, p.207-212, 2004.

KONIDAKIS, I. *et al.* Erasable and rewritable laser-induced gratings on silver phosphate glass. **Applied Physics A**, [S.l.], v.124, p.839, 2018a.

KONIDAKIS, I. *et al.* Effect of composition and temperature on the second harmonic generation in silver phosphate glasses. **Optical Materials**, [S.l.], v.75, p.796-801, 2018b.

KOUDELKA, L. *et al.* Structure and properties of potassium niobato-borophosphate glasses. **Journal of Non-Crystalline Solids**, [S.l.], v.354, p.129-133, 2018.

KRIEGER, U.K.; LANFORD, W.A. Field assisted transport of Na^+ ions, Ca^{2+} ions and electrons in commercial soda-lime glass i: experimental. **Journal of Non-Crystalline Solids,** [S.l.], v.102, p.50-61, 1988.

LEPICARD, A. **Design of surface chemical reactivity and optical properties in glasses.** 2016. 293p. Thesis (PhD in Chemistry) - Université de Bordeaux, Bordeaux (France), 2016.

LEPICARD, A. *et al.* Micro-structuring the surface reactivity of a borosilicate glass via thermal poling. **Chemical Physics Letters,** [S.l.], v.664, p.10-15, 2016.

LEPICARD, A. *et al.* Demonstration of dimensional control and stabilization of second harmonic electro-optical response in chalcogenide glasses. **Optical Material Express, [S.l.],** v.08, n.06, p.1613-1624, 2018.

LIGNY, D. de.; MÖNCKE, D. Colors in glasses. *In:* MUSGRAVES, J.D.; HU, J.; CALVEZ, L. **Springer Handbook of Glass**. Springer International Publishing, 2019. p. 297-342.

LIMA, C. L. J. de. **Vidros fosfatos de metais de transição** = Transition metal phosphate glasses. 2014. 110p. Thesis (Master in Material Science and Engineering) - Universidade Federal de Alfenas, Poços de Caldas, 2014.

LIMA, C.L.J. de. *et al.* Crystallization study of niobium potassium phosphate glasses. CBECIMAT - CONGRESSO BRASILEIRO DE ENGENHARIA E CIÊNCIA DOS MATERIAIS. 21., 2014, Cuiabá, MT, Brazil. **Anais** […]. [s.*n.*]: Cuiabá, 2014. p.1219-1226.

LIMA, C.L.J. de. *et al.* Thermal, Structural and Crystallization Study of Niobium Potassium Phosphate Glasses. **Materials Research**, São Carlos, v.18, 2015.

LINO, J.V. **Preparação e caracterização de vidros de fosfato de tungstênio contendo nanopartículas metálicas de prata, ouro e platina** = Preparation and characterization of tungsten phosphate glasses containing metallic silver, gold and platinum nanoparticles. 2013. 76p. Thesis (Master in Material Science and Engineering) - Universidade Federal de Alfenas, Poços de Caldas, 2013.

LO, N. T. **Second harmonic generation in germanotellurite glass ceramics doped with silver oxide.** 2016. 154p. Thesis (PhD in Chemistry) - Université de Bordeaux, Bordeaux (France), 2016.

LOPES, O.F. *et al.* Óxidos de nióbio: uma visão sobre a síntese do Nb_2O_5 e sua aplicação em fotocatálise heterogênea =Niobium oxides: an insight into Nb_2O_5 synthesis and its application in heterogeneous photocatalysis. **Química Nova**, São Paulo, v.38, p. 106-117, 2014.

LUMEAU, J., GLEBOVA, L., GLEBOV, L.B. Influence of UV-exposure on the crystallization and optical properties of photo-thermo-refractive glass. **Journal of Non-Crystalline Solids,** [S.l.], v.354, p.425-430, 2008.

LUMEAU, J.; ZANOTTO, E.D. A review of the photo-thermal mechanism and crystallization of photo-thermorefractive (PTR) glass. **International Materials Reviews**, United Kingdom, v.62, p.348-366, 2017.

MA, N.L. **Dissolution behavior of phosphate glasses**. 2014. 234p. Thesis (PhD in Ceramic Engineering) - Missouri University of Science and Technology, Missouri, 2014.

MA, R. *et al.* Stabilization of ultra-small $[Ag_2]^{2+}$ and $[Ag_m]^{n+}$ nano-clusters through negatively charged tetrahedrons in oxyfluoride glass networks: To largely enhance the luminescence quantum yields. **Physical Chemistry Chemical Physics**, [S.l.], v.34, p.22638-22645, 2017.

MAESTRI, S.A. **Vidros e vitrocerâmicas no sistema binário $NaPO_3$-Ta_2O_5** (Glass and glass-ceramics in the binary system $NaPO_3$-Ta_2O_5)**.** 2018. 104p. Thesis (Master in Material Science and Engineering) - Universidade Federal de Alfenas, Poços de Caldas, 2018.

MAGON, C.J. *et al.* Electron Paramagnetic Resonance (EPR) studies on the photo-thermo ionization process of photo-thermo-refractive glasses. **Journal of Non-Crystalline Solids**, [S.l.], v.452, p.320-324 (2016).

MAHDY, E.A., AHMED, H.Y., FARAG, M.M. Combination of Na-Ca-phosphate and fluorapatite in wollastonite-diopside glass-ceramic: degradation and biocompatibility. **Journal of Non-Crystalline Solids**, [S.l.], v.566, p.120888, 2021.

MAHFOUDHI, M. **Eu^{3+} ion environment modification by Electron and femtosecond laser irradiation in metaphosphate and polyphosphate glasses**. 2019. 223p. Thesis (PhD in Physics) - Université Paris-Saclay (France), 2019.

MALAKHO, A. **Second order optical nonlinearity in the crystals, glasses and glass-ceramic oxides containing vanadium and niobium**. 2006. 135p. Thesis (PhD in Chemistry) - Université de Bordeaux, Bordeaux (France), 2006.

MALAKHO, A. *et al.* Crystallization and second harmonic generation in thermally poled niobium borophosphate glasses. **Journal of Solid-State Chemistry,** [S.l.], v.178, p.1888-1897, 2005.

MARCONDES, L.M. **Vidros e vitrocerâmicas contend óxido de nióbio para dispositivos luminescentes** = Glasses and glass-ceramics containing niobium oxide for luminescent devices. 2019. 163p. Thesis (PhD in Chemistry) - Universidade Federal de Alfenas, 2019.

MARCONDES, L.M. *et al.* Transparent glass and glass-ceramic in the binary system $NaPO_3$-Ta_2O_5. **Journal of American Chemistry Society**, USA, v.103, p.1647-1655, 2019.

MARCONDES, L.M. *et al.* High tantalum oxide content in Eu^{3+}-doped phosphate glass and glass-ceramics for photonic applications. **Journal of Alloys and Compounds**, [S.l.], v.842, p.155853, 2020.

MARCONDES, L.M. *et al.* Structural and optical characterization of tungsten phosphate glasses containing silver and erbium. **Optical Materials**, [S.l.], v.132, p.112717, 2022.

MASSERA, J. **Nucleation and growth behavior of tellurite-based glasses suitable for mid-infrared applications.** 2009. 233f. Thesis (PhD in Materials Science and Engineering) - Clemson University, Clemson (United States), 2009.

MATOS, I. R. M. **Caracterização estrutural e espectroscópica de vitrocerâmicos baseados em vidros teluretos dopados com íons de érbio** = Structural and spectroscopic characterization of glass-ceramics based on telluride glasses doped with erbium ions. 2012. 78p. Thesis (Master in Physics) - Universidade Federal de Alagoas, Maceió, 2012.

MENDONÇA, C.R. **Dinâmica de não linearidades ópticas em macromoléculas e oligômeros** = Dynamics of optical nonlinearities in macromolecules and oligomers. 2000. 147p. Thesis (PhD in Science: Basic Pysics) - Universidade de São Paulo, São Carlos, 2000.

MOCHALOV, L.A. *et al.* Preparation of glasses in the Ge-S-I system by plasma-enhanced chemical vapor deposition. **Optical Materials,** [S.l.], v.46, p.310-313, 2015.

MOLLA, A.R. *et al.* Transparent Eu^{3+}-doped ferroelectric bismuth titanate glass-ceramic nanocomposites: fabrication and properties. **Journal of the American Chemistry Society,** USA, v.95, n.10, p.3056-3063, 2012.

MORASSUTI, C. *et al.* Eu^{3+}- doped alumino-phosphate glass for ratiometric thermometer based on the excited state absorption. **Journal of Luminescence,** [S.l.], v.193, p.39-43, 2018.

MUÑOZ, F. *et al.* Phosphate glasses. *In:* MUSGRAVES, J.D.; HU, J.; CALVEZ, L. **Springer Handbook of Glass**. [S.l.], Springer International Publishing, 2019. p. 553-594.

MYERS, R. A. *et al.* Large second-order nonlinearity in poled fused sílica. **Optics Letters**, [S.l.], v.16, n.22, p.1732-1734, 1991.

NALIN, M. *et al.* Materiais vítreos e luz: parte 1 = Vitreous materials and light: part 1. **Química Nova**, São Paulo, v.39, p.328-339, 2016.

NASR, P. **A theoretical study of Maker Fringe measurements in poled multi-layer silica structures focusing on the impact of layer quantity and spacing**. 2012. 80p. Thesis (Master in Applied Science and Electric and Computational Engineering) - Carleton University, Ottawa, Canada, 2015.

NOWAK, I.; ZIOLEK, M. Niobium Compounds: Preparation, Characterization, and Application in Heterogeneous Catalysis. **Chemical Reviews**, Washington, v. 99, p. 3603-3624, 1999.

OL'SHIN, P.K. *et al.* Optic properties of niobium-phosphate glasses containing lithium, sodium, and potassium oxides. **Glass Physics and Chemistry**, [S.l.], v.43, p.294-297, 2017.

OLIVEIRA, R.E.P.de. **Fabricação e caracterização de fibras ópticas contendo nanopartículas de ouro e conversão de frequências em microrressonadores em anel** = Fabrication and characterization of optical fibers containing gold nanoparticles and frequency conversion in ring microresonators. 2014. 96p. Thesis (PhD in Electrical Engineering) - Universidade Presbriteriana Mackenzie, São Paulo, 2014.

ÖSTERBERG, U.; MARGULIS, W. Dye laser pumped by Nd:YAG laser pulses frequency doubled in a glass optical fiber. **Optics Letters,** [S.l.], v.11, n.08, p.516-518, 1986.

PARTYKA, J. *et al.* Effect of addition of BaO on sintering of glass-ceramic materials from SiO_2-Al_2O_2-Na_2O-K_2O-CaO/MgO system. **Journal of Thermal Analysis and Calorimetry**, [S.l.], v.125, n.03, p.1095-1103, 2016.

PASCUAL, M. J. **Glass and glass-ceramic:** a general overview. Ceramic and glass Institute, Madrid, Spain, 2015. Available in: http://www.cost-newgen.org/wp-content/uploads/2016/06/1B-Glasses-and-Ceramics-A-general-Overview-MJ-Pascual.pdf. Access: 03 jun. 2022.

PILAQUINGA, F. *et al.* Silver nanoparticles as a potential treatment against SARS-CoV-2: A review. **Wiley Interdiscip Rev Nanomed Nanobiotechnol**, [S.l.], v.13, 1707, 2021.

POIRIER, G.Y. *et al.* Second Harmonic Generation in sodium tantalum germanate glasses by thermal poling. **Journal of Physics Chemistry C,** [S.l.], v.123, p.26528-26535, 2019.

POIRIER, G.Y. *et al.* Microscaled design of linear and non-linear optical properties in tantalum germanate glasses by thermal poling. **Journal of Materials Chemistry C**, [S.l.], v.10, p.10310-10319, 2022.

QUIQUEMPOIS, Y. *et al.* Second-order nonlinear susceptibility in As_2S_3 chalcogenide thin glass films. **Electronics Letters,** England, v.36, n.08, p.733-734, 2000.

QUIQUEMPOIS, Y.; GODBOUT, N.; LACROIX, S. Model of charge migration during thermal poling in silica glasses: evidence of a voltage threshold for the onset of a Second-Order Nonlinearity. **Physical Review A,** [S.l.], v.65, p.438161-4381614, 2002.

QUIQUEMPOIS, Y., KUDLINSKI, A., MARTINELLI, G. Zero-potential condition in thermally poled silica samples: evidence of a negative electric field outside the depletion layer. **Journal of Optical Society of America B,** USA, v.22, n.03, p.598-604, 2005.
RACHKOVSKAYA, G.E., BOBKOVA, N.B. Semiconducting niobate-phosphate glasses. Structure and properties. **Journal of Non-Crystalline Solids**, [S.l.], v.90, p.617-620, 1987.

REDKOV, A.V.; MELEHIN, V.G.; LIPOVSKII, A.A. How does thermal poling produce interstitial molecular oxygen in silicate glasses? **Journal of Physics Chemistry C,** [S.l.], v.119, p.17298-17307, 2015.

REIS, R. G. C. de S. **Fotoluminescência de Eu/Tb e de complexos Eu/Tb com ligantes tta ou acac incorporados em sílica mesoporosa** = Photoluminescence of Eu/Tb and Eu/Tb complexes with tta or acac ligands incorporated into mesoporous silica. 2012. 61p. Thesis (Master in Chemistry) - Universidade Federal do Mato Grosso do Sul, Campo Grande, 2012.

REMONTE, A. R. V. **Síntese e caracterização de nanocompósitos vitrocerâmicos transparentes à base de SiO_2-ZrO_2 dopados com íons Eu^{3+} e Er^{3+} via processo sol-gel =** Synthesis and characterization of transparent glass-ceramic nanocomposites based on SiO_2-ZrO_2 doped with Eu^{3+} and Er^{3+} ions via sol-gel process. 2008. 78p. Thesis (Master in Chemistry) - Universidade de São Paulo, Ribeirão Preto, 2008.

REPORT OCEAN. **Advanced glass market 2022 key applications, new technology and forecast till 2030.** 2022. Available in: https://www.designerwomen.co.uk/advanced-glass-market-2022-key-applications-new-technology-and-forecast-till-2030/. Access: 02 jul. 2022.

RIAÑO, L. P. N. **Preparação e caracterização óptica de vidros dopados com terras raras contendo nanoestruturas de prata** = Preparation and optical characterization of rare earth doped glasses containing silver nanostructures. 2006. 120p. Thesis (PhD in Material Science) - Universidade Federal de Pernambuco, Recife, 2006.

ROJAS, G. A. Q. **Polarização eletrotérmica de vidros e fibras ópticas** = Electrothermal poling of glasses and optical fibers. 2005. 247p. Thesis (PhD in Physics) - Pontifícia Universidade Católica do Rio de Janeiro, Rio de Janeiro, 2005.

ROMÃO, R.M. **Termometria óptica baseada em vidros fosfatos dopados com Er^{3+}** = Optical thermometry based on Er^{3+}-doped phosphate glasses. 2011. 97p. Thesis (Master in Condensed Matter Physics) - Universidade Federal de Alagoas, Maceió, 2011.

RUPP, J.L.M. *et al.* Time-temperature-transformation (TTT) diagrams for crystallization of metal oxide thin films. **Advanced Functional Materials**, Weinheim, v.20, n.17, p.2807-2814, 2010.

SANDER, M. *et al.* Controlled surface crystallization of lithium-zinc-alumosilicate glass-ceramics using thermal poling. **Journal of the American Ceramic Society,** USA, v.105, p.3279-3290, 2021.

SANTOS, F.P.deS. **Propriedades fotocromáticas dos vidros fosfatos PWSA e PZABP** = Photochromatic properties of PWSA and PZABP phosphate glasses. 2021. 134p. Thesis (PhD in Physics) - Universidade Federal de Alagoas, Maceió, 2021.

SAUTER, E.G. **Nonlinear Optics**. 1st ed. 323p. [S.l.], Wiley-Interscience, 1996.

SEER, H.J.; MORAES, L.C.de. Nióbio (Niobium). *In:* PEDROSA-SOARES, A.C.; VOLL, E.; CUNHA, E.C. **Recursos Minerais de Minas Gerais** (Mineral Resources of Minas Gerais). Belo Horizonte: Companhia de Desenvolvimento de Minas Gerais (CODEMGE), 2018.

SENE, F.F.; MARTINELLI, J.R.; GOMES, L. Synthesis and characterization of niobium phosphate glasses containing barium and potassium. **Journal of Non-Crystalline Solids,** [S.l.], v.348, p.30-37, 2004.

SENN, F. *et al.* Influencing the crystallization of glass-ceramics by ultrashort pulsed laser irradiation after nucleation. **New Journal of Glass and Ceramics**, [S.l.], n.08, p.01-11, 2018.

SHOULDERS, W.T.*et al.* Thermal poling behavior and SHG stability in arsenic-germanium sulfide glasses. **Optical Material Express,** [S.l.], v.03, n.06, p.70-710, 2013.

SIDEL, S. M. **Síntese e caracterização de vidros teluritos** = Synthesis and characterization of tellurite glasses. 2011. 86p. Thesis (PhD in Material Science) - Universidade Estadual Paulista, Ilha Solteira, 2011.

SILVA, R. A. **Estudo das propriedades mecânicas e químicas de vidros fosfatos com adição de óxido de nióbio** = Study of the mechanical and chemical properties of phosphate glasses with addition of niobium oxide. 2022. 180p. Thesis (Master in Material Science and Engineering) - Universidade Federal de Alfenas, Poços de Caldas, 2022.

SILVA, R. R. C. **A luminescência do Eu^{3+} para elucidação estrutural:** apropriação e utilização de conceitos e linguagens por estudantes de iniciação científica = The Eu^{3+} luminescence for structural elucidation: appropriation and use of concepts and languages by scientific initiation students. 2010. 66p. Thesis (Master in Science) - Universidade de Franca, Franca, 2010.

SIMON, S., CACAINA, D., BALASZ, I. Thermal and structural investigation of niobium phosphate glasses. **Modern Physics Letters B**, [S.l.], v.20, p.281-287, 2006.

SOARES-PINTO, D.; NAVES, C. Interferômetro de Mach-Zehnder e a escolha retardada quântica = Mach-Zehnder interferometer and quantum delayed choice. **Revista Ciência Brasileira de Ensino de Física,** São Paulo, v.43, e20210085, 2021.

SOUSA, B.P. *et al.* Phosphate glasses with high tantalum oxide contents: Thermal, structural and optical properties. **Materials Chemistry and Physics**, Netherlands, v.239, p.121996, 2020.

SOUZA, A. E. de. **Síntese e caracterização de vidros foto-termo-refrativos para aplicações fotônicas e obtenção de monocristais em sistemas vítreos** = Synthesis and characterization of photo-thermo-refractive glasses for photonic applications and obtaining single crystals in systems vitreous. 2019. 126p. Thesis (PhD in Chemistry) - Universidade Estadual Paulista, Araraquara, 2019.

SOUZA, G. D. de. *et al.* Silver: Brief history, properties and applications. **Educación Química,** São Paulo, v.24, p.14-16, 2013.

SMOGOR, H. *et al.* Effect of silver on phase separation and crystallization of niobium oxide containing glasses. **Journal of Solid-State Chemistry**, [S.l.], v.182, p.1351-1358, 2009.

STOLEN, R.H., TOM, H.W.K. Self-organized phase-matched harmonic generation in optical fibers. **Optics Letters,** [S.l.], v.12, n.08, p.585-587, 1987.

STUNDA-ZUJEVA, A. *et al.* Glass Formation and Crystallization in P_2O_5-Nb_2O_5-CaO-Na_2O system. **Materials Science and Applied Chemistry**, Latvia, v.34, p. 21-28, 2017.

SZCZESNIAK, P.A. **The Mineral Industry of Brazil**. Reston: United States Geological Survey, 2021.

TAKAGI, H. *et al.* Electrostatic Imprint Process for Glass. **Applied Physics Express,** [S.l.], v.01, n.02, 024003, 2008.

TANAKA, K. *et al.* Second harmonic generation in electrically poled Li_2O-Nb_2O_5-TeO_2 glasses. **Journal of Non-Crystalline Solids**, [S.l.], v.185, n.01-02, p.123-126, 1995.

TANAKA, K. *et al.* Optical second harmonic generation in poled MgO-ZnO-TeO_2 and B_2O_3-TeO_2 glasses. **Journal of Non-Crystalline Solids**, [S.l.], v.203, p.49-54, 1996.

TANAKA, K. *et al.* Large optical second-order nonlinearity of poled WO_3-TeO_2 glass. **Optics Letters,** [S.l.], v.25, n.04, p.251-253, 2000.

THIEL, C. W. **Energies of rare-earth ion states relative to host bands in optical materials from electron photoemission spectroscopy.** 2003. 380p. Thesis (PhD in Physics) - Montana State University, Bozeman (United States of America), 2003.

THOMAS, R. L. **Synthesis and characterization of tellurium oxide glasses for photonic applications.** 2013. 182p. Thesis (PhD in Photonic) - Cochin University of Science and Technology, Kerala (India), 2013.

TONG, A.S.K. *et al.* Effect of sodium addition and thermal annealing on second-order optical nonlinearity in thermally poled amorphous Ta_2O_5 thin films. **Journal of Applied Physics,** [S.l.], v.125, n.01, 015104, 2019.

VARSHNEYA, A. K. **Fundamentals of inorganic glasses.** 2nd ed. Sheffield: Society of Glass Technology, 2006. 570p.

VASILEVA, A.A. *et al.* Structural features of silver-doped phosphate glasses in zone of femtosecond laser-induced modification. **Journal of Solid-State Chemistry**, [S.l.], v.230, p.56-60, 2015.

VERBIEST, T.; CLAYS, K.; RODRIGUEZ, V. **Second-order nonlinear optical characterization techniques:** an introduction, CRC Press, Boca Raton, 2009.

VICENTE, F. S. de. **Estudo da mudança estrutural fotoinduzida em filmes de vidros a base de polifosfato de amônio** = Study of photoinduced structural change in ammonium polyphosphate-based glass films. 2004. 181p. Thesis (PhD in Material Science and Engineering) - Universidade de São Paulo, São Carlos, 2004.

VIGOUROUX, H. Crystallization and Second Harmonic Generation of lithium niobium silicate glass ceramics. **Journal of American Ceramic Society**, USA, v.94, n.07, p.2080-2086, 2011.

VIVAS, M.G. **Espectroscopia óptica não linear de nanomateriais:** fundamentos e aplicações = Nonlinear optical spectroscopy of nanomaterials: fundamentals and applications. Minicurso Congresso Nacional de Física, Química e Engenharia de Materiais da UFSJ, 2021.

VOGEL, W. **Chemistry of Glass**. New York: John Wiley & Sons Inc, 1985.

WANG, X. *et al.* Photochemical response triggered by ultrashort laser Gaussian-Bessel beams in photo-thermo-refractive glass. **Optics Express**, [S.l.], v.28, p.31093, 2020.

ZACHARIASEN, W. H. The atomic arrangement in glass. **Journal of American Society.** USA, 1932.

ZANOTTO, E.D.; MAURO, J.C. The glassy state of matter: Its definition and ultimate fate. **Journal of Non-Crystalline Solids**, [S.l.], v.471, p.490-495, 2017.

ZARZYCKI, J. **Glasses and the vitreous state**. New York: University Press, 1991.

ZEGHLACHE, H. *et al.* Stabilization of the second-order susceptibility induced in a sulfide chalcogenide glass by thermal poling. **Journal of Applied Physics,** [S.l.], v.101, n.08, 101063, 2007.

ZERLIM, A. **Estudo da dissolução de vidros niobofosfato em água e em solução simuladora de fluído fisiológico** = Evaluation of the dissolution rate of niobium phosphate glasses in water and simulated body fluid solution. 2008. 91p. Thesis (Master in Science - Nuclear Technology Materials) - Universidade de São Paulo, São Paulo, 2008.

ZILIO, S.C. **Óptica moderna:** fundamentos e aplicações = Modern optics: fundamentals and applications. Universidade de São Paulo. Instituto de Física de São Carlos, 2016.

ZHAO, M. *et al.* Effect of microstructure on up-conversion luminescent of $Tb^{3+/}Yb^{3+}$ co-doped phosphate glass and glass-ceramic. **Materials Letters,** [S.l.], v.243, p.73-76, 2019.

ZHAO, J.; EBENDORFF-HEIDEPRIEM, H. Direct doping of nanoparticles in glass shows potential for smart applications. **SPIE - International society for optics and photonics**, sd, 2016.

CHAPTER II - CHARACTERIZATION TECHNIQUES

CHAPTER II – CHARACTERIZATION TECHNIQUES

Considering the different techniques that were used to characterize the materials, this chapter present a summary/ brief description of the techniques used for this work.

II-1 THERMAL ANALYSIS AND X-RAY DIFFRACTION

Differential Scanning Calorimetry (**DSC**) is a thermal analysis very usual for glasses characterization. From the DSC curves is possible to obtain the characteristic temperatures: glass transition (T_g), crystallization onset (T_x), crystallization peak (T_c) and melting (of the crystalline phase) (T_m)[27]. The thermal stability to crystallization can be characterized by the (T_x-T_g) difference. The higher this value, the more stable the glass against crystallization (MENCZEL; GREBOWICZ, 2023; ZHENG *et al.*, 2019).

X-ray diffraction (**XRD**) technique is used to follow the evolution of the phases and determine the type of arrangement or crystalline structure of the material, or even the absence of crystallinity. The glass diffractogram is characterized by not presenting peaks due to the absence of periodicity, with just a halo that is a characteristic of materials that only present short-range order. On the other hand, crystalline structures present well-defined diffraction peaks for planes of atoms, obeying Bragg's Law and presenting a characteristic diffractometric pattern, allowing their identification through the angular positions and relative intensities of the diffracted peaks (WARREN, 1940; WASEDA; MATSUBARA; SHINODA, 2011).

II-2 SPECTROSCOPIC ANALYSIS

Different spectroscopies techniques are used for optical analysis of glasses. Among different optical properties of glasses, transparency window is often one of the essential: at one extreme there is the limit in the ultraviolet (UV)-visible (Vis) region, where occurs the band gap - corresponding to the energy difference between the conduction and valence bands of the glass matrix (below this limit the glass will absorb through the transition between these two bands and will no longer be transparent); and at the other extreme the infrared (IR) region, corresponding to the multiphonon frontier, referring to the vibrations of chemical bonds and their harmonics, i.e., energies that are multiples of the fundamental vibration energies of these

[27] These temperatures depend on the heating rate used during measurements (THOMAS, 2013).

bonds. Thus, these two extremes delimit the transparency window of glasses, being intrinsic to the material, depending directly on the composition. **UV-Vis-Nir spectroscopy** for glasses, in addition to the transparency window, also is used to observe bands due to absorptions in this region, depending on the composition of the glass, e.g., doped with rare-earth. **IR spectroscopy** (or FTIR - Fourier Transform InfraRed) is used either to determine one of the extremes of the glass transparency window, or also for structural analysis, since it is vibrational and acts in addition to **Raman spectroscopy**. For a vibrational mode to be active in the IR it is due to a variation of the dipole moment; in Raman, however, it must give rise to a polarizability variation. Some vibrational modes can be active in IR and not in Raman, and vice versa; or being in both, and therefore the techniques are considered complementary. From the analysis, a spectrum is obtained in which, from the positions, width and shape of the peaks, it is possible to obtain information about the structural character of the sample (LARKIN, 2018; PERKAMPUS, 1992).

In the **photoluminescence** spectroscopy is possible to obtained the emission and excitation spectra. Through this spectrum one can study the radiative decay of the system and obtain information such as point symmetry, oscillator strength and the type of transition. An excitation spectrum is obtained by monitoring the emission intensity of a given transition as the excitation wavelength varies. The result is a spectrum that brings information about the absorbed energy that is effectively observed in the luminescence of the monitored transition. An excitation spectrum can, for example, bring evidence of energy transfer between different active centers of the material (TEETS, 2021).

II-3 ATOMIC FORCE MICROSCOPY

Atomic Force Microscopy (**AFM**) is a technique that consists of scanning the surface of a sample with a probe not only to visualize its topography, but also to measure the surface properties of a material through the PeakForce mode which records force curves on the surface. In addition, electrical properties such as surface potential can be measured using Kelvin Probe Force Microscopy (KPFM). When using this mode, measurements normally involve two steps. Topography and mechanical properties are first mapped using PeakForce mode. In a second step, the surface potential is measured in KPFM mode, sweeping the surface with the cantilever at a fixed height. This technique allows accessing surface properties and correlating them with surface topology (HAUGSTAD, 2012; VOIGTLÄNDER, 2019).

II-4 ELEMENTARY CHEMICAL ANALYSIS

Time of Flight Secondary-Ion Mass Spectrometry (**ToF-SIMS**) is a destructive surface analysis technique, that is possible measure the depth profiles produced by the removal of surface layers. In a homogeneous case (without material change), this allows deducing the elemental concentration of the glass as a function of the depth. Thus, this technique makes it possible to monitor the concentration of mobile ions, e.g., in glass after Thermal Poling, verifying the concentration profile as layers of material are removed (FEAM, 2015). **Profilometry** is a technique used to extract topographical data from a surface and it is possible theoretically to assess the roughness as low as a nanometer. It can be made by mechanical analysis (where a metallic probe scans the surface) or optical analysis (where a light or laser beam scans the surface without direct interaction with the surface). Considering a poled glass, this technique is useful combining with ToF-SIMS to verify the length of the layer of mobile ions depletion (NanoScience Instruments, 2023).

Wavelength-Dispersive X-Ray Spectroscopy (**WDS**) is a quantitative analysis that allows measuring the characteristic X-rays generated by individual elements[28] (trace elements level) measured at spot sizes as small as a few micrometers. So, it is possible, e.g., to quantify the final composition of glasses (HENRY; GOODGE, 2016). For WDS used in this work, the optical system (consisting of primary filter, diaphragm, slit, attenuator, crystal and detector) installed in the spectroscopic chamber is used to analyze and count fluorescent x-rays. Different types of crystalline materials are applied, so-called analysis crystals located between the sample and the detector, moved according to the Bragg to measure fluorescent x-rays of a specific wavelength. The goniometer scanning range varies depending on the detector. Up to 10 types of crystals can be fixed in the device's spectroscopic system, being selected according to the wavelength range depending on the elements analyzed. The crystal and detector can be arbitrarily matched according to the wavelength range.

Elemental analysis of surfaces in Scanning Electron Microscopy is performed using Energy Dispersive Spectroscopy (**EDS**), which measures the energy and intensity distribution of X-ray signals generated by the electron beam striking the surface of the specimen. The elemental composition at a point, along a line, or in a defined area, can be determined to a high degree of precision. Elemental maps are often used to locate areas rich in elements present in

[28] WDS cannot determine elements below atomic number 5 (boron).

concentrations greater than 1% by weight. So, this technique allows for example, through an elemental mapping, verify the depletion of mobile ions after Thermal Poling (GIBSON, 2005).

II-5 MAKER FRINGES EXPERIMENT

"Maker Fringes" experiment is used to verify the SHG and when data such as refractive index and thickness of depletion layer that presents the second harmonic is available, it also allows to quantify the second order nonlinear optical susceptibility - $\chi^{(2)}$ - comparing the response of the sample with that of a reference (usually quartz). In addition, with this experiment there is the possibility of determining the origin of the second harmonic response (KARAM, 2020; NASR, 2015).

This measurement consists of a second harmonic ellipsometry technique that involves illuminating the sample at frequency ω and recording its response at 2ω by varying the angle of incidence at a fixed polarization, called **θ-scan**, or varying the polarization at a fixed angle of incidence, called **ψ-scan**. The system used in this work is located at the *Institut des Sciences Moléculaires* (ISM) and consists of a nanosecond laser operating at 1550 nm and 30 Hz (maximum pulses of 100 μJ per 20 ns) with a beam size of 100 μm. Therefore, SHG is measured at 775 nm (half the wavelength), and can be measured in transmission (used in this research) or in reflection mode.

The experiment setup scheme is shown in Figure II-1, in which the laser beam first passes through a power control device (λ/2 plate and Glan polarizer). An optical fiber collects part of the scattered beam to measure the incident intensity I_ω. The combination of the following half-wave (λ/2) and quarter-wave (λ/4) plates allows controlling the incident polarization state. The angle associated with the polarization is the angle Ψ, which varies from 0 to 360° and allows successively achieving vertical, left circular, horizontal, right circular and vertical polarizations (via elliptical polarizations). The beam then passes through a filter that allows to remove any previous second harmonic response and is sent to the sample. The sample can perform a rotation around the optical axis, in which the angle associated with this rotation is the angle θ. The second harmonic response is then analyzed and filtered to keep only the harmonic. It is measured by a photomultiplier and the signal is sent to an oscilloscope. In the case where the polarized light is parallel to the plane of incidence (horizontal) it is named as P, in case it is perpendicular (vertical) it is named as S - Figure II-2A (KARAM, 2020).

Figure II-1 - Set up scheme of the Maker Fringes experiment.

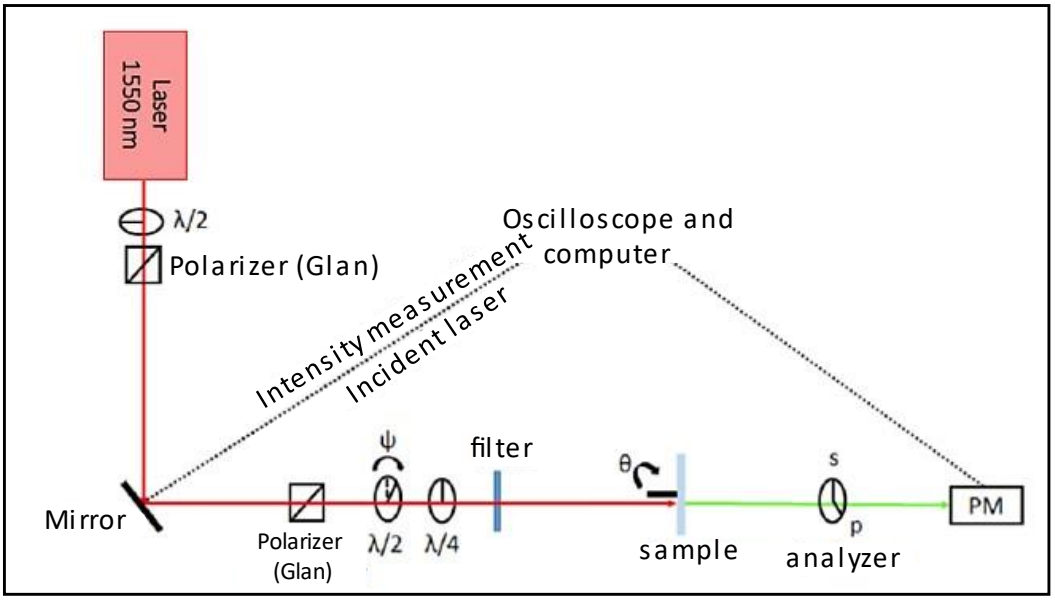

Reference: Translated from KARAM (2020, p.67).

Figure II-2 - A) Illustrative scheme of the measurement of Maker Fringes and B) Variation of the optical path during the second harmonic intensity measurement as a function of the incidence angle.

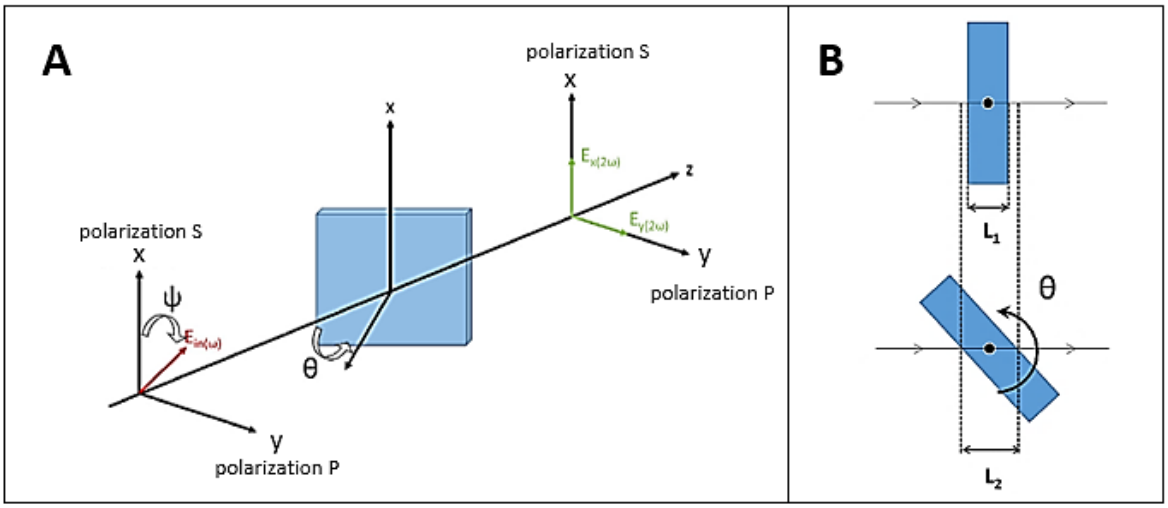

Reference: A) LEPICARD (2016, p.72) and B) KARAM (2020, p.68).

As described, it is possible to perform two types of measurements:

(1) **θ-scan:** measurements are made as a function of the angle θ, fixing the incident and analyzed polarization (S or P)[29]. During this measurement, varying the incidence angle θ allows the optical path length, L, to be varied, as shown in Figure II-2B. L increases with sample

[29] Named as: θ-ij with i,j = P,S, i being the incident polarization, j the analyzed polarization.

rotation by a factor of L/cosθ and for each multiple of Lc, the SHG goes from a maximum to a minimum. Many of these peaks appear as “fringes”, hence the name of the technique.

(2) **ψ-scan:** the measurements in this case are made with the fixed incidence angle θ and varying the polarization. Two variations in the measurement are performed, ψ-P and ψ-S, where P and S correspond to the fixed analyzed polarization, varying the angle ψ, and, therefore, the incident polarization. These measurements allow probing the different terms of the tensor (to which a rotation has been applied, since the measurement is not carried out at 0°). The ψ-P allows probing the first row of the tensor, and ψ-S the second. These measurements are particularly important because they allow to determine the ratio of the two components of the tensor in the case of $C\infty v$ symmetry and, therefore, to deduce the origin of the second harmonic signal (refer to Chapter I-6.1).

The adjustment of the parameters is made using a program developed by V. Rodriguez (ISM) that allows the modeling of multilayer anisotropic optical media (linear and non-linear) (RODRIGUEZ; SOURISSEAU, 2002). An example of the response obtained from the θ-pp measurement is shown in Figure II-3 for a poled niobium borophosphate glass.

Figure II-3 - Maker Fringes measurement of a poled bpn glass.

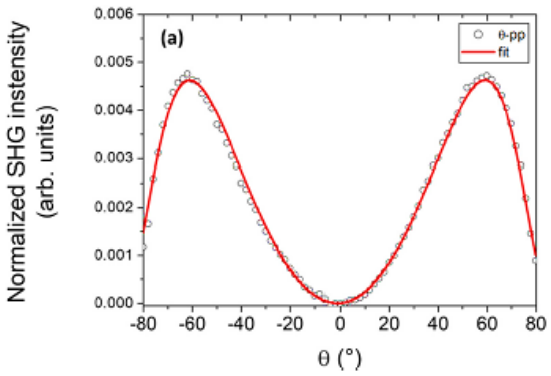

Reference: KARAM *et al.* (2020, p.09).

II-6 MICRO-SHG/MICRO-RAMAN/MICRO-LUMINESCENCE CORRELATION

To correlate the structural measurements (Raman), non-linear optical properties (SHG) and luminescence in the poled and non-poled areas, it is possible to use a coupling and measuring these properties on the same position and a mapping can be performed. Figure II-4 presents a schematic of the coupling used in this work, developed in the ISM, which allows

performing these three measurements exactly at the same position on the sample without having to move it.

Figure II-4 - Micro-Raman (luminescence)/ micro-SHG set-up scheme.

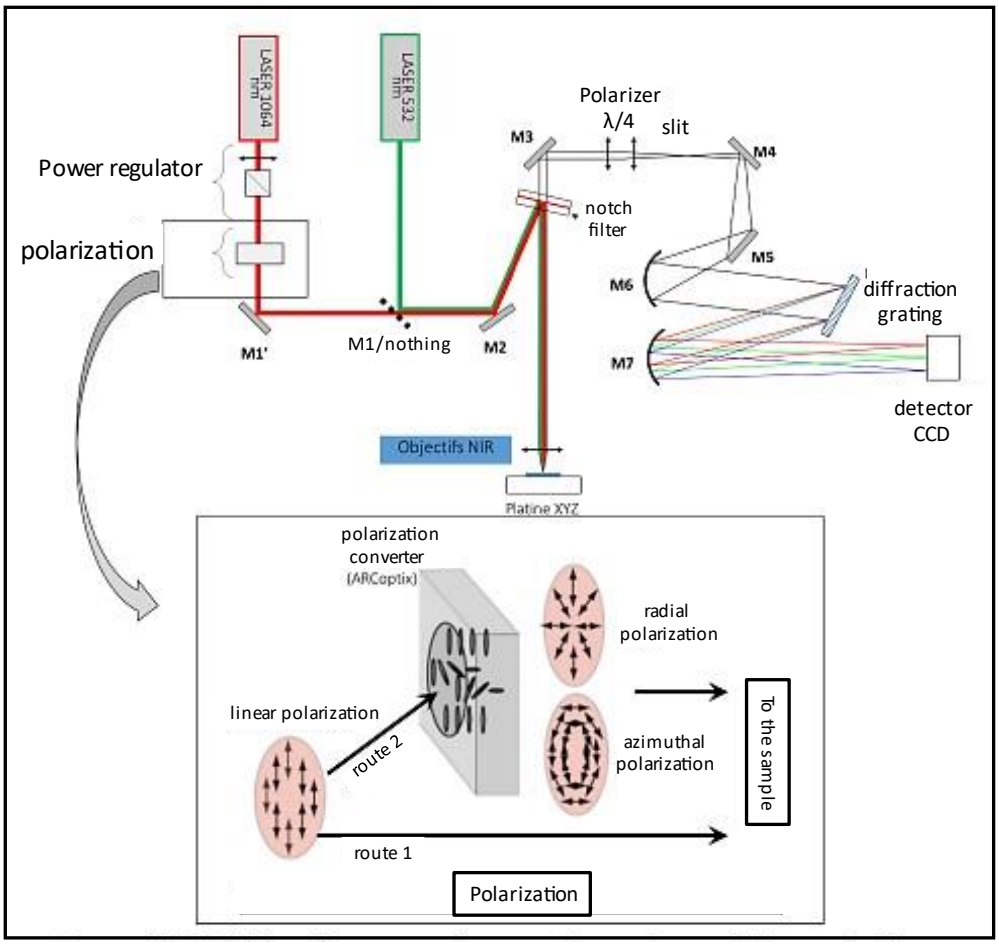

Reference: Translated from KARAM (2020, p.75).

A confocal Raman HR800 micro spectrometer (Horiba/Jobin Yvon) was modified and is equipped with two laser sources: a 532 nm laser for Raman/luminescence and a picosecond laser (EKSPLA PL2200) at 1064 nm for the second harmonic. The laser (at 1064 or 532 nm) is sent to the sample, the backscattered light is sent to a Notch filter that cuts the laser's wavelength, then to a grating that diffracts it onto a CCD sensor (Charge-Coupled Device). In the optical path of the laser at 1064 nm, it is possible to choose different polarizations. In fact, there is a choice between two routes: the first leaves the polarization unchanged (linear, but that allows the polarization state of the light to be adjusted to linear-X or linear-Y) and the second passes through a polarization converter (ARCoptix). The latter consists of liquid crystals that, depending on the voltage applied to them, allow modifying the incident linear polarization into azimuthal or radial polarization. For the Raman/luminescence analysis it is possible to use

polarizers both in the incident light and in the detection of the light reflected in the sample (h - horizontal or v - vertical).

In the measurements, the use of a confocal microscope and an automated XY translation table makes it possible to carry out the mapping, thus obtaining measurements in a predetermined area.

II-7 REFRACTIVE INDEX

The **refractive index (n)** is described by the difference of the light speed in different means, with deviation in the propagation direction and it's according to Snell's law. There are different techniques that can be used to measure the refractive index; in this work it was used Brewster angle and a spectroscopic ellipsometry. The **Brewster angle** (θ_B) is described by Halliday, Resnick and Walker (2016) and the Figure II-5 shows the set-up scheme used in this work for this measurement, in which the mirrors correspond to the dotted lines and are movable, allowing the measurement to be performed by varying the wavelengths without changing the configuration.

Figure II-5 - Set-up scheme for measuring the refractive index using the Brewster angle method.

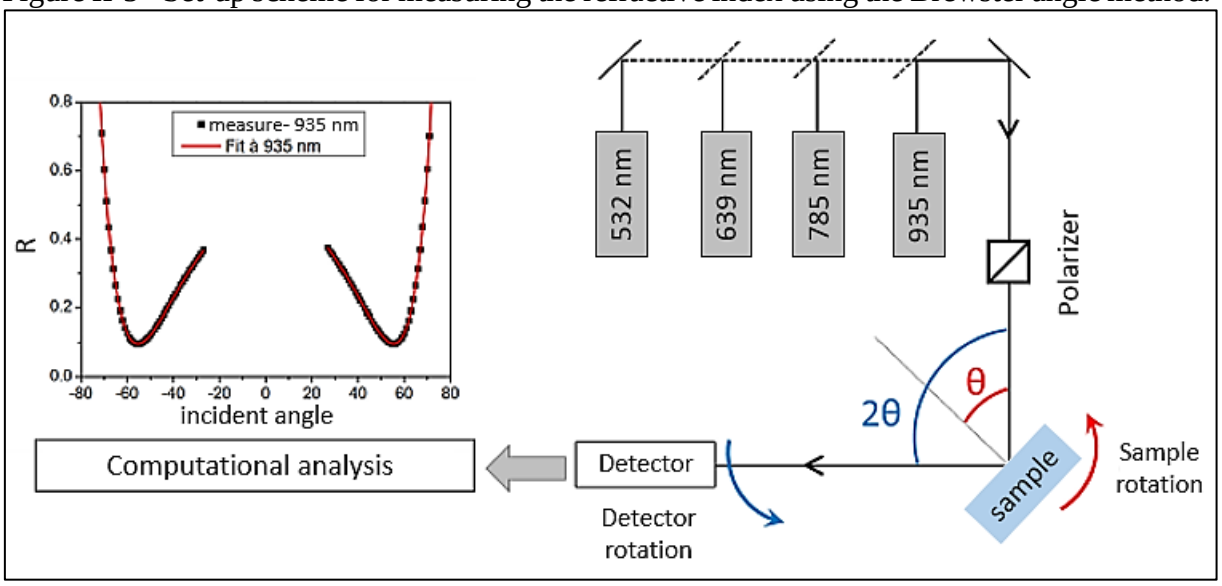

Reference: Modified from KARAM (2020, p.63).

An example of what is obtained in the measurement is also shown, in which the black dots correspond to the measurement taken and the red line the adjustment of the parameters that allow identifying the refractive index according to the wavelength used. The measurement of the Brewster angle consists of illuminating the sample with P-polarized light varying the angle

of incidence (θ) and measuring the reflection in 2θ to observe the extinction of the reflection. The angle of incidence varies from -80° to 80° which allows obtaining the graph shown in Figure II-5. The index is then determined by adjusting the parameters to obtain a precision of ± 0.05 depending on the quality of the adjustment through developed software at ISM.

The **spectroscopic ellipsometry** is a technique that is based on the measurement of the change in polarization state of a light beam caused by the reflection on the material surface or the transmission trough the material. In the equipment, a beam of collimated monochromatic light passes through a polarizer and then the polarized light beam reaches the surface of the sample, suffering a reflection. The polarization state of the reflected beam is then determined, and a comparison is made between the polarization states of the incident and reflected beams. These beam polarization parameters are related to the refractive index, which is obtained through computational modeling of the equations that describe this phenomenon (GONÇALVES; IRENE, 2002).

II-8 PHASE CONTRAST TECHNIQUE

Thermal Micropoling may induce index variation in glasses, so to measure that it can be used a technique based on wave front analysis using a SID4Bio camera developed by the PHASICS company that it makes possible to obtain a quantitative image of the phase variation induced by the Optical Path Difference (OPD) when the light passes through the sample. The camera is placed on a transmission microscope and a white light is sent through the sample. The sensor is based on a CCD camera with a modified Hartmann Mask placed in front. The incident light beam is diffracted by the mask into four replicas to create an interferogram on the CCD as shown in Figure II-6 (KARAM, 2020; KHALIL, 2019).

The light passing through an object with different refractive index change is delayed and creates a difference in the optical path. The final output of the wave front sensor, i.e., the results extracted is an intensity image and a phase image showing the optical path difference (OPD) created by the light after passing by the sample, as shown in Figure II-7. This optical path variation depends on the product of the index variation and the thickness of the zone presenting a different index (KARAM, 2020; KHALIL, 2019).

Figure II-6 - Diagram of the SID4Bio wave front sensor working principle.

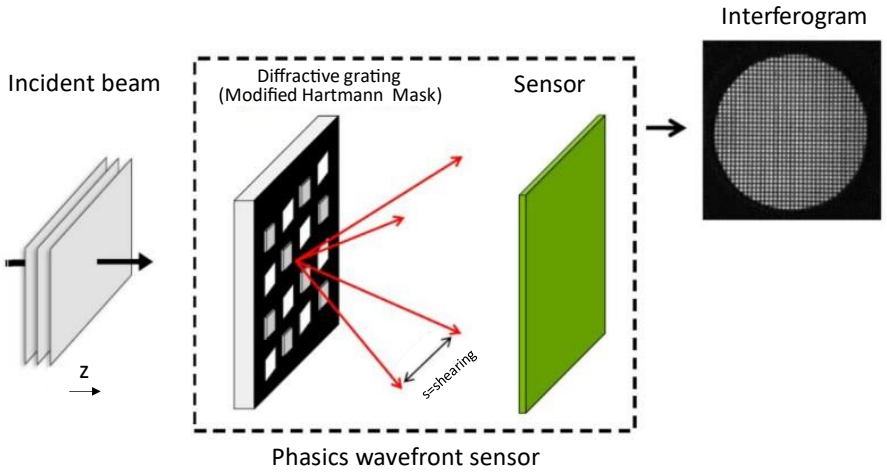

Reference: KHALIL (2019, p.82).

Note: The incident beam is diffracted by the modified Hartmann Mask into four replicas making an interferogram on the sensor (CCD camera).

Figure II-7 - SID4Bio installed on a transmission microscope. The light is diffracted by the grating creating the interferogram on the CCD camera giving an output of an intensity and phase image.

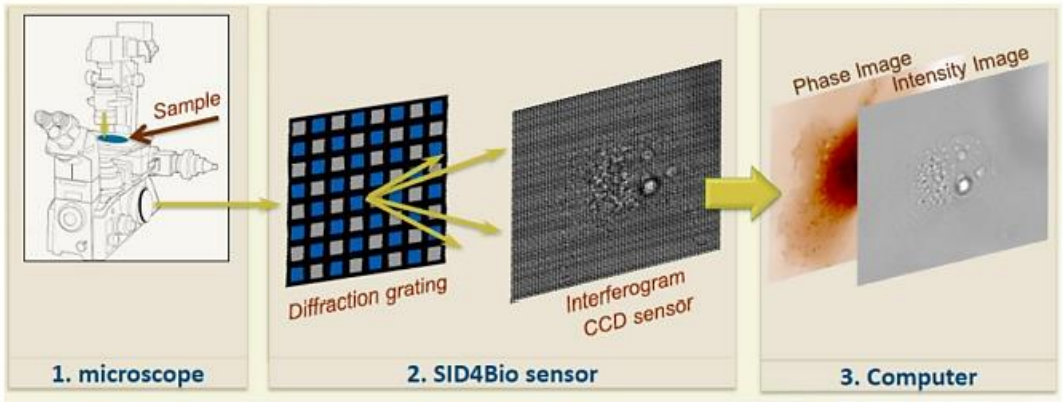

Reference: KHALIL (2019, p.83).

REFERENCES

FEAM, S. **An Introduction to Time-of-Flight Secondary Ion Mass Spectrometry (ToF-SIMS) and its Application to Materials Science**. [S.l.], Morgan & Claypool Publishers, 66p, 2015.

GIBSON, L.T. Archaeometry and antique analysis: metallic and ceramic objects. *In:* WORSFOLD, P.; POOLE, C.; TOWNSHEND, A. **Encyclopedia of Analytical Science**. Elsevier, 2005. p.117-123.

GONÇALVES, D.; IRENE, E. A. Fundamentals and applications of spectroscopic ellipsometry. **Química Nova**, São Paulo, v.25, p.794-800, 2002.

HALLIDAY, D.; RESNICK, R.; WALKER, J. **Fundamentos de Física:** óptica e física moderna = Fundamentals of Physics: optics and modern physics. Translation of BIASI, R.S. 10th. Rio de Janeiro: LTC, 2016.

HAUGSTAD, G. **Atomic Force Microscopy:** understanding basic modes and advanced applications. [S.l.]: John Wiley & Sons, Inc., 2012.

HENRY, D.; GOODGE, J. **Wavelength-Dispersive X-Ray Spectroscopy (WDS)**. Geochemical Instrumentation and Analysis. 2016. Available in: https://serc.carleton.edu/research_education/geochemsheets/wds.html. Access: 22 sept. 2023.

KHALIL, A.A. **Direct laser writing of a new type of optical waveguides and components in silver containing glasses**. 2019. 268p. Thesis (PhD in Physical and Engineering Sciences) - Université de Bordeaux/ Université Laval, 2019.

KARAM, L. **Structuration multi-échelle et multifonctionnelle de nouveaux matériaux vitreux pour la photonique intégrée** = Multiscale and multifunctional structuring of new glassy materials for integrated photonics. 2020. 275p. Thesis (PhD in Chemistry Science) - Université de Bordeaux, Bordeaux, France, 2020.

KARAM, L. *et al.* Electrically micro-polarized amorphous sodo-niobate film competing with crystalline lithium niobate second-order optical response. **Advanced Optical Materials**, Weinheim, v.08, n.13, p.2000202, 2020.

LARKIN, P.J. **Spectroscopy and Materials Characterization**: principals and spectral interpretation. [S.l.]: Elsevier, 2nd, 2018.

LEPICARD, A. **Design of surface chemical reactivity and optical properties in glasses.** 2016. 293p. Thesis (PhD in Chemistry) - Université de Bordeaux, Bordeaux (France), 2016.

MENCZEL, J.; GREBOWICZ, J. **Handbook of Differential Scanning Calorimetry**. 1st. [S.l.]: Butterworth-Heinemann, 874p, 2023.

NANOSCIENCE INSTRUMENTS. **Profilometry**. Available in: https://www.nanoscience.com/techniques/profilometry/. Access: 2023.

NASR, P. **A theoretical study of Maker Fringe measurements in poled multi-layer silica structures focusing on the impact of layer quantity and spacing**. 2012. 80p. Thesis (Master in Applied Science and Electric and Computational Engineering) - Carleton University, Ottawa, Canada, 2015.

PERKAMPUS, H-H. **UV-VIS Spectroscopy and Its Applications**. 1st, Springer Berlin, Heidelberg, 244p, 1992.

RODRIGUEZ, V.; SOURISSEAU, C. General Maker-fringe ellipsometric analyzes in multilayer nonlinear and linear anisotropic optical media. **Journal of the Optical Society of America B**, USA, v.19, p.2650-2664, 2002.

TEETS, T.S. Photoluminescence. **American Chemical Society,** 2021. Available in: https://pubs.acs.org/action/showCitFormats?doi=10.1021/acsinfocus.7e5014&href=/doi/10.1021/acsinfocus.7e5014. Access: 15 oct. 2023.

THOMAS, R. L. **Synthesis and characterization of tellurium oxide glasses for photonic applications.** 2013. 182p. Thesis (PhD in Photonic) - Cochin University of Science and Technology, Kerala (India), 2013.

VOIGTLÄNDER, B. **Atomic Force Microscopy**. Springer Nature Switzerland AG, 2nd, 331p, 2019.

WARREN, B.E. X-ray Diffraction Study of the Structure of Glass. **Chemical Review**, Washington, v.26, p.237-255, 2011.

WASEDA, Y.; MATSUBARA, E.; SHINODA, K. **X-ray diffraction crystallography:** introduction, examples and solved problems. 1st. Springer Berlin, Heidelberg, 310p, 2011.

ZHENG, Q. *et al.* Understanding Glass through Differential Scanning Calorimetry. **Chemical Reviews**, Washington, v.119, p.7848-7939, 2019.

CHAPTER III - PREPARATION AND CHARACTERIZATION OF PHOSPHATE GLASSES WITH TANTALUM OXIDE CONTENTS

CHAPTER III - PREPARATION AND CHARACTERIZATION OF PHOSPHATE GLASSES WITH TANTALUM OXIDE CONTENTS

This chapter focuses on the preparation and characterization of glasses in the $NaPO_3$-Ta_2O_5 system both undoped and doped with Eu^{3+}, with tantalum oxide contents from 40 to 50 mol%. The glass samples were synthesized using the melt/quenching method; and characterized by: DSC, XRD, Raman Spectroscopy, Infrared Spectroscopy, UV-Vis Spectroscopy, Refractive Index measurements and Photoluminescence.

III-1 GLASSES PREPARATION

Glasses in the **$NaPO_3$-Ta_2O_5** system were prepared with tantalum oxide contents of 40, 45, 47.5 and 50 mol%. Furthermore, the same glass compositions were doped with europium oxide - **$99.83[(100-x)\ NaPO_3$-$xTa_2O_5]$-$0.17Eu_2O_3$** (x = 40, 45, 47.5, 50). The following reagents were used: Ta_2O_5 (Alfa Aesar, 99.993%), $NaH_2PO_4.2H_2O$ (Prolabo, 99%), and in the case of doped glasses, Eu_2O_3 (Acros Organics, 99.99%). At high temperatures, monosodium phosphate decomposes, according to equation III-1. All glasses were prepared at the *Institut de Chimie de la Matiére Condensée de Bordeaux* (ICMCB), in Bordeaux/France.

$$NaH_2PO_{4(s)} \xrightarrow{\Delta} NaPO_{3(s)} + H_2O_{(g)} \qquad \text{(III-1)}^{30}$$

Table III-1 shows the nominal molar composition of each glass, the nomenclature used throughout the text, the theoretical percentage of each element in the respective glass, and the theoretical Ta/P ratio.

The glasses were prepared using the traditional method of melt/quenching, in which the precursors were weighed (25 g), grinded and homogenized in a porcelain mortar. Then, the starting powders was transferred to a platinum crucible and subsequently put in a furnace at room temperature and heated at a rate of 10°C.min^{-1} to 1000°C for 1 to 2 hours. After this step, the material was removed from the furnace and homogenized again in the mortar, replaced in the crucible and then taken to the furnace (Carbolite-Gero BLF - bottom loading furnace) for melting at temperatures varying from 1600 to 1615°C, depending on the sample, for ~25 minutes. The quenching was carried out directly in the crucible, immersed in water, and taken for annealing while still hot to avoid material breakage (UHLIG U5 furnace). The annealing

[30] The decomposition kinetics of monosodium phosphate is described in Vlase, Vlase and Doca (2005).

temperature varied from 800 to 860°C for 7 hours, and subsequent cooling at 4°C.min^{-1} to room temperature, then being removed from the crucible - as shown in Figure III-1A.

Table III-1 - Nominal molar composition of glasses and theoretical elementary composition.

Glass sample composition	Nomenclature	Na (%)	P (%)	Ta (%)	O (%)	Eu (%)	Ta/P
$60NaPO_3$-$40Ta_2O_5$	Na40Ta	10.34	10.34	13.79	65.51	-	1.33
$55NaPO_3$-$45Ta_2O_5$	Na45Ta	9.32	9.32	15.25	66.10	-	1.63
$52.5NaPO_3$-$47.5Ta_2O_5$	Na47.5Ta	8.82	8.82	15.97	66.39	-	1.81
$50NaPO_3$-$50Ta_2O_5$	Na50Ta	8.33	8.33	16.67	66.67	-	2.00
$99.83[60NaPO_3$-$40Ta_2O_5]$-$0.17Eu_2O_3$	Na40Ta:Eu	10.327	10.327	13.770	65.494	0.059	1.33
$99.83[55NaPO_3$-$45Ta_2O_5]$-$0.17Eu_2O_3$	Na45Ta:Eu	9.309	9.309	15.232	66.090	0.058	1.63
$99.83[52.5NaPO_3$-$47.5Ta_2O_5]$-$0.17Eu_2O_3$	Na47.5Ta:Eu	8.81	8.811	15.944	66.377	0.057	1.81
$99.83[50NaPO_3$-$50Ta_2O_5]$-$0.17Eu_2O_3$	Na50Ta:Eu	8.322	8.322	16.643	66.657	0.057	2.00

Reference: AUTHOR.

Figure III-1 - Tantalum phosphate glasses images: (A) Na40Ta after being removed from crucible; (B) Na47.5Ta:Eu polished; and (C) Na50Ta:Eu polished.

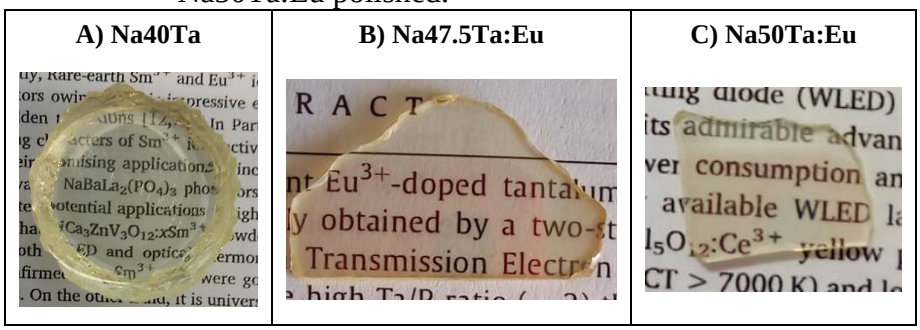

Reference: AUTHOR.

After preparing the glasses, they were cut and polished until they reached a thickness of 1 mm and the desired optical quality. For polishing, 15 and 9 µm alumina were used, respectively; and then 2.5 µm cerium oxide. Figure III-1B shows the Na47.5Ta:Eu glass after going through the cutting and polishing steps. There were difficulties in the preparation of the Na50Ta:Eu glass, since 50 mol% of tantalum oxide is at the limit of the glass forming domain, and consequently the addition of europium oxide, even in small amounts, makes it difficult to prepare large samples. After some attempts, it was only possible to obtain a small piece of glass in this composition using 20 g, presented in Figure III-1C after polishing.

III-2 X-RAY DIFFRACTION AND THERMAL ANALYSIS OF GLASSES

X-ray Diffraction (XRD) patterns of the powdered samples were recorded with a PANanalitycal X'pert PRO MPD diffractometer located at ICMCB, in Bragg-Brentano θ-θ geometry using a CuKα radiation (λ = 0.15418nm), in the 2θ range of 8-80º. Figure III-2 presents the results for the prepared tantalum phosphate glasses, and as expected, they only present the characteristic halo of non-crystalline materials, including the Na50Ta:Eu sample.

Figure III-2 - XRD of tantalum phosphate glasses.

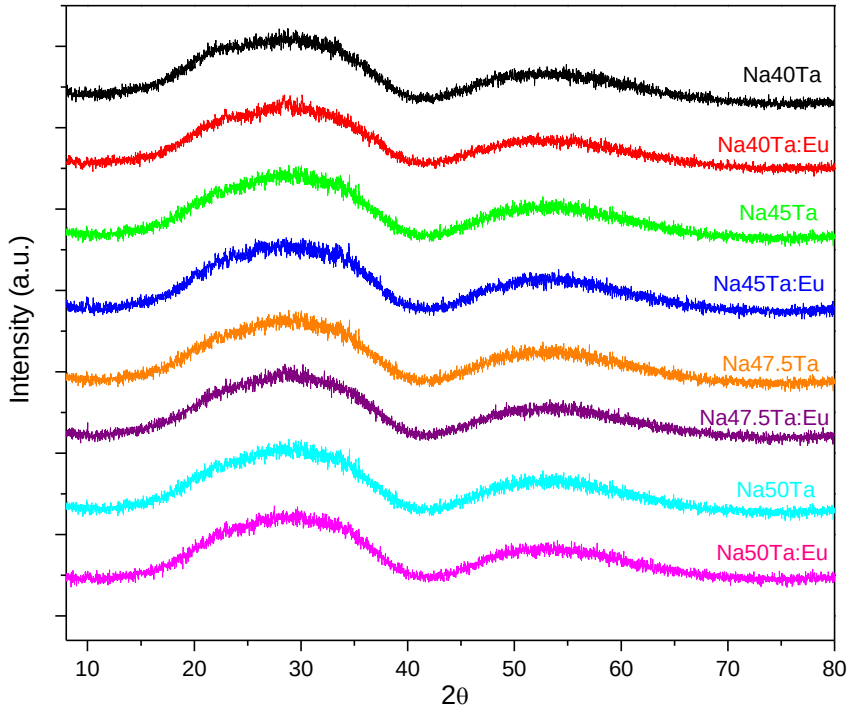

Reference: AUTHOR.

For **Thermal Analysis** the DSC technique was employed, and the curves were determined in a Netzsch DTA 404 PC equipment with a DSC sensor - located at ICMCB. The measurement was performed in bulk samples, using a platinum crucible, room atmosphere, in two heating stages: from 40 to 600°C with a heating rate of 20°C.min^{-1}; and from 600 to 1200°C with a heating rate of 10°C.min^{-1}. The DSC curves are shown in Figure III-3A, with the Tg range enlightened in B and C, for the undoped and doped samples, respectively.

Figure III-3 - DSC curves of tantalum phosphate glasses (A), Tg range of undoped glasses (B) and doped glasses (C).

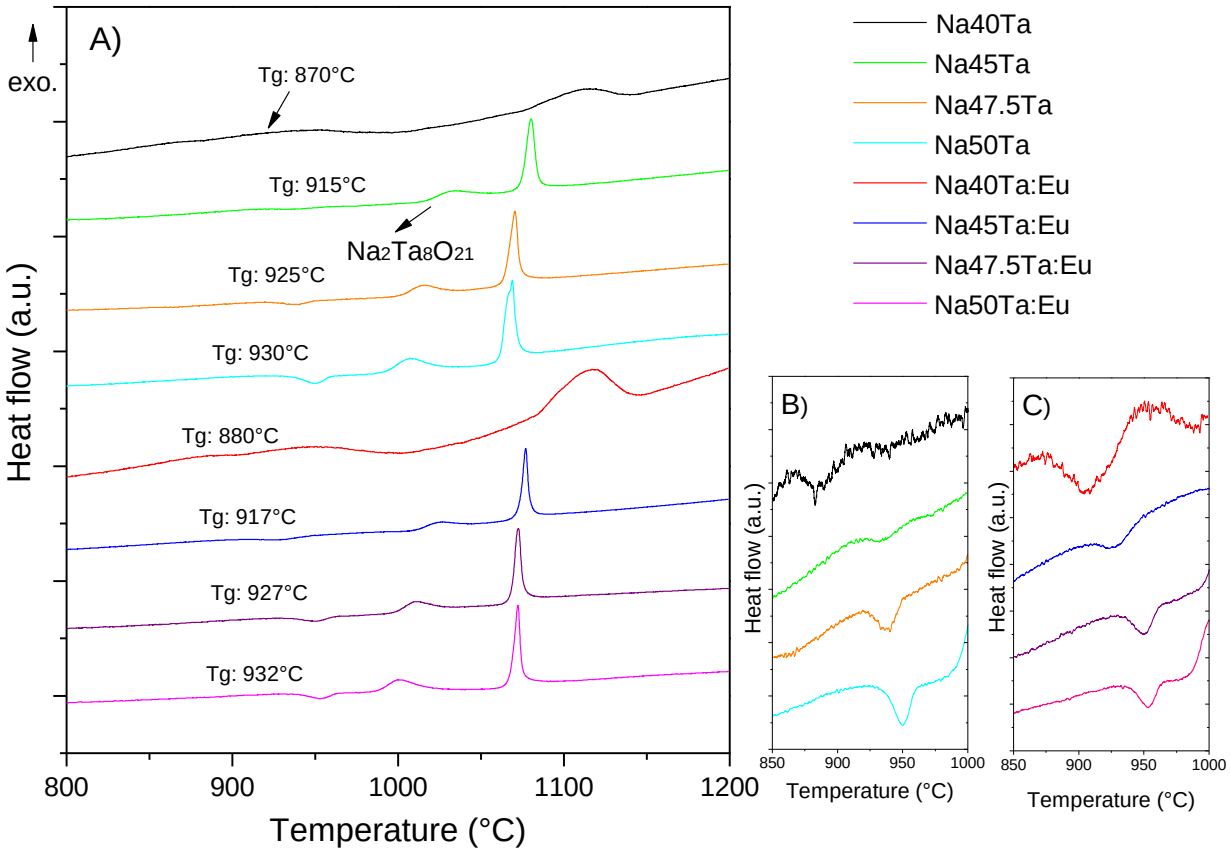

Reference: AUTHOR.

Table III-2 presents the characteristic temperature values of each glass composition obtained from the DSC curves. From the data, it appears that there is an increase in the Tg value with the increment of tantalum in the glass matrix. This increase was already expected, as observed by Marcondes *et al.* (2019), since it is related to the higher connectivity of the vitreous network, with tantalum assuming a higher coordination number (clusters [TaO_6]) acting as an intermediary. These values are also in accordance with those obtained by Maestri (2018) in which the glass containing 50 mol% of tantalum oxide presented a Tg of 925°C and in accordance with the characteristic increase of the addition of transition metal oxides in phosphate glasses. Regarding the addition of europium oxide, considering the error, no clear difference is observed for the glasses doped comparing to their respective undoped glasses.

Table III-2 - Characteristics temperatures of tantalum phosphate glasses.

Glass sample	Tg (°C)	Tx_1 (°C)	Tx_1-Tg (°C)	Tc_1 (°C)	Tx_2 (°C)	Tc_2 (°C)
Na40Ta	870	1070	200	1112	-	-
Na45Ta	915	1015	100	1033	1070	1080
Na47.5Ta	925	998	73	1015	1061	1070
Na50Ta	930	991	61	1007	1057	1068
Na40Ta:Eu	880	1080	200	1117	-	-
Na45Ta:Eu	917	1009	92	1025	1068	1076
Na47.5Ta:Eu	927	994	67	1010	1062	1072
Na50Ta:Eu	932	986	54	1000	1064	1072

Reference: AUTHOR.

These Tg values are much higher than those of tungsten phosphate glasses ($40KPO_3$-$60WO_3$) studied by Lima (2014) of 561°C. These characteristic temperatures are also higher than for the corresponding niobium phosphate glasses: the $50KPO_3$-$50Nb_2O_5$ molar composition glass prepared by Lima (2014) presented a Tg value of 739°C, the $50NaPO_3$-$50Nb_2O_5$ glass a Tg value of 703°C (CASSANI, 2022) and the niobium borophosphate glasses studied by Karam (2020) showed Tg values between 641 to 681°C. Therefore, the addition of tantalum to the phosphate glass allowed the network to become even more connected than with the addition of other transition metals, such as niobium, due to the higher molar mass; however, the thermal behavior of both type of glasses can be considered similar.

Still, when comparing the values of (T_{x1}-T_g) related with the thermal stability against crystallization, this value decreases with the increase of tantalum oxide. At the same time that T_g increases, the T_{x1} decreases with the addition of tantalum. This decrease in thermal stability is also related to the presence of [TaO_6] clusters that are progressively formed and act as "crystallization nuclei", thermal behavior also described in niobium phosphate glasses. Despite the decrease, for some glasses this value is higher than the aforementioned tungsten phosphate glasses (142°C) studied by Lima (2014). This stability parameter is important for the preparation of large pieces or lower cooling processing as well as optical fiber drawing.

Regarding the crystallization peaks, a second low temperature event "appears" for Ta_2O_5 contents of 45 mol% or higher, which, as shown in Figure III-3, corresponds to the crystalline phase $Na_2Ta_8O_{21}$, according to previous studies by the research group. This crystalline phase is not present in the sample containing 40 mol% of Ta_2O_5, indicating that it only exists when the phosphate glasses contain high tantalum contents, in agreement with the

progressive formation of TaO_6 clusters acting as crystallization nuclei of this sodium tantalate phase. This same behavior is observed in niobium phosphate glasses, in which the similar phase $Na_2Nb_8O_{21}$ only appears with high Nb_2O_5 contents (MALAKHO *et al.*, 2005). The group's previous studies pointed to the appearance of this crystalline phase in the composition with 50 mol% of Ta_2O_5.

III-3 STRUCTURAL ANALYSIS OF TANTALUM PHOSPHATE GLASSES

For structural analysis of glasses, Raman and IR spectroscopies were performed. Since the polarizability of tantalum is greater than that of phosphorus, Raman spectra can provide better information about the tantalate network while IR spectroscopy about phosphate bonds, hence the importance of combining two techniques.

Raman measurements were performed using an XploRA PLUS micro-Raman spectrometer (Horiba), located at the ISM, calibrated with a Si standard. The analysis was performed on samples polished on one side only, in the range of 150 to 1200 cm^{-1}, acquisition time of 15s, objective of 50x, with laser of 532 nm. The spectra of the undoped samples are shown in Figure III-4, which present the broad bands characteristic of glasses and it is noted that higher the tantalum content (Na50Ta), stronger the Raman response (higher intensity), since tantalum is the heaviest element in these glasses and features an extended electron cloud that is highly polarizable, contributing to this increase in the Raman signal, especially in tantalum unities. For example, at ~640 cm^{-1}, the Na50Ta response is reduced by a quarter (25%) when considering the Na40Ta sample.

Figure III-4 - Raman spectra of undoped tantalum phosphate glasses.

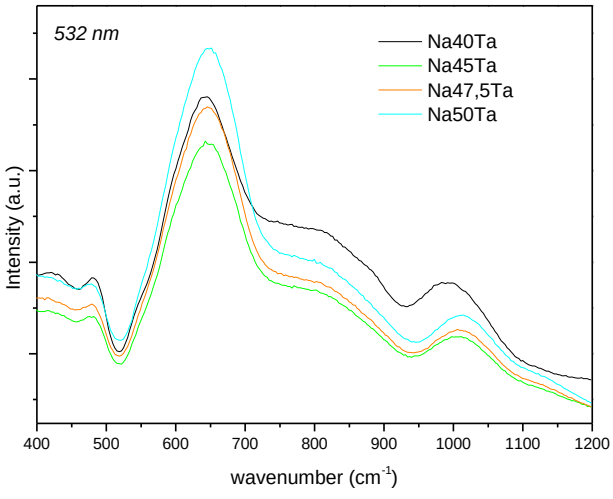

Reference: AUTHOR.

Raman spectra of glasses undoped and doped normalized are present in Figure III-5, which it is observed that there are differences in the responses of the material doped comparing to the undoped using this wavelength. In the samples with europium (FIGURE III-5B), the bands do not appear with the same profile as the undoped samples, although they follow the same tendency in relation to the relative intensity of bands with the increase of tantalum. This difference is probably related to the incidence wavelength corresponds to an Eu^{3+} absorption ($^5D_1 \leftarrow ^7F_{0.1}$), and therefore, the measured signal does not present only Raman signal, but also luminescence. Furthermore, band 1 in samples without europium is centered around 640 cm^{-1}, while in samples with europium there is a displacement of approximately 40cm^{-1}, indicating a distortion due to the presence of this ion.

Figure III-5 - Raman spectra using a 532 nm laser: (A) undoped glasses normalized at 640 cm^{-1} and (B) Eu^{3+}-doped glasses normalized at 680 cm^{-1}.

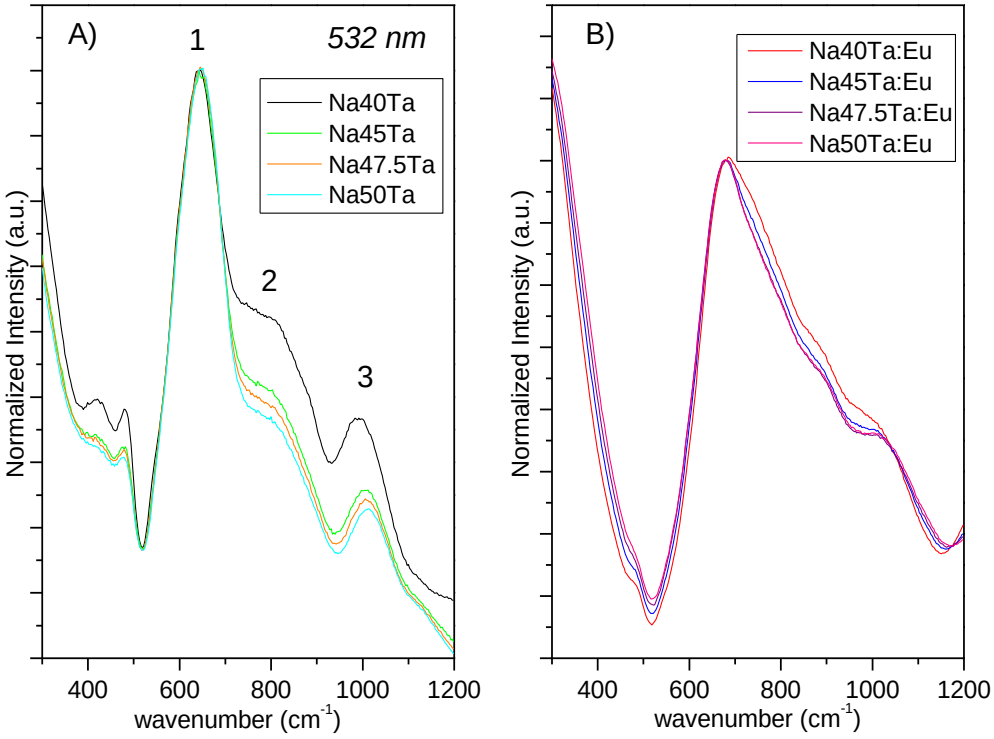

Reference: AUTHOR.

According to Sousa *et al.* (2020) and Marcondes *et al.* (2019), **band 1**, located between 525 and 740 cm^{-1} corresponds to Ta-O-Ta units linking [TaO_6] octahedrons in a three-dimensional tantalate network. At 630 cm^{-1}, the lattice is perfectly regular - all octahedrons connected at their vertices - as in a perovskite crystalline phase like $KTaO_3$ (HU; TENG, 2007; ONISHI, 2019). The more this band moves towards higher energies, the more the lattice is distorted. Between 740 and 850 cm^{-1} - **band 2**, corresponds to the so-called “isolated” bonds in

the Ta-O-Ta octahedron, that is, bonded only to the phosphorus tetrahedra. Also, according to Muñoz *et al.* (2019), P-O-P symmetric stretching occurs between 690-790 cm^{-1}. **Band 3** - between 940 and 1100 cm^{-1}, according to Rajaofara *et al.* (2021) are the more covalent Ta-O bond stretching modes, since oxygen is involved in an ionic bond with Na^{+}. According to Marcondes *et al.* (2019), Sousa *et al.* (2020) and Hirao, Todoroki and Soga (1994) this band can be attributed to the P-O terminal bonds of phosphate units. Regardless of which of the two bonds, it is a terminal bond with sodium in which it breaks the continuity of the vitreous network; and in the samples with less tantalum, the amount of sodium was higher (according to Table III-1).

Comparing the glasses, with the increase in the concentration of tantalum, bands 2 and 3 decrease in relation to band 1. With regard to band 3, since it is related to terminal bonds, the decrease with increasing tantalum may indicate higher connectivity of the vitreous network, which would be in agreement with the increase in Tg observed by the DSC analysis.

For structural analysis by infrared spectroscopy, measurements were performed by reflectance in primary vacuum (minimizes H_2O and CO_2) in a Fourier Vertex 70 V spectrometer also located at the ISM, equipped with a Globar type source, a detector of deuterated triglycine sulfate (DTGS) and a mid/far infrared beam splitter. A mirror is used as a reference and the spectra were obtained from 150 to 2000 cm^{-1} with a resolution of 4 cm^{-1}. From these data, absorbance spectra were obtained by Kramers-Krönig transformation[31], in which the absorption coefficient (α) is obtained after extracting the optical constants *n* and *k*, that correspond to the real and imaginary parts of the refraction index, respectively[32]. For this, a program developed in the ISM was used, which allows, from the reflectance in a correctly chosen range, to directly calculate the optical constants *n* and *k*, and from these data, the value of the absorption coefficient was calculated ($\alpha = 4\pi\tilde{\nu}k$) (KARAM, 2020). Figure III-6 shows the absorption spectra obtained after normalization in band 1.

Since infrared data are hardly found in tantalum phosphate glasses, mode attributions were based on niobium phosphate glasses which have already shown to give similar structural behaviors. The band around 640 cm^{-1} (1) in which the curves were normalized corresponds to that observed in the Raman spectra and related to the Ta-O-Ta units linking the [TaO_6] octahedra in a three-dimensional tantalate network. The band located from 990 to 1120 cm^{-1} (2)

[31] The mathematical description of the Kramers-Krönig transformation can be consulted in Kamitsos *et al.* (1990).
[32] The main difference between the transmission and the reflection technique is that the transmission spectra only probe the imaginary part while the reflection spectra probe the imaginary and real part of the refraction index (LEPICARD, 2016).

decrease with the increase of tantalum in the glass, as well as the “shoulder” from 1120 to 1200 cm^{-1} (3), and also there is a shift to higher energies for higher tantalum contents. According to the measurements carried out in the same analysis of the niobium borophosphate glasses studied by Karam (2020), these bands are associated with the bonds of the phosphate entities; and they are more evident in the infrared than in the Raman analysis precisely due to the polarizability of tantalum. The first one is attribute to asymmetric stretching modes of isolated orthophosphate units, i.e., isolated from other phosphors chains or units, but bonding to tantalum as P-O-Ta. The last one is attribute to asymmetric stretching modes of P-O-P bridges and terminal P-O bonds in pyrophosphate entities. So, it can be seen that the addition of tantalum causes these bands to be reduced, since the amount of phosphate in the glass decreases.

Figure III-6 - Normalized infrared absorption spectra obtained through Kramers-Krönig analysis of the measured reflectance data of tantalum phosphate glasses.

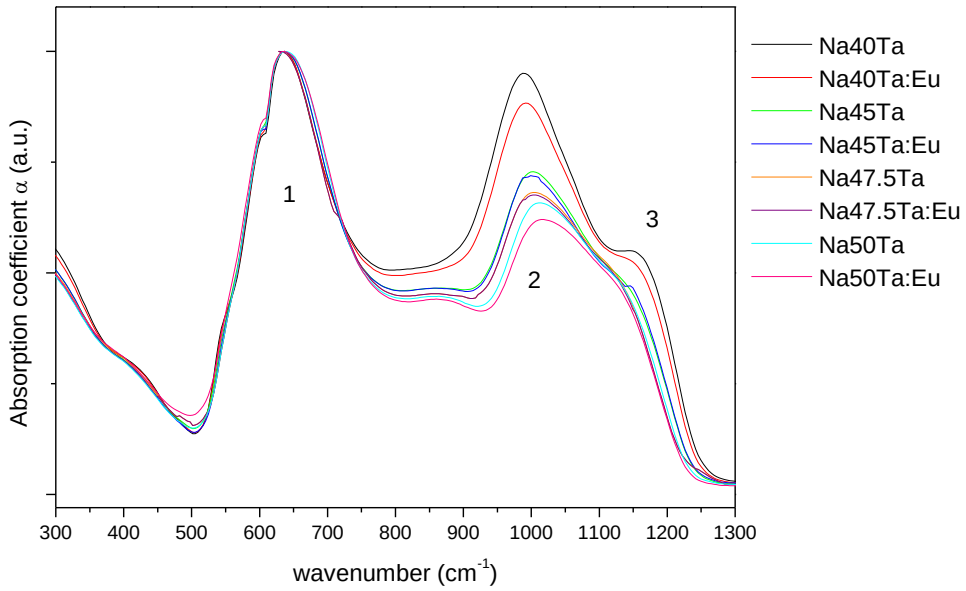

Reference: AUTHOR.

Therefore, Figure III-7 presents a diagram summarizing the structural evolution observed in phosphate glasses with the addition of tantalum oxide (that is from a pure phosphate glass until a “saturated” phosphate glass with tantalum); which follows the same tendency also observed by Sousa *et al.* (2020) and Marcondes *et al.* (2019) and niobium phosphates (CASSANI, 2022; KARAM, 2020; LEPICARD, 2016; LIMA, 2014; MALAKHO *et al.*, 2005; PASTENA, 2016).

Initially, pure phosphates do not have tantalum in their composition and are formed by phosphate chains with P-O-P bonds (such as bands 2 and 3 in IR relating to phosphate bonds).

With the addition of Ta_2O_5, tantalum begins to insert itself into the phosphate chains, and Ta-O-P-type bonds (Raman band 2 and IR band 2) are progressively observed. When the amount of tantalum becomes higher, there is a "saturation" in the main phosphate chains, and then these cations form regions rich in tantalum because they can no longer be inserted in the main chain, occurring the formation of $[TaO_6]$ clusters (Raman band 1/ IR band 1). Thus, the tantalum rich glass possesses both the TaO_6 clusters and tantalum inserted inside in the main phosphate chains. These tantalum rich regions are related to the appearance of the second low temperature crystallization peak observed in the DSC (above 40 mol% of Ta_2O_5), unlike the other phase which is a tantalum-phosphate phase.

Figure III-7 - Representative scheme of the structural evolution of phosphate glasses with the addition of tantalum oxide.

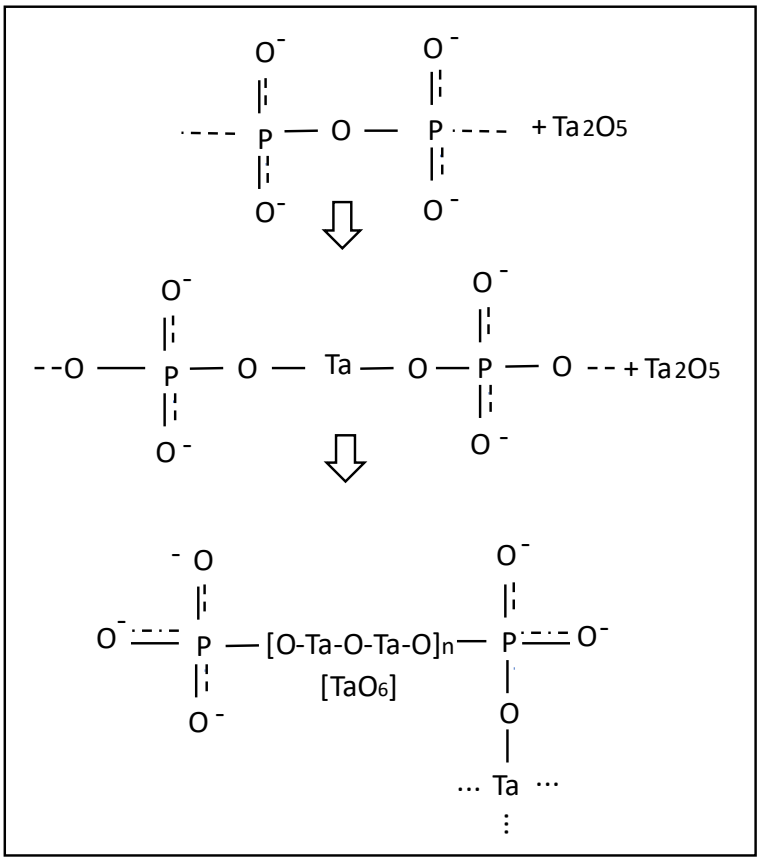

Reference: AUTHOR.

According to Malakho *et al.* (2005), in niobium phosphate glasses, the octahedrons $[NbO_6]$ arrangement in the glass structure is necessary to induce high second-order optical nonlinearity after Thermal Poling. In this way, glasses containing high concentrations of

tantalum in which the formation of agglomerates [TaO_6] occur, allowing the precipitation of the tantalate phase, could present a similar behavior.

III-4 OPTICAL ANALYSIS OF GLASSES: TRANSPARENCY, REFRACTIVE INDEX AND LUMINESCENCE

The investigated optical properties in these glasses were: transparency in the ultraviolet-visible region, refractive index, and, in the case of doped glasses, luminescence.

To verify the transparency of the glasses, the %T (transmittance) was measured in the UV-Vis region of the electromagnetic spectrum using the Agilent Cary 5000 double beam spectrometer, located at the ICMCB, varying the wavelength between 200 and 2000 nm, step of 1 nm, with the spectra of undoped and doped glasses shown in Figure III-8 and Figure III-10, respectively. According to results, the transparency limit in the UV-Vis region decreases slightly with tantalum addition, ranging from 298 nm in the sample with 40 mol% of Ta_2O_5 to 306 nm in the sample with 50 mol% of Ta_2O_5, without much difference between the samples with 47.5 and 50 mol% of Ta_2O_5.

Figure III-8 - Transmission spectra of undoped tantalum phosphate glasses.

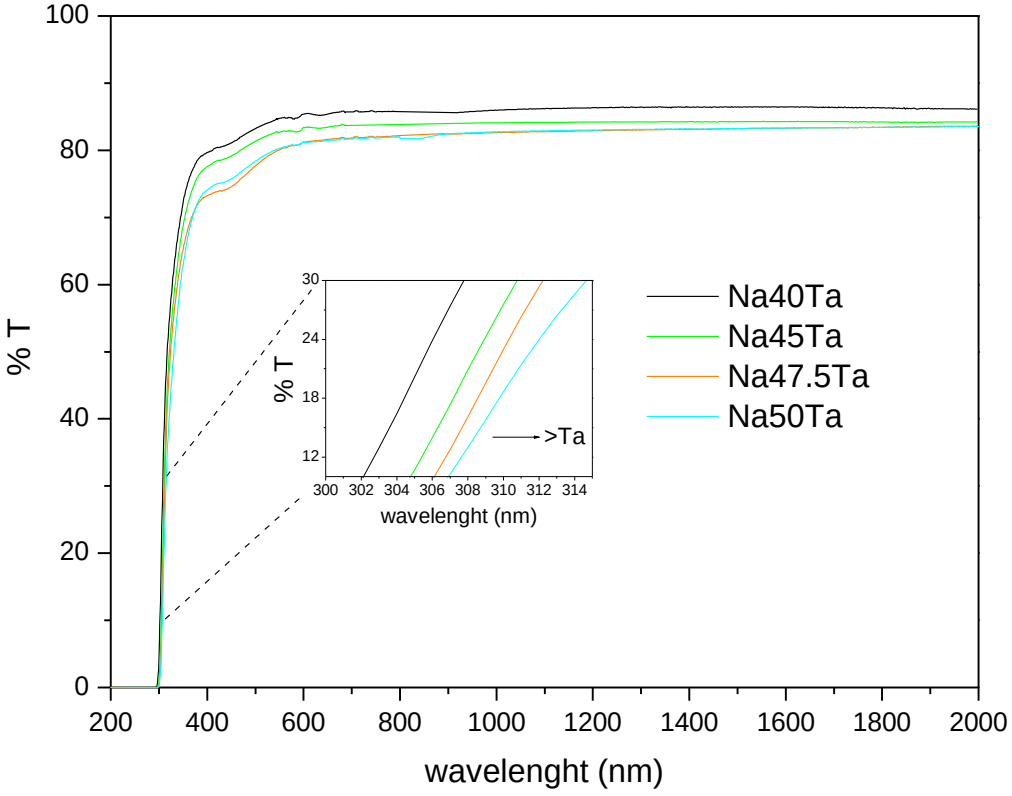

Reference: AUTHOR.

To verify this modification, the band-gap energies were obtained considering the indirect band-gap, in which the graph of $(\alpha h\upsilon)^2$ *versus* energy (eV) was plotted as shown in Figure III-9. As observed, despite not being such pronounced, there are a decrease of band-gap from 4.15 to 4.06 eV with increment of tantalum. This is due to the insertion of octahedrons [TaO_6] in the phosphate network, since tantalum is a heavier atom, reducing the band gap. The %T of the material also shows a small reduction with the addition of tantalum oxide, going from 85% in the Na40Ta sample to 81% in the Na50Ta sample. This behavior was already observed in tantalum phosphate glasses (MARCONDES *et al.*, 2019; SOUSA *et al.*, 2020), niobium phosphate glasses (KARAM, 2020; LIMA, 2014; PASTENA, 2016) as well as in tantalum germanate glasses (CUNHA *et al.*, 2021; POIRIER *et al.*, 2019) and can be related with higher refractive indices resulting in stronger reflection.

Figure III-9 - Band-gap (indirect) obtained for undoped tantalum phosphate glasses.

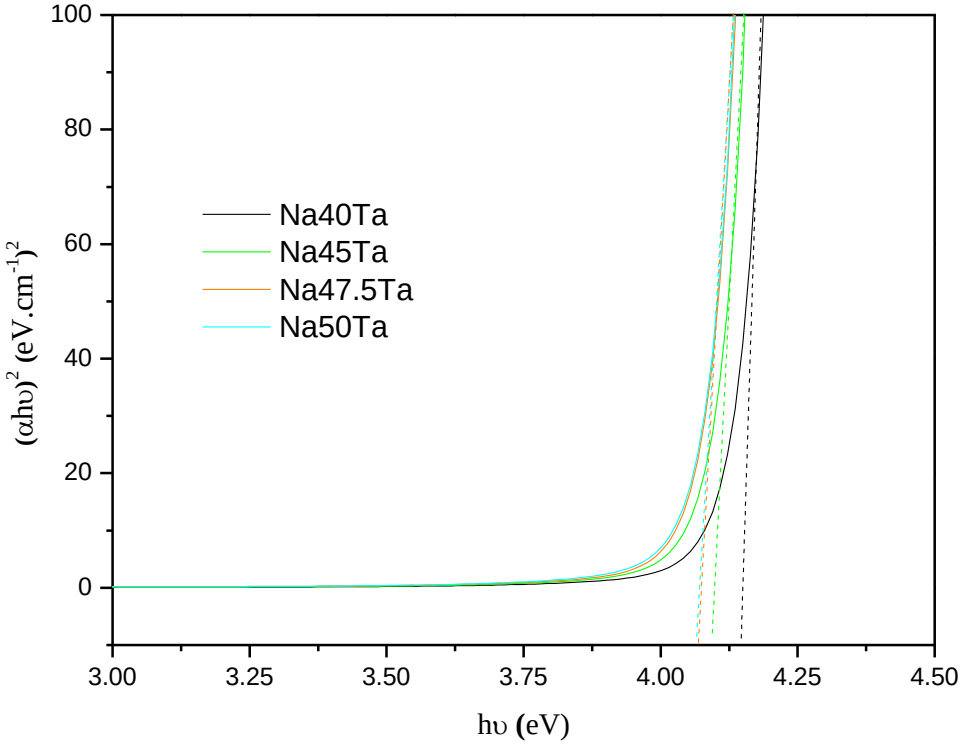

Reference: AUTHOR.

Through the spectra of the doped samples, it is possible to observe the bands related to the Eu^{3+} ion absorptions due to the $^5L_6 \leftarrow ^7F_0$ (395 nm) and $^5D_2 \leftarrow ^7F_0$ (465 nm) transitions. Furthermore, the same behavior regarding the addition of tantalum is observed in these samples. However, there is a greater reduction of transparency in the Na50Ta:Eu sample; which, as previously mentioned, was visually observed during sample preparation. It could probably be due to a slight crystallization, with crystals so small that they could not be detected under the

conditions measured in XRD, but that influenced the transparency of the material due to scattering; but still being transparent in a range within the visible-infrared range.

Figure III-10 - Transmission spectra of Eu^{3+}-doped tantalum phosphate glasses.

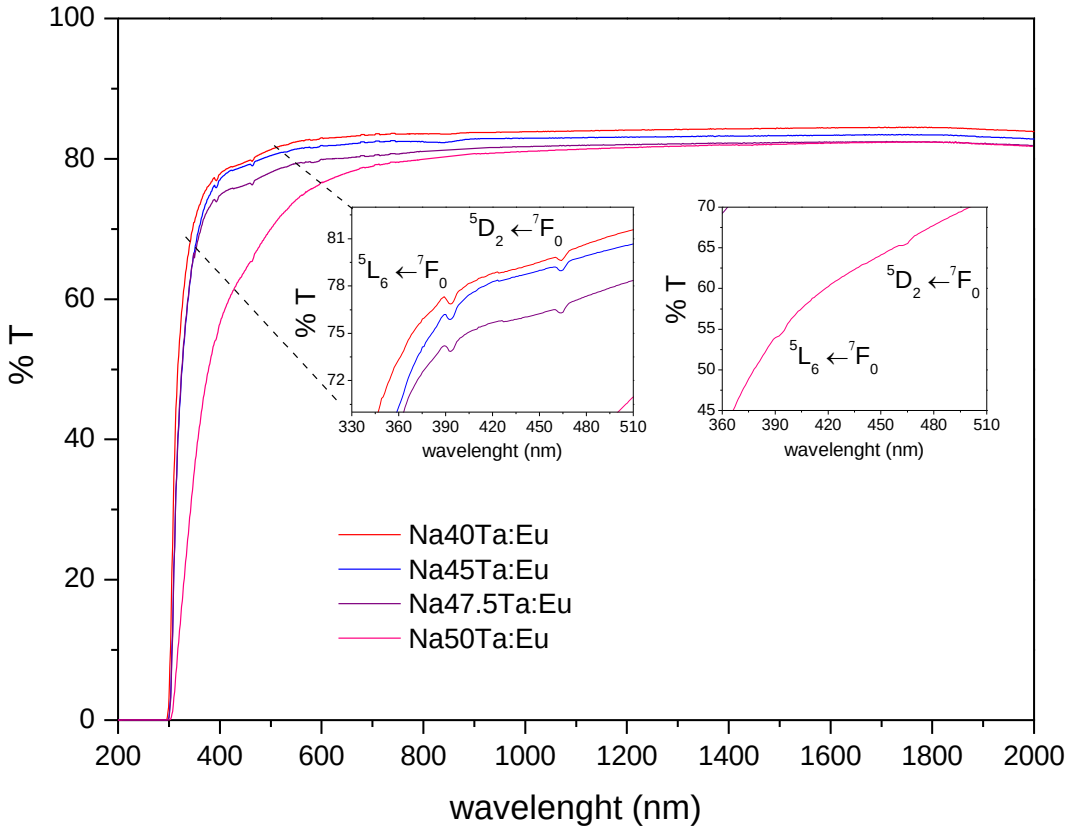

Reference: AUTHOR.

Refractive indices were measured at the ISM using the Brewster angle method described in Chapter II-7, varying the measurement angle from -80 to 80°, with a 2° step. Measurements were collected on the sample polished on one side only using lasers with wavelengths of 532, 639, 785 and 935 nm. The data obtained after using the program developed in the ISM are presented in the graph of Figure III-11, in which the refractive index decreases for higher wavelengths as they are inversely proportional to the speed of light propagation in the medium; and consequently, inversely proportional to the wavelength.

It is observed that with the increase of tantalum oxide, there is an increase in the refractive index, related with a higher overall polarizability. Comparing the doped and undoped glasses, there is no significant difference in the values, which are within the measurement error; this variation only occurs in the 50Ta:Eu sample, in which the refractive index is lower than that of undoped glass. Through the %T measurements, it was observed that this sample

presented optical properties relatively different from the others, which can also be observed in the refractive index measurement.

Figure III-11 - Refractive indices of tantalum phosphate glasses obtained from Brewster angle.

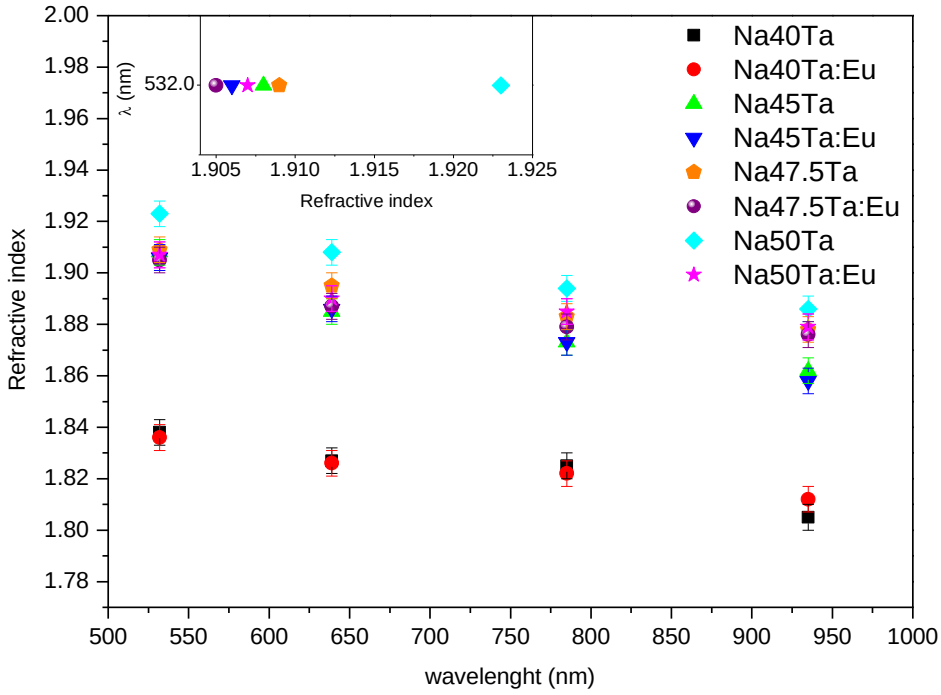

Reference: AUTHOR.

In order to obtain refractive index values at other wavelengths, Cauchy's equation was used ($n(\lambda) = A + B/\lambda^2$) (MISTRIK *et al.*, 2017), which is an empirical dispersion law equation and it is valid when the material does not have optical absorption in the visible, like these glasses. The plotted adjustments are present in Figure III-12.

In general, the data were well adjusted to the model according to the error of the measurements. The index values for the 1550 nm and 1064 nm wavelengths are shown in Table III-3, which correspond to the wavelength of the lasers used in the measurements of the Maker Fringes experiment and micro-SHG for the glasses after Thermal Poling (presents in Chapter IV), respectively.

Table III-3 - Refractive indices of glasses obtained from Cauchy's equation.

λ (nm)	Na40Ta	Na40Ta:Eu	Na45Ta	Na45Ta:Eu	Na47.5Ta	Na47.5Ta:Eu	Na50Ta	Na50Ta:Eu
1064	1.808	1.812	1.857	1.855	1.873	1.871	1.882	1.875
1550	1.802	1.807	1.848	1.846	1.865	1.870	1.875	1.870

Reference: AUTHOR.

Figure III-12 - Adjustment curves of the refractive index as a function of the wavelength obtained by Cauchy's equation.

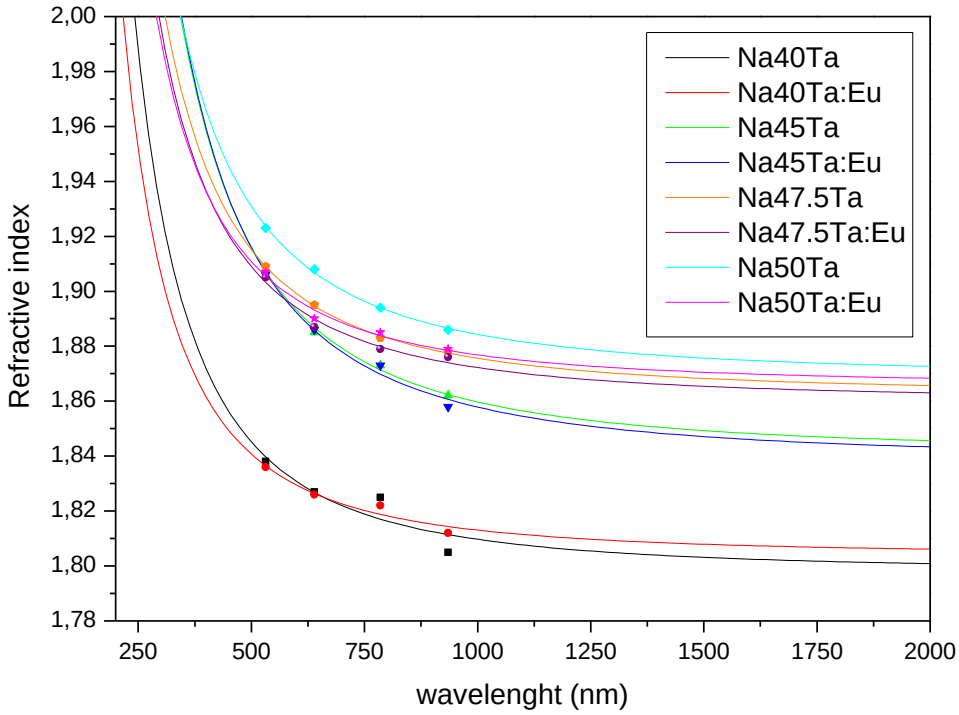

Reference: AUTHOR.

Photoluminescence measurements were performed on doped glasses containing 40 and 47.5 mol% of tantalum oxide (Na40Ta:Eu and Na47.5Ta:Eu), at the ICMCB, with powdered samples, using a Fluorolog spectrometer, front-face mode. Excitation spectra were obtained for emission at 612 nm (with 370 nm filter); whereas emission spectra were collected for excitation at 395 and 465 nm. For the Na40Ta:Eu sample, an integration time of 0.2s, step of 0.5nm, entrance slits of 1 mm; exit slits of 0.2 mm; and intermediate slit of 5 mm were used. For the Na47.5Ta:Eu sample, the spectra were measured with an integration time of 0.2s, step of 0.2nm, entrance and exit slits of 0.25 mm; and intermediate slit of 5 mm.

Figure III-13 presents the emission (λ_{exc} = 395 nm) and excitation (λ_{em} = 612 nm) normalized spectra for the Na47.5Ta:Eu glass, in which the peaks related to the characteristic transitions of Eu^{3+} are observed in the excitation spectrum, that is, from the $^7F_{0.1}$ level to the excited states $^5D_1$ - 535 nm, $^5D_2$ - 465 nm, $^5D_3$ - 416 nm, $^5L_6$ - 395 nm, $^5G_2$ - 382nm, $^5D_4$ - 363 nm e $^5H_3$ - 320 nm; and in the emission spectrum the peaks related to the transitions starting from the $^5D_0$ excited state to the ground states ^7F_J (J=0,1,2,3 and 4).

Figure III-13 - Normalized excitation spectra (λ_{em}: 612 nm) and emission spectra (λ_{exc}: 395 nm) of Na47.5Ta:Eu glass.

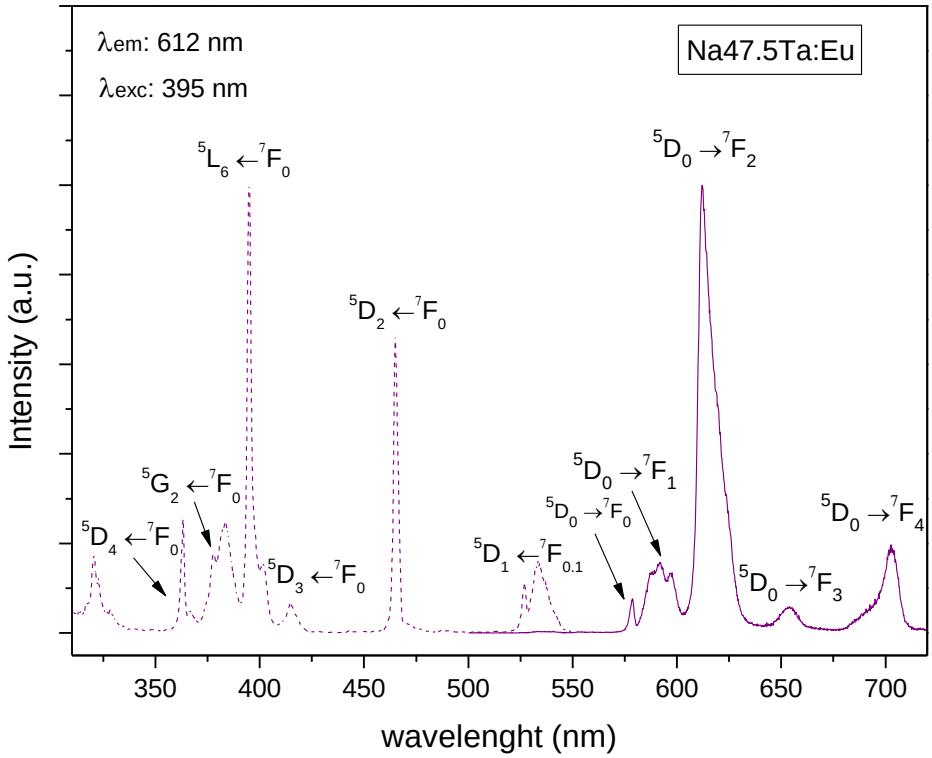

Reference: AUTHOR.

For comparison, Figure III-14 presents the emission spectra normalized at the $^5D_0 \rightarrow {}^7F_1$ (591 nm) transition, with excitation wavelength at 395 nm and 465 nm for both glasses. The spectra have wider peaks, because in glasses each ion is inserted in a different site from the other, and together they expand the width of the line. Since the Eu^{3+} ion is also used as a structural probe, the asymmetry ratios were calculated, that is, the ratio between the areas of the $^7F_2/^7F_1$ transitions. For the Na40Ta:Eu sample excited at 395 nm, this ratio was 4.79 and 5.52 for excitation at 465 nm. For the sample Na47.5Ta:Eu at 395 nm the asymmetry ratio was 5.03 and at 465 nm it was 5.69. According to these values, it is possible to infer that in both glasses the ion is in an environment of low symmetry, with an increase in this ratio with the addition of tantalum. This same trend was observed by Sousa *et al.* (2020) in potassium tantalum phosphate glasses and niobium phosphate glasses by Pastena (2016).

Figure III-14 - Normalized emission spectra in the $^5D_0 \rightarrow ^7F_1$ (591 nm) transition of Na40Ta:Eu and Na47.5Ta:Eu glasses with excitation wavelength of 395 and 465nm.

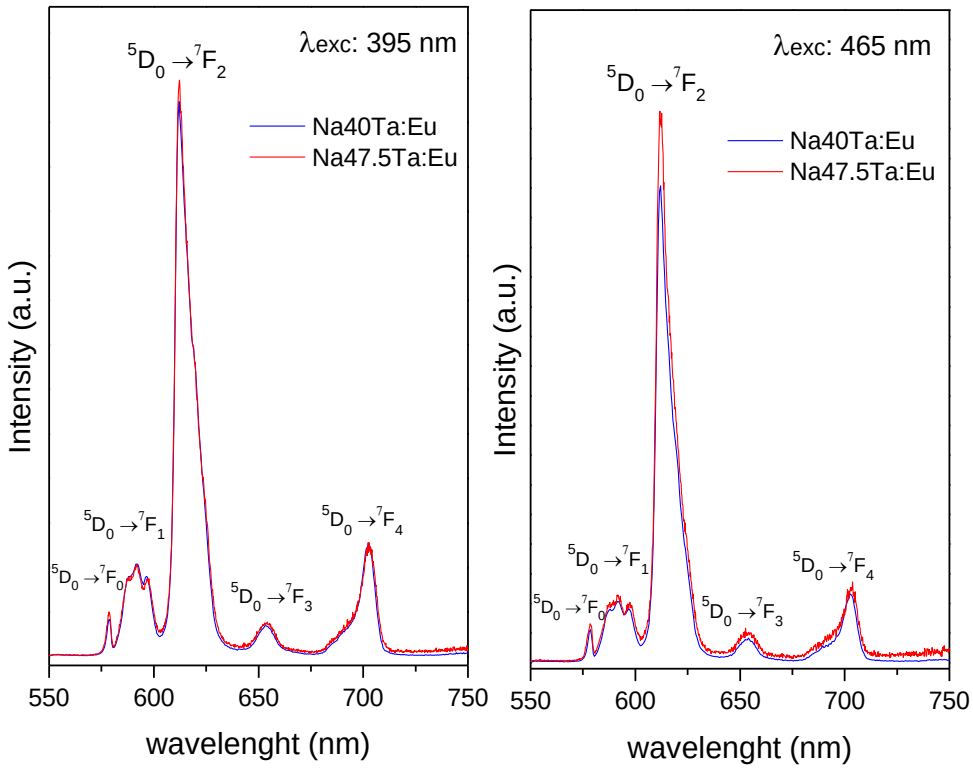

Reference: AUTHOR.

So, considering the higher polarizability of tantalum, with its addition into phosphate glasses it is observed some modifications in the optical properties of glasses. With the increase of refractive index, that increases loss of Fresnel reflection and consequently decreasing transparency of the material, as decreasing band-gap. Also, tantalum increment causes a decrease in symmetry around europium ions.

CONCLUSIONS

Synthesizing the results presented in Chapter III, according to the primary goals, homogeneous and transparent sodium phosphate glasses containing high amount of tantalum oxide (ranging from 40 to 50 mol%), both undoped and doped with Eu^{3+}, were prepared by melt-quenching around 1600°C. These glasses were characterized; and the addition of tantalum in the vitreous network promoted an increase in T_g, that is, increasing network connectivity (as measured by DSC). In addition, it was observed that phase separation for crystallization of the perovskite phase $Na_2Ta_8O_{21}$ occurs for Ta_2O_5 contents of 45 mol% or higher, which is an important parameter for preparation of glass-ceramics. The presence of this phase is related to the appearance of regions rich in [TaO_6] units, according to the structural analysis carried out through Raman and Infrared spectroscopy measurements. These [TaO_6] clusters in the glass in the glass structure are interesting, since they promote higher overall polarizability with related specific optical properties such as higher refractive indices and improved nonlinear optical properties.

Also, the addition of tantalum in the glass slightly red-shifts the band-gap as usually observed with incorporation of heavier elements. The glasses also exhibit a high transparency (~80%) and relatively high refractive index values, this latter increasing with tantalum content. With the measured refractive index data, it was possible to perform an adjustment using Cauchy's equation to obtain these values in other wavelengths. By photoluminescence measurements it was verified that the addition of tantalum to europium-doped glasses leads to an increase in the $^7F_2/^7F_1$ asymmetry ratio, suggesting a decreasing symmetry around these ions.

REFERENCES

CASSANI, R. **Estudo de cristalização em vidros fosfatos alcalinos contendo óxido de nióbio** = Study of crystallization in alkaline phosphate glasses containing niobium oxide. 2022. 100p. Thesis (Master in Material Science and Engineering) - Universidade Federal de Alfenas, Poços de Caldas, 2022.

CUNHA, C.R.da. *et al.* Crystallization of bronze-like perovskite in potassium tantalum germanate glasses: Glass ceramic preparation and its optical properties. **Optical Materials,** [S.l.], v.122, partB, p.111803, 2021.

HIRAO, K., TODOROKI, S., SOGA, S. Origin of inhomogeneous linewidth of Eu^{3+} fluorescence in phosphate and borophosphate glasses. **Journal of Non-Crystalline Solids**, [S.l.], v.175, p.263-269, 1994.

HU, C.; TENG, H. Influence of structural features on the photocatalytic activity of $NaTaO_3$ powders from different synthesis methods. **Applied Catalysis A,** [S.l.], v.331, p.44-50, 2007.

KARAM, L. **Structuration multi-échelle et multifonctionnelle de nouveaux matériaux vitreux pour la photonique intégrée =** Multiscale and multifunctional structuring of new glassy materials for integrated photonics. 2020. 275p. Thesis (PhD in Chemistry Science) - Université de Bordeaux, Bordeaux, France, 2020.

KAMITSOS, E.I. *et al.* Infrared reflectance spectra of lithium borate glasses. **Journal of Non-Crystalline Solids**, [S.l.], v.126, p.52-67, 1990.

LEPICARD, A. **Design of surface chemical reactivity and optical properties in glasses.** 2016. 293p. Thesis (PhD in Chemistry) - Université de Bordeaux, Bordeaux (France), 2016.

LIMA, C.L.J. **Vidros fosfatos de metais de transição** = Transition metal phosphate glasses. 2014. 110p. Thesis (Master in Material Science and Engineering) - Universidade Federal de Alfenas, Poços de Caldas, 2014.

MAESTRI, S.A. **Vidros e vitrocerâmicas no sistema binário $NaPO_3$-Ta_2O_5** = Glass and glass-ceramics in the binary system $NaPO_3$-Ta_2O_5. 2018. 104p. Thesis (Master in Material Science and Engineering) - Universidade Federal de Alfenas, Poços de Caldas, 2018.

MALAKHO, A. *et al.* Crystallization and second harmonic generation in thermally poled niobium borophosphate glasses. **Journal of Solid-State Chemistry,** [S.l.], v.178, p.1888-1897, 2005.

MARCONDES, L.M. *et al.* Transparent glass and glass-ceramic in the binary system $NaPO_3$-Ta_2O_5. **Journal of American Chemistry Society**, USA, v.103, p.1647-1655, 2019.

MISTRIK, J. *et al.* Optical properties of electronic materials: fundamentals and characterization. *In:* KASAP, S.; CAPPER, P. **Springer Handbook of Electronic and Photonic Materials**. Springer, Boston, MA. 2017. p.47-77.

MUÑOZ, F. *et al.* Phosphate glasses. *In:* MUSGRAVES, J.D.; HU, J.; CALVEZ, L. **Springer Handbook of Glass**. [S.l.]: Springer International Publishing, 2019. p.553-594.

ONISHI, H. Sodium tantalate photocatalysts doped with metal cations: why are they active for water splitting?. **Chem Sus Chem,** Weinheim, v.12, p.01-11, 2019.

PASTENA, B.L.de. **Vidros e vitrocerâmicas de fosfato de nióbio** = Niobium phosphate glass and glass ceramics. 2016. 94p. Thesis (Master in Material Science and Engineering) - Universidade Federal de Alfenas, Poços de Caldas, 2016.

POIRIER, G.Y. *et al.* Second Harmonic Generation in sodium tantalum germanate glasses by thermal poling. **Journal of Physics Chemistry C,** [S.l.], v.123, p.26528-26535, 2019.

RAJAOFARA, Z. *et al.* Mapping the second and third order nonlinear susceptibilities in a thermally poled microimprinted niobium borophosphate glass. **Optical Materials,** [S.l.], v.11, n.10, p.3411, 2021.

SOUSA, B.P. *et al.* Phosphate glasses with high tantalum oxide contents: Thermal, structural and optical properties. **Materials Chemistry and Physics**, Netherlands, v.239, p.121996, 2020.

VLASE, T.; VLASE, G.; DOCA, N. Kinetics of thermal decomposition of alkaline phosphates. **Journal of Thermal Analysis and Calorimetry**, [S.l.], v.80, p.207-210, 2005.

CHAPTER IV - THERMAL POLING AND MICROPOLING IN SODIUM TANTALUM PHOSPHATE GLASSES

CHAPTER IV - THERMAL POLING AND MICROPOLING IN SODIUM TANTALUM PHOSPHATE GLASSES

This chapter presents the modifications induced in the properties of sodium high tantalum phosphate glasses (studied in Chapter III) when subjected to Thermal Poling and Micropoling. In this sense, the glasses synthesized in the $NaPO_3$-Ta_2O_5 system, both undoped and doped with europium were submitted to Thermal Poling. Poling and Micropoling were carried out using homogeneous and microstructured electrodes respectively and characterizations were subsequently performed on poled glasses by Maker Fringes, micro-SHG/Raman/luminescence, optical microscopy, AFM and phase contrast measurements.

IV-1 THERMAL POLING AND MICROPOLING OF GLASSES

Thermal Poling and Micropoling of undoped and doped sodium tantalum phosphate glasses (presented in Chapter III) were carried out at the ISM. Initially electrodes to be used as anodes were prepared with a 0.5 cm^2 area, consisting of glass slides with a thin film of indium tin oxide (ITO - 100 nm and 8 -12 Ω/sq - which is conductive and transparent) cleaned in acetone and then in propanol, both in ultrasound for 10 minutes. These were microstructured using pulsed laser ablation (ps) working at 1064 nm using the system presented in Chapter II-6, with the beam focused on the sample with a microscope and dimensioned using an automated XY translation table, with the system controlled by a camera, using a program developed at ISM. The parameters (laser power, objective, speed) were chosen in order to selectively remove the entire thickness of the ITO layer, thus, forming a periodic pattern with conductive areas alternated with non-conductive areas according to the chosen structures.

The structures consisted of squares and circles of 30 and 40 µm spaced by 20 µm, and lines of varying thickness with 3500 µm in length. With slight variations, the structures were made at a distance of 1000 µm (0.1 cm) from the upper and left lateral of the electrode, as shown in Figures IV-1/2, which show two different arrangements, with the main difference being the number of rows, keeping the same number of columns, and Figure IV-3 presents a micrograph (20x objective) of the electrode in the region of the square patterns with 40 µm just after the laser ablation.

Figure IV-1 - Design 01 of microstructures on the anode electrode.

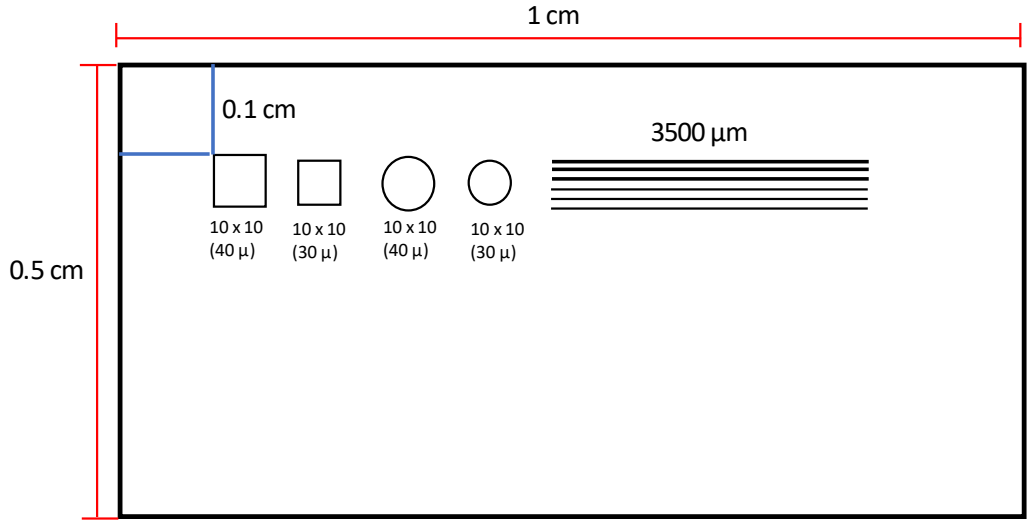

Reference: AUTHOR.

Figure IV-2 - Design 02 of microstructures on the anode electrode.

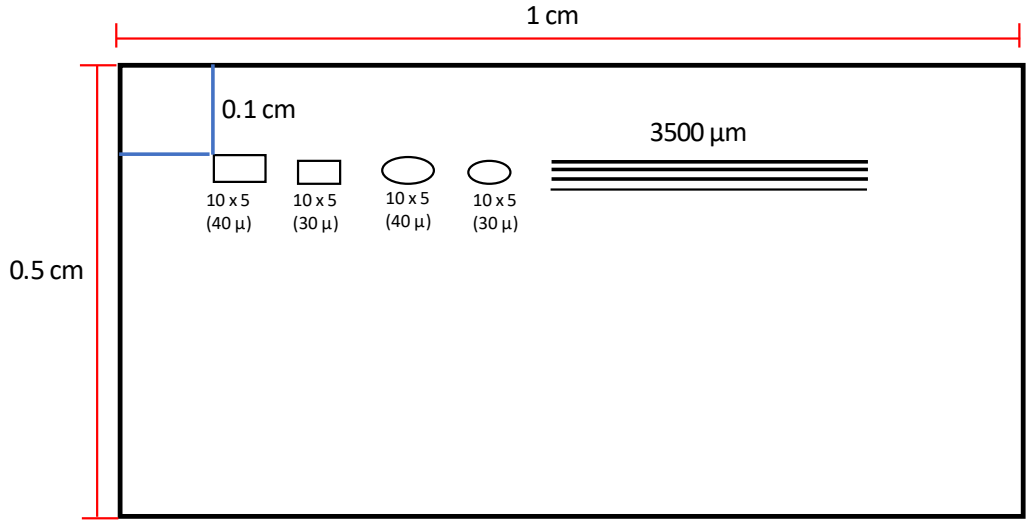

Reference: AUTHOR.

Figure IV-3 - Micrograph of ITO electrode right after ablation - 20x.

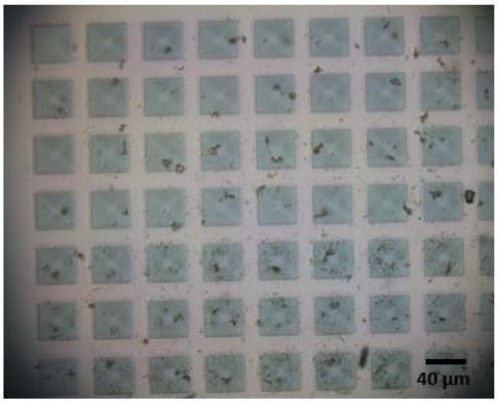

Reference: AUTHOR.

As pointed out in Chapter I-6.4, the anode electrode can be microstructured or homogeneous. In this case, the electrode was considered both, structured - as the described microstructures were obtained, as well as homogeneous - most of the electrode does not have a microstructure (according to the design presented) and, therefore, consisting of an area considered homogeneous for Thermal Poling and further analysis. Thus, in practical terms, it was considered that both Thermal Poling and Thermal Micropoling occurred concomitantly.

After ablation, the electrodes were again cleaned with acetone and propanol and the electrode sides without ITO to become conductors were metallized by chromium/gold deposition (100 nm) using the Q3000T D equipment (Quorum). On the sides, in order to ensure conductivity, conductive silver ink was also applied.

For Thermal Poling, the cell consisted of a hermetic enclosure (blocking anode) that allows achieving a primary vacuum, with an atmosphere control (N_2 - 6L.min^{-1}), and the humidity remained very close to zero. The system also has an observation window and the heating system consists of a heating cartridge inserted in the metal part, also serving as a cathode. A thermocouple allows to control the temperature, with a heating limit of 300°C. A high voltage source (Brandenburg ALPHA III model 3707) is connected to the cell and a program controls the high voltage source, the ramp rate, the maximum current and recording its variation over time.

For Poling experiments, it was used an assembly consisting of the fixed metallic cathode, a n-doped silicon wafer with the same size as the ITO electrode, followed by a 150μm-thick borosilicate slide in contact with the sample (used to prevent the sample from adhering to the cathode, impairing the optical quality; and also functioning as an open cathode able to receive the Na^+ ions migrating from the sample). Next, the glass to be poled (sample) was placed, and then, on the anode side, the prepared ITO electrode, which was fixed in the voltage application system. Figure IV-4**a** presents the assembly scheme described, in **b** is the image of the assembly with a top view before the connections, in **c** the system already with the connections, and in **d** is the Poling cell closed and in operation.

The system was heated to 250°C at a rate of 15°C.min^{-1} (except the first attempt on the Na40Ta sample which was heated to 300°C), and after reaching the chosen temperature and humidity close to zero, a DC voltage was applied (150 V.min^{-1} rate). After the standard time of 30 minutes, the temperature was reduced, with the DC voltage maintained until reaching 50°C, and then the voltage was turned off and the sample removed. As the Poling cell was connected to the high voltage generator, the electric current (i) generated by the migration of mobile ions was measured.

Figure IV-4 - Thermal Poling: (a) diagram of the system assembly, (b) image after assembly, (c) image after making the system connections, and (d) image of the system during the Thermal Poling experiment of the Na40Ta sample.

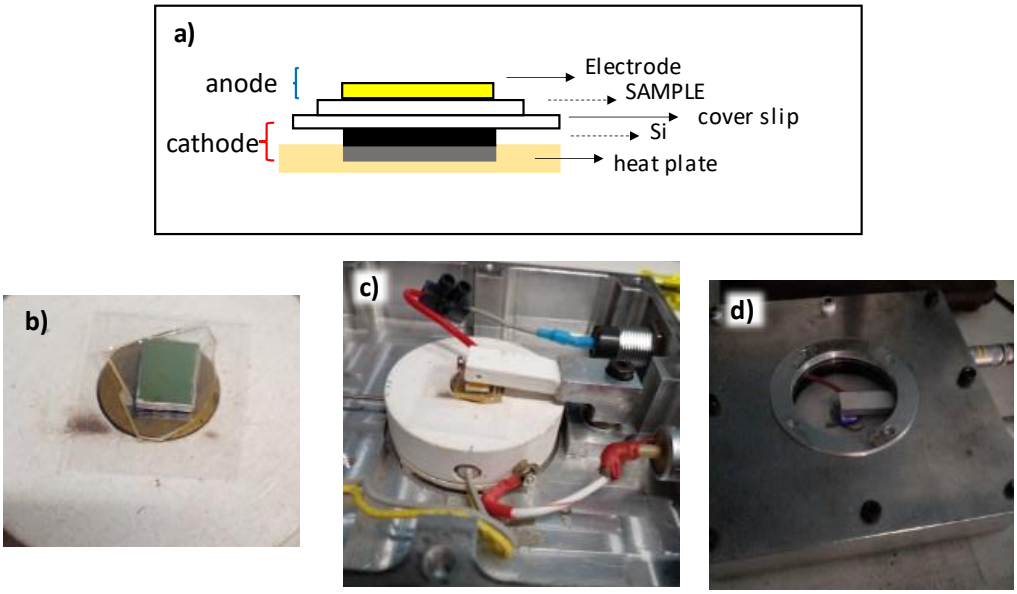

Reference: AUTHOR.

The glasses described in Chapter III that were thermally poled are: Na40Ta, Na45Ta / Na45Ta:Eu, Na47.5Ta / Na47.5Ta:Eu, and Na50Ta. Several tests were performed (varying specially the DC voltage) - as summarized in Table IV-1.

Table IV-1 - Summary of the Thermal Poling/Micropoling tests carried out on the sodium tantalum phosphate glasses.

Sample	**Na40Ta**					
Thickness (mm)	0.7		1			
Temperature (°C)	300	250	250			
Voltage (V)	1500	1400	1300	700	600→500	500

Sample	**Na45Ta**			**Na45Ta:Eu**	**Na50Ta**
Thickness (mm)	1			1	1
Temperature (°C)	250			250	250
Voltage (V)	700→500	650	600	600	700

Sample	**Na47.5Ta**		**Na47.5Ta:Eu**	
Thickness (mm)	1		1	
Temperature (°C)	250		250	
Voltage (V)	700	900*	700	900

Reference: AUTHOR.
* Electrode without microstructure.

Figure IV-5 shows the applied DC voltage curves and the detected electric current generated by the migration of mobile ions in the Na40Ta glass during the Thermal Poling experiments. The expected current curve is a decay after reaching the threshold of the applied voltage, since the ions migrate towards the cathode over the treatment time, and the resistivity of the anodic layer increases. In samples with 40 mol% of Ta_2O_5, the Poling did not occur as expected, as can be seen from the curves. Several samples broke during the experiment (Figure IV-6), even before reaching the voltage plateau, such as the first sample that was initially poled at 300°C (reason for the lower temperature for further tests). In other tests, despite the fact that the glasses did not break, the measurements were not as adequate, e.g., according to the curve in Figure IV-5C. In addition, in almost all tests with these samples, an electric spark was observed (not observed at 500V, but also no current detected).

Figure IV-5 - Data (DC voltage applied and detected current) from Thermal Poling tests on Na40Ta glass.

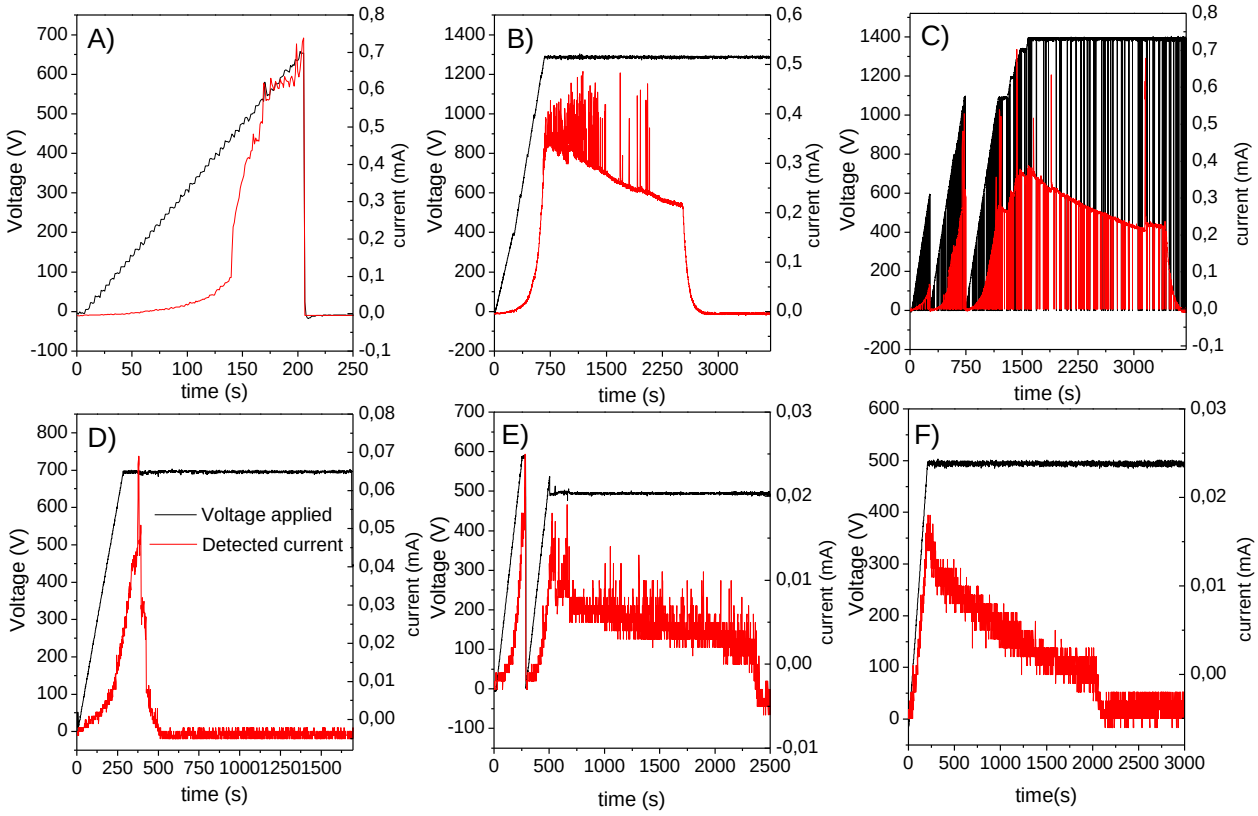

Reference: AUTHOR.
Note: corresponding to parameters of Table IV-1 - A) 1500V, B) 1400V, C) 1300V, D) 700V, E) 600→500V and F) 500V.

Figure IV-6 - Image of Na40Ta glass after different Thermal Poling tests.

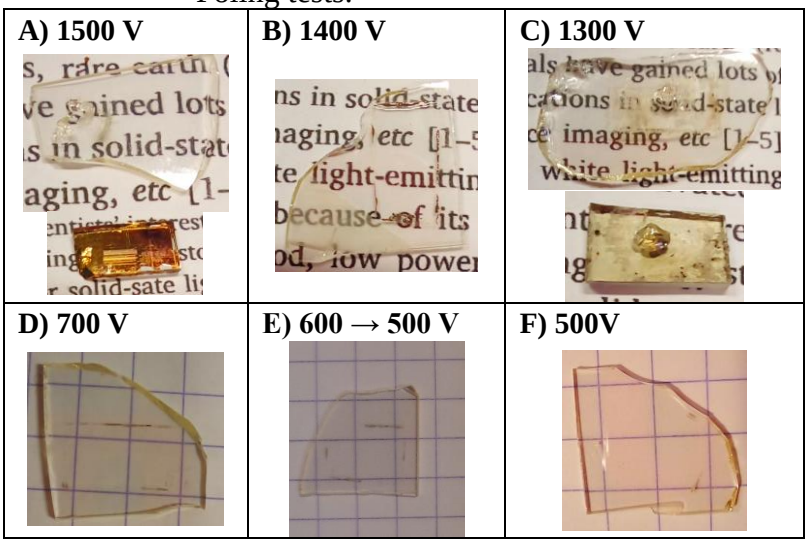

Reference: AUTHOR.

Figure IV-7 presents the current curves obtained after Thermal Poling on Na45Ta, Na45Ta:Eu and Na50Ta samples. Some problems were identified during the tests of the Na45Ta sample (A and B); however, the expected and controlled curve was obtained when using the voltage of 600V. The same voltage being applied for the sample doped with europium, which also was controlled and without electric spark as occurred with the Na40Ta sample. For Na50Ta sample, the test was carried out with 700V, also showing the expected behavior of the electric current[33].

Figure IV-8 shows the curves during the experiments on Na47.5Ta and Na47.5Ta:Eu samples, which also presented the expected electric current curve without any of the previous problems occurring, such as electric sparks and sample breakage. As observed, for this undoped glass, a slight difference in the current profile is observed, that may be attribute to the material during its preparation considering the high amount of tantalum into this glass, but that did not affect the poling tests. Since they correspond to the glasses with the highest percentage of tantalum oxide in which the doped sample was also obtained, subsequent studies were focused on them, mainly trying higher applied voltage (900V).

[33] The Na50Ta sample was only tested using 700V, and therefore, the possibility of increasing the voltage during treatment was not verified.

Figure IV-7 - Data (DC voltage applied and detected current) from Thermal Poling tests on: (A-C) Na45Ta, (D) Na45Ta:Eu and (E) Na50Ta glasses.

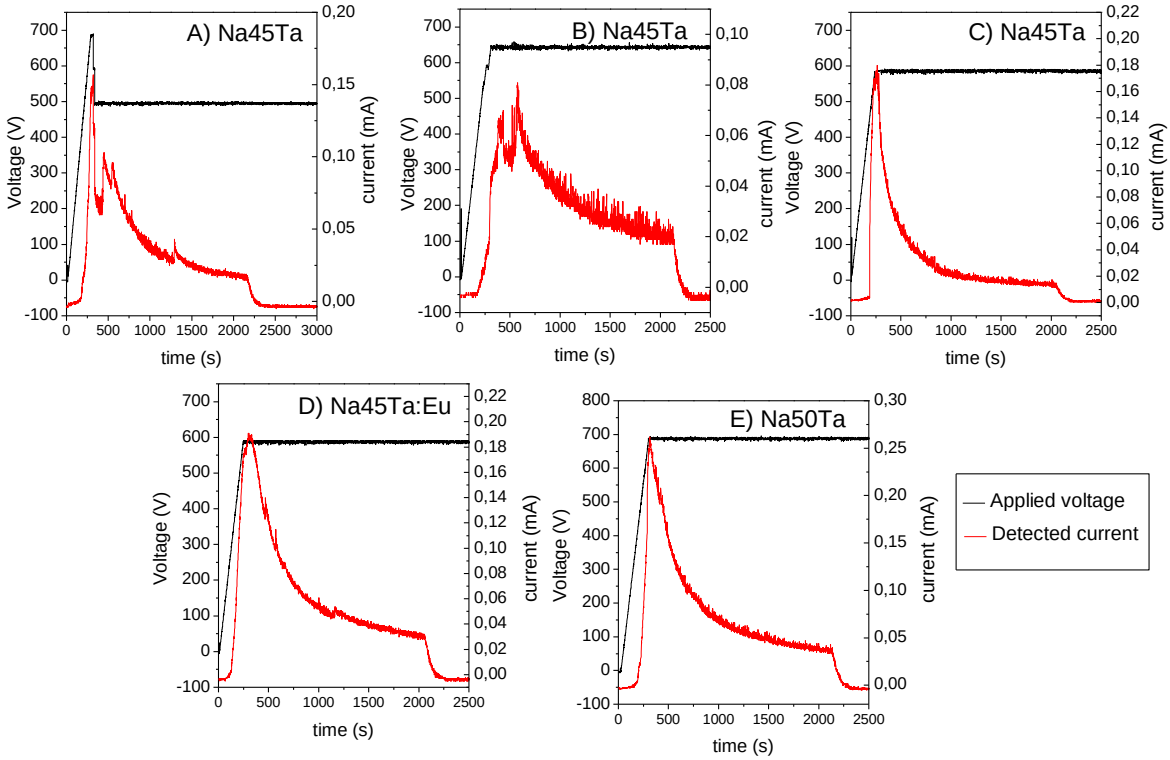

Reference: AUTHOR.
Note: corresponding to parameters of Table IV-1 - A) 700→500V, B) 650V, C) 600V, D) 600V and E) 700V.

Figure IV-8 - Data (DC voltage applied and detected current) from Thermal Poling tests on: (A-B) Na47.5Ta and (C-D) Na47.5Ta:Eu glasses.

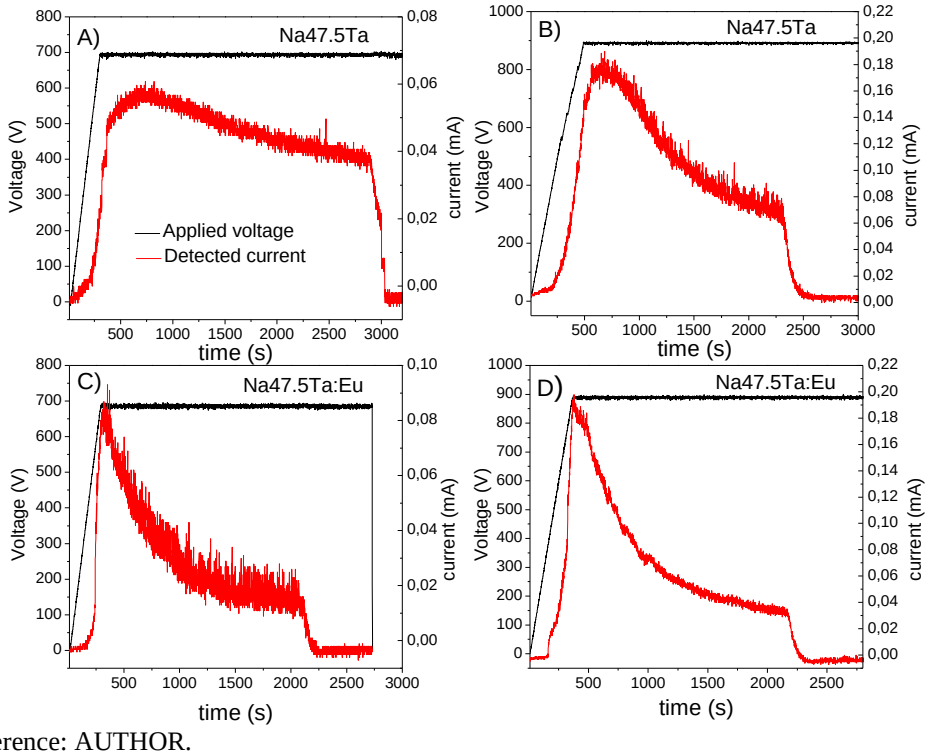

Reference: AUTHOR.
Note: corresponding to parameters of Table IV-1 - A) 700V, B) 900V, C) 700V and D) 900V.

Thus, it was possible to successfully apply Thermal Poling in sodium phosphate glasses with different tantalum oxide contents from 45 to 50 mol%. It is worth noting that, as previously mentioned, there are several factors that can influence the material response after Poling, including the experimental poling parameters. Among these parameters is the applied voltage, which in this work can be considered relatively low. For example, in the tantalum germanate glasses studied by Poirier *et al.* (2019) voltages up to 2250V were used; 1600V in the niobium borophosphate glasses studied by Lepicard (2016); and 2000V in works reported by Malakho *et al.* (2005). It is also important to point out that in these examples the T_g values of the glasses are lower than the glasses studied in this work; this being one of the reasons why the temperature of 300°C was chosen at first; whereupon it was reduced to 250°C. This could be related to the fact that the high Tg value in tantalum phosphate glasses are associated with regions rich in [TaO_6] units, and the Poling deals with the migration of Na^+ ions.

In this case, the same temperature of 250°C was used in all thermal poling tests in order to keep at least one fixed parameter. However, it is important to consider that the poling temperature also influences the final response. As studied by Karam *et al.* (2020a), for Thermal Poling on niobium borophosphate glasses, varying the sodium content in the glass, keeping the Nb/P ratio at 1.53; the authors observed the need of adjusting the temperature as a function of Tg (related to the percentage of sodium). Still, in the case of glass with a higher sodium content (lower T_g) it presented results that were considered unsatisfactory, since a high current ($1mA.cm^{-2}$) was observed, resulting in a damaged surface with loss of optical quality. Based on this, it is likely that something similar may have occurred with the Na40Ta glasses, which correspond to the studied glass with the highest sodium content and the lowest T_g. By way of comparison, in the first test performed at 300°C, the sample rupture occurred when the current reached 1.4 $mA.cm^{-2}$ (and voltage still at 700V). Another point to be considered is that sodium departure induces charge compensation processes to occur; and according to Lepicard (2016), the lack of these processes could lead to dielectric breakdown of the glass. This may be one of the reasons explaining our observations of electric sparks.

For these reasons, temperature and voltage are key factors in thermal poling, together with the electrodes nature, poling atmosphere, etc.

IV-2 CHARACTERIZATION OF THERMAL POLING ON SODIUM TANTALUM PHOSPHATE GLASSES

In order to have a first insight of the glass response to Thermal Poling on the homogeneous area, SHG measurements were first performed using the Maker Fringes experiment (described in Chapter II-5). Measurements were performed at the ISM, with a nanosecond laser operating at 1550 nm and 30 Hz (maximum pulse energy of 100 μJ per 20 ns) with a spot size of 100 μm, in transmission mode. Two types of measurements were performed: according to the incidence angle (θ-scan), varying the θ angle from -80 to 80° and step of 2°; and according to the polarization of the incident radiation (ψ-scan - p or s) varying the angle ψ from 0 to 180° fixing the angle θ at 60° and a step of 2°.

Figure IV-9 presents both the θ-scan (on the left) and the ψ-scan (on the right) measurements of Na45Ta-600V, Na45Ta:Eu-600V and Na50Ta-700V samples.

Figure IV-9 - Results obtained during the Maker Fringes experiment, θ-scan (left) and ψ-scan (right), of the samples: (A) Na45Ta - 600V, (B) Na45Ta:Eu - 600V and (C) Na50Ta - 700 V.

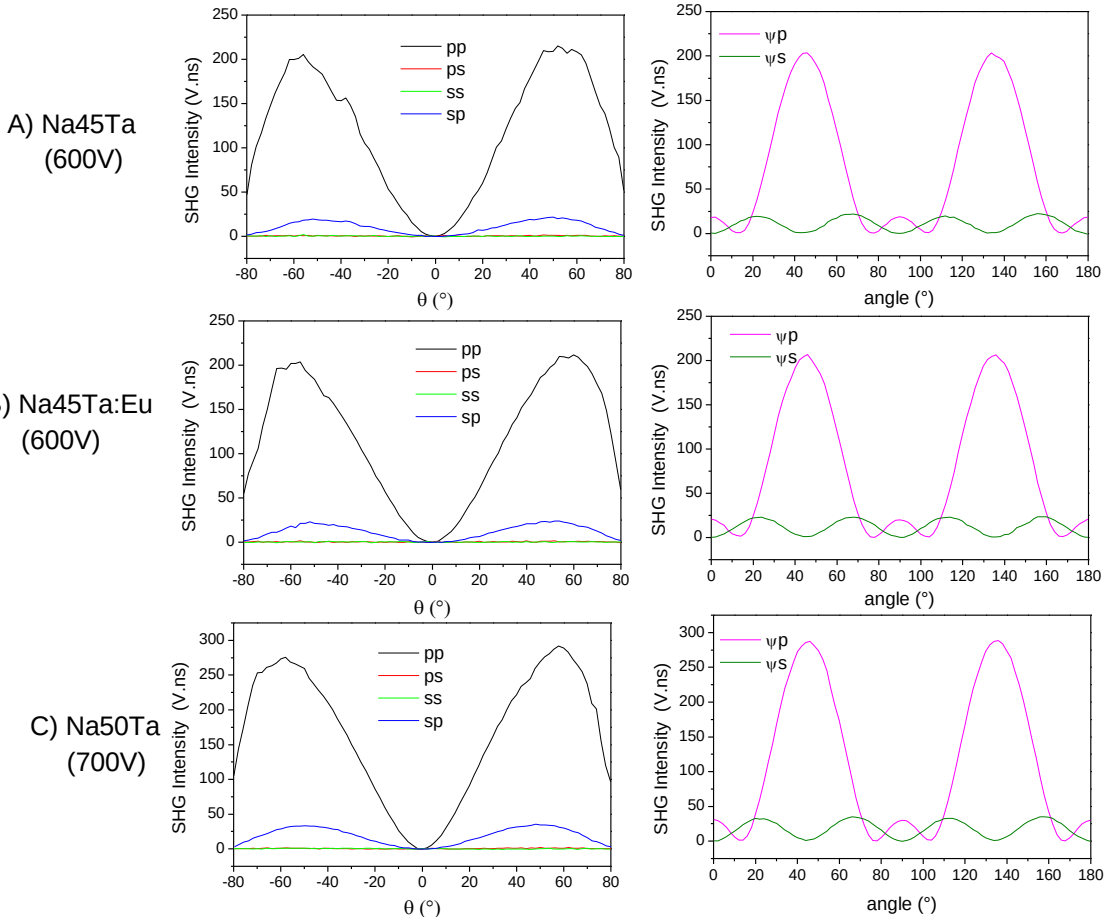

Reference: AUTHOR.

As the measurements were made with different amplifications, for comparison it is more appropriate to use the ratio[34] $I_{2\omega}/I_{\omega}^{2}$, normalizing according to the amplification factor. Thus, Figure IV-10 presents the graphs for the Na45Ta-600V, Na45Ta:Eu-600V and Na50Ta-700V samples of the normalized θ-pp measurements.

Figure IV-10 - SHG measurements (θ-pp) normalized: Na45Ta-600V, Na45Ta:Eu-600V and Na50Ta-700 V.

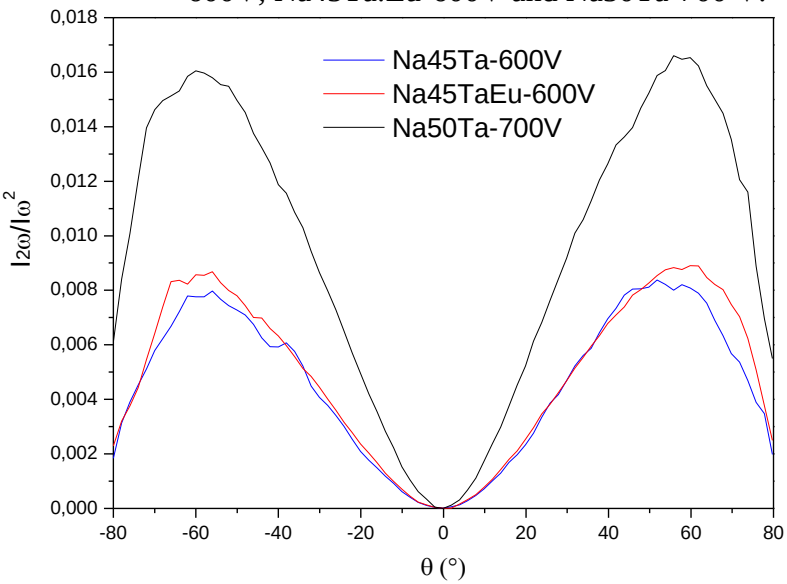

Reference: AUTHOR.

The θ-scan (left) and ψ-scan (right) measurements of the Na47.5Ta sample (700V and 900V) are shown in Figure IV-11 and Figure IV-12 shows the measurements of the Na47.5Ta:Eu sample. Likewise, as different amplifications were used during the analysis, Figure IV-13 shows the graph of the θ-pp measurement considering the ratio $I_{2\omega}/I_{\omega}^{2}$ and adjusting according to the amplification for the Na47.5Ta and Na47.5Ta:Eu samples.

[34] The response of the material varies quadratically with the incident laser power (LEPICARD, 2016).

Figure IV-11 - Results obtained during the Maker Fringes experiment, θ-scan (left) and ψ-scan (right), of the Na47.5Ta sample for: (A) 700V and (B) 900V.

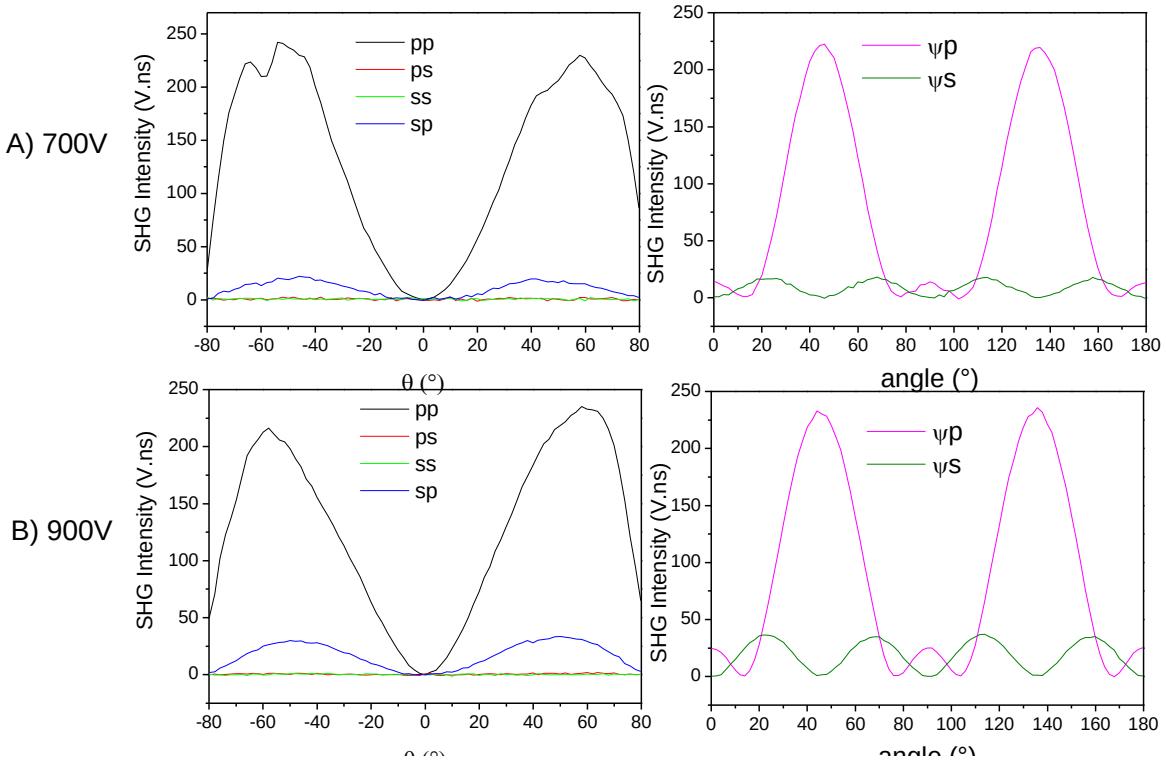

Reference: AUTHOR.

Figure IV-12 - Results obtained during the Maker Fringes experiment, θ-scan (left) and ψ-scan (right), of the Na47.5Ta:Eu sample for: (A) 700V and (B) 900V.

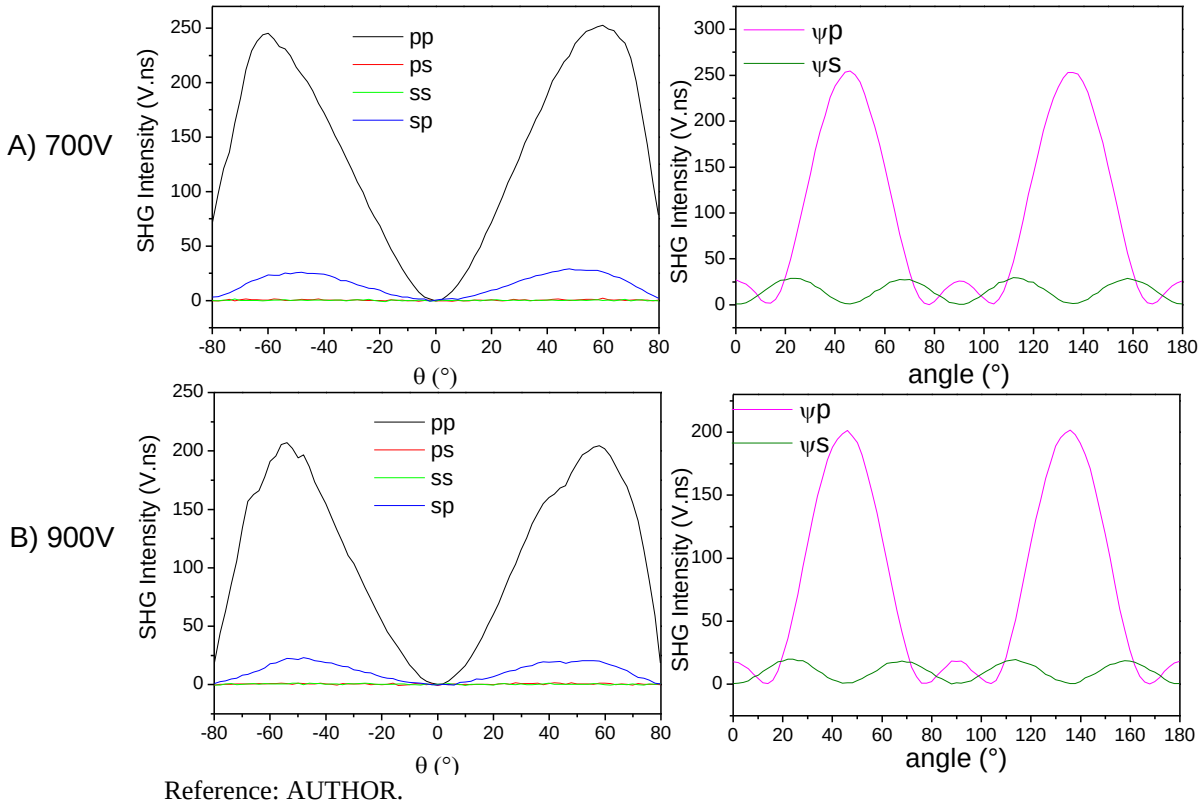

Reference: AUTHOR.

Figure IV-13 - SHG measurements (θ-pp) normalized of: (A) Na47.5Ta sample and (B) of Na47.5Ta:Eu sample.

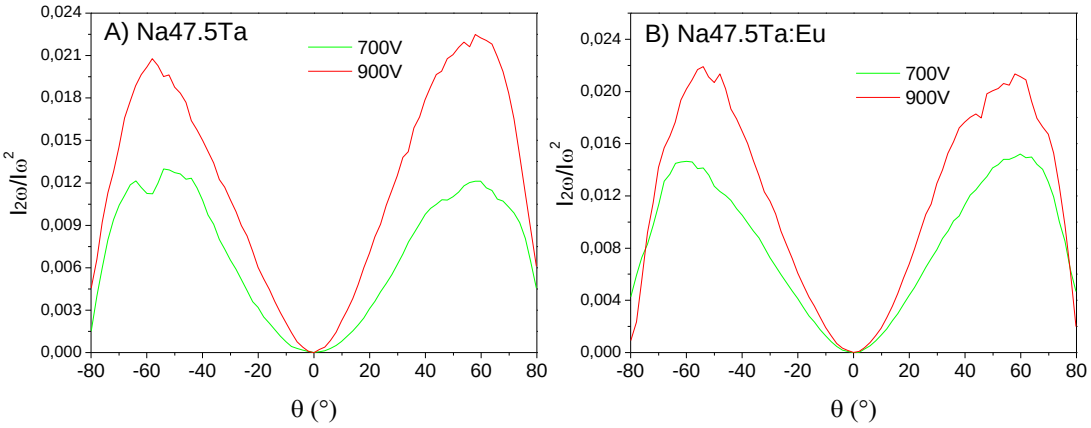

Reference: AUTHOR.

According to the results, all samples exhibited SHG, that means, Thermal Poling performed on the glasses broke their centrosymmetry, allowing the material to generate second harmonic, even with treatments using relatively low voltages. Another important point is the symmetry between the sides of the measures, indicating homogeneity. Furthermore, only one fringe is observed for all poled samples, this is due to the thickness of the active layer of SHG being smaller than the coherence length of the propagation medium.

Table IV-2 presents the maximum values obtained from the $I_{2\omega}/I_{\omega}^2$ ratio for the glasses after Thermal Poling. Regarding these data, it appears that there is an increase as the amount of tantalum increase in the glass matrix, which could be related to the greater polarizability of tantalum (value of $\chi^{(3)}$). It is also verified that the increase in voltage applied during treatment also influenced the SHG response, increasing the value of the intensity ratio. Another observation is that in samples containing europium when compared to undoped equivalents (Na45Ta:Eu- 600V; and Na47.5Ta:Eu - 700 and 900V), all showed a slight increase.

Table IV-2 - Maximum calculated values of the $I_{2\omega}/I_{\omega}^2$ ratio based on measurements of Maker Fringes after Thermal Poling.

Na45Ta-600V	**Na45Ta:Eu-600V**	**Na50Ta-700V**	**Na47.5Ta-700V**	**Na47.5Ta:Eu-700V**	**Na47.5Ta-900V**	**Na47.5Ta:Eu-900V**
0.008	0.009	0.016	0.013	0.015	0.020	0.022

Reference: AUTHOR.

To discuss the origin of this SHG present in glasses (i.e., due to EFISH and/or reorientation) it is necessary to verify the ratio between $\chi_{zzz}^{(2)}/\chi_{zxx}^{(2)}$ or d_{33}/d_{31} and whether or not there is a deviation from the value 3, corresponding to the EFISH model (which is most

likely in glasses). However, at first, it is possible to suggest that the SHG origin in these glasses is really the EFISH model, because according to Lepicard (2016), when the signal is purely EFISH, the intensity must return to zero at angles 0, 45, 90, 135 and 180° in the ψ-s data, which is what was observed in the measurements.

Considering that, Maker fringes data were simulated using a general matrix formulation of linear and non-linear multilayer model (RODRIGUEZ; SOURISSEAU, 2002) for two chosen samples: Na50Ta-700V and Na47.5Ta:Eu-900V. These data simulations were performed also considering other parameters such as refractive index (at the incident and SHG wavelengths presented in Chapter III) and thickness of poled layer.

The thickness of poled layer was obtained by a ToF-SIMS analysis, thus, sodium, tantalum, phosphorus and europium concentration profile under the anode was determined by ToF-SIMS that were performed on a TOF-SIMS 5 - IONTOF equipment at PLACAMAT (*PLatforme Aquitaine de CARactérisation des MATériaux*) in Bordeaux-FR and the depth after that was verified using an optical and mechanical profilometer at ICMCB.

By these data (Figure IV-14), the depletion layer of sodium under the anode surface after Thermal Poling could be identified while the other elements remain motionless along the whole probed thickness. The apparent small decrease of P, Ta and Eu contents out of the poled layer is not attributed to atomic motion but to a relative lower atomic content of the glass composition considering that sodium is also present. As observed, the depleted layer is almost free of sodium as its content falls to values close to 0. The depth of depletion layer was estimated, being 1.7 µm for Na47.5Ta:Eu-900V and 0.9 µm for Na50Ta-700V.

Figure IV-14 - ToF-SIMS depth profile glass constituents (oxygen not represented) after Thermal Poling of sample: A) Na47.5Ta:Eu-900V and B) Na50Ta-700V.

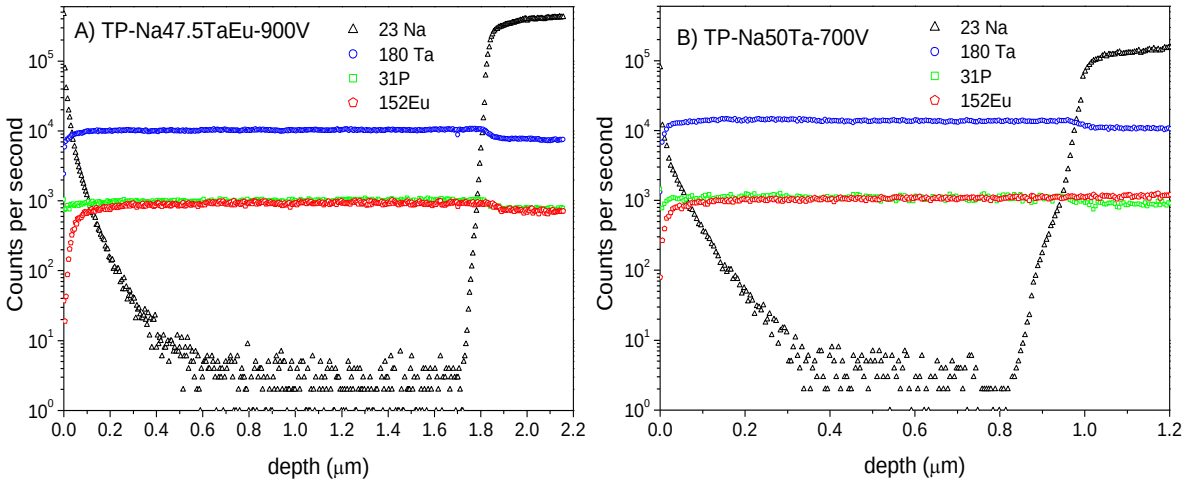

Reference: AUTHOR.
Note: The 0µm mark corresponds to the glass surface at the anode side.

Simulations performed on the chosen samples are in agreement with an EFISH model for SHG. Second-order nonlinear optical susceptibilities $\chi^{(2)}$ were extracted from these simulations, being 1 pm/V for Na50Ta-700V sample and 0.72 pm/V for Na47.5Ta:Eu-900V. As disposed in Table I-3, these values are higher than the ones obtained for germano-silicate fiber, sodium-niobium-germanate glass, tellurites, and some of the chalcogenides. Also comparing to a tantalum germanate glass (POIRIER *et al.*, 2019) poled at 1350V, our tantalum phosphate glasses exhibit $\chi^{(2)}$ values 2 to 3 times higher.

Since higher voltages could be applied on the Na47.5Ta:Eu glass, other measurements were focused on this sample. In this sense, a micro-SHG mapping was carried out in the cross-section of this sample (as shown in Figure IV-15), using the assembly scheme described in Chapter II-6, with a 1064 nm ps laser. As can be seen from Figure IV-16, the SHG response is located under the anode[35]. In addition, through the image it is verified that the thickness of the layer is around 2 µm, which is in accordance with ToF-SIMS data. As an example, the niobium borophosphate glasses in which the SHG response was evaluated according to the variation in sodium content presented thickness values between 1.53 to 2.6 µm - 800V (KARAM *et al.*, 2020a); while in the tantalum germanate glasses, it was 5.5 µm for the highest voltage (2250V), and 2.5 µm for the lowest (900V and 1350V) (POIRIER *et al.*, 2019).

Figure IV-15 - Diagram illustrating the geometry of the micro-SHG/Raman/luminescence analysis in cross section: (a) the poled sample is cut in half and (b) is analyzed at the edge along a line from the poled surface on the anode side towards to the cathode side.

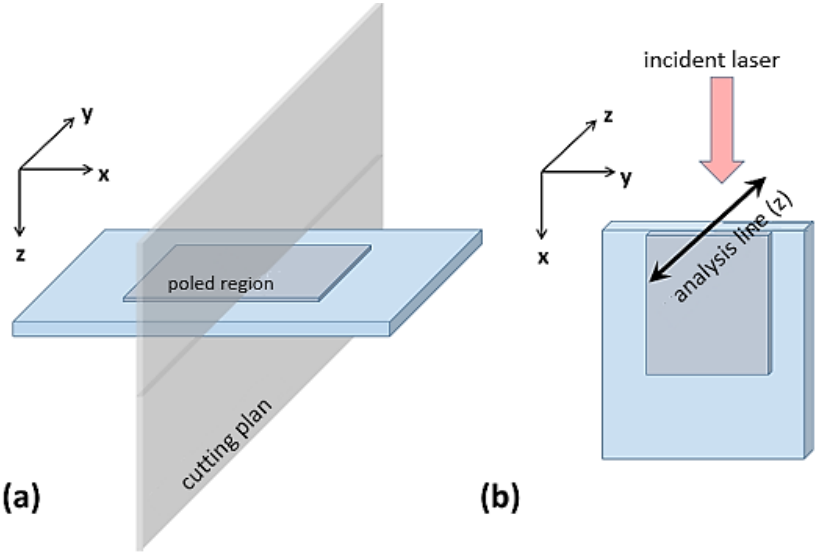

Reference: Translated from KARAM (2020, p.99).

[35] It is pointed out that when performing the cross-section break of the sample, the sample did not present a completely flat section, which make it a little difficult to focus on the measurement.

Figure IV-16 - Micro-SHG mapping of Na47.5Ta:Eu-900V sample.

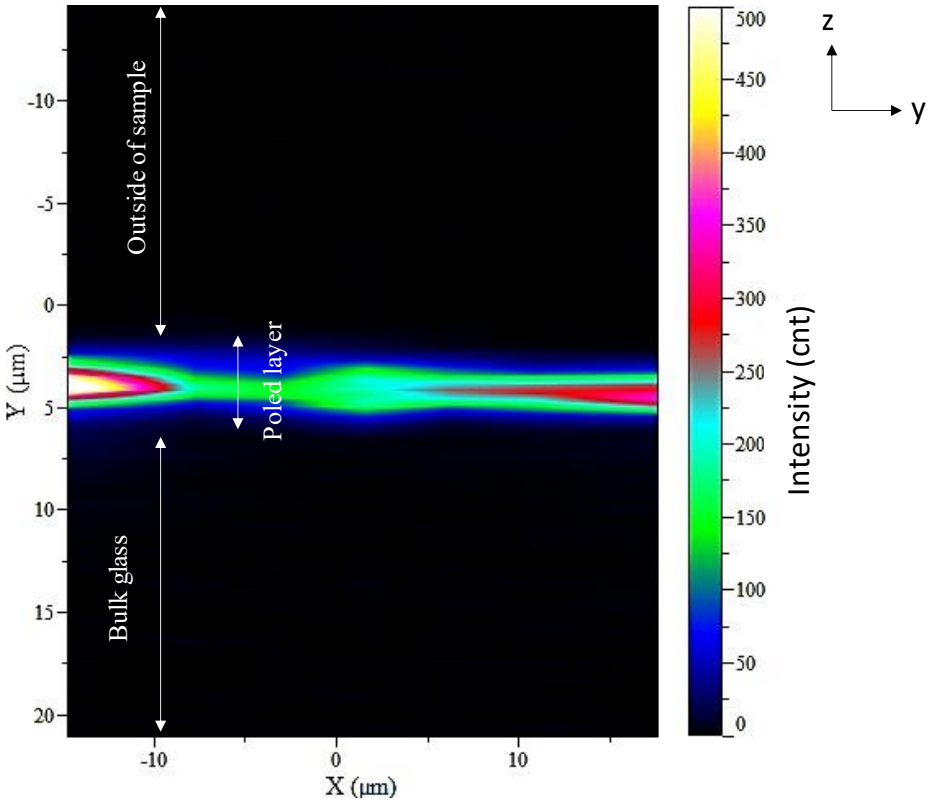

Reference: AUTHOR.

To evaluate the structural modifications induced by the Poling and spatially correlate it with the SHG, the measurement of the micro-Raman mapping was performed at the same position as micro-SHG using the 532 nm cw laser. Measurements were performed using VV, HH and VH[36] polarizers; as the modifications did not change with the polarizations, only the HH results are shown (FIGURE IV-17). Figure IV-17**A** presents one of the spectra obtained in the poled layer and one of the spectra in the sample bulk (unpoled area) after normalization at 685 cm^{-1}. As the sample was doped with europium, the relative Raman measurements are being influenced by luminescence (showing a broadband, since the Raman spectrum was collected under a 532 nm excitation that corresponds to $^5D_1 \leftarrow ^7F_{0.1}$ absorption transition of Eu^{3+}), making it difficult to establish a precise relative comparison between the bands. However, in general, it is noted that there is a small shift of the bands in the poled layer. The Ta/P ratio of the glass in the poled and non-poled area, in principle, does not change; since the change occurs with the sodium ion. Therefore, it is possible to consider that the difference would be the decrease in the relative amount of sodium ion in the SHG active layer, maintaining the same Ta/P ratio. In the Raman studied in a niobium borophosphate glasses, in which the Nb/P ratio is kept constant

[36] V - vertical and H - horizontal.

with variation in the percentage of sodium (KARAM *et al.*, 2020a), it is verified that the less sodium in the glass, the greater distortion occurs with shift of the Raman towards higher values. Therefore, it is possible to assume that this displacement is due to a distortion generated by the depletion of sodium in the poled layer.

Figure IV-17 - Micro-Raman (HH polarizers) measurement correlated to SHG in the cross-section of the Na47.5Ta:Eu-900V sample: (A) poled and non-poled spectra normalized spectra at 685 cm^{-1} and (B) spatial evolution of the indicated ranges in A and the SHG profile.

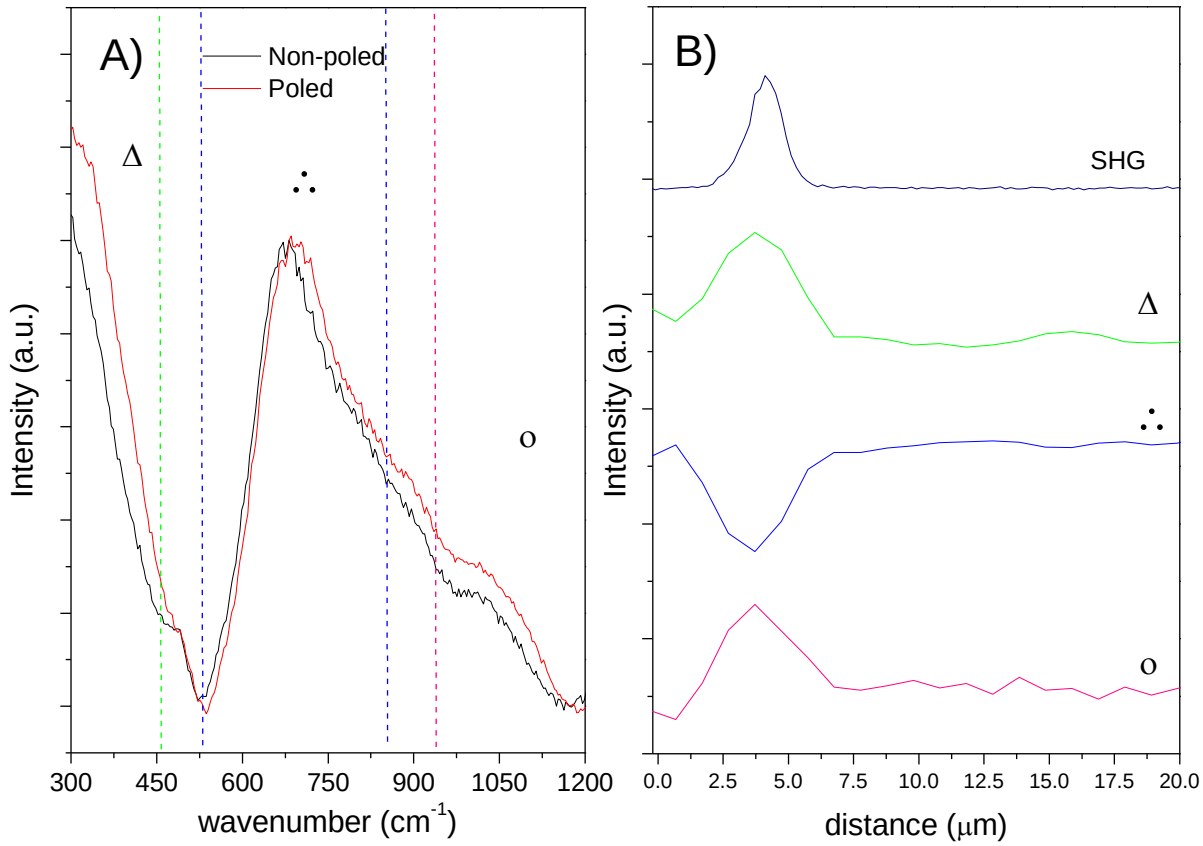

Reference: AUTHOR.
Note: Relative intensities in (B) were modified for better curve presentation.

To spatially correlate the structural change with SHG response, LabSpec5 program was used, in which the mapped curves were normalized[37], and a difference was made subtracting all spectra from one of the curves in the non-poled layer. The spatial evolution of the ranges delimited in the Raman presented in Figure IV-17**A** (green, blue and pink/symbols) after performing this subtraction is shown in Figure IV-17**B** along with the SHG profile; as well as the resulting mapping intensity after these subtraction is shown in Figure IV-18.

[37] The mapping corresponds to different Raman spectrum in different points in a pre-determined area (same as SHG). Figure IV- A shows, e.g., one of the spectra localized in the poled layer and one in the bulk of glass.

Figure IV-18 - Micro-Raman (HH polarizers) mapping after subtraction for the ranges shown in Figure IV-17 of Na47.5Ta:Eu-900V.

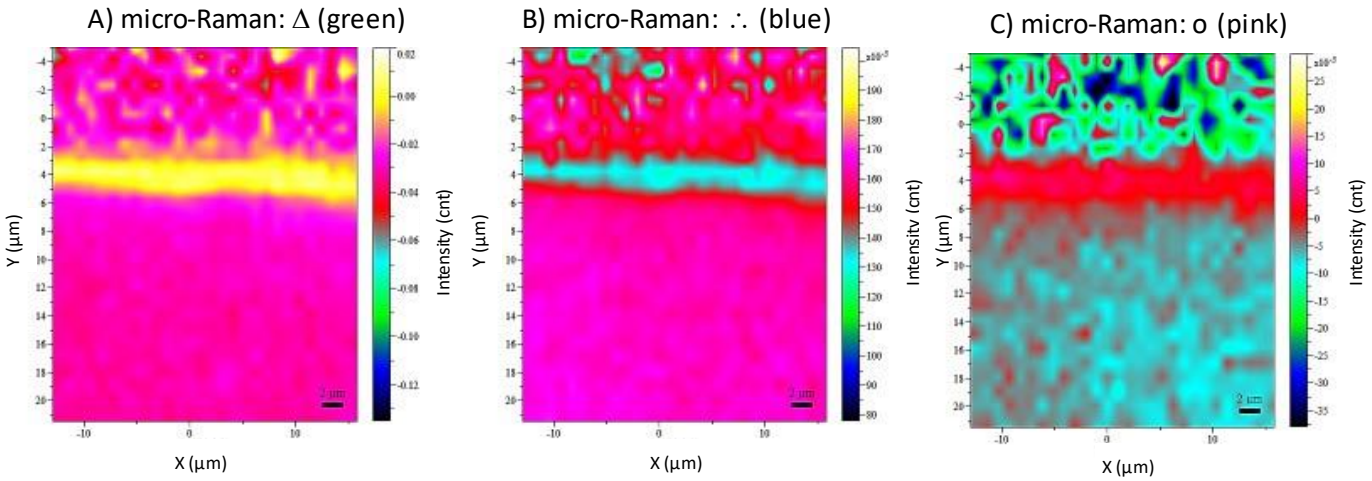

Reference: AUTHOR.

In the green/Δ range (<450 cm^{-1}) the intensity is higher in the poled layer compared to the non-poled one. This band is related to the deformation of the octahedron [TaO_6], therefore, this increase would be related to depletion of sodium, because in this way the vitreous network cannot maintain its organization to compensate the sodium charge, suffering this distortion. Furthermore, this rearrangement in the structure also changes the bonds of the octahedrons in the 3D network of the [TaO_6] clusters, as observed by the mapping of the blue/∴ range (540 to 830 cm^{-1}) that decreases in the poled layer in compared to non-poled one. Finally, the mapping of the pink/o range (>950 cm^{-1}) increases in the poled layer. In the niobium borophosphate glasses varying the percentage of sodium already mentioned (KARAM *et al.*, 2020a) it is indicated that this band can also be attributed to bonds in orthophosphate entities, and the less sodium in the glass. Therefore, it is suggested that the increase in intensity in this range could be related to the formation of these monomers i.e. phosphate tetrahedra only bonded to TaO_6 units.

In conclusion, through these mappings in cross-section, it is demonstrated that there is a spatial correlation between the area in which structural changes and the SHG are detected, which corresponds to the poled layer under the anode.

Since this glass was doped with europium (Na47.5Ta:Eu), micro-luminescence was also mapped using the 532 nm cw laser. As for Raman data, Figure IV-19A presents the micro-luminescence measurement of one of the spectra obtained in the poled layer and one of the spectra in the bulk (non-poled), both normalized in the transition $^5D_0 \rightarrow {}^7F_1$ (591 nm). The spatial evolution of the transitions after being normalized using the LabSpec5 software, and subtracted

from the spectrum of the non-poled layer is shown in Figure IV-19B along with the SHG profile, and the mappings related to these transitions in Figure IV-20.

Figure IV-19 - A) Micro-luminescence normalized spectra (λ_{exc} = 532 nm) of Na47.5Ta:Eu-900V glass of poled and non-poled areas and B) spatial evolution of the $[^5D_0] \rightarrow {}^7F_{0,1,2}$ transitions and SHG profile.

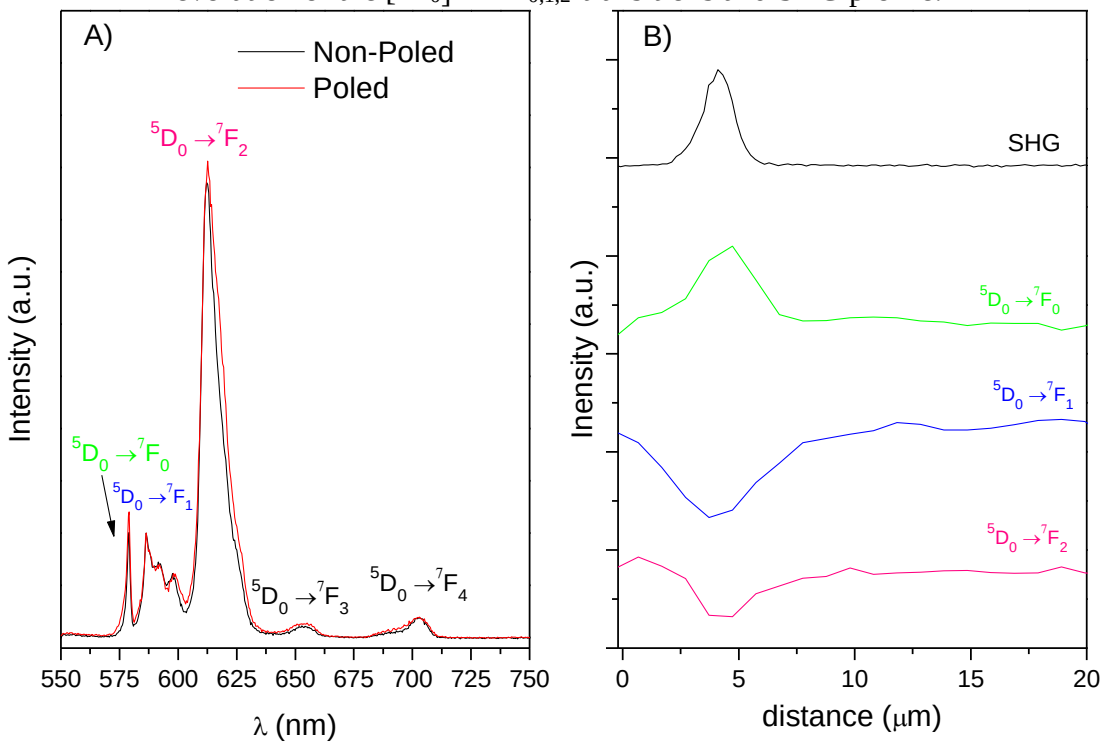

Reference: AUTHOR.
Note: Relative intensities in (B) were modified for better curve presentation.

Figure IV-20 - Micro-luminescence mapping related to $[^5D_0] \rightarrow {}^7F_{0,1,2}$ transitions of Na47.5Ta:Eu-900V after the subtraction from a non-poled spectrum.

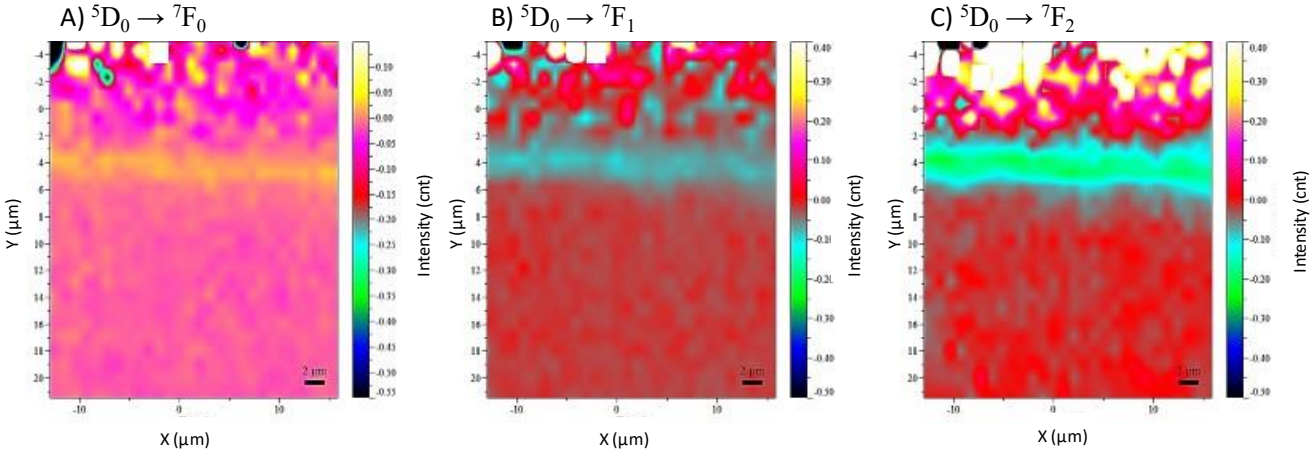

Reference: AUTHOR.

The asymmetry ratios - $^7F_2/^7F_1$ - in the spectra of Figure IV-19A are 4.57 for the poled area and 3.93 for the non-poled area. Thus, from these measurements, it can be inferred the structural rearrangement in the poled layer promotes a lower symmetry around Eu^{3+} ions. As seen in the luminescence measurements in Chapter III (FIGURE III-14), the greater the amount of tantalum in the glass, the greater the asymmetry ratio. In addition, through the mappings it is possible to verify that there is also a spatial correlation between changes in luminescence with the SHG active layer and Raman.

IV-3 EVALUATION OF THERMAL MICROPOLING OF SODIUM TANTALUM PHOSPHATE GLASSES

Regarding Thermal Micropoling, all successfully poled samples presented the imprinted patterns, pointing out that micropoling is also suitable for microstructuring of sodium tantalum phosphate glasses using our experimental conditions. Figures IV-21-23 present optical micrographs (20x objective) of the patterns (squares, circles and lines) imprinted on Na45Ta-600V, Na45Ta:Eu-600V and Na50Ta-700V samples.

Figure IV-21 - Micrographs of Na45Ta-600V sample: (a) 40µm squares (20x) and (b) lines (20x).

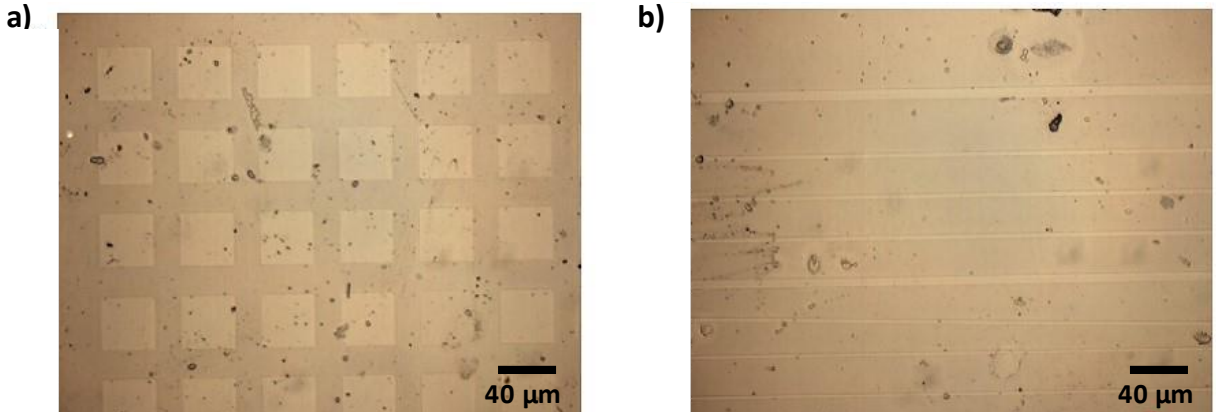

Reference: AUTHOR.

Figure IV-22 - Micrographs of Na45Ta:Eu-600V sample: (a) 30µm squares (20x) and (b) 40µm circles (20x).

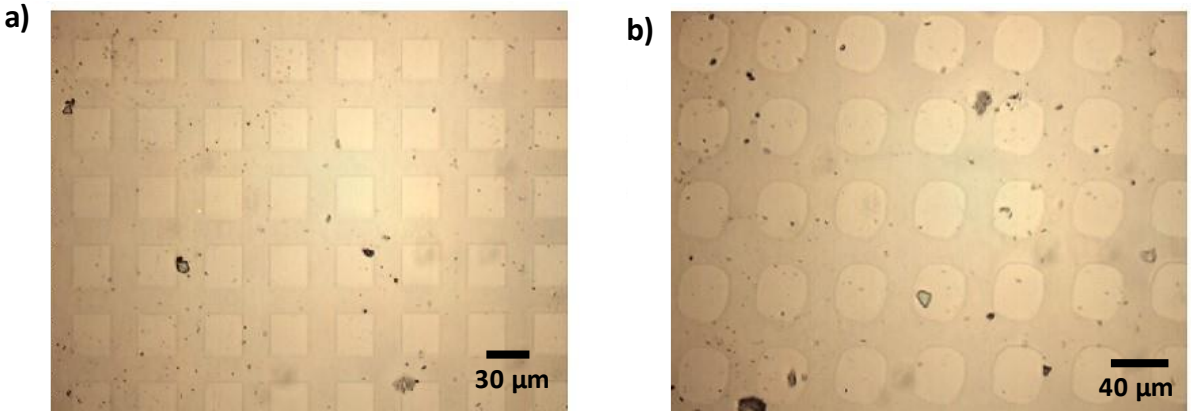

Reference: AUTHOR.

Figure IV-23 - Micrographs of Na50Ta-700V sample: (a) lines (20x) and (b) 40µm squares (20x).

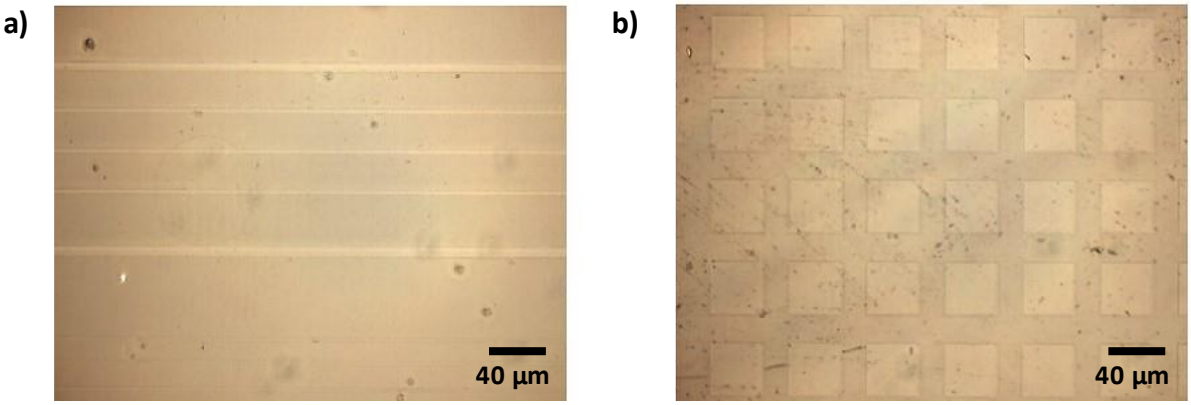

Reference: AUTHOR.

Figure IV-24 presents optical micrographs of some of the patterns imprinted in the Na47.5Ta sample poled at 700V; Figures IV-25/26 show optical micrographs of the patterns imprinted for the Na47.5Ta:Eu sample poled at 700V with a 20x and 50x objective, respectively. And Figures IV-27-30 show the optical micrographs of the patterns imprinted for the same sample (Na47.5Ta:Eu) poled at 900V, with 20x, 50x and 100x objectives. These samples are presented in more detail, because, as previously stated, the main studies were performed on these samples.

Figure IV-24 - Micrographs of Na47.5Ta-700V sample: (a) 30µm squares (20x) and (b) lines (20x).

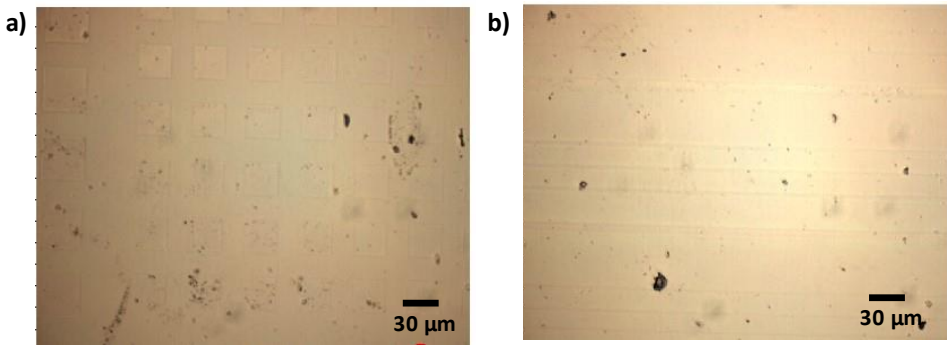

Reference: AUTHOR.

Figure IV-25 - Micrographs of Na47.5Ta:Eu-700V sample: (a) 30µm circles (20x) and (b) lines (20x).

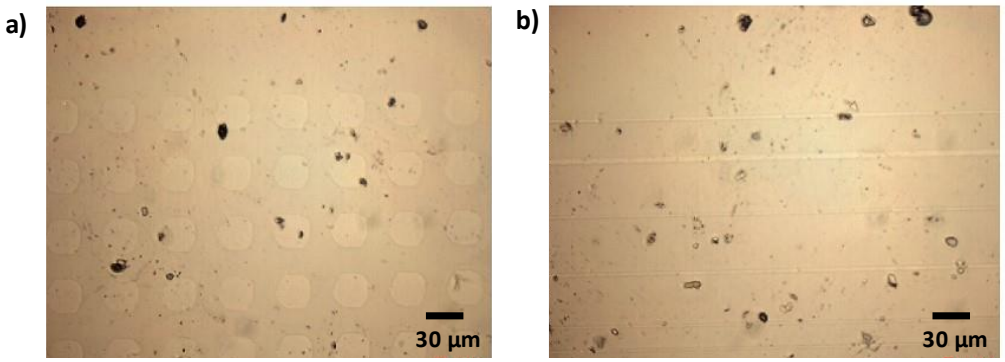

Reference: AUTHOR.

Figure IV-26 - Micrographs of Na47.5Ta:Eu-700V sample: (a) 30µm squares (50x), (b) lines (50x), (c) 40µm circles (50x) and (d) 30µm circles (50x).

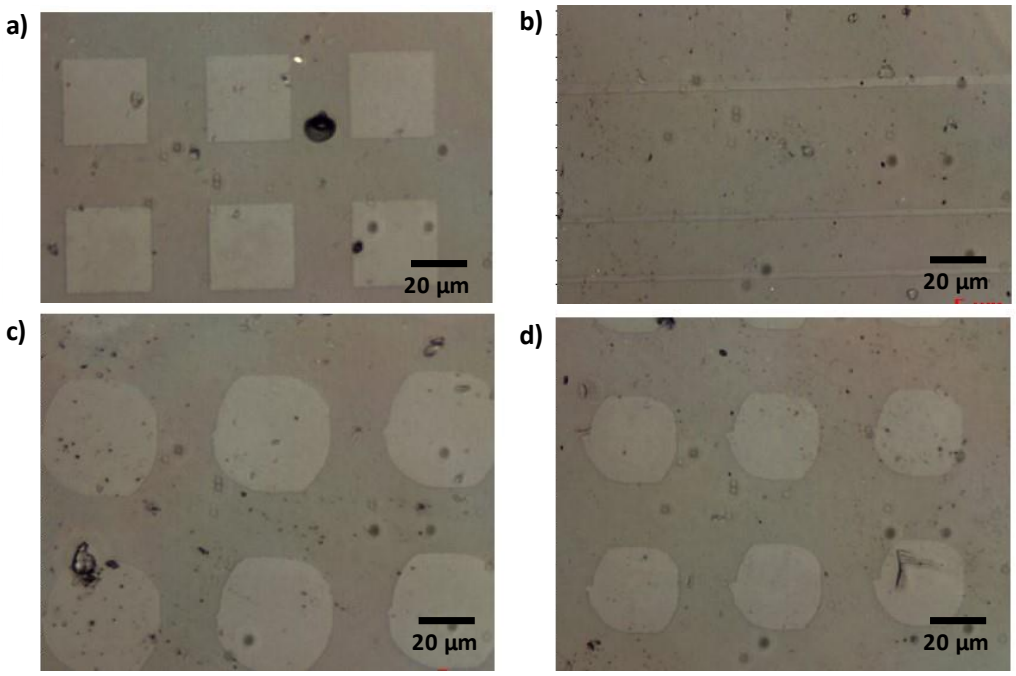

Reference: AUTHOR.

Figure IV-27 - Micrographs of Na47.5Ta:Eu-900V sample: (a) 40µm squares (20x), (b) 30µm squares (20x), (c) 40µm circles (20x) and (d) 30 and 40µm circles (20x).

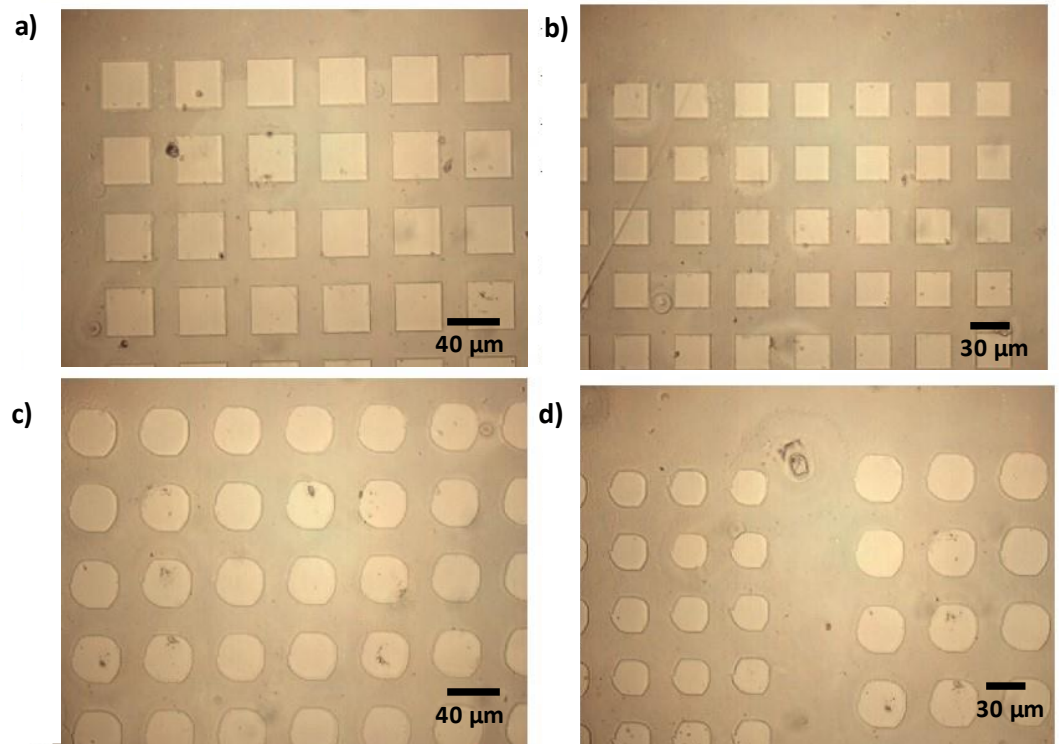

Reference: AUTHOR.

Figure IV-28 - Micrographs of Na47.5Ta:Eu-900V sample: (a) 40µm squares (50x), (b) 30µm squares (50x), (c) 40µm circles (50x) and (d) 30 and 40µm circles (50x).

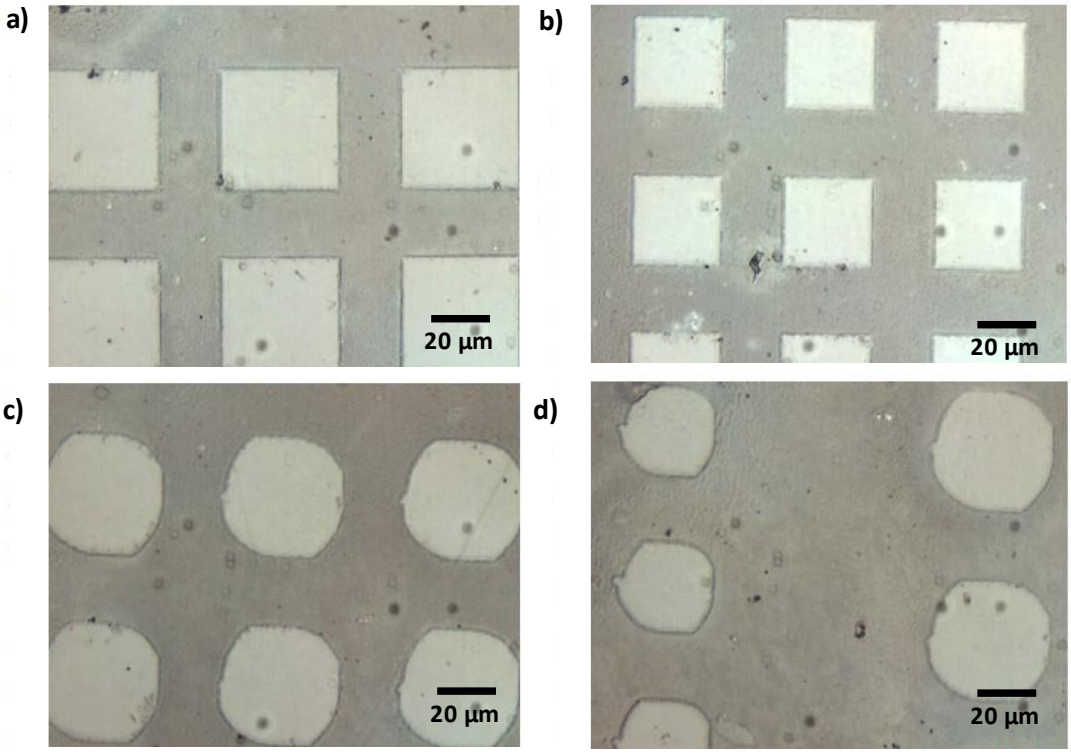

Reference: AUTHOR.

Figure IV-29 - Micrographs of Na47.5Ta:Eu-900V sample: (a) 40µm squares (100x), (b) 30µm squares (100x), (c) 40µm circles (100x) and (d) 30 µm circles (100x).

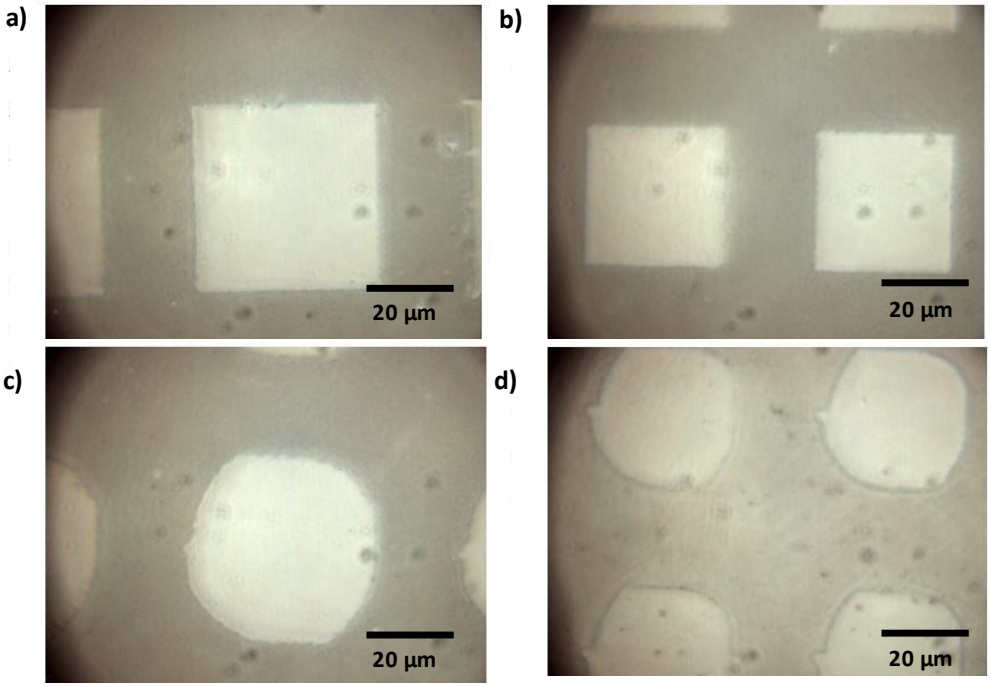

Reference: AUTHOR.

Figure IV-30 - Micrographs of Na47.5Ta:Eu-900V sample of lines structures: (a) 20x, (b) 50x and (c) 100x.

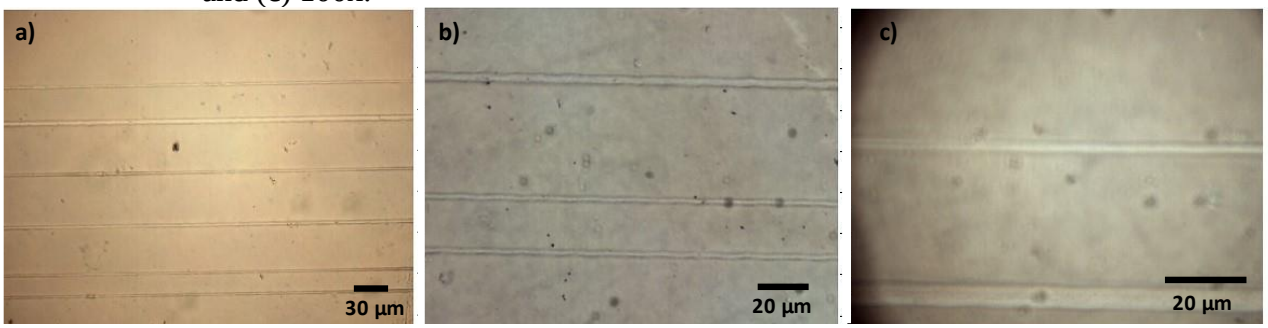

Reference: AUTHOR.

Micro-Raman mapping using a 532 nm cw laser using the assembly presented in Chapter II-6 was performed on the surface of Na47.5Ta:Eu-900V sample on the anode side, as shown in Figure IV-31A. The measurement was made in the 30 µm square located on the edge (next to the circles) - Figure IV-31B (remembering that as the ITO was removed, the area within the square corresponds to the unpoled area where the charge migration process is not expected to occur).

Figure IV-31 - A) Diagram illustrating the geometry of the micro-Raman analysis on the microstructure - surface on the anode side and (B) microstructure on which the measurement was taken - square 30 µm from the edge.

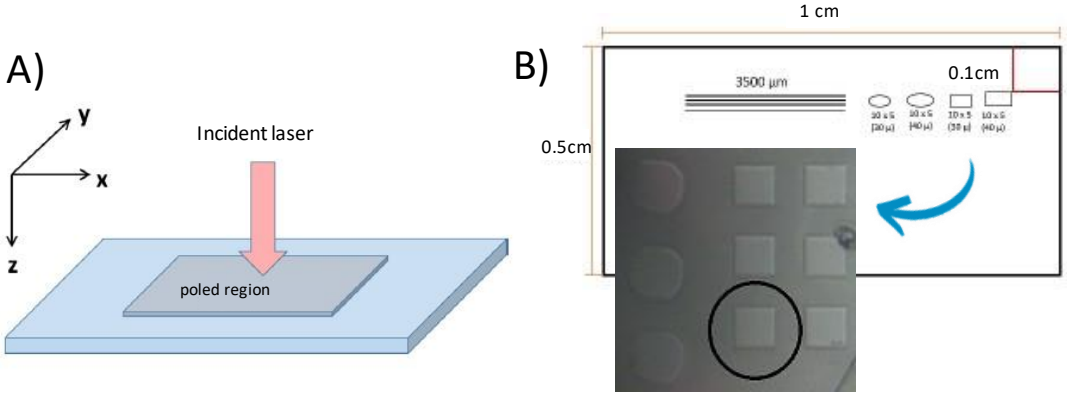

Reference: A) Translated from KARAM (2020, p.102) and B) AUTHOR.

Figure IV-32A shows one of the spectra (HH polarizers) in the poled area (outside the square) and one of the spectra in the non-poled area (inside the square). As in the cross-section, Raman signal is stronger in the poled area than in the non-poled one. The spatial evolution of the delimited ranges (blue and green/symbols) after performing the subtraction by the spectrum of the non-poled area (same procedure made in the cross-section) is shown in Figure IV-32B/C - in the vertical and horizontal directions of the square; as well as the mapping after the subtraction is presented in Figure IV-33. As observed by these results, it appears that these signal intensities are well spatially correlated with the imprinted patterns.

Figure IV-32 - Micro-Raman measurement (HH polarizers) in a microstructure of Na47.5Ta:Eu-900V sample: (A) spectrum of the poled and non-poled area, (B) spatial evolution of the wavenumber ranges indicated (green and blue) on the x-axis and (C) on the y-axis.

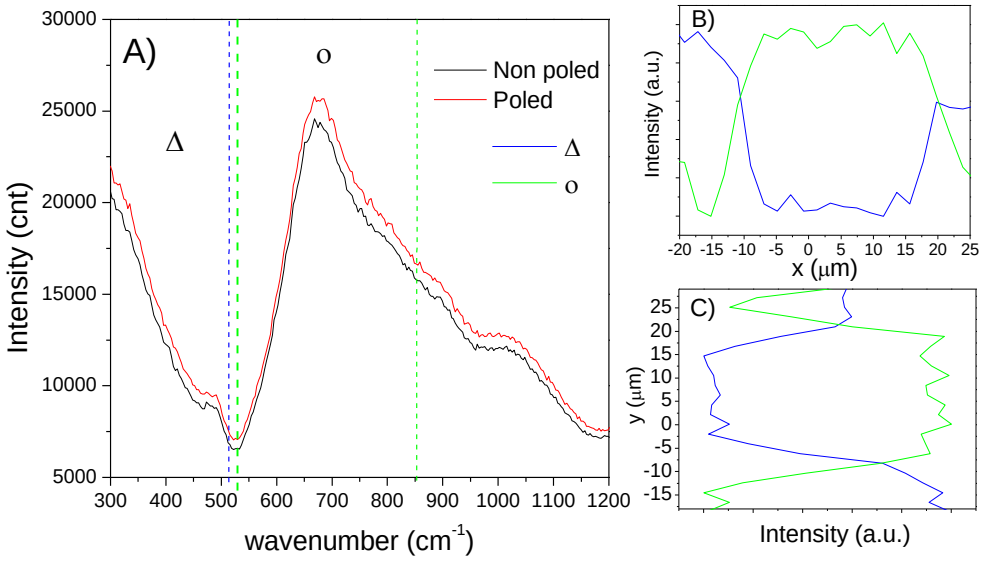

Reference: AUTHOR.

Figure IV-33 - Micro-Raman (HH polarizers) mapping for the ranges delimited in Figure IV-32.

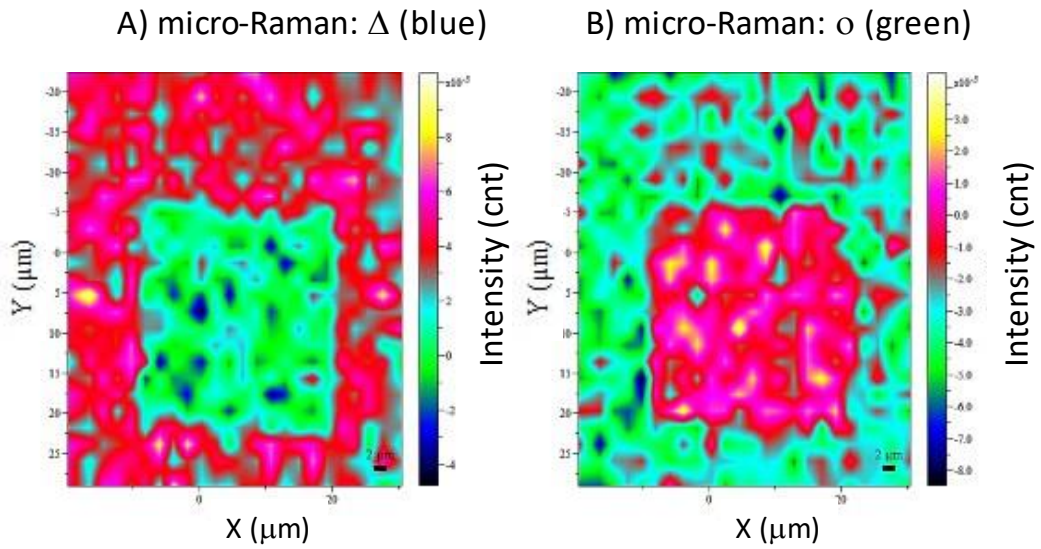

Reference: AUTHOR.

In order to correlate structural changes with NLO properties in a micrometer level due to the poling, micro-SHG microscopies were performed on the surface of the same micro-poled sample (Na47.5Ta:Eu-900V) using the modified micro-Raman spectrometer HR800 (Horiba/Jobin Yvon) already presented in Chapter II-6 with a 1064 nm ps laser as the excitation source, a 100x objective with a numerical aperture of 0.9. Linear polarizations XX or YY were used (the first letter represents the incident polarization and the second the analyzed polarization). As shown in Figure IV-34 for squares and circles, regardless of the polarization, the second harmonic response is spatially localized at the boundaries between the poled and non-poled areas. These SHG data support the ability of micropoling to spatially enhance the second-order nonlinear response of the material depending on the electrode pattern.

The SHG signals in XX (Figure IV-34 A-D) and YY (Figure IV-34 E-H) show that they depend strongly on the polarization of the incident light. This spatial distinction of the signal implies that the $\chi^{(2)}$ terms tested by the two polarization states are different. Table IV-3 presents the different terms of the tensor $\chi^{(2)}$ probed by a linear-X and linear-Y polarization, analyzed according to X and Y and denoted (XX) and (YY) respectively (EL-DIB, 2023).

Figure IV-34 - Micro-SHG of the microstructures imprinted on the glass surface Na47.5Ta:Eu: (A-D) XX polarization and (E-H) YY polarization.

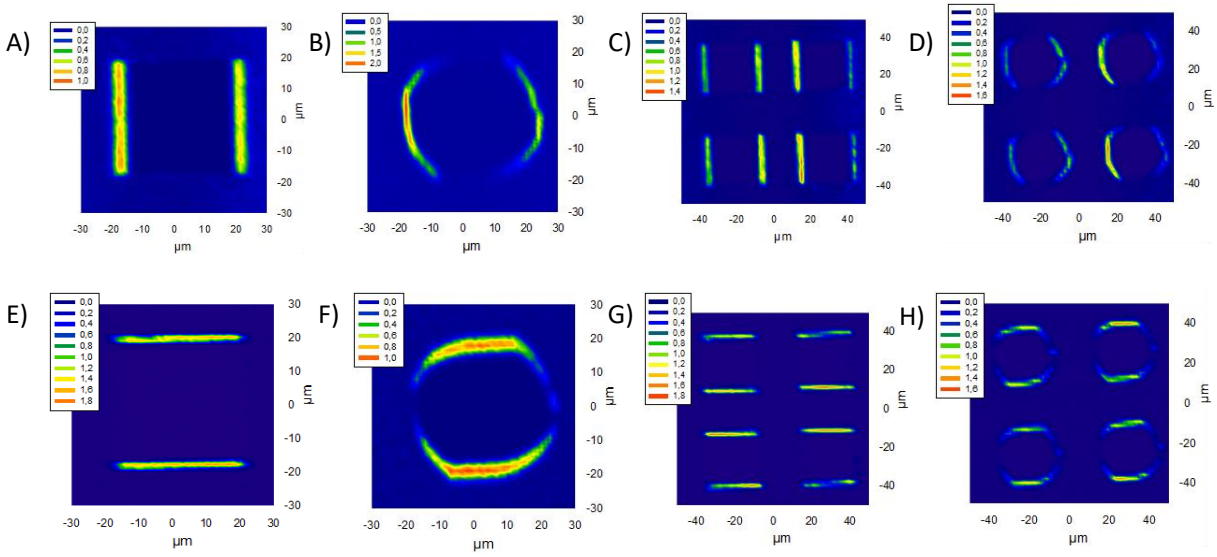

Reference: AUTHOR.

Table IV-3 - Terms of the second order nonlinear susceptibility tensor probed by the different incident polarizations XX and YY.

	$\chi^{(2)}$ **probed terms**	
Polarization	**on the plan**	**out of plan**
XX	d_{11}, d_{12}	d_{31}
YY	d_{22}, d_{21}	d_{31}

Reference: EL-DIB (2023, p.128).

Predominant edge effects at the interface between the poled/non-poled area occur and may be related to an enhancement of the induced field located at this interface. This high field intensity must be related to the directional control of the current during the poling processing which governs the direction of the charge gradients and subsequently the geometry of the induced static fields. Thus, the induced static electric field is not only out of the plane (case of homogeneous poling) but also in the plane (FIGURE IV-35).

Figure IV-35 - Representative diagram of the static electric field induced after poling treatment.

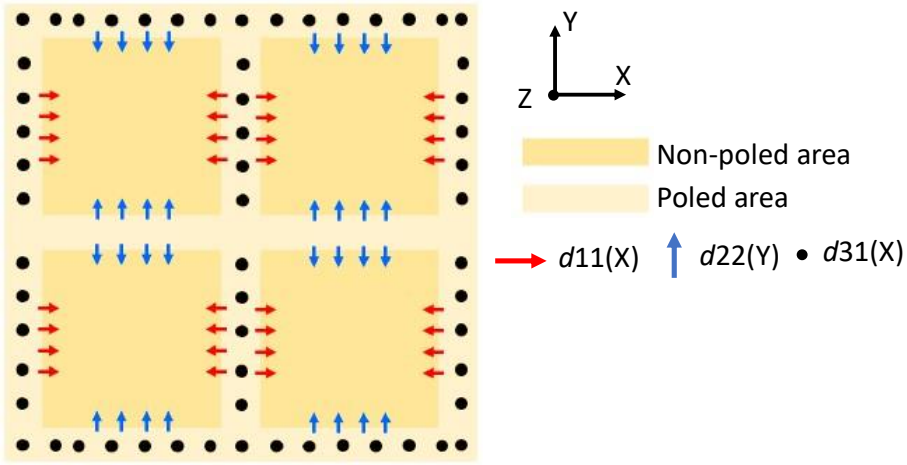

Reference: Modified from EL-DIB (2023).

Atomic Force Microscopy (AFM) measurements were performed to probe topology variations of the glass after Thermal Micropoling. The measurements were made at the ISM with Bruker Dimension Icon equipment, in PeakForce mode. For comparison, the measurement was made in a 30µm square of two samples Na47.5Ta:Eu-700V and Na47.5Ta:Eu-900V - Figure IV-36; and a 30µm circle from both samples - Figure IV-37.

Figure IV-36 - AFM measurement on the microstructures - 30µm square of the Na47.5Ta:Eu sample after Thermal Micropoling: A) 700V, B) 900V and C) topology profile recorded in both images.

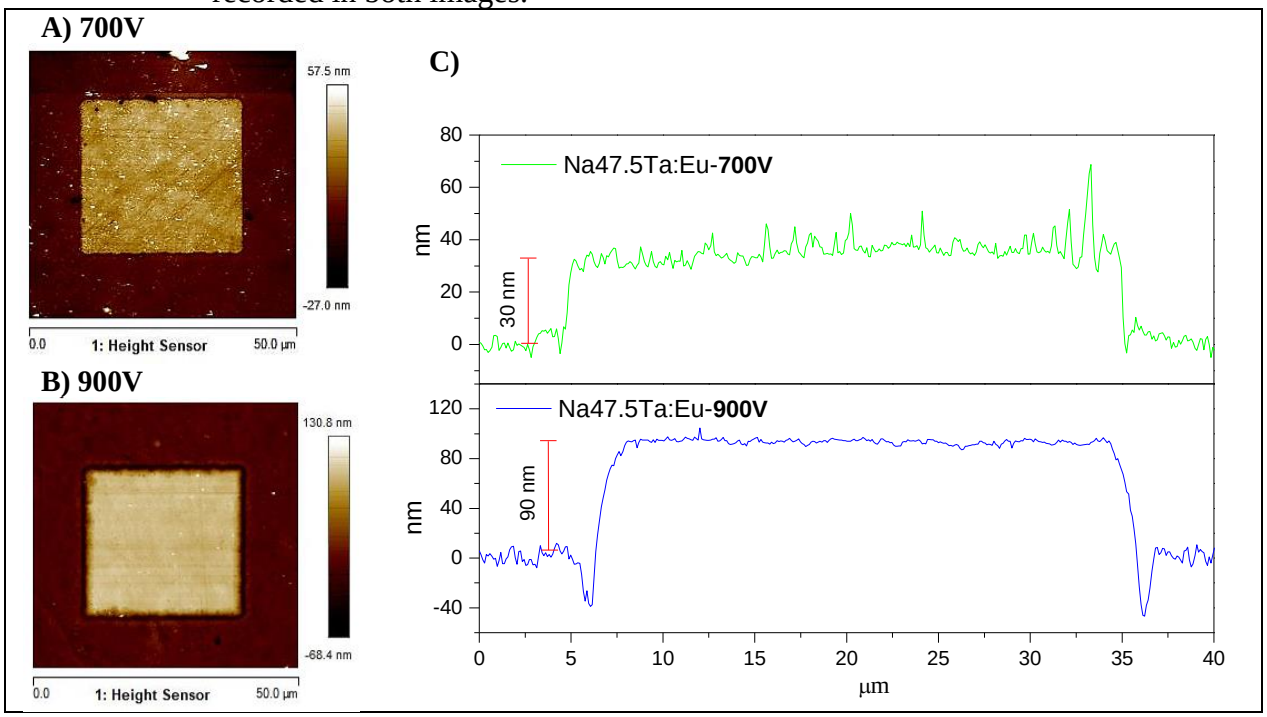

Reference: AUTHOR.

Figure IV-37 - AFM measurement on the microstructures - 30µm circle of Na47.5Ta:Eu sample after Thermal Micropoling: A) 700V, B) 900V and C) topology profile recorded in both images.

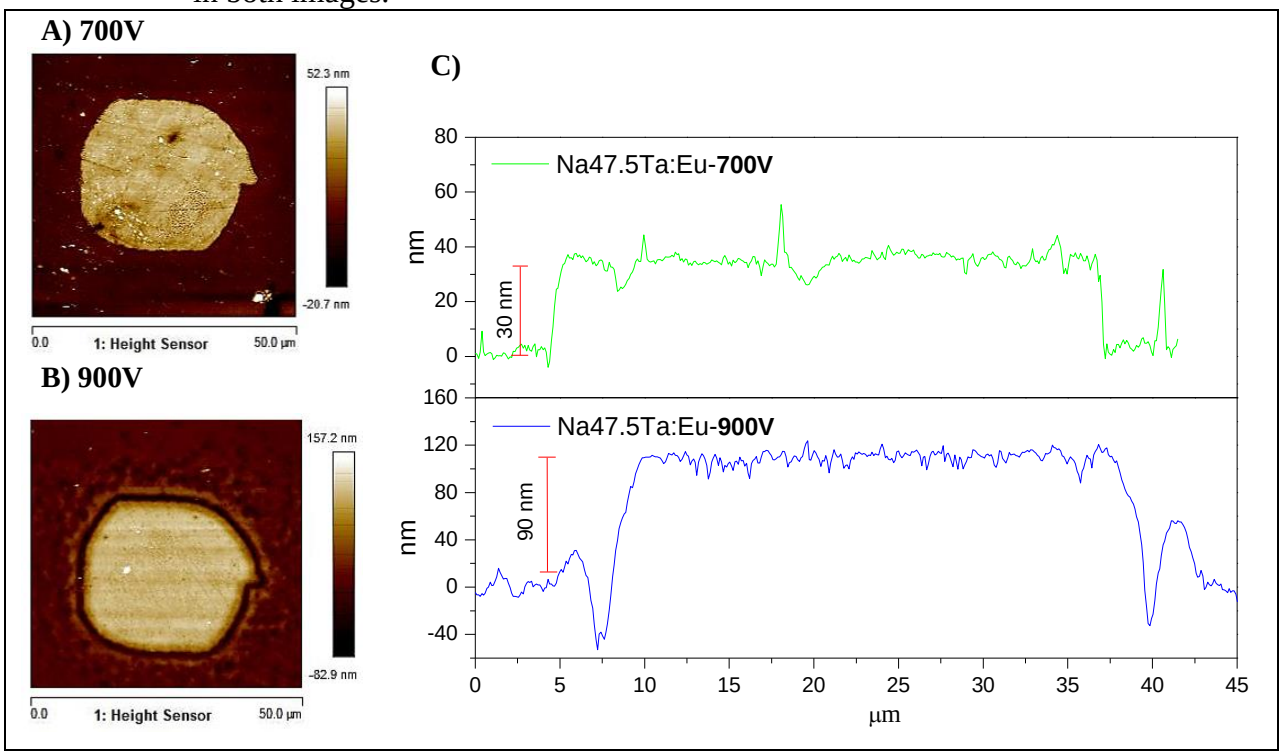

Reference: AUTHOR.

Through the measurements, it is possible to verify that the Thermal Micropoling induced a change in the topology of the glasses, which presented a surface contraction of the poled area of around 30nm for the sample poled with 700V; and 90 nm for the sample poled with 900V. Additionally, as for micro-SHG data, a strong edge effect is denoted, especially Na47.5Ta:Eu-900V sample. According to Poirier *et al.* (2022, p.10311), "thermal micropoling promotes more complex charge density distributions and strong edge effects between the poled and non-poled surfaces".

Additionally, since Thermal Micropoling promotes large compositional variations between poled and non-poled areas, linear optical properties should also be impacted by the treatment as already observed in other glassy systems, e.g., by Karam *et al.* (2020b), Lepicard *et al.* (2018) and Poirier *et al.* (2022). So, the refractive index changes along the imprinted microstructures were accessed by the phase contrast technique that was described in Chapter II-8, in which a wave front sensor SID4Bio by Phasics Inc placed inside an optical microscope was used to record the phase image of the microstructures. This measurement was performed in a transmission mode under white light illumination. The results presented in Figure IV-38 show a clear optical contrast between the poled area and unpoled microstructures on the glass surface. Since the optical path difference (OPD) is directly related to (i) the topology changes,

(ii) the poled layer thickness and (iii) refractive index variations, one could conclude that the thermal micropoling also induces a refractive index contrast whose intensity is dependent of the glass composition and experimental poling conditions.

Figure IV-38 - Phase contrast images of micro-poled sample Na47.5Ta:Eu-900V.

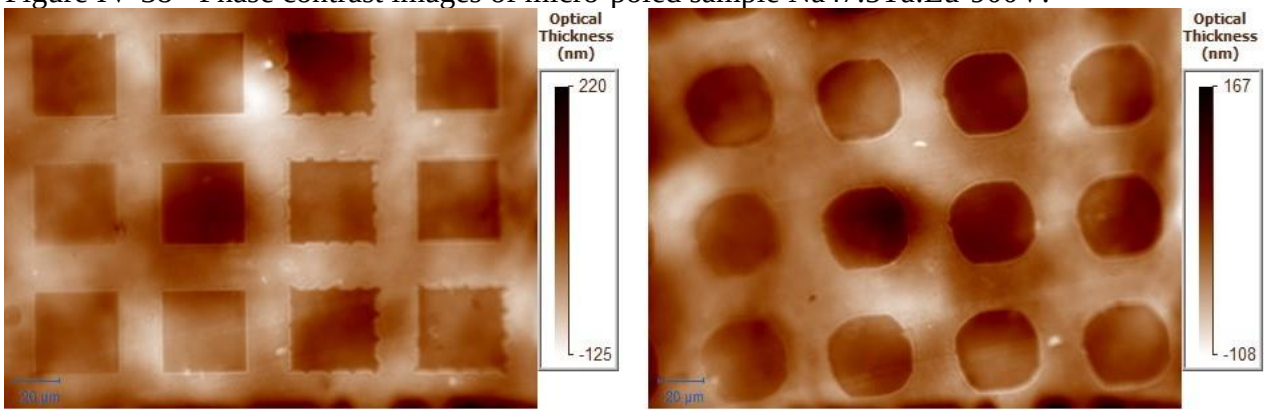

Reference: AUTHOR.

The quantitative refractive index variations are under determination; however, one could note that the background is not very flat, which normally occur in bulk samples when index inhomogeneities within the volume are not “reproducible” spatially.

CONCLUSIONS

Glasses in the $NaPO_3$-Ta_2O_5 system, undoped and doped with europium, were submitted to Thermal Poling and Micropoling experiments. Glasses with 40 mol% of Ta_2O_5 were hardly thermally poled; since the formation of electric sparks occurred during the process; resulting in inconsistent results, including material breakage. On the other hand, for higher tantalum oxide contents (45 to 50 mol%), thermal poling treatments could be successfully carried out using relatively low voltages (< 1000V).

Still, it was possible to evaluate the generation of the second harmonic in the glasses after Poling using Maker Fringe measurements; as detected in all poled glasses. In this way, the Poling promoted the breaking of glass centrosymmetry, allowing these materials to present non-linear optical properties related to $\chi^{(2)}$. A certain homogeneity was also observed due to the symmetry of the measurements. Maker Fringes results indicated that SHG is due to the EFISH model, which is expected for glasses. $\chi^{(2)}$ was obtained by data simulations with values of 1 pm/V for Na50Ta-700V sample and 0.72 pm/V for Na47.5Ta:Eu-900V. By measuring the micro-SHG of the europium-doped sample containing 47.5 mol% of Ta_2O_5 and poled at 900V, it was verified that the SHG is active in the layer under the anode (as expected) due to the migration of sodium ions beneath this region, with a thickness of approximately 2 μm as corroborated by ToF-SIMS measurements. This measurement in the cross-section was correlated with the micro-Raman and micro-luminescence mapping that are different from the bulk of the material.

Concerning Micropoling, the use of the microstructured electrode allowed an imprinting on all poled glasses. Micro-Raman measurement distinguishes between the poled and non-poled area corresponding to the area that ITO was removed from the electrode. An edge effect was observed in the micro-poling of micro-SHG measurement, in which the intensity signal is influenced by the polarization state. A change in the topology was observed by the AFM, being around 90 nm for Na47.5Ta:Eu-900V, as also an edge effect. And an index variation was also possible to induce by poling on the tantalum phosphate glasses. Thus, it is concluded that the use of Thermal Micropoling is promising for controlling optical properties in the studied glasses.

REFERENCES

EL-DIB, G. **Fibres optiques en verre de borophosphate de niobium pour des applications en optique non linéaire** = Niobium borophosphate glass optical fibers for applications in nonlinear optics. 2023. 182p. Thesis (PhD in Ceramic Materials and Surface Treatment) – Université de Limoges, France, 2023.

KARAM, L. **Structuration multi-échelle et multifonctionnelle de nouveaux matériaux vitreux pour la photonique intégrée** = Multiscale and multifunctional structuring of new glassy materials for integrated photonics. 2020. 275p. Thesis (PhD in Chemistry Science) - Université de Bordeaux, Bordeaux, France, 2020.

KARAM, L. *et al.* The effect of the sodium content on the structure and the optical properties of thermally poled sodium and niobium borophosphate glasses. **Journal of Applied Physics,** [S.l.], v.128, 043106, 2020a.

KARAM, L. *et al.* Electrically micro-polarized amorphous sodo-niobate film competing with crystalline lithium niobate second-order optical response. **Advanced Optical Materials**, Weinheim, v.08, 2000202, 2020b.

LEPICARD, A. **Design of surface chemical reactivity and optical properties in glasses.** 2016. 293p. Thesis (PhD in Chemistry) - Université de Bordeaux, Bordeaux (France), 2016.

LEPICARD, A. *et al.* Long-lived monolithic micro-optics for multispectral GRIN applications. **Scientific Reports**, [S.l.], v.08, 7388, 2018.

MALAKHO, A. *et al.* Crystallization and second harmonic generation in thermally poled niobium borophosphate glasses. **Journal of Solid-State Chemistry,** [S.l.], v.178, p.1888-1897, 2005.

POIRIER, G.Y. *et al.* Second Harmonic Generation in sodium tantalum germanate glasses by thermal poling. **Journal of Physics Chemistry C,** [S.l.], v.123, p.26528-26535, 2019.

POIRIER, G.Y. *et al.* Microscaled design of linear and non-linear optical properties in tantalum germanate glasses by thermal poling. **Journal of Materials Chemistry C**, [S.l.], v.10, p.10310-10319, 2022.

RODRIGUEZ, V.; SOURISSEAU, C. General Maker-fringe ellipsometric analyzes in multilayer nonlinear and linear anisotropic optical media. **Journal of the Optical Society of America B**, USA, v.19, p.2650-2664, 2002.

CHAPTER V - PREPARATION AND CHARACTERIZATION OF EUROPIUM-DOPED TANTALUM PHOSPHATE GLASS-CERAMICS

CHAPTER V - PREPARATION AND CHARACTERIZATION OF EUROPIUM-DOPED TANTALUM PHOSPHATE GLASS-CERAMICS

This chapter presents the preparation and characterization of glass-ceramics obtained by the traditional method of heat treatment from pristine glass with molar composition $99.83[52.5NaPO_3\text{-}47.5Ta_2O_5]\text{-}0.17Eu_2O_3$ studied in Chapter III. For this purpose, a crystallization study was performed with thermal treatments in one or two steps, varying the treatment time. The material was characterized by: DSC, XRD, Photoluminescence, Uv-Vis transparency and Refractive index.

V-1 CRYSTALLIZATION STUDY FOR GLASS-CERAMICS PREPARATION

For the crystallization study performed to prepare phosphate glass-ceramics with high tantalum oxide contents, the glass composition **$99.83[52.5NaPO_3\text{-}47.5Ta_2O_5]\text{-}0.17Eu_2O_3$** (Na47.5Ta:Eu) described in Chapter III was chosen. This composition was chosen for its high tantalum oxide content together with europium doping without devitrification tendencies during synthesis together with satisfactory results obtained with Thermal Poling experiments (as disposed in Chapter IV).

The traditional method of Heat Treatment (HT) with controlled crystallization temperatures and times was employed, using a Carbolite tube furnace located at ICMCB. At first, glass-ceramic (GC) was prepared following two heating steps: 939 °C / 30 minutes + 964 °C / Δtime (T_g and T_{x1} for this glass were 927°C and 994°C, respectively - Table III-2). In addition, to verify the complete crystallization of the sample, HT was performed at 1000°C/3h, i.e., above T_{x1}, resulting in a completely opaque sample. The times of the second step varied for 15 min, 30 min, 1h and 1h30, in which the appearance of the samples can be verified in Figure V-1.

Figure V-1 - Glass-ceramics obtained from Na47.5Ta:Eu glass with HT in two steps varying the time.

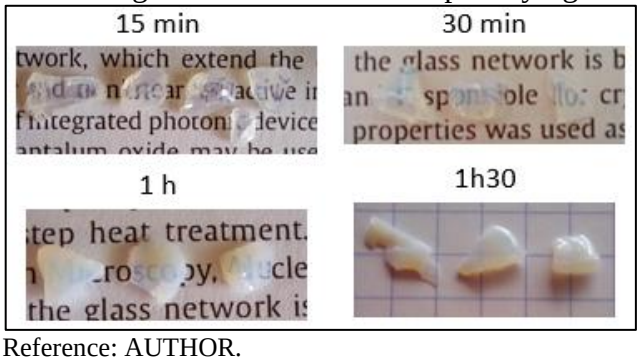

Reference: AUTHOR.

In a second set, a HT using only one step was tested, that is, without the previous described step (939 °C/ 30 minutes), but only at 964 °C/ Δtime (t = 30min, 1h, 1h30).

V-2 THERMAL ANALYSIS AND X-RAY DIFFRACTION OF GLASS-CERAMICS

Both XRD and DSC were performed to verify the crystallization of the samples, and the analysis parameters correspond to those already described in Chapter III-2, for the pristine glass. Regarding the glass-ceramics obtained with two steps, Figure V-2 shows the diffractograms and Figure V-3A the corresponding DSC curves.

Figure V-2 - Diffractograms of glass-ceramics obtained with two heating steps varying the time and the completely crystallized glass-ceramic (1000°C/3h).

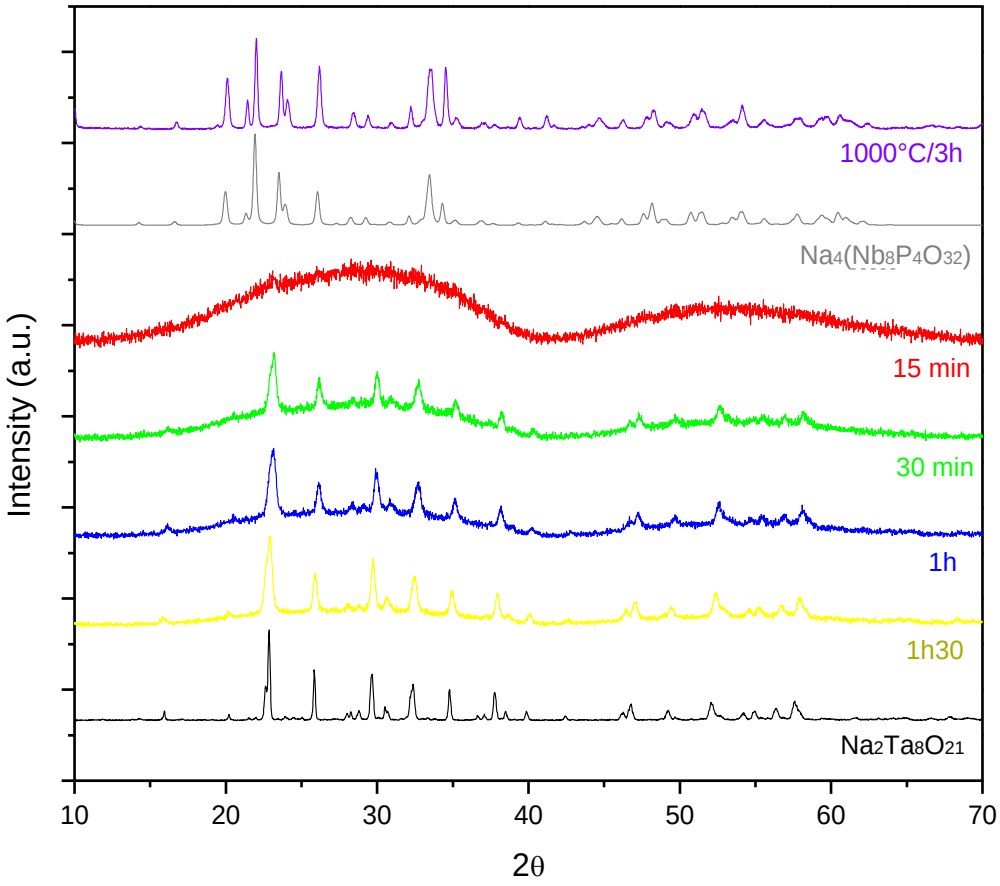

Reference: AUTHOR.

Analyzing the diffractograms, it is verified that the Na47.5Ta:Eu glass crystallized at 1000°C/3h, the peaks are very similar to those of the crystalline phase PDF85-2478 - $Na_4(Nb_8P_4O_{32})$. Despite not having niobium in the composition of the material, due to the similarity between Nb and Ta, it is considered that the corresponding crystalline phase is the

one in which tantalum replaces niobium i.e. $Na_4(Ta_8P_4O_{32})$, but not yet catalogued in a data base. This phase has also been reported in the tantalum phosphate glass-ceramic studied by Marcondes *et al.* (2019). It is also noticed that this phase corresponds to the glass compounds ($NaPO_3$-Ta_2O_5) multiplied by 4, indicating that is a phase that is crystallized from the whole glass matrix. For treatments performed below T_{x1} in two heating steps, the identified crystalline phase is $Na_2Ta_8O_{21}$, which is a perovskite bronze-like crystalline phase (CUNHA *et al.*, 2021; MARCONDES *et al.*, 2019). Also, as the research group already knows, this last one corresponds to lower temperature exothermic peak that appears in the DSC curves of the pristine glass and, as it was the objective, it was the only crystalline phase obtained in these glass-ceramics. Also, this phase, as briefly described in Chapter I-3.1, according to Vigouroux *et al.* (2011), within the family of NLO crystals, there is great interest, especially niobates and tantalates with cations in octahedral oxygen sites in perovskite structures. Another interesting point is that this is a phase, according to Marcondes *et al.* (2019), that crystallizes homogeneously in the volume of the glass, and not just from the surface.

Figure V-3 - DSC curves of glass-ceramics varying HT times: (A) Two steps (and GC prepared using 1000°C/3h) and (B) One step.

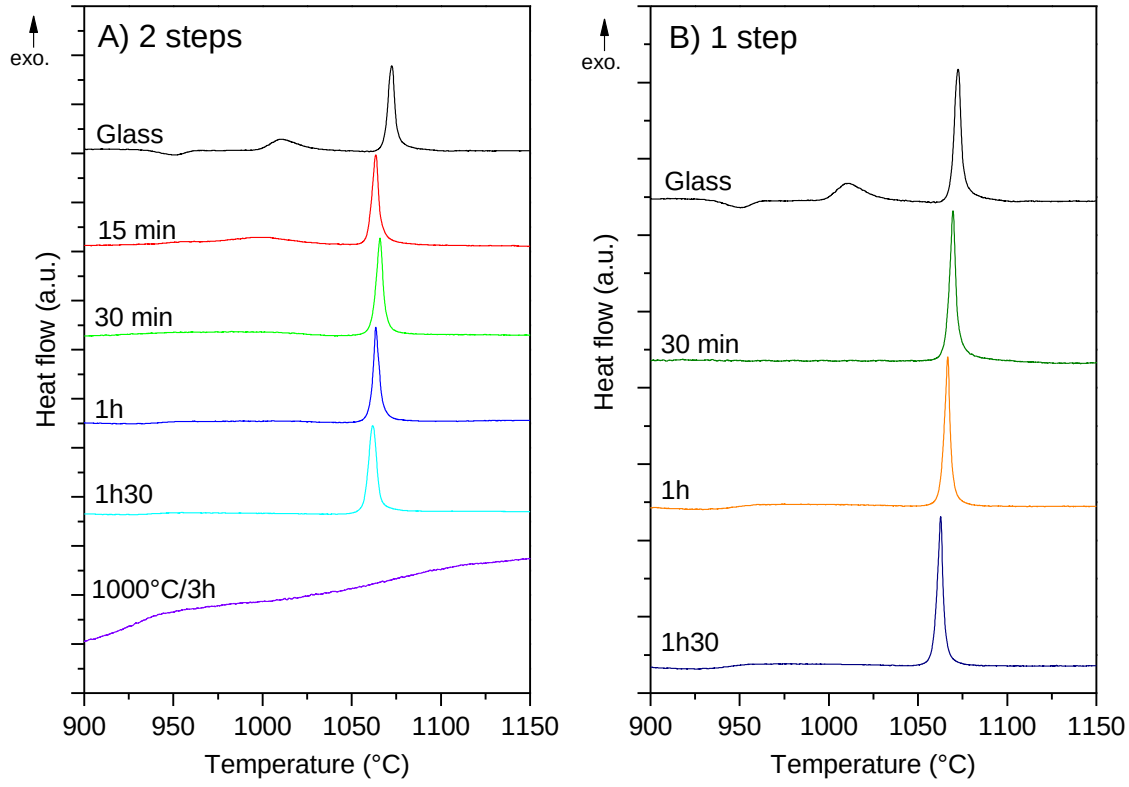

Reference: AUTHOR.

The behavior of tantalum phosphate glasses is the same as niobium phosphate glasses, as studied by Malakho *et al.* (2005), Lepicard (2016), Karam (2020), Cassani (2022), in which phase separation (i.e., of the crystalline phases that appear as the exothermic peaks in the DSC) occurs for higher transition metal contents, which in this case is tantalum. So, the $Na_2Ta_8O_{21}$ crystalline phase corresponds to the first low temperature crystallization peak of the glass that appears in the DSC curve and the second DSC peak corresponding to another crystalline phase, $Na_4(Ta_8P_4O_{32})$ - related with crystallization of the remaining glassy phase. Comparing the XRD curves with those of the DSC, it is verified that as the heat treatment time increases, the first peak in the DSC decreases while the peaks in the diffractograms become sharper and more intense.

Regarding the glass-ceramics obtained with one heating step, Figure V-3B presents the DSC curves and Figure V-4 the diffractograms. The same behavior of the previous GC is observed, in which the peaks in the diffractograms are more defined for longer HT times and the first crystallization peak decreases and vanishes.

Figure V-4 - Diffractograms of glass-ceramics varying heat treatment times in just one heating step.

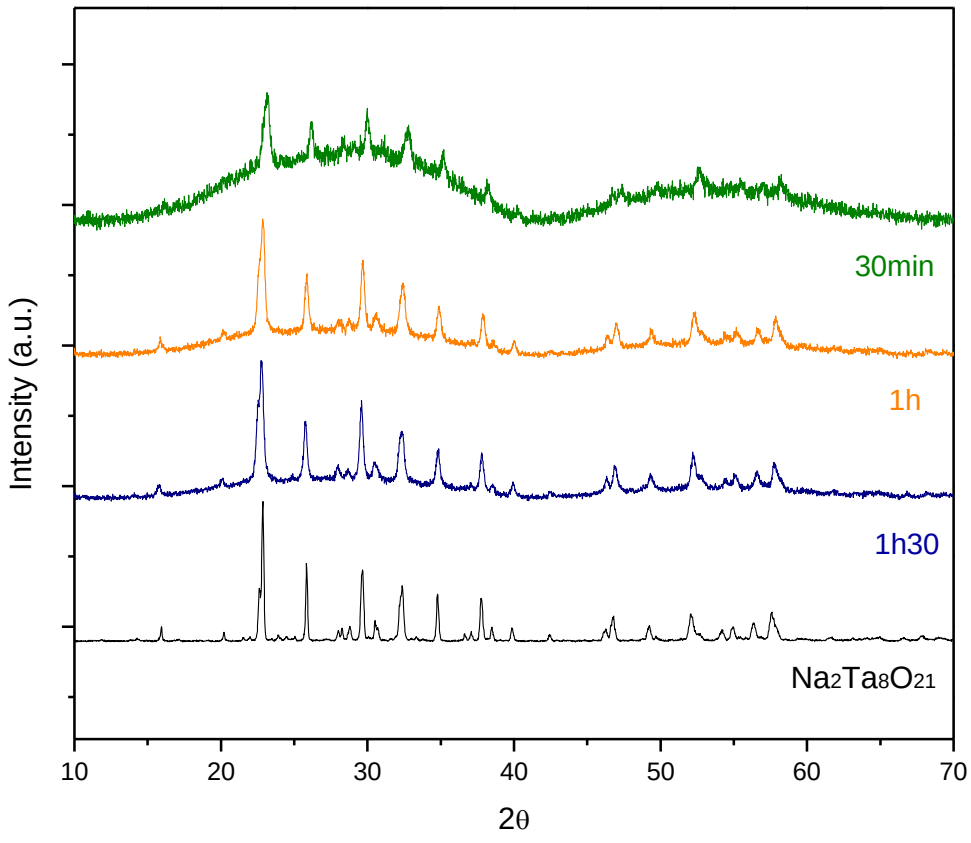

Reference: AUTHOR.

The degree of crystallinity (%) was estimated for these glass-ceramics through diffractograms, in which the respective areas of diffraction peaks and diffraction halo were integrated - the values are shown in Table V-1. The sample that was considered "completely crystallized", that is, the one at 1000°C/3h, showed a high degree of crystallinity, around 80%. In relation to the other samples, there is an increase in the degree of crystallinity with time, reaching approximately 45% after 1h30. When comparing treatments in 1 or 2 steps, an almost insignificant increase is observed for treatments with only one step, in comparison to two steps.

Table V-1 - Degree of crystallinity (%) and crystallite size estimated of glass-ceramics.

HT	2 steps				1 step			1000°C
Time	15 min	30 min	1h	1h30	30 min	1h	1h30	3 h
Degree of crystallinity (%)	13.22	24.93	36.11	43.79	25.08	38.14	44.72	80.21
Average crystallite size (nm)	- -	- -	- -	- -	10	23	27	- -

Reference: AUTHOR.

Furthermore, the diffractograms were used to estimate the crystallite sizes of GC (treated in one heating step) by Scherrer's equation (equation V-01) (DIAS *et al.*, 2021).

$$L = \frac{K\lambda}{\beta_{(hkl)}\cos\theta} \qquad \text{(V-01)}$$

where K is a shape constant, assumed as 0.90 for spherical-like crystals; λ is the radiation wavelength (CuKα = 1.5406 Å); θ (rad) is half the diffraction angle (2θ) for a specific (hkl)-plane; $\beta_{(hkl)}$ (rad) is the corrected-peak broadening (in 2θ) arising from the nanometric size of the crystallites, and L is the crystallite size.

For Scherrer analysis, the broadening of the peaks due to micro-strain is assumed to be negligible. The instrumental correction is made by means of a pattern that presents large crystals and no peak broadening from crystallites. The broadening of the peaks observed for the pattern is, therefore, almost purely instrumental. Equation V-02 is used to discount the instrumental broadening from the total diffraction peaks broadening observed for the samples:

$$\beta_{(hkl)} = \sqrt{B^2_{(hkl)} - b} \qquad \text{(V-02)}$$

where $B_{(hkl)}$ (rad) is the full width at half maximum of the sample peak, and b (rad) is the same parameter, but measured for the diffraction peaks of the pattern. Quartz was used as an instrumental standard for all measurements.

The estimated crystallite sizes for GC treated in one heating step are disposed in Table V-1.

In order to compare the HT in one or two heating steps, Figure V-5 presents the diffractograms (A) and the DSC (B) for the heat treatment in 1h30. Just by these two analyses, it is verified that there is no significant difference between the two heat treatment methods used in these samples.

Figure V-5 - A) Diffractograms and B) DSC of glass-ceramics HT for 1h30 in one and in two steps.

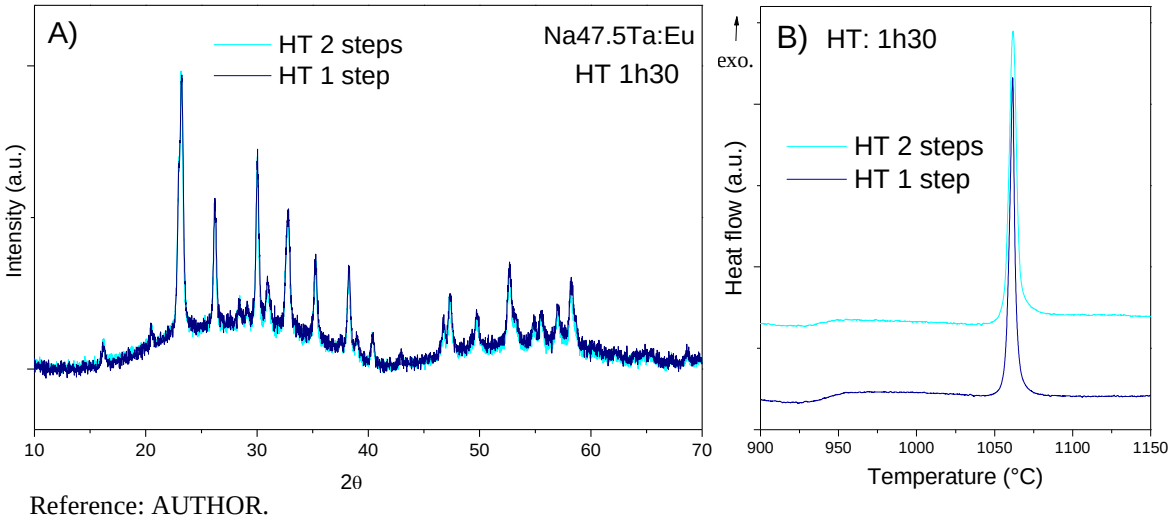

Reference: AUTHOR.

V-3 OPTICAL ANALYSIS OF GLASS-CERAMICS

Photoluminescence measurements were also performed in the glass-ceramics, since europium ion is used as a structural probe. These measurements were performed at the ICMCB on powdered samples, using a Fluorolog spectrometer, front-face mode. The spectra were measured with an integration time of 0.2 s, step of 0.2 nm, entrance and exit slits of 0.25 mm; intermediate slit of 5 mm and with a 370 nm filter for the excitation spectrum. Excitation spectra were obtained using 612 nm; and emission spectra with 395 nm.

Figure V-6 shows the excitation spectra of glass-ceramics obtained in one heating step with emission at 612 nm (normalized to 395nm), Figure V-7 shows the emission spectra with excitation at 395 nm (normalized to 591 nm) and Figure V-8 shows the excitation and emission

spectra of GC prepared using 1000°C/3h. As expected, the excitation spectra show the characteristic transitions of Eu^{3+}, that is, from the $^7F_{0.1}$ level to the excited states $^5D_1$ - 535 nm, $^5D_2$ - 465 nm, $^5D_3$ - 416 nm, $^5L_6$ - 395 nm, $^5G_2$ - 382nm, $^5D_4$ - 363 nm and $^5H_3$ - 320 nm; and the emission spectra of the transitions from the $^5D_0$ excited state to the ground states ^7F_J (J=0,1,2,3 and 4).

Figure V-6 - Normalized excitation spectra with emission wavelength of 612 nm of glass-ceramics.

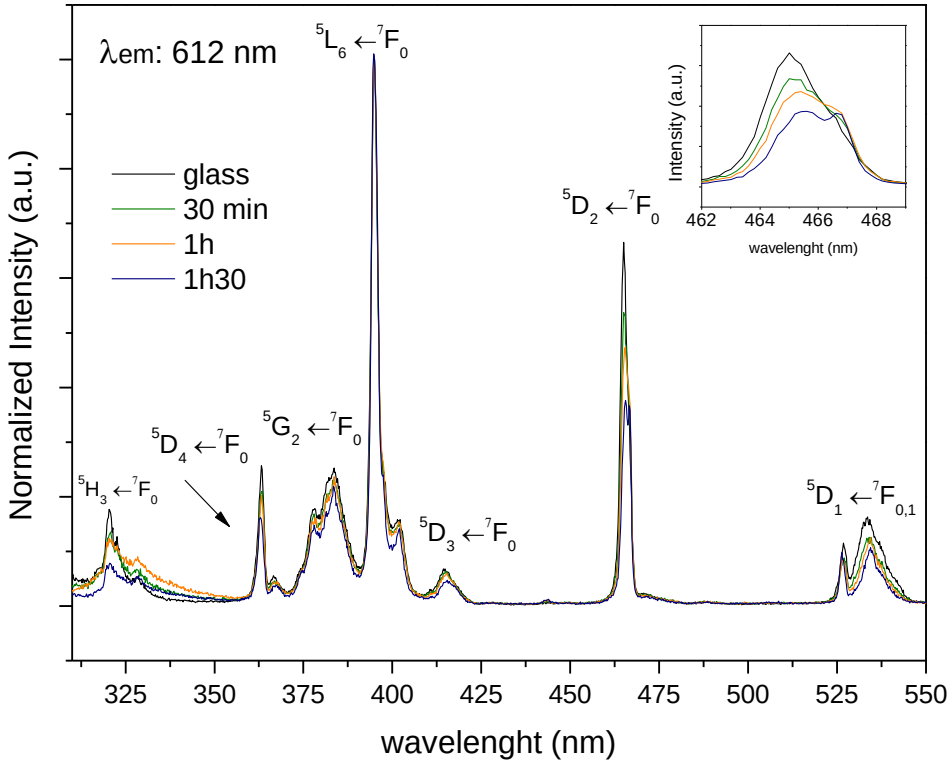

Reference: AUTHOR.

As mentioned in Chapter I-5.3, the europium ion is used as a structural probe, and the ratio of the transitions [$^5D_0 \rightarrow$] $^7F_2$/ $^7F_1$ is indicative of the symmetry around the ion. This ratio of the areas under the peaks of these two transitions is shown in Figure V-7. A decrease in the ratio is observed as the heat treatment time increases, indicating an increase in symmetry around the Eu^{3+} ion. Regarding XRD/DSC analysis, this increase in symmetry is probably due to the increase in crystallinity of the material, thus indicating that europium ions are inserted in these crystals. In the case of the sample with HT 1000°C/3h (FIGURE V-8), despite being more crystalline than the others (higher degree of crystallinity), its asymmetry ratio is higher, indicating the presence of the Eu^{3+} ion in a less symmetrical environment; and similar to 30 minutes of treatment. It may seem contradictory at first, but this difference is probably due to the crystalline phase in which the ion is inserted. As already shown, the most crystallized phase

corresponds to the equivalent of the $Na_4(Nb_8P_4O_{32})$ phase, which is monoclinic; and the other samples the crystalline phase is the phase of interest $Na_2Ta_8O_{21}$, which is orthorhombic, so more symmetrical.

Figure V-7 - Normalized emission spectra with excitation wavelength of 395 nm of the glass-ceramics.

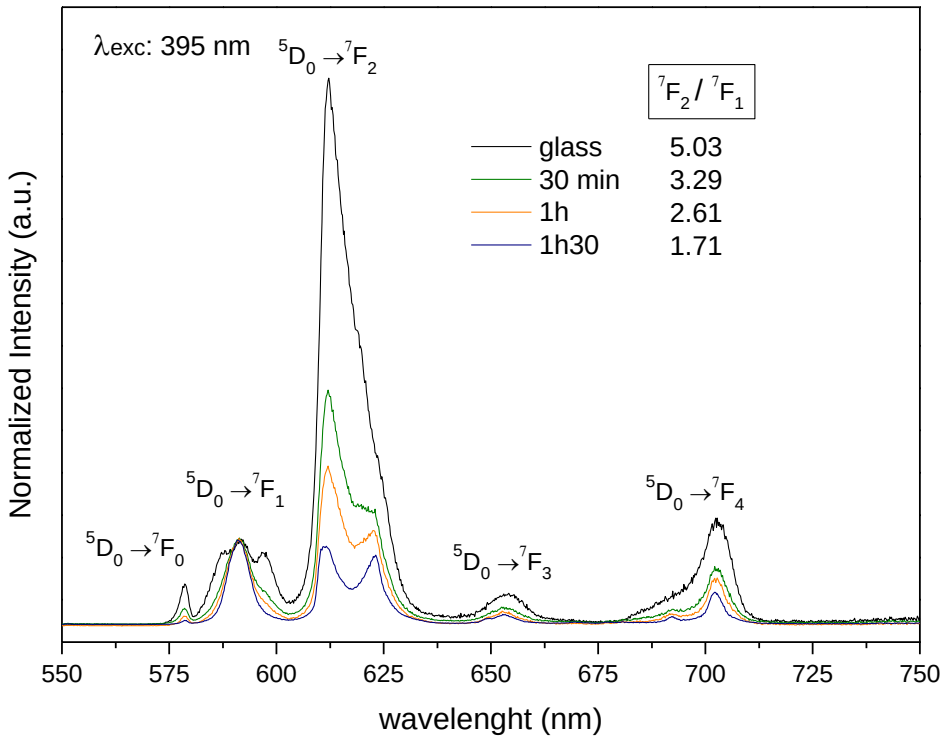

Reference: AUTHOR.

Also, as mentioned by Binnemans (2015), the presence of the $^5D_0 \rightarrow {}^7F_0$ transition indicates that the ion is in an environment of low symmetry, as this transition is prohibited by the Laporte rule. However, experimentally this transition is sometimes detected because of wavefunction mixing between several ^7F_n levels but is only observed if Eu^{3+} is out of an inversion center. In the spectra it is possible to notice that the relative intensity of this transition decreases as the heat treatment time increases, corroborating the previous notes. Finally, the Stark components of emission bands become narrower and split one another (mainly for the $^5D_0 \rightarrow {}^7F_0$ transition) as usually observed in crystalline environments. All these Eu^{3+} spectral changes with increasing crystallinity together with XRD and DSC results are a clear indication that Eu^{3+} are incorporated inside the sodium tantalate crystallites during the crystallization process.

Figure V-8 - (A) Excitation spectra with emission wavelength of 612 nm and (B) Emission spectra with excitation wavelength of 395 nm of the completed crystalized glass-ceramic (1000°C/3h).

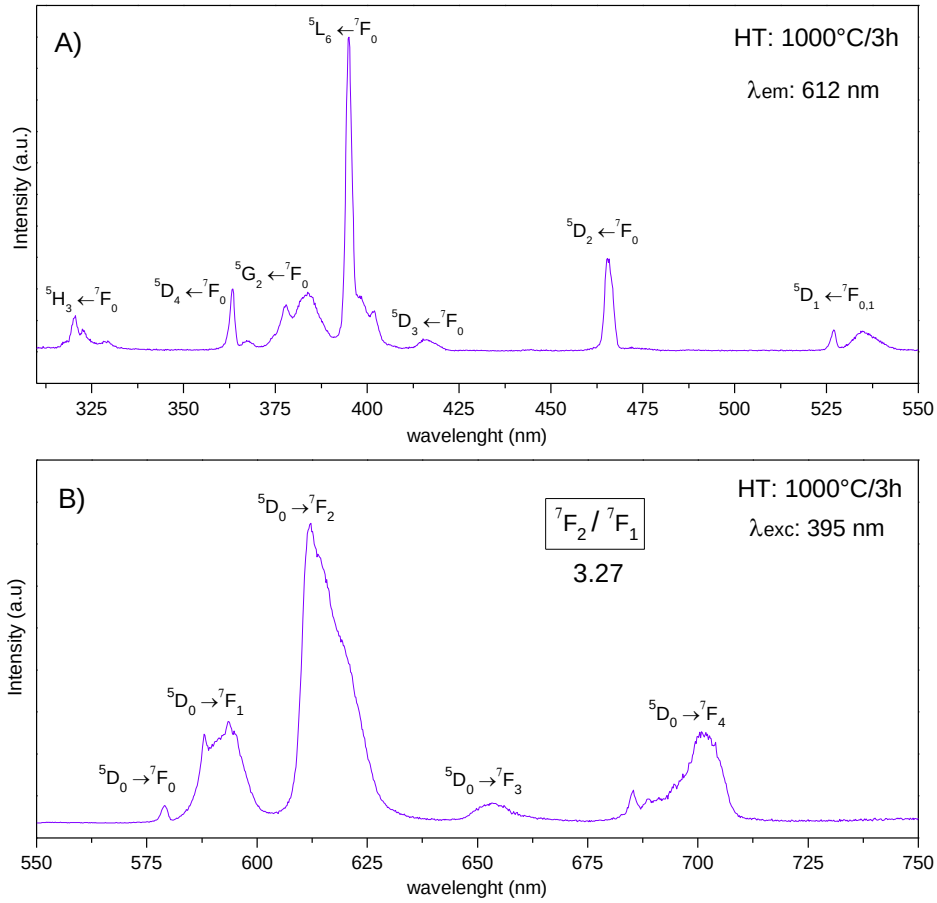

Reference: AUTHOR.

Additionally, Judd-Ofelt radiative parameters of pristine glass and glass-ceramics were calculated from the emission spectra (BINNEMANS, 2015; CUNHA *et al.*, 2021; MARCONDES *et al.*, 2020) and are shown in Table V-2. A decrease was observed for the Ω_2 values with increasing crystallization times (as also Ω_4). The Ω_2 parameter is usually related to the covalence of the Eu-O bonds (REISFELD; JØRGENSEN, 1987) and angular changes in the local coordination geometry of the RE (SILVA *et al.*, 2016). This decrease in the glass-ceramics can be related with a higher symmetry in relation to glass network and agrees with the proposed discussion for the [$^5D_0 \rightarrow$] $^7F_2$/ $^7F_1$ ratio and the migration/ approximation of Eu^{3+} ions to the crystalline phase (CUNHA *et al.*, 2021).

Table V-2 - Judd-Ofelt parameters (Ω_λ x10^{-20} cm^2) of the pristine glass and glass-ceramics.

Sample	Ω_2	Ω_4
Glass	8.31	3.93
GC_{30min}	5.22	2.55
GC_{1h}	4.29	2.12
GC_{1h30}	2.83	1.45

Reference: AUTHOR.

Finally, in order to verify the difference between the spectra of the heat treatment in one or two heating steps, Figure V-9 shows the comparison between the glass-ceramics treated in 1h30, with the emission (λ_{exc}: 395 nm) and excitation (λ_{em}: 612 nm) spectra.

Figure V-9 - Excitation and emission spectra of glass-ceramics heat-treated in one and two steps for 1h30 - λ_{em}:612 nm e λ_{exc}: 395 nm.

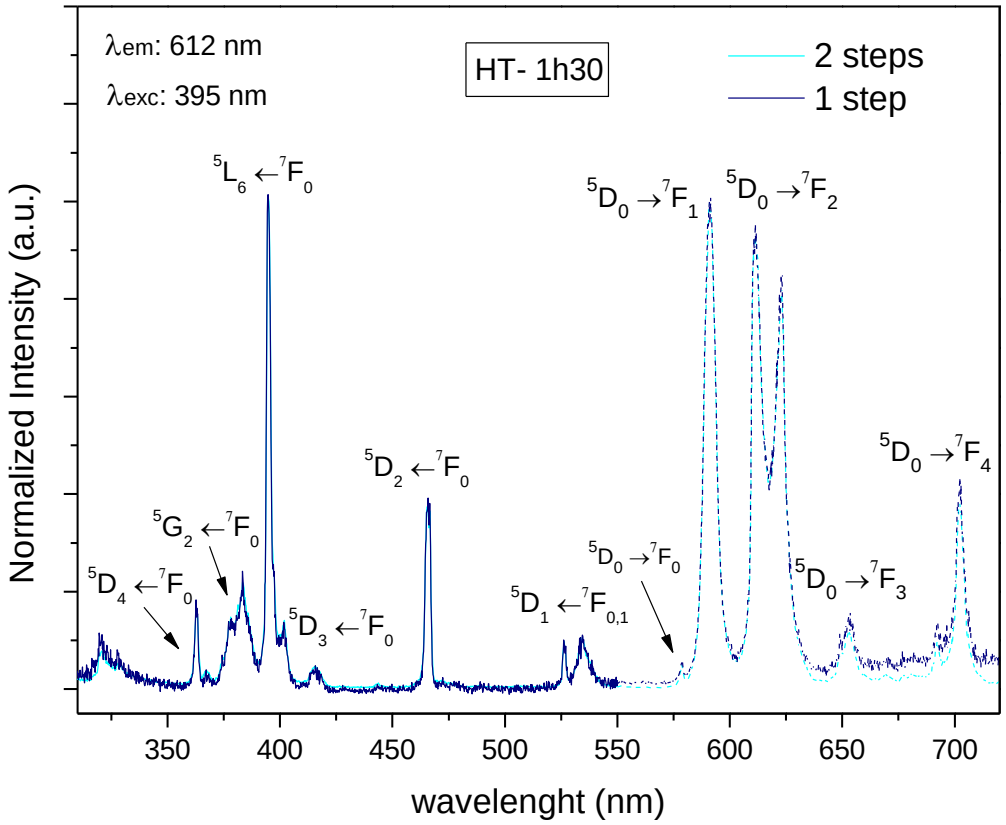

Reference: AUTHOR.

Comparing the spectra, there is no noticeable change in symmetry around the europium ion when using the one- or two-step heat treatments. Thus, in general, just by these analyses, no major differences were observed to prepare a glass-ceramic using one or two steps.

So, for other optical analysis, GC were obtained from the already polished glass, using only one heating step. The Transmittance (%T) was measured in the GC HT for 30 minutes, 1

hour and an intermediate one, HT for 45 minutes; using the same parameters that were previously used for the glasses - Chapter III-4. Figure V-10 presents the images of these glass-ceramics and Figure V-11 presents the %T spectra for these GC compared to the pristine glass, in which a reduction in transparency in the visible region is verified, with sample GC - 1h presenting, for example, 55% transparency around 775 nm (corresponding to the SHG in the experiment of Maker Fringes). However, in the near infrared, the transparency is very similar to that of the pristine glass.

Figure V-10 - Images of glass-ceramics HT in one step.

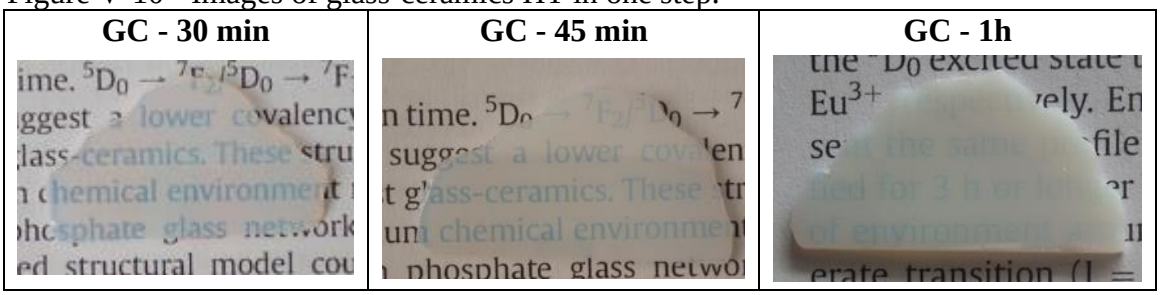

Reference: AUTHOR.

Figure V-11 - Transmission spectra of Na47.5Ta:Eu glass and glass-ceramics HT in one step.

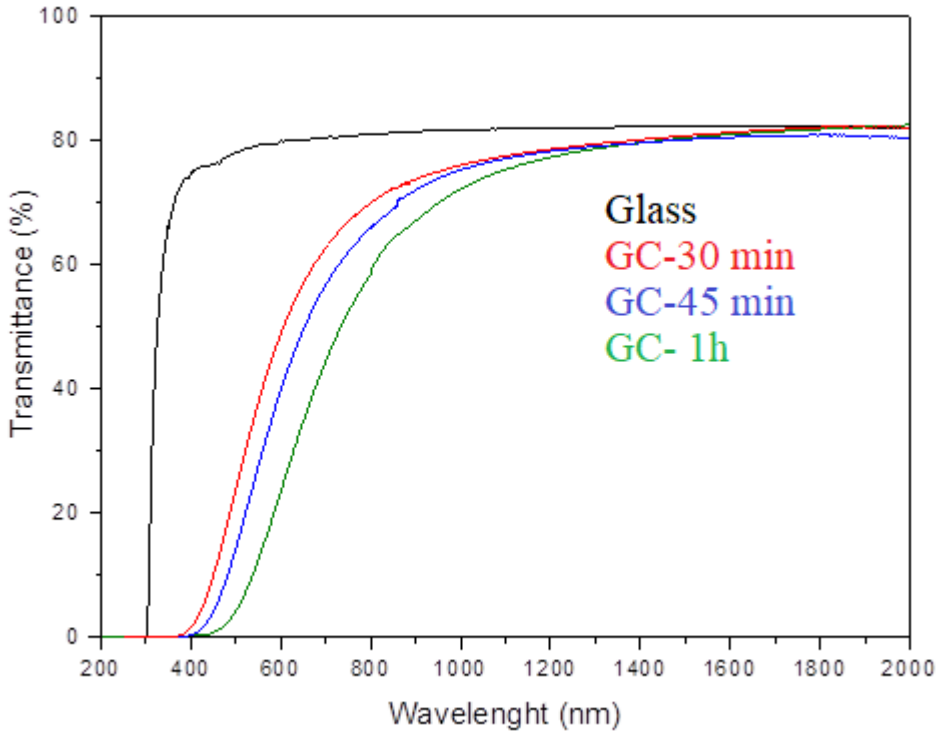

Reference: AUTHOR.

So, longer heat treatments promote a clear increasing loss of transparency at lower wavelengths attributed to scattering effects. Since the average crystallite size remains much smaller than the incident light for all glass-ceramics (already calculated), it is inferred that light scattering could be associated with a high refractive index difference between the crystals and glass host or partial agglomeration of these nanocrystals.

Refractive index was measured for the same GC, using the Brewster angle method, with lasers of 532, 639, 785 and 935 nm. Additionally, as in Chapter III, it was used the Cauchy's equation to obtained the index values in other wavelengths. Table V-3 presents the value of refractive index in 1550 and 775 nm wavelengths.

Table V-3 - Refractive index values for GC HT in one step.

Sample	**n (1550 nm) ±0.01**	**n (775 nm) ±0.01**
GC- 30 min	1.98	2.00
GC- 45min	1.98	2.01
GC- 1h	1.97	1.99

Reference: AUTHOR.

The refractive index measured for the GC is higher than the pristine glass, with a difference around of 0.11 ± 0.01. So, this difference starts influence the transparency of the material (and probably also agglomeration), due to scattering, as observed visually and also by transparency measurement.

Chapter V

CONCLUSIONS

According to the objective, glass-ceramics from sodium phosphate glass with 47.5 mol% of Ta_2O_5 doped with europium were prepared and characterized. The study for preparing the glass-ceramics occurred using the traditional method of heat treatment, using one or two steps. The glass-ceramics were characterized by DSC, XRD, photoluminescence, Uv-Vis transparency and refractive index. A priori, no significant changes were observed using one or two steps of heat treatment, highlighting that this study was not so detailed.

Through the characterizations, the presence of only the crystalline phase $Na_2Ta_8O_{21}$ was identified, thus achieving the objective of prepare a GC with a single tantalate crystalline phase. For a heat treatment at higher temperature/time, the $Na_4(Ta_8P_4O_{32})$ crystalline phase was identified, representing the second exothermic peak of DSC curve, and also a phase that is related to the entire glass matrix. The degree of crystallinity was estimated from the diffractograms, which increases with longer heat treatment time maintaining the temperature (from 25% for the sample treated in 30 minutes to 45% for the sample treated for 1h30). Crystallites sizes estimated by Scherrer's equation indicate that the glass-ceramics presents small size crystals. By photoluminescence it was verified that the europium ion is present in the crystalline phase; since the ratio of $[^5D_0 \rightarrow] \ ^7F_2/ \ ^7F_1$ transitions decreases with the increase of the degree of crystallinity of the material and also the behavior of $^5D_0 \rightarrow \ ^7F_0$ transition. The transparency of the glass-ceramics was reduced and red-shifting, as the presence of crystals increases scattering, probably due to refractive index differences between glass and crystals (that increases in the GC comparing to pristine glass) and/or agglomeration.

Therefore, it is concluded that it was possible to obtain and characterize relatively transparent europium-doped tantalum sodium phosphate glass-ceramics.

REFERENCES

BINNEMANS, K. Interpretation of europium (III) spectra - A review. **Coordination Chemistry Reviews**, [S.l.], v.295, n.01, p.01-45, 2015.

CASSANI, R. **Estudo de cristalização em vidros fosfatos alcalinos contendo óxido de nióbio** = Study of crystallization in alkaline phosphate glasses containing niobium oxide. 2022. 100p. Thesis (Master in Material Science and Engineering) - Universidade Federal de Alfenas, Poços de Caldas, 2022.

CUNHA, C.R.da. *et al.* Crystallization of bronze-like perovskite in potassium tantalum germanate glasses: Glass ceramic preparation and its optical properties. **Optical Materials,** [S.l.], v.122, partB, p.111803, 2021.

DIAS, J.A. *et al.* Phase evolution and optical properties of nanometric Mn-doped TiO_2 pigments. **Materials Today Communications**, [S.l.], v.27, p.102295, 2021.

KARAM, L. **Structuration multi-échelle et multifonctionnelle de nouveaux matériaux vitreux pour la photonique intégrée =** Multiscale and multifunctional structuring of new glassy materials for integrated photonics. 2020. 275p. Thesis (PhD in Chemistry Science) - Université de Bordeaux, Bordeaux, France, 2020.

LEPICARD, A. **Design of surface chemical reactivity and optical properties in glasses.** 2016. 293p. Thesis (PhD in Chemistry) - Université de Bordeaux, Bordeaux (France), 2016.

MALAKHO, A. *et al.* Crystallization and second harmonic generation in thermally poled niobium borophosphate glasses. **Journal of Solid-State Chemistry,** [S.l.], v.178, p.1888-1897, 2005.

MARCONDES, L.M. *et al.* Transparent glass and glass-ceramic in the binary system $NaPO_3$-Ta_2O_5. **Journal of the American Chemical Society**, USA, v.103, p.1647-1655, 2019.

MARCONDES, L.M. *et al.* High tantalum oxide content in Eu^{3+}-doped phosphate glass and glass-ceramics for photonic applications. **Journal of Alloys and Compounds**, [S.l.], v.842, p.155853, 2020.

REISFELD, R., JØRGENSEN, C.K. Excited state phenomena in vitreous materials. **Handbook on the Physics and Chemistry of Rare Earth**, [S.l.], v.09, p.01-90, 1987.

SILVA, I.G.N. *et al.* Highly luminescent Eu^{3+}-doped benzenetricarboxylate based materials. **Journal of Luminescence**, [S.l.], v.170, part2, p.364-368, 2016.

VIGOUROUX, H. *et al.* Crystallization and Second Harmonic Generation of lithium niobium silicate glass ceramics. **Journal of the American Chemical Society,** USA, v.94, n.07, p.2080-2086, 2011.

CHAPTER VI - EFFECT OF THERMAL POLING IN EUROPIUM-DOPED TANTALUM PHOSPHATE GLASS-CERAMICS

CHAPTER VI – EFFECT OF THERMAL POLING IN EUROPIUM-DOPED TANTALUM PHOSPHATE GLASS-CERAMICS

This chapter presents the effect of Thermal Poling applied in glass-ceramics obtained by the traditional heat treatment method from a glass with molar composition $99.83[52.5NaPO_3\text{-}47.5Ta_2O_5]\text{-}0.17Eu_2O_3$ already presented in Chapter V. The same poling parameters used for glasses (presented in Chapter IV) were tested for these glass-ceramics. Subsequently, measurements of ToF-SIMS/ profilometry, Infrared reflectance, micro-SHG/luminescence correlation and Maker Fringes were performed to evaluate the treatment and calculate the second order susceptibly $\chi^{(2)}$.

VI-1 THERMAL POLING OF GLASS-CERAMICS

Glass-ceramic samples were prepared from an already polished glass - molar composition $99.83[52.5NaPO_3\text{-}47.5Ta_2O_5]\text{-}0.17Eu_2O_3$ (Na47.5TaEu) - of about 1 mm thickness and using the methodology described in Chapter V for one step of heat treatment. Thermal Poling of the GC took place following the same methodology described in Chapter IV-1 , at the ISM. The sample was placed in the Thermal Poling cell between a cathode and an anode. The cathode was constituted of a n-doped silicon wafer and a 150μm-thick borosilicate slide in contact with the sample and working as an “open” electrode for sodium migration. The anode was made of borosilicate glass slide covered with an ITO film (100 nm and 8 -12 Ω/sq), with a 1x0.5cm dimension and the electric contact was ensured by covering the ITO free surface and sides by chromium/ gold deposition using the Q3000T D (Quorum) equipment. The sample was heated from room temperature to 250ºC at a heating rate of 15 °C.min^{-1} under nitrogen flow (6L.min^{-1}). An increasing DC voltage of 150 V.min^{-1} was applied to the sample up to 900V. After some time, temperature was decreased until reaching 50°C (keeping the voltage applied). Finally, the voltage was stopped and the sample removed from the Poling cell.

As a first Thermal Poling experiment, glass-ceramic sample treated for 1 hour (GC_{1h}) was chosen to understand the overall behavior of these glass-ceramics under Poling. However, around 12 minutes under a 900V voltage, the current curves suddenly “jumped” and sparks could be observed. The experiment had to be stopped and the GC sample presented a burned appearance (Figure VI-1A).

Figure VI-1 - Thermal Poling: applied voltage and detected current curves for samples treated at 250°C-900V: (A) GC_{1h}-12min and (B) GC_{45min}-10min.

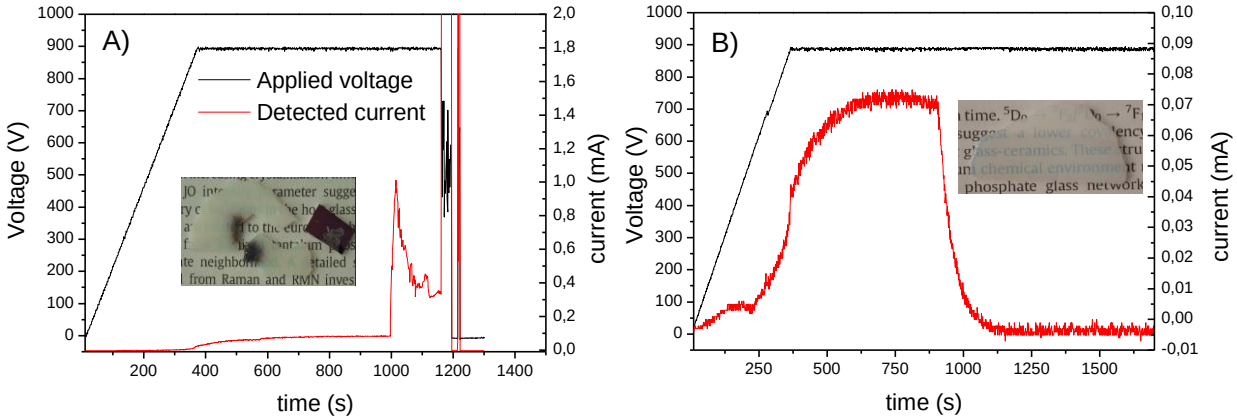

Reference: AUTHOR.

This behavior was attributed to a higher electrical conductivity of GC when compared to the pristine glass related with sodium tantalate crystallites. For this reason, the next experiment was carried out on a less crystallized sample, with treatment of 45 minutes (GC_{45min}). Under the same experimental conditions (250ºC, 900V, N_2), the Thermal Poling experiment was carried out for only 10 min and an increasing current related with charge migration was successfully detected (Figure VI-1B). The decrease observed in the figure occurred after starting the temperature reduction. So, a first interesting result was that the current did not exponentially increase and dropped when reaching the final constant voltage but slowly increases until heating was stopped. Such behavior suggests a lower charge migration kinetic in GC. However, another experiment for 15 min resulted in the same conduction problems.

The next experiment was conducted on a less crystallized sample, 30 minutes of heat treatment (GC_{30min}). Since no undesirable issue related with current jumps and sample burning were registered, Thermal Poling was applied for 1h30 at 900V and 250ºC. The voltage and current curves for the pristine glass and GC_{30min} under the same Thermal Poling conditions (250ºC, 900V) are resumed in Figure VI-2. The final current drop for each sample is related with the end of heating step. From the respective current curves, it clearly appears that the sodium migration mechanism and kinetic is different in the pristine glass and final glass-ceramic. In fact, the current intensity observed in a Poling experiment is proportional to the density of mobile charges flowing from the anode to the cathode per time and area units (DUSSAUZE *et al.*, 2012). Hence, since the same anode sizes (around 0.5 cm^2) and Poling conditions (250ºC, 150 $V.min^{-1}$ to 900V) were used for both experiments, it is possible to relate the current intensity in both cases with the quantity of migrating sodium and migration rate from the anode to the cathode.

Figure VI-2 - Thermal Poling: applied voltage and detected current curves for samples treated at 250°C-900V: pristine glass and GC_{30min}-1h30.

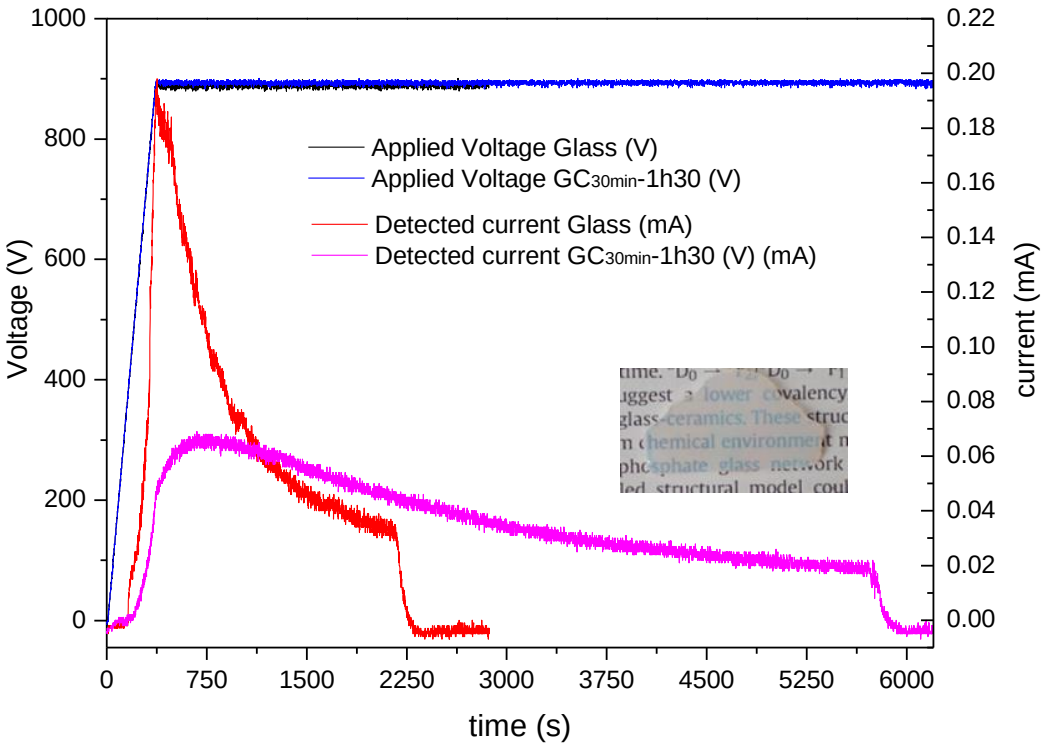

Reference: AUTHOR.

In the case of the pristine glass and as usually observed in glasses (as already presented in Chapter IV), after reaching a threshold voltage, the current quickly increases together with the applied voltage due to higher migration rate for higher voltages. After reaching a constant voltage, the current decreases because ion migration is increasingly difficulted by the formed charge space until the internal electric field reaches values close to the applied voltage. However, for GC_{30min} the current increase is slower but still continues after reaching the constant voltage and remains almost constant for about 10 min before starting to decrease. Such behavior means that sodium migration is somewhat difficulted in glass-ceramics because of the presence of large sodium tantalate crystallites ($Na_2Ta_8O_{21}$) along this migration direction. Besides, it can be inferred that lower current intensities in the glass-ceramic are related with a lower sodium content participating to this migration process, as part of sodium ions are inserted in the crystallites and are not supposed to move.

VI-2 SODIUM DEPLETION ON GLASS-CERAMICS AFTER THERMAL POLING

To verify the depletion of sodium ions (Na^+) in the material after Thermal Poling, the sodium concentration profile under the anode was determined by Time-of-Flight secondary ion

mass spectroscopy (ToF-SIMS) that were performed on a TOF-SIMS 5 - IONTOF equipment located at PLACAMAT and the depth after that was verified using an optical and mechanical profilometer at ICMCB. Figure VI-3 presents these data for both glass-ceramics (GC_{45min}-10min and GC_{30min}-1h30) and for the pristine glass (that was already shown in Figure IV-14).

Figure VI-3 - ToF-SIMS depth profile of sodium in the glass and glass-ceramics after Thermal Poling.

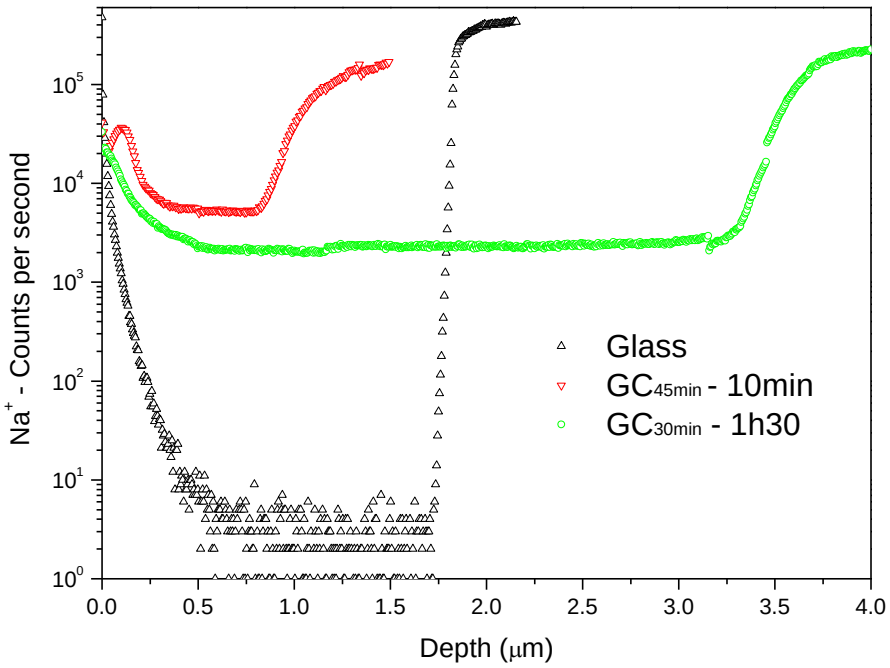

Reference: AUTHOR.
Note: The 0μm mark corresponds to the material surface at the anode side.

For all Thermal Poling experiments, a sodium depleted layer can be identified as a sodium content decrease beneath the anode surface. Depth of sodium depletion were estimated to be around 3.2 μm for GC_{30min}-1h30 and 0.8 μm for GC_{45min}-10min. As expected, longer Thermal Poling times promote the formation of thicker depleted layers since sodium migration is a kinetic process. For the glass sample, the depleted layer is almost free of sodium as its content falls to values close to 0. However, for the glass-ceramics the depleted layer still contains a significative sodium content, in agreement with previous assumptions by the current curves that only sodium ions from the remaining glassy phase are able to migrate through the vitreous network.

Another detail from these ToF-SIMS data supports the assumed migration model: besides the differences in poled layer thickness, the more crystallized glass-ceramic GC_{45min}-10min presents a higher sodium content in the depleted layer than the less crystallized one $GC3_{0min}$-1h30. Therefore, since more crystallized GC contains more sodium ions in the

crystalline phase, this result is in agreement with the assumption that such “crystalline” sodium ions are not involved in the migration process.

VI-3 EFFECT OF THERMAL POLING ON STRUCTURAL OF GLASS-CERAMICS

For a better understanding of the structural changes induced by thermal poling in glass-ceramics, infrared reflectance spectra were collected at the cathode and anode side (poled layer) in GC_{45min}-10min and in the glass after thermal poling presented previously. The measurement was made at ISM using the same parameters described for glasses in Chapter III and absorption spectra obtained by the Kramers-Krönig analysis, as also presented in Chapter III. The results are shown in Figure VI-4.

Figure VI-4 - Infrared absorption spectra of the glass, poled glass, glass-ceramic GC_{45min}-10min and poled glass-ceramic GC_{45min}-10min.

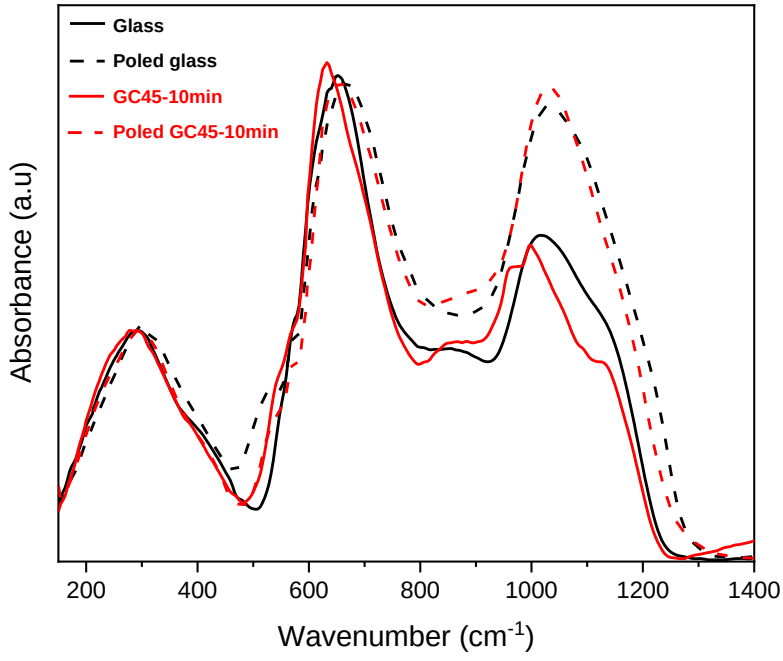

Reference: AUTHOR.

As already mentioned, infrared mode attributions and structural discussion of tantalum phosphate glasses were based on niobium phosphate glasses. Three main broad absorption bands regions are clearly identified between 150 and 475 cm^{-1}, 475 and 800 cm^{-1}, and 900 and 1250 cm^{-1}. The low frequency feature composed of several vibrational bands is attributed to bending modes of $[TaO_6]$ units in the tantalate network overlapped with bending modes of PO_4 units from a sodium phosphate network. Infrared broad band between 475 and 800 cm^{-1} is

mainly attributed to the tantalate network and constituted of two vibrational modes at 630 cm^{-1} and 730 cm^{-1} attributed to asymmetric stretching vibrations of Ta-O-Ta in regular and distorted 3D [TaO_6] networks respectively (DUSSAUZE *et al.*, 2007; KAMITSOS *et al.*, 1995; KARAM *et al.*, 2020).

For both poled glass and glass-ceramic broadening and shift to higher frequency after thermal poling is related with a stronger contribution of the stretching mode attributed to distorted [TaO_6] units in the 3D [TaO_6] network. Since crystallization of the $Na_2Ta_8O_{21}$ phase is not completed in this sample and considering that only part of sodium ions takes part in the crystallization event, it is inferred that only sodium from the remaining glassy phase is depleted in the vicinity of [TaO_6] rich regions. As a result, [TaO_6] octahedra from the remaining vitreous tantalate network suffer charge compensation mechanisms through progressive distortion of such units, as already described in niobium phosphate glasses for decreasing sodium contents (KARAM *et al.*, 2020).

Finally, the high frequency bands between 900 and 1250 cm^{-1} is mainly related with the phosphate network. One can clearly see from these infrared spectra that the phosphate network is much more affected by thermal poling than the tantalate network with a relative higher intensity after treatment as well as variations of intensity ratios between the fundamental overlapped modes. This region between 900 and 1250 cm^{-1} is mainly constituted of three contributions centered at 965, 1030 and 1120 cm^{-1}. The low and high frequency modes are related with asymmetric stretching of P-O-P bridges and terminal P-O bonds in pyrophosphate entities $P_2O_7^{4-}$ respectively. The central component at 1030 cm^{-1} is attributed to asymmetric stretching mode of isolated orthophosphate units PO_4^{3-}. It is worth noting that these entities are isolated from other phosphate chains or units but surely at least partially bonded to tantalum through P-O-Ta bridges. Based on the nominal glass composition (99.83[52.5$NaPO_3$-47.5Ta_2O_5]-0.17Eu_2O_3), the Na/P/Ta ratio is approximately 1/1/1.8. In this sense, pyrophosphate units can be understood as P_2O_7 entities with two NBO oxygens balanced by Na^+ and two other oxygens bonded to tantalum and are labeled $(P_2O_7)^{2-}{}_{2Na,2Ta}$. Following the same reasoning, orthophosphate units are supposed to be linked to one NBO and two tantalum atoms and described as $(PO_4)^{-}{}_{1Na,2Ta}$ (Figure VI-5).

Figure VI-5 - Phosphate units in the sodium tantalum phosphate glass and glass-ceramic.

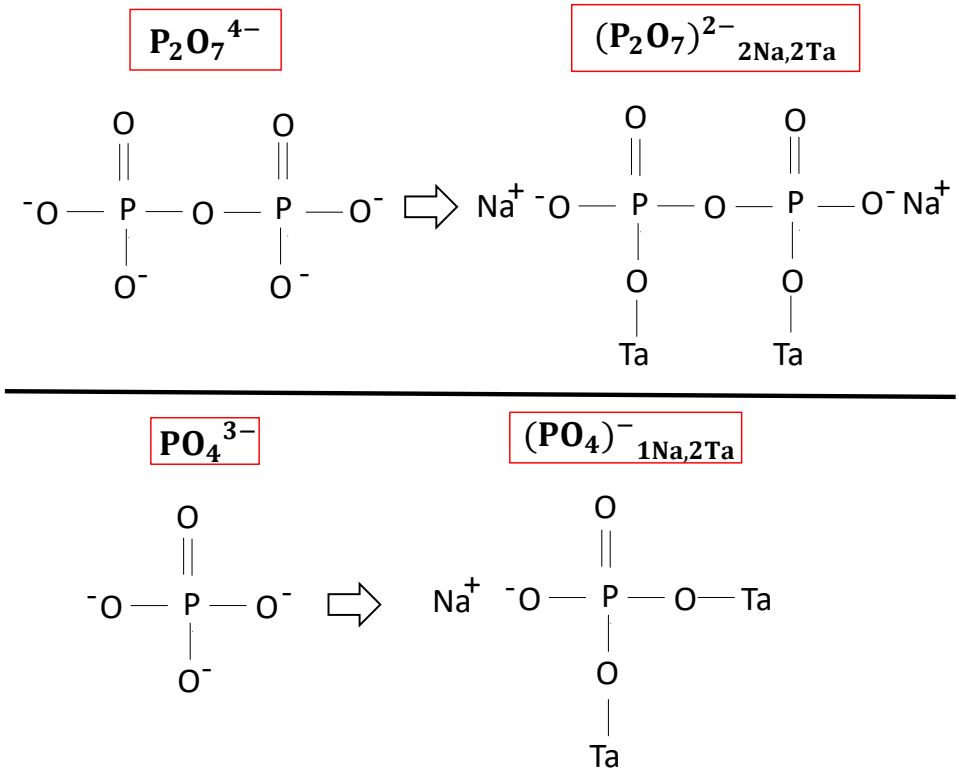

Reference: AUTHOR.

For both glass and glass-ceramic samples, the effect of thermal poling on the structural rearrangements in the poled layer is almost similar with a decrease in the contributions of the pyrophosphate modes and a consequent stronger contribution of the orthophosphate entities. Such behavior can be understood by the fact that sodium loss near terminal oxygens of these phosphate units must be counterbalanced by formation of more P-O-Ta bonds, converting initial $(P_2O_7)^{2-}{}_{2Na,2Ta}$ units in $(PO_4)_{3Ta}$ units, as demonstrated in Figure VI-6. In fact, orthophosphate units are supposed to bond to three tantalum atoms to compensate for the sodium departure. The higher intensity ratio of the phosphate broad band in respect to the tantalate band can be understood by a higher absorption coefficient of $(PO_4)_{3Ta}$ units when compared to $(PO_4)^{-}{}_{1Na,2Ta}$. Such strong variations in the intensity ratio between these bands has also been described in niobium phosphate glasses (KARAM *et al.*, 2020). From an overall structural description, it appears that thermal poling promotes stronger structural changes in the phosphate network, explaining the structural similarity between poled glass and glass-ceramic.

Figure VI-6 - Phosphate units during thermal poling with sodium departure and bonding formation in the depletion layer.

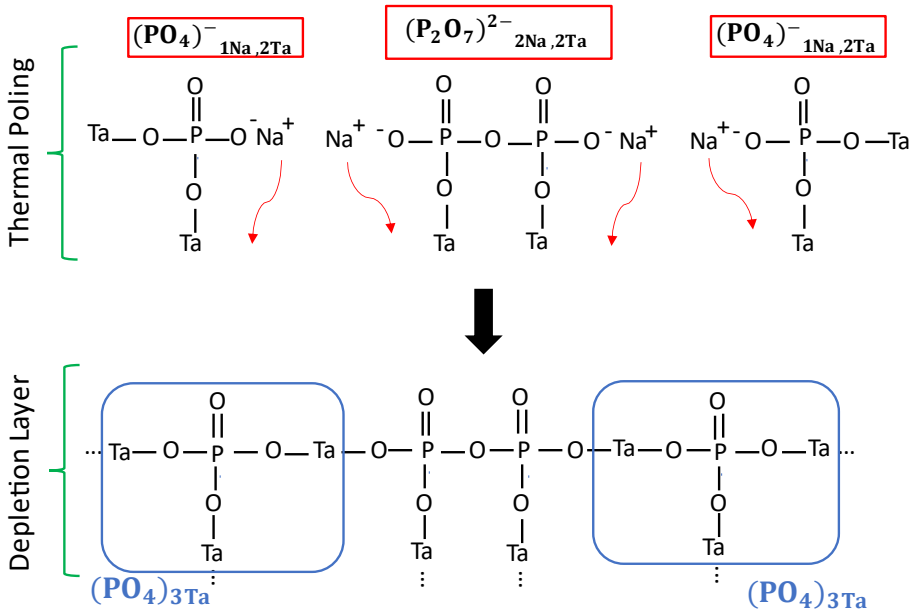

Reference: AUTHOR.

Since the GC were doped with europium ions, using as a structural probe, micro-luminescence measurements were performed on the cross-section of poled glass-ceramic GC_{45min}-10min under excitation at 532 nm at ISM - Figure VI-7.

Figure VI-7 - Eu^{3+} emission spectra of sample GC_{45min}-10min on the cross-section inside and outside of the poled layer.

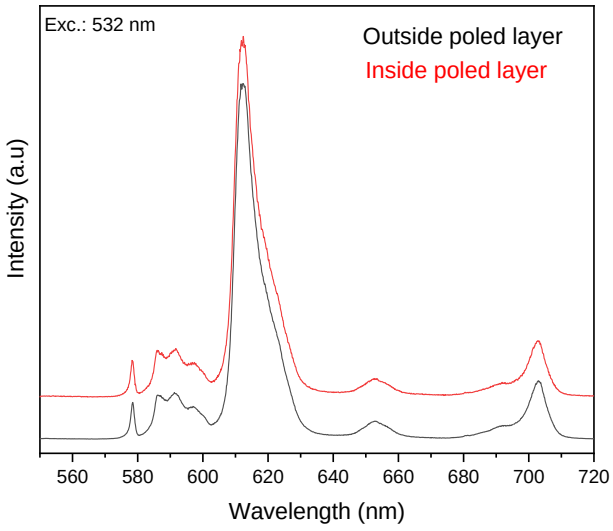

Reference: AUTHOR.

Under these experimental conditions, it appears that Eu^{3+} emission spectra inside and outside of the poled layer are almost identical. Such result is unexpected since structural

changes denoted after poling would modify europium environment. However, one should remember that sample GC_{45min}-10min is a partially crystallized glass-ceramics with part of Eu^{3+} ions already inserted in sodium tantalate crystallites whereas the others are supposed to be in a dominant amorphous tantalate environment expected to crystallize for longer heat-treatments. Since infrared data have already shown that the tantalate network is not drastically modified by poling, it can be assumed that europium ions don´t feel the structural modifications occurring mainly in the phosphate network.

VI-4 EFFECT OF THERMAL POLING ON SHG PROPERTIES OF GLASS-CERAMICS

Since the GC_{30min}-1h30 was poled for a longer time, a micro-SHG mapping was performed at the poled surface cross-section of this sample (as in Figure IV-15)[38]. That was made at ISM in backscattering mode on a modified micro-Raman spectrometer HR800 (Horiba/Jobin Yvon) using a ps pulsed laser at 1064 nm, as previously described in Chapter II-6. The SHG mapping is shown in Figure VI-8.

Figure VI-8 - Micro-SHG mapping of sample GC_{30min}-1h30 at the poled surface cross-section.

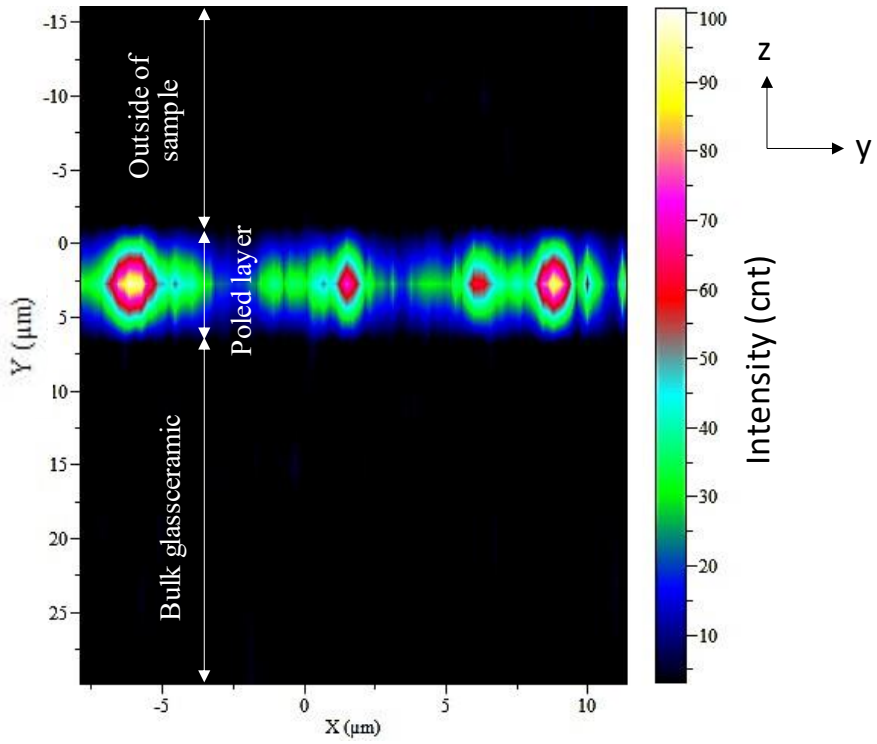

Reference: AUTHOR.

[38] Breaking the sample on its cross-section was even more difficult for the glass-ceramic than for the glass, so the sample did not have a completely flat section, which may make it a little difficult to focus on the measurement.

As observed, a SHG signal is in fact detected beneath the anodic surface, confirming that sodium migration in GC also promotes a charge separation, such charge space being at the origin of a static electric field orthogonal to the poled surface and mostly concentrated in the poled layer. Micro-SHG results also support previous thickness estimations with a poled layer thickness around 3 μm.

The macro-SHG response of these GC materials was also investigated using the Maker Fringes setup described in Chapter II-5. Figure VI-9 refer to the SHG intensity as a function of the incident angle using a p-polarization for both the incident beam and detected SHG (θ-pp scan), varying the θ angle between -80 to 80°, a step of 2°, transmission mode, for samples (A) GC_{45min}-10min and (B) GC_{30min}-1h30. These experiments were carried out before and after Thermal Poling for both GC.

Figure VI-9 - Macro-SHG measurements on Thermally poled glass-ceramics as a function of the incident angle with a fixed p-polarization state for both incident beam and detected SHG (θ-pp): (A) GC_{45min}-10min and (B) GC_{30min}-1h30.

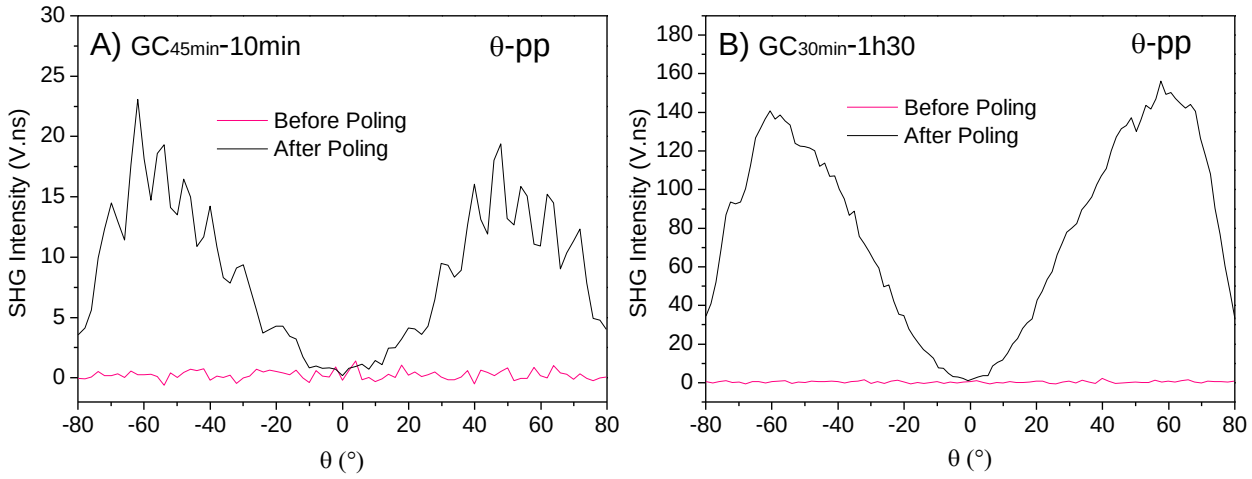

Reference: AUTHOR.

As already reported in Chapter I, some glass-ceramics compositions may sometimes generate SHG signals if specific conditions i.e., the crystal phase is non-centrosymmetric (VERBIEST; CLAYS; RODRIGUEZ, 2009) and these crystals are orientated in regions larger than the coherence length. However, the sodium tantalum phosphate glass-ceramics did not exhibit any SHG signal before Poling, in agreement with luminescence data for these GC presented in Chapter V-3, pointing out a centrosymmetric environment around Eu^{3+} inside the sodium tantalate phase, and since materials with a center of symmetry do not show SHG, this could explain this absence in the GC before Poling. The same behavior is observed in the glass-ceramic prepared by Malakho *et al.* (2005) from a glass with molar composition of

$0.52(0.95NaPO_3\text{-}0.05Na_2B_4O_7)\text{-}0.48Nb_2O_5$, containing $Na_2Nb_8O_{21}$ crystalline phase. Therefore, it is consistent to consider that the SHG signal in the poled glass-ceramics is due to the poling treatment, since, in principle, the crystals alone have no influence on the SHG response.

Still, it is possible to observe a slightly different profile for the glass-ceramic than for the glass, with the presence of overmodulations, mainly in the GC for which the Poling occurred for only 10 minutes. According to Dussauze *et al.* (2013), such a signal is typical of optical interferences that occur between two SHG-active layers with a large difference in thickness, which can be attributed to (i) a thin anodic layer and (ii) an SHG response in the bulk. By measuring SHG before Poling, SHG does not occur in the material (that is, in the bulk); if so, it is assumed that the first option would then be due; and that with a longer poling time, this layer probably increases, reducing these overmodulations.

Figure VI-10 presents the same measurement (θ-pp) as well as the θ-sp, and the ψ-scan measurements (p or s) varying the angle ψ from 0 to 180° fixing the angle θ at 60° for both poled GC. Both θ-scans and ψ-scans were able to identify a SHG signal with an increasing intensity for longer Poling times. Thus, one can expect that SHG is related with sodium migration and presence of the static electric field mainly implanted in the poled layer. Such electro-optical effect, as described in Chapter I-6.3, is known as Electric Field Induced Second Harmonic (EFISH) with its intensity governed by the second order optical susceptibility $\chi^{(2)}$, itself related to the third order optical susceptibility $\chi^{(3)}$. However, since other mechanisms at the origin of SHG such as molecular reorientation can take place during poling, Maker fringes data were simulated using a general matrix formulation of linear and nonlinear multilayer model (RODRIGUEZ; SOURISSEAU, 2002).

In the case of a pure EFISH mechanism (i.e., SHG is only due to the static electric field implanted by thermal poling), the NLO layer can be described by a $C_{\infty V}$ symmetry and the associated contracted 3X6 SHG tensor contains two non-zero components $\chi^{(2)}_{zzz}$ and $\chi^{(2)}_{zxx}$ whose ratio $\chi^{(2)}_{zzz}/\chi^{(2)}_{zxx} = 3$ (review Chapter I-6). For this simulation, it was used the refractive index at the incident and SHG wavelengths that was determined by the Brewster angle method (presented in Chapter V) whereas the poled layer thickness was extracted from the ToF-SIMS measurements. Since Maker fringes experiments were performed in transmission mode, scattering losses of glass-ceramics were also taken into account to improve the final quantitative data (Table VI-1). As presented in Figure VI-10, fitting results on a basis of a $C_{\infty V}$ symmetry are in good agreement with experimental θ and ψ -scans. In addition, the ratio $\chi^{(2)}_{zzz}/\chi^{(2)}_{zxx}$, which was not fixed during simulation, gives a value around 3 in agreement with an EFISH

model for SHG. Finally, second-order nonlinear optical susceptibilities $\chi^{(2)}$ were extracted from these simulations as resumed in Table VI-1. Despite the fact that second order nonlinear optical properties could be induced in these materials through the EFISH mechanism, it appears that $\chi^{(2)}$ values are around one order of magnitude lower in glass-ceramics (0.04 pm/V for GC_{45min}-10min and 0.016 pm/V for GC_{30min}-1h30) than in the precursor glass (0.72 pm/V) under the same poling conditions.

Figure VI-10 - Macro-SHG measurements on thermally poled glass-ceramics: I - θ-pp: A) GC_{45min}-10min and B) GC_{30min}-1h30; II - ψ-s and ψ -p): C) GC_{45min}-10min and D) GC_{30min}-1h30.

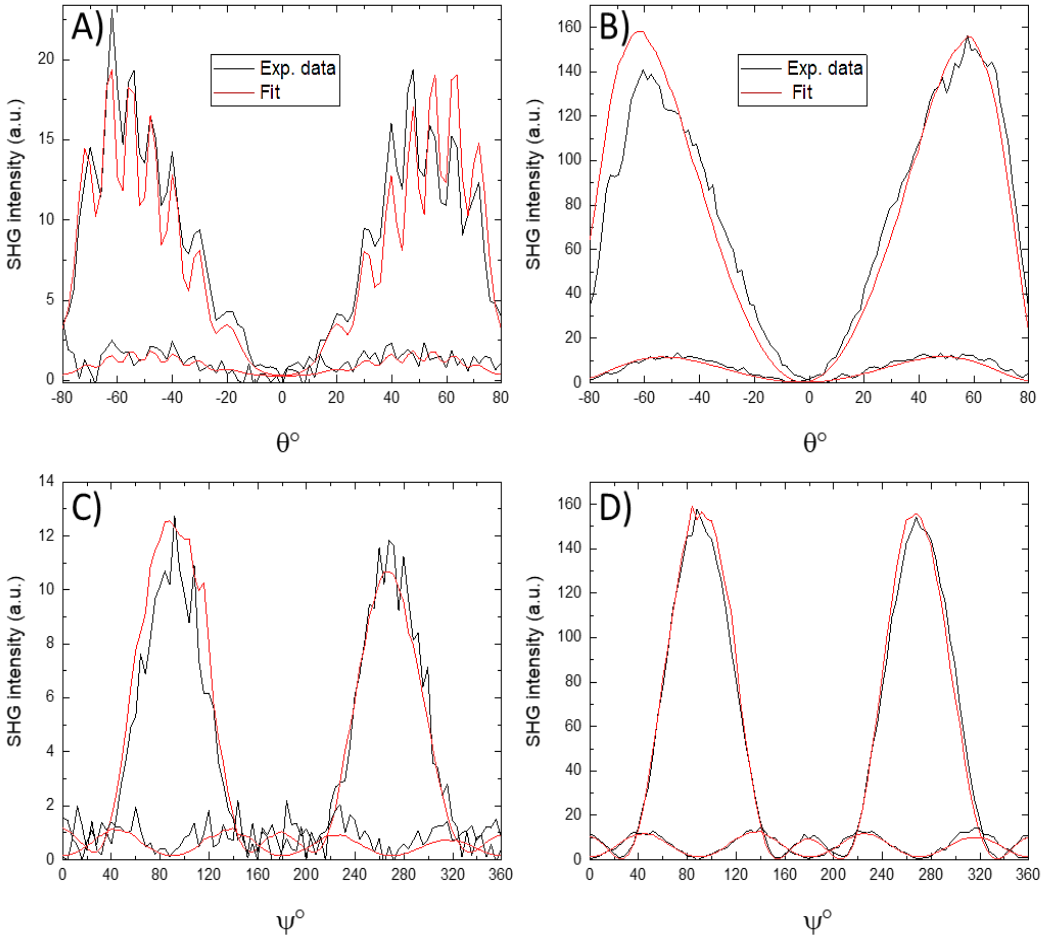

Reference: AUTHOR.

To summarize, this study has pointed out three main observations regarding thermal poling of GC: (i) a decrease of the dielectric breakdown strength when the level of crystallization increase, (ii) the charge dissociation process at the anodic poled layer, inducing sodium depletion and structural rearrangements, appears mainly within the glassy matrix and

(iii) the strength of the implanted static electric field is decreased by more than one order of magnitude for the GC as compared to the poled glass.

Table VI-1 - Scattering losses at 1550nm and 775nm, poled layer thickness and second order non-linear optical susceptibility values at the anode and cathode sides for poled glass-ceramics GC_{45min}-10min and GC_{30min}-1h30.

Sample	**GC_{45min}-10min**		**$GC30_{min}$-1h30**	
Scattering losses (1550 nm) [cm^{-1}]	0.09		0.06	
Scattering losses (775 nm) [cm^{-1}]	0.86		0.5	
L [µm]	1.25		3.19	
$\chi^{(2)}_{zzz}/\chi^{(2)}_{zxx}$	3		3	
$\chi^{(2)}_{zzz}$ [$pm.V^{-1}$]	Anode	Bulk	Anode	Bulk
	0.04	-0.002	0.016	ND

Reference: Available by Dr. MARC DUSSAUZE.

To explain such observations, it is taken in account the large variations of dielectric constant expected between the glassy and crystalized phases which impose to consider the GC in this study as composite dielectric systems. In such a case, it is well known that interfacial polarization phenomena will occur and can considerably modify the dielectric properties of these inhomogeneous media as described by the Maxwell-Wagner-Sillars effect. This is notably an actual subject of investigation to optimize GC properties for high energy density capacitor applications (HUANG *et al.*, 2010; PAN *et al.*, 2006; PENG *et al.*, 2020; VAN BEEK, 1960).

As observed in ferroelectric glass-ceramics, the breakdown strength decreases significantly because of interface polarization linked to high contrast of dielectric constant between the glassy and the crystallized phases (HUANG *et al.*, 2010). Similarly, it is expected that the interface polarizations promote bulk charge accumulations at each interface of the composite dielectric material which decrease drastically the breakdown strength. This has avoided to use a sufficiently high voltage during the poling treatments of GC samples exhibiting a degree of crystallinity above 28%. In addition, as interfacial polarization effects promote bulk charge accumulations, this directly diminish the number of charges within the space charge layer at the anodic interface as observed with the EFISH responses lowered by more than one order of magnitude in the GC under study as compared to the homogeneous glassy material. It points out that an optimization of dielectric contrast between glassy and crystallized phases in the formulation/fabrication of GC is a key point to adapt such kind of composite dielectric materials to classical thermal poling treatments.

CONCLUSIONS

The effect of Thermal Poling in europium-doped sodium tantalum phosphate glass-ceramics was studied. It was possible to carry out the Thermal Poling in two glass-ceramics; one using 10 minutes and the other using 1h30; these being prepared with different times and thus different degrees of crystallinity/transparency. A different behavior was observed during the Poling of the glass-ceramics when compared to the pristine glass (using the same parameters). It is suggested a model of the mechanism involved and that explain this difference, mainly due to the fact that sodium ions (Na^+) in the crystalline phase do not migrate within the material, but only those that are still within the glassy phase. That is corroborated by the current curves and the sodium depletion on the anode side measured by ToF-SIMS. The main structural changes occur in the phosphate network with pyrophosphate units being converted to orthophosphate units during poling.

Also, the second harmonic generation of the poled glass-ceramics was evaluated through the measurements of Micro-SHG and Maker Fringes; in which it was verified that the poling treatment itself promotes its generation, considering the lack of SHG signal in the non-poled GC. The estimated SHG active layer for the GC_{45min}-10min is around 0.8 μm and for the GC_{30min}-1h30 is 3.2 μm. By data simulations it was confirmed that the origin of SHG is related to EFISH model. Additionally, it was calculated the $\chi^{(2)}$ of the GC, that is a one magnitude lower than the respective poled glass.

Therefore, it is concluded that it was possible to carry out Thermal Poling experiments in sodium tantalum phosphate glass-ceramics; develop a model to explain the main differences comparing to poling of glasses of same compositions, and to assess modifications on the materials and SHG responses due to treatment.

REFERENCES

DUSSAUZE, M. *et al.* Structural rearrangements and second-order optical response in the space charge layer of thermally poled sodium-niobium borophosphate glasses. **Journal of Physical Chemistry C,** Washington, v.111, p.14560-14566, 2007.

DUSSAUZE, M. *et al.* Thermal Poling of optical glasses: mechanisms and Second-Order Optical properties. **Int Journal of Applied Glass Science**, [S.l.], v.03, n.04, p.309-320, 2012.

DUSSAUZE, M. *et al.* Thermal poling behavior and SHG stability in arsenic-germanium sulfide glasses. **Optical Materials Express**, [S.l.], v.03, n.06, p.700-710, 2013.

HUANG, J. *et al.* Correlation between dielectric breakdown strength and interface polarization in barium strontium titanate glass ceramics. **Applied Physics Letter**, [S.l.], v.96, p.042902, 2010.

KAMITSOS, E.I. *et al.* **Physics and Chemistry of Glasses**, [S.l.], v.36, p.141, 1995.

KARAM, L. *et al.* The effect of the sodium content on the structure and the optical properties of thermally poled sodium and niobium borophosphate glasses. **Journal of Applied Physics,** [S.l.], v.128, 043106, 2020.

MALAKHO, A. *et al.* Crystallization and second harmonic generation in thermally poled niobium borophosphate glasses. **Journal of Solid-State Chemistry,** [S.l.], v.178, p.1888-1897, 2005.

PAN, M-J, *et al.* The Effect of interfacial polarization on the energy density of ferroelectric glass-ceramics. *In:* IEEE INTERNATIONAL SYMPOSIUM ON THE APPLICATIONS OF FERROELECTRICS, 15., 2006, Sunset Beach. **Anais** […]. Sunset Beach: IEEE, 2006, p.25-28.

PENG, X. *et al.* The effect of glass network structure on interfacial polarization in Na_2O–K_2O–Nb_2O_5–SiO_2–BaO glass-ceramics. **Journal of Alloys and Compounds**, [S.l.], v.845, p.155645, 2020.

RODRIGUEZ, V.; SOURISSEAU, C. General Maker-fringe ellipsometric analyzes in multilayer nonlinear and linear anisotropic optical media. **Journal of the Optical Society of America B**, USA, v.19, p.2650-2664, 2002.

VAN BEEK, L.K.H. The Maxwell-Wagner-Sillars effect, describing apparent dielectric loss in inhomogeneous media. **Physica,** [S.l.], v.26, p.66-68, 1960.

VERBIEST, T.; CLAYS, K.; RODRIGUEZ, V. **Second-order nonlinear optical characterization techniques:** an introduction, CRC Press, Boca Raton, 2009.

CHAPTER VII - STUDY OF NIOBIUM PHOSPHATE GLASSES CONTAINING SILVER

CHAPTER VII - STUDY OF NIOBIUM PHOSPHATE GLASSES CONTAINING SILVER

This chapter presents the preparation and characterization of phosphate glasses containing 45 mol% of Nb_2O_5 and silver in different amounts. For this, glasses were synthesized using the melt/quenching method; and characterized by: DSC, XRD, WDS, Raman Spectroscopy, UV-Vis and IR Spectroscopies and Refractive Index. Additionally, as a preliminary study, the glass containing sodium and 5 mol% of silver was thermally poled and evaluated by EDS.

VII-1 GLASSES PREPARATION

Potassium or sodium phosphate glasses containing 45 mol% of niobium oxide (Nb_2O_5) - without and with silver and also co-doped with antimony - were prepared using the traditional method of melt/quenching. The following precursor reagents were used: Nb_2O_5 (CBMM[39], optical grade), KH_2PO_4 (Vetec Química Final LTDA, 99%), NaH_2PO_4 (Nuclear, 99.9%)[40], $AgNO_3$ (Vetec Quimica, 99.8 %), and Sb_2O_3 (Merck, Emsure®). All glasses were prepared at the Materials Research Laboratory at UNIFAL in Poços de Caldas-MG (LABMAT-PC).

Table VII-1 presents the nominal molar composition of each prepared glass sample, the nomenclature used throughout the text, and the theoretical Nb/P ratio for all glasses.

Table VII-1 - Niobium phosphate glasses prepared: nominal molar composition, nomenclature and Nb/P ratio.

Glass Sample Composition	Nomenclature	Nb/P
$55KPO_3$-$45Nb_2O_5$	K45Nb	1.63
$54KPO_3$-$45Nb_2O_5$-$1AgNO_3$	K45Nb:1Ag	1.67
$52KPO_3$-$45Nb_2O_5$-$3AgNO_3$	K45Nb:3Ag	1.73
$50KPO_3$-$45Nb_2O_5$-$5AgNO_3$	K45Nb:5Ag	1.80
$46KPO_3$-$45Nb_2O_5$-$9AgNO_3$	K45Nb:9Ag	1.95
$52.5KPO_3$-$45Nb_2O_5$-$2.5Sb_2O_3$	K45Nb:Sb	1.71
$47.5KPO_3$-$45Nb_2O_5$-$5AgNO_3$-$2.5Sb_2O_3$	K45Nb:5AgSb	1.89
$55NaPO_3$-$45Nb_2O_5$	Na45Nb	1.63
$52NaPO_3$-$45Nb_2O_5$-$3AgNO_3$	Na45Nb:3Ag	1.73
$50NaPO_3$-$45Nb_2O_5$-$5AgNO_3$	Na45Nb:5Ag	1.80
$50.5NaPO_3$-$45Nb_2O_5$-$3AgNO_3$-$1.5Sb_2O_3$	Na45Nb:3AgSb	1.78
$47.5NaPO_3$-$45Nb_2O_5$-$5AgNO_3$-$2.5Sb_2O_3$	Na45Nb:5AgSb	1.89

Reference: AUTHOR.

[39] *Companhia Brasileira de Metalurgia e Mineração* (Brazilian Company of Metallurgy and Mining).
[40] As already mentioned in a previous chapter, at high temperatures, monobasic potassium/sodium phosphate decomposes to KPO_3/$NaPO_3$.

According to El-Sharkawy, Al-Shihry and Youssef (2006), silver nitrate decomposes as (equation VII-01):

$$2AgNO_{3\,(s)} \rightarrow Ag_2O_{(s)} + 2NO_{2(g)} + 1/2\ O_{2(g)}$$
$$Ag_2O_{(s)} \rightarrow 2Ag^{+} + 1/2\ O_{2(g)} \qquad \text{(VII-01)}$$

Precursors reagents were weighed, grinded and homogenized in an agate mortar, placed in a platinum crucible and then the crucible was taken in an oven (EDG 3PS, Innovatec or EDG-10P-S) for melting at 1170°C (potassium) or 1330°C (sodium) for 30 to 45 minutes. The quenching step was performed directly in the crucible exposed to air. After quenching, the glass was taken for annealing at 600-640°C for 12 hours and subsequent cooling at 5°C.min^{-1} until reaching room temperature, then being removed from the crucible, cut and polished - Figure VII-1.

Figure VII-1 - Preparation of niobium phosphate glasses in the crucible.

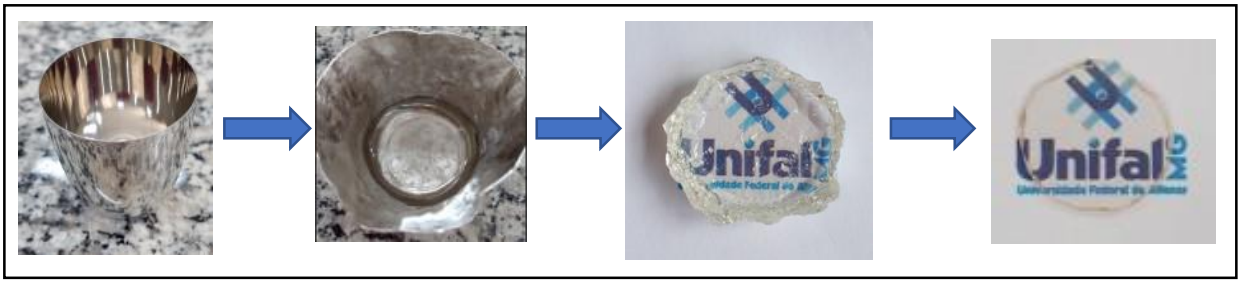

Reference: AUTHOR.

Glasses were cut and then polished in a Fortel model PLF polisher at LABMAT-PC, using water as solvent and sandpaper with grit numbers 400, 800, 1200 and 2400 and a 1 µm, 0.3 µm and 0.05 µm alumina. Figure VII-2 shows photos of all the glasses after polishing, and as can be seen, all glasses are visually transparent. It is also observed that the glasses containing antimony are colored. As reported by Santos (2021) for phosphate glasses with tungsten co-doped with silver and antimony, increasing silver amount, the color of the glass changed from yellow, to orange and then brown. The studied glass containing potassium co-doped with Ag and Sb presented a yellow color that was not observed in the glass doped only with silver in the same amount. However, the glass doped only with antimony also presented a yellow color; so, in this case not necessarily is possible yet to attribute the color of the glass only due to co-doping.

Figure VII-2 - Niobium phosphate glasses prepared.

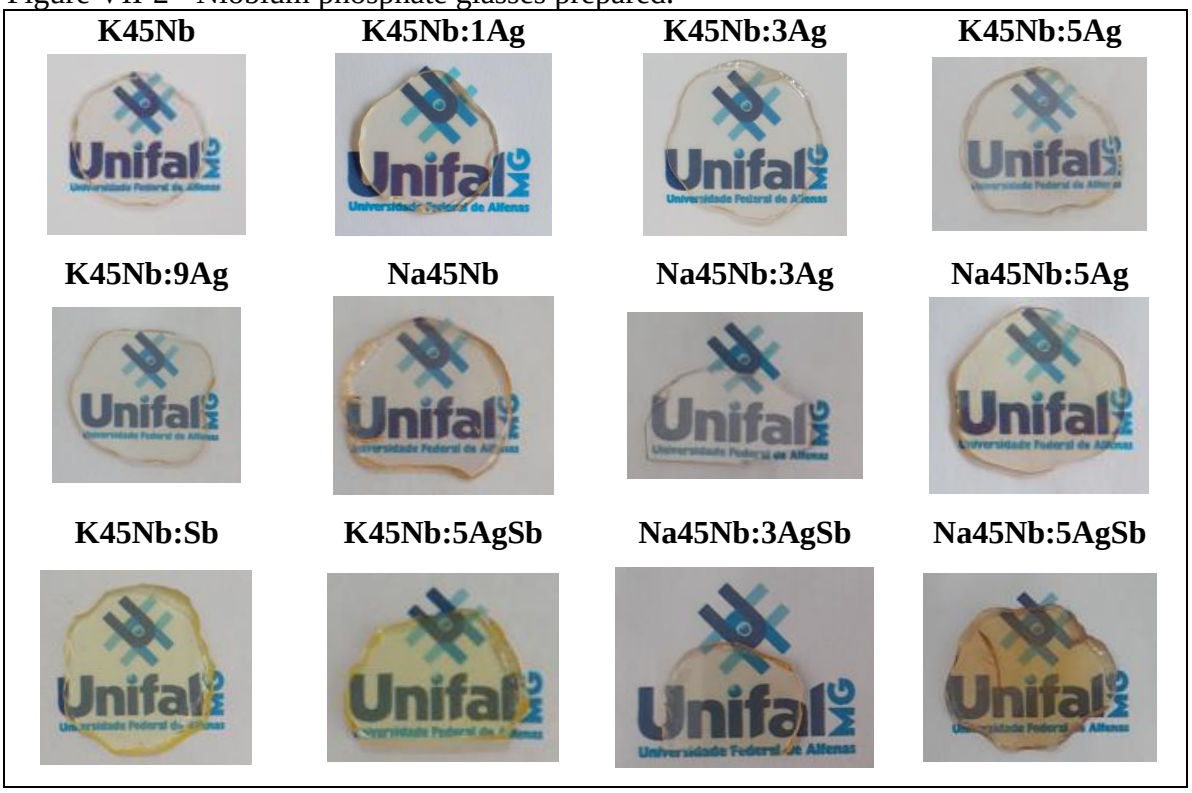

Reference: AUTHOR.

In the case of glasses containing sodium, two different co-doping were performed, with 3 and 5 mol% of silver. Na45Nb:3AgSb glass does not present a visually yellow color as the other glasses; however, Na45Nb:5AgSb glass presented an orange color. So, a glass doped only with antimony was prepared (Na45Nb:Sb), and as shown in Figure VII-3, it presented a yellowish color. So, in this case, sodium phosphate high niobium glass prepared as described, the co-doping is somehow affecting the color of the glass.

Thus, the Na45Nb:5AgSb glass was prepared with different annealing conditions: (i) no annealing, (ii) annealing at temperature of Tg minus 40°C (already presented in Figure VII-2) and (iii) annealing at temperature of Tg (Tg value was obtained from DSC curve that is presented in the next topic). Figure VII-3 presents photos of these samples after polishing, and as can be seen the annealing temperature influences in the characteristics of the final glass. Probably, antimony induced reduction and agglomeration of Ag-NP as the annealing temperature increases, and that can be better discussed through an Uv-Vis absorption (presented in a next topic).

Figure VII-3 - Na45Nb:Sb glass and Na45Nb:5AgSb glass samples prepared with different annealing conditions.

Na45Nb:Sb	Na45Nb5Ag:Sb		
	No annealing	Annealing (Tg-40°C)	Annealing (Tg)
			

Reference: AUTHOR.

Also, it is important to mention that it was possible to incorporate high amount of silver ions into the glasses (9 mol% - nominal - for glass with potassium) maintaining the high amount of niobium oxide (45 mol% - nominal). Phosphate glasses are known for their high solubility of several oxide modifiers and intermediates (DMITRYUK *et al.*, 1996), e.g., Hsu *et al.* (2010) incorporated 10 mol% of silver oxide in a sodium phosphate glass with molar composition $27Na_2O$-$9Al_2O_3$-$54P_2O_5$-$10Ag_2O$, that is, with a high amount of phosphate (54 mol%). An amount of 15 mol% of AgCl was incorporated in a potassium phosphate glass containing 25.5 mol% P_2O_5 and 34 mol% of WO_3, that is, with a W/P ratio of 0.67 (Marcondes *et al.*, 2022), which is almost 3 times lower than Nb/P ratio of sample K45Nb:9Ag. In this work, the amount of phosphate was not that high (23 to 27.5 mol% P_2O_5), so, even with the higher amount of niobium related to phosphate, it was possible to incorporate a high amount of silver ions into this glass composition.

VII-2 X-RAY DIFFRACTION AND THERMAL ANALYSIS OF GLASSES

For samples containing potassium, XRD spectra of the powdered glasses were recorded using a Rigaku Ultima IV equipment located at UNIFAL crystallography laboratory - *campus* Santa Clara - Alfenas, in Bragg-Brentano θ-θ geometry with CuKα wavelength (λ= 1.5418 Å), continuous scanning, step of 0.1° in 2θ, ranging from 10 to 70°. For samples containing sodium, XRD spectra of the powdered glasses were recorded using a Rigaku DMax/2500PC equipment, located at UNIFEI (Federal University of Itajubá) crystallography laboratory - *campus* Itabira with CuKα wavelength (λ= 1.5418 Å), continuous scanning, step of 0.1° in 2θ, ranging from 10 to 70°. As expected, all samples present only the characteristic halo of non-crystalline materials, as presented in Figure VII-4.

Figure VII-4 - XRD of silver niobium phosphate glasses with: (A) potassium and (B) sodium.

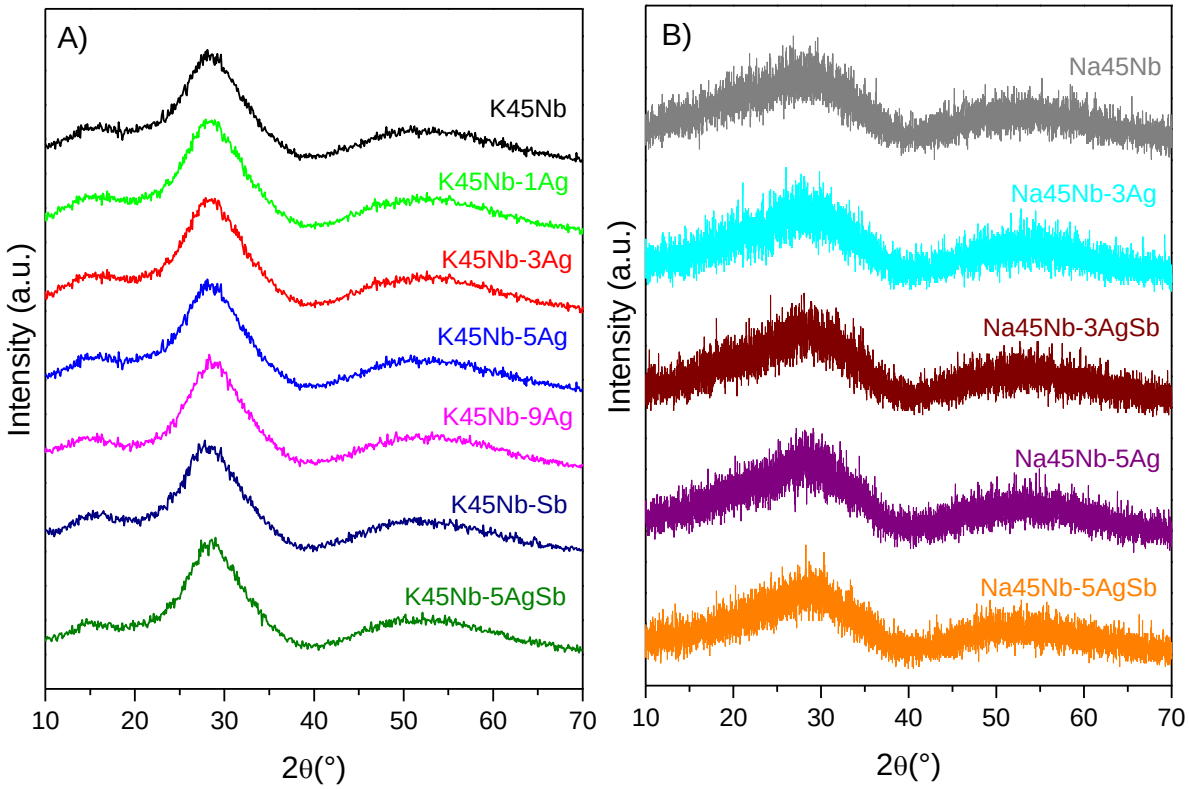

Reference: AUTHOR.

Thermal analysis measurements of glasses were made by DSC at the LABMAT-PC in a Netzsch STA 449 Jupiter F3 equipment from 200°C to 1200°C with heating rate of 10°C.min^{-1}, N_2 purge gas flow 100mL.min^{-1} and protection 20mL.min^{-1}, in a covered Pt/Rh crucible. Figure VII-5 presents the DSC curves of silver niobium phosphate glasses and Table VII-2 presents the characteristic temperatures taken from the curves.

From the data it is observed that all glasses present the glass transition and also two exothermic events related to crystallization of two well distinguish crystalline phases. According to studies of Cassani (2022), for glasses composition $50MPO_3$-$50Na_2O_5$ (M = Na or K), the crystalline phases obtained after heat treatment performed was attributed to $Na_2Nb_8O_{21}$, $NaNbO_3$, Nb_2O_5 and an unknown phase. In the case of the glass studied for Malakho *et al.* (2005), composition of $52NaPO_3$-$48Nb_2O_5$, the phases after heat treatment are attributed to a sodium niobate phase (probably $Na_2Nb_8O_{21}$) and to $Na_4Nb_8P4O_{32}$ (similar to phosphate glasses containing tantalum presented in Chapter V).

Figure VII-5 - DSC curves of silver niobium phosphate glasses with: A) potassium and B) sodium.

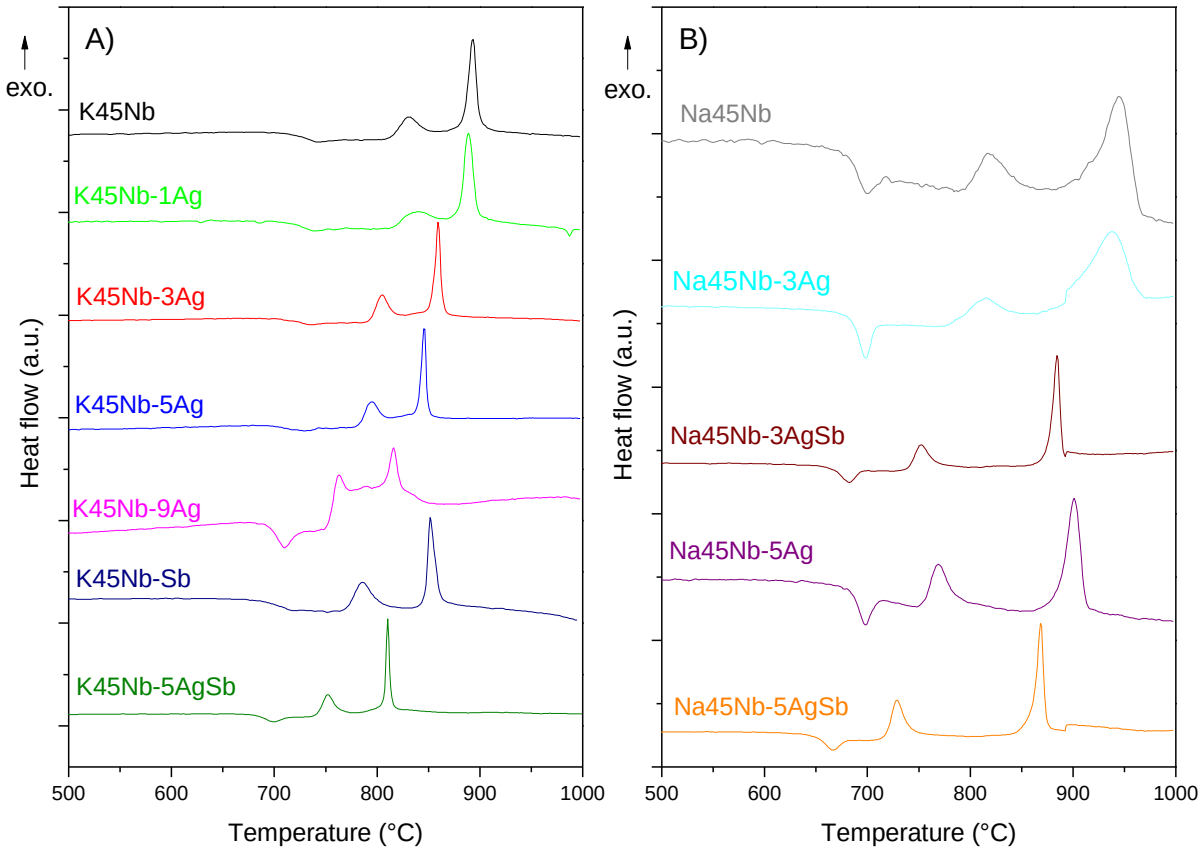

Reference: AUTHOR.

Table VII-2 - Characteristic temperatures of silver niobium phosphate glasses.

Sample	Tg (°C)	Tx_1 (°C)	Tx_1-Tg (°C)	Tc_1 (°C)	Tx_2 (°C)	Tc_2 (°C)
K45Nb	712	810	98	830	870	890
K45Nb:1Ag	716	806	90	845	874	889
K45Nb:3Ag	702	786	84	805	845	860
K45Nb:5Ag	693	776	83	795	835	845
K45Nb:9Ag	690	749	59	762	796	816
K45Nb:Sb	685	763	78	786	835	851
K45Nb:5AgSb	683	735	52	751	786	810
Na45Nb	682	794	112	820	890	945
Na45Nb:3Ag	675	775	100	815	880	938
Na45Nb:3AgSb	662	734	79	753	864	884
Na45Nb:5Ag	670	749	79	769	859	900
Na45Nb:5AgSb	638	712	74	728	837	868

Reference: AUTHOR.

The undoped glasses presented Tg values expected for glasses of these compositions. The $50KPO_3$-$50Nb_2O_5$ glass prepared by Lima (2014) presented a Tg value of 739°C and this value was 734°C for the glass of same composition prepared by Silva (2022); and the $50NaPO_3$-$50Nb_2O_5$ glass prepared by Cassani (2022) a Tg value of 703°C. Comparing the presence of the different alkaline modifiers, sodium glasses present a lower Tg, which was already observed by Cassani (2022).

With the increase of silver contents, it is observed that Tg decreases (as better observed by the graph in Figure VII-6A). For the glass $58NaPO_3$-$42Nb_2O_5$ with 0.5% of silver (FARGIN *et al.*, 2009; SMOGOR *et al.*, 2009) no significant effect of the silver addition on glass Tg was noticed, only an increase in the slope of the curve from T_x. In this case only a small amount of silver was added into the glass. Otherwise, a decrease in T_g was observed by Hsu *et al.* (2010) and Marcondes *et al.* (2022) with silver increment. So, the Ag addition may stabilize NBO in the glass matrix, decreasing the mean bond strength and network connectivity.

Figure VII-6 - A) T_g (°C) and B) T_{x1}-T_g (°C) of niobium phosphate glasses with increase of silver content.

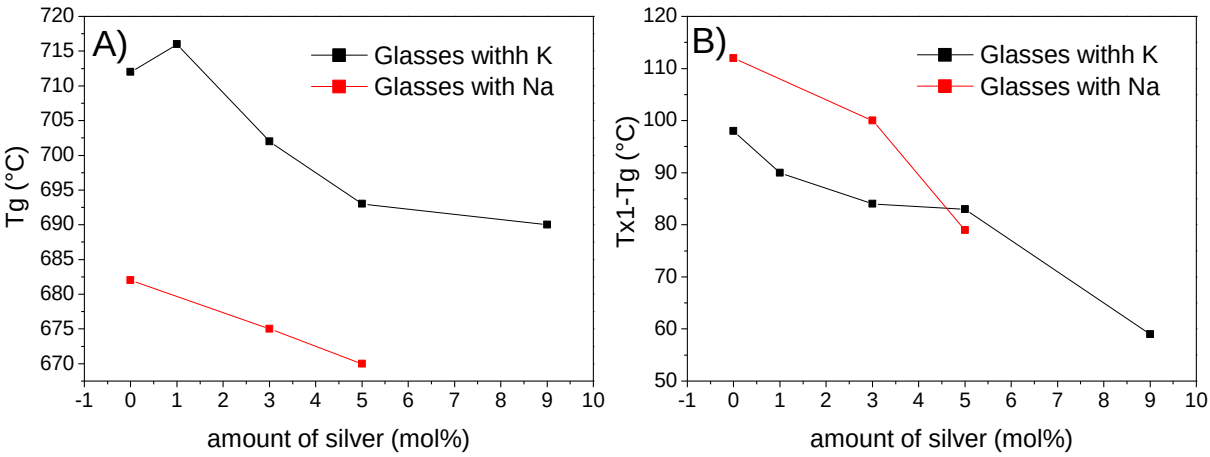

Reference: AUTHOR.

Concerning the values of (T_{x1}-T_g), that indicate the thermal stability against crystallization, it decreases with silver increment (Figure VII-6B), achieving almost 50°C for K45Nb:9Ag. It is known that silver ions can be considered as a nucleating agent promoting the crystallization phenomenon (FARGIN *et al.*, 2009; GLEBOV, 2004; SMOGOR *et al.*, 2009).

Regarding the Na45Nb:5AgSb glass that was prepared with annealing at Tg temperature and without annealing, Figure VII-7 presents the corresponding DSC curves. As observed, there is no significant difference in the curves and characteristics temperatures, except for a slight decrease in the Tc of the second peak. Also, glass transition of annealed glasses presented an

endothermic phenomenon, reported as an enthalpic relaxation of the network, that is not observed in the glass without annealing. This effect is directly related to the thermal history of the glass. Thermodynamically, an annealed glass achieves a reduced enthalpy state compared to an unannealed glass of the same composition. Then, when the sample is reheated during thermal analysis, the atoms absorb energy at temperatures close to Tg, acquiring greater mobility and thus a thermodynamic equilibrium characteristic of a rubbery material (BARBOSA, 2017).

Figure VII-7 - DSC curves of Na45Nb:5AgSb glass samples with different annealing conditions.

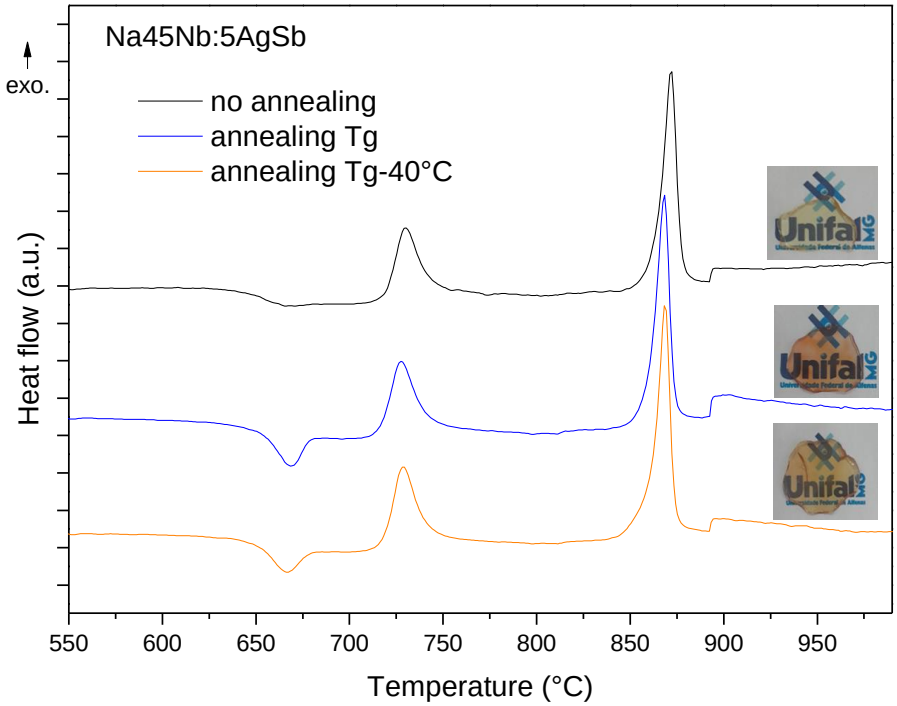

Reference: AUTHOR.

VII-3 WAVELENGTH-DISPERSIVE X-RAY AND RAMAN SPECTROSCOPIES

To verify the composition of niobium phosphate glasses, Wavelength-Dispersive X-Ray Spectroscopy (WDS) were performed on samples in the Vitreous Materials Laboratory (LaMaV - *Laboratório de Materiais Vítreos*) at UFSCAR (Federal University of São Carlos, *Universidade Federal de São Carlos*) using an WDXRF Rigaku ZSX Orimus II equipment and results expressing as an oxide (Ox-wt.%) after the matrix correction and atomic proportions based on a fixed oxygen normalization basis. Experimental results of oxides (wt.%) comparing

to theoretical composition [41] are shown in Table VII-3. Phosphate is expressed as $2MPO_3 \rightarrow P_2O_5 + M_2O$ (M = Na or K).

First, as expected and confirmed by experimental results, the amount of silver in fact increases in the samples. Also, as silver increases, the amount of phosphate and alkaline decreases.

Table VII-3 - Theoretical and Experimental (WDS) % wt. of oxides in niobium phosphate glasses.

Glass Sample	% wt.									
	Theoretical					Experimental (WDS)				
	P_2O_5	M_2O	Nb_2O_5	Ag_2O	Sb_2O_3	P_2O_5	M_2O	Nb_2O_5	Ag_2O	Sb_2O_3
K45Nb	21.15	14.04	64.81	-	-	15.5	13.0	71.5	-	-
K45Nb:1Ag	20.77	13.78	64.82	0.63	-	14.6	12.6	71.9	0.90	-
K45Nb:3Ag	20.00	13.27	64.85	1.88	-	13.5	12.0	71.9	2.60	-
K45Nb:5Ag	19.23	12.77	64.86	3.14	-	13.2	11.6	72.0	3.20	-
K45Nb:9Ag	17.71	11.75	64.89	5.65	-	12.3	10.2	72.1	5.40	-
K45Nb:Sb	19.72	13.09	63.33	-	3.86	15.3	10.4	70.6	-	3.70
K45Nb:5AgSb	17.86	11.85	63.36	3.07	3.86	13.0	9.03	71.5	2.42	4.05
Na45Nb	22.21	9.70	68.09	-	-	15.6	7.13	77.0	-	-
Na45Nb:3Ag	20.95	9.15	67.93	1.97	-	14.7	6.90	76.3	2.10	-
Na45Nb:5Ag	20.12	8.78	67.82	3.28	-	14.3	7.36	75.2	3.14	-
Na45Nb:3AgSb	20.03	8.74	66.85	1.94	2.44	13.3	6.48	75.5	1.97	2.75
Na45Nb:5AgSb	18.61	8.12	66.06	3.19	4.02	13.1	5.81	74.1	3.21	3.78

Reference: AUTHOR.

Comparing theoretical values with experimental values, in all samples the amount of phosphate is much less than expected by the nominal composition, and consequently, the %wt. of niobium higher. That can be explained by the loss of phosphate at high temperatures, that is observed experimentally. In fact, higher the melting temperature, higher the loss of phosphate, as observed by the study of Cassani (2022) in which the loss increases with temperature and time, and it is intensified above 1300°C.

Thus, these results confirm that the final glasses have an even higher Nb/P ratio than previously estimated from nominal composition (shown in Table VII-4). Actually, the ratio varies from 2.46 for K45Nb to 3.13 for K45Nb:9Ag; and from 2.63 for Na45Nb to 2.80 for Na45Nb:5Ag. For these glasses the higher theoretical ratio was 1.95 for K45Nb:9Ag. So, silver was incorporated in glasses that contain in average 54.86 ± 1.52 mol% Nb_2O_5 and only 19.63 ± 1.22 mol% P_2O_5.

[41] Theoretical composition was calculated in terms of Ag_2O instead of $AgNO_3$ accordingly with equation VII-01.

Table VII-4 also shows the theoretical and experimental % of silver into glasses, considering the molar composition of glass containing silver oxide. Since phosphate is lost, the % of silver is higher than predicted theoretically.

Table VII-4 - Theoretical (T) and Experimental (E) ratios of Nb/P and Ag (%).

Glass Sample	Nb/P (T)	Nb/P (E)	Ag (%) (T)	Ag (%) (E)
K45Nb	1.63	2.46	-	-
K45Nb:1Ag	1.67	2.63	1.005	1.520
K45Nb:3Ag	1.73	2.86	3.045	4.472
K45Nb:5Ag	1.80	2.91	5.128	5.514
K45Nb:9Ag	1.95	3.13	9.424	9.521
K45Nb:Sb	1.71	2.46	-	-
K45Nb:5AgSb	1.89	2.93	5.128	4.344
Na45Nb	1.63	2.64	-	-
Na45Nb:3Ag	1.73	2.79	3.045	3.546
Na45Nb:5Ag	1.80	2.80	5.128	5.252
Na45Nb:3AgSb	1.78	3.05	3.045	3.398
Na45Nb:5AgSb	1.89	3.02	5.128	5.635

Reference: AUTHOR.

To study the structural modifications, Raman spectroscopy of silver niobium phosphate glasses was performed using an XploRA PLUS micro-Raman spectrometer (Horiba), located at the C-Labmu (multiuser lab complex, *complexo de laboratórios multiusuários*) in Ponta Grossa State University (UEPG - *Universidade Estadual de Ponta Grossa*). The analysis was performed on polished samples, in the range of 150 to 1500 cm^{-1}, acquisition time of 30s, objective of 50x, with laser of 638 nm. Figure VII-8 presents the normalized spectra (at 655 cm^{-1}) for potassium niobium phosphate glasses according to the increase in silver content, Figure VII-9 presents the normalized spectra (at 655 cm^{-1}) of potassium niobium phosphate glasses containing 5 mol% of Ag and Figure VII-10 presents the normalized spectra (at 665 cm^{-1}) for sodium niobium phosphate glasses.

Raman bands attributions were already described by Cassani (2022), Karam *et al.* (2020), Lima (2014) and Silva (2022). **Band 1** located around 215 cm^{-1} could be attributed to deformations of O-Nb-O bonds in [NbO_6] octahedra, suggesting the incorporation of niobium atoms in the octahedral geometry in the glass network. **Band 2** located between 385 and 500 cm^{-1}, can be attributed to the Nb-O stretching bonds that share edges in the [NbO_6] octahedron or PO_4 tetrahedron. Between 500 and 740 cm^{-1} - **band 3**, Nb-O-Nb units linking [NbO_6] octahedrons in a three-dimensional niobate network are present. The region between 740 and 880 cm^{-1} - **band 4**, corresponds to the so-called “isolated” bonds in the Nb-O-Nb octahedron,

that is, bonded only to the phosphorus tetrahedra. Also, according to Muñoz *et al.* (2019), P-O-P symmetric stretching occurs between 690-790 cm^{-1}. **Band 5** between 880 and 970 cm^{-1} correspond to bonds in the Nb-O-P sequence connecting the niobium octahedron and the phosphorus tetrahedron. Or it can be attributed to P-O-P asymmetric stretching. In **bands 6** - higher than 970 cm^{-1} are the more covalent Nb-O bond stretching modes. Also, this band can be attributed to the P-O terminal bonds of phosphate units.

Figure VII-8 - Raman spectra of potassium niobium phosphate glasses with increasing silver content.

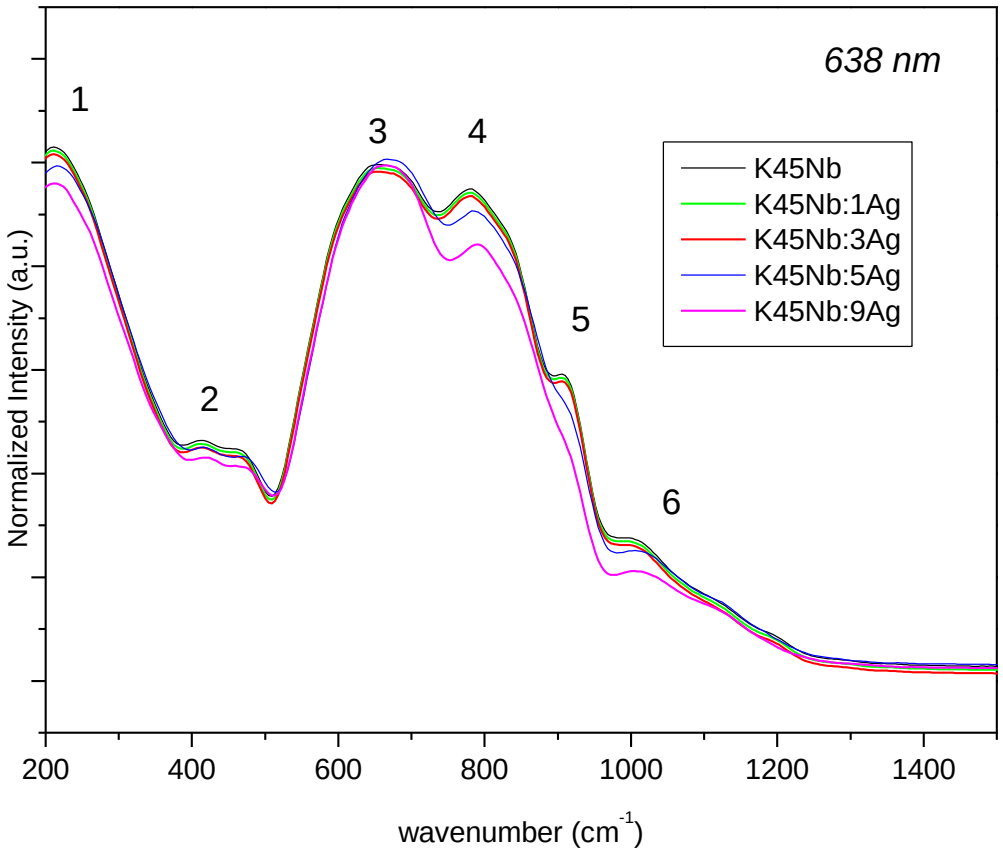

Reference: AUTHOR.

So, for potassium niobium phosphate glasses with increment of silver, it is observed that all bands decrease when comparing to band 3. As observed by WDS measurements, and as expect, the Nb/P ratio increases with Ag addition, since Ag replaces phosphate, so the bonds linkage to P also decrease. For the glass co-doping with Sb, less phosphate is present, so these bands decrease even more.

Figure VII-9 - Raman spectra of potassium niobium phosphate glasses with 5%$AgNO_3$.

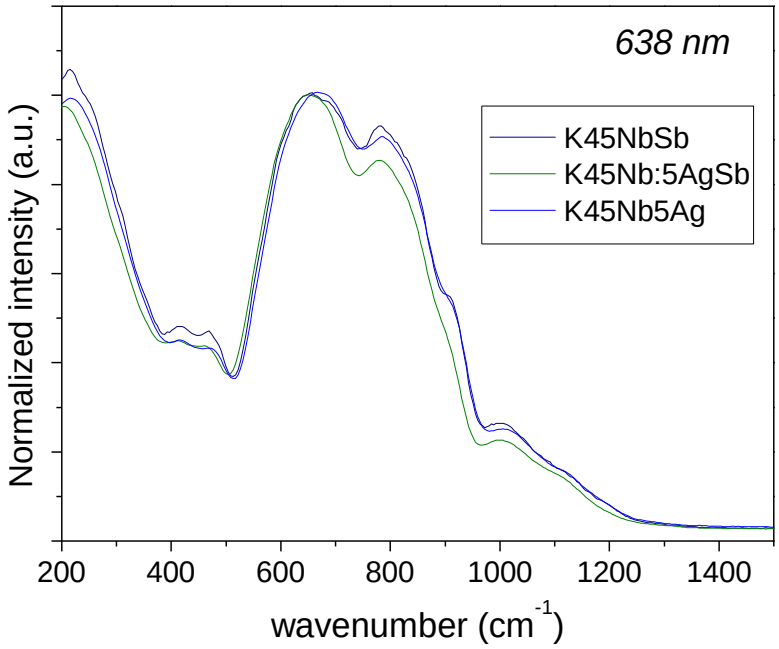

Reference: AUTHOR.

Figure VII-10 - Raman spectra of sodium niobium phosphate glasses with increasing silver content.

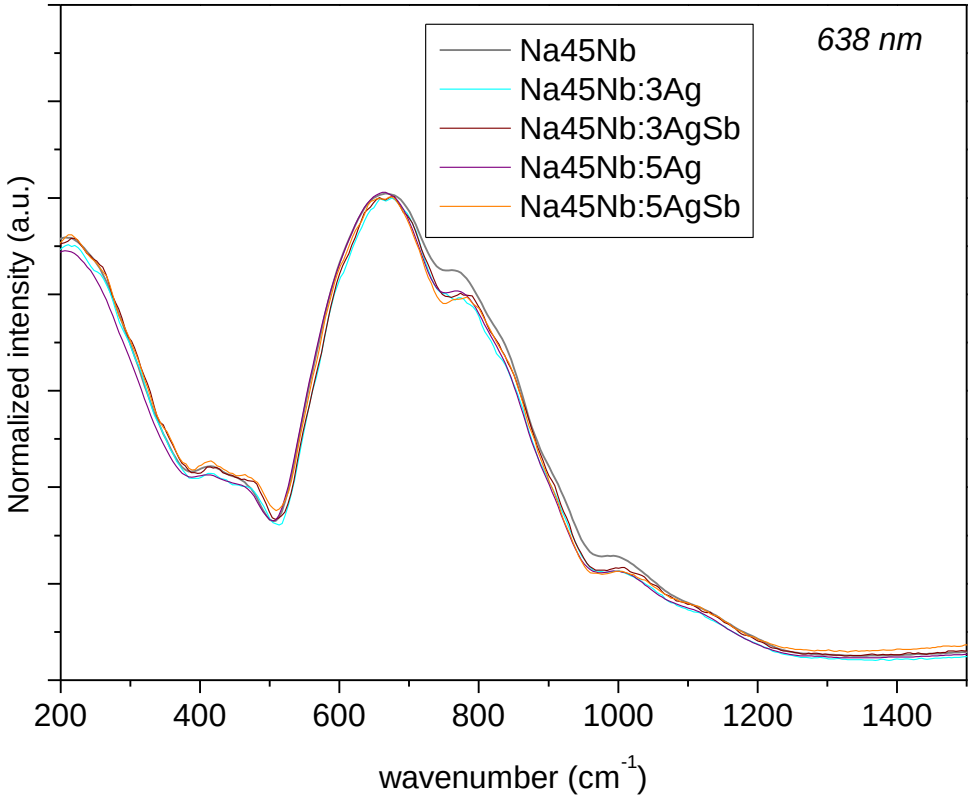

Reference: AUTHOR.

In case of sodium niobium phosphate glasses, the decrease of the bands compared to band 3, is also observed, but in a lower scale. That is probably related to the ionic radius of potassium when compared to sodium. Fargin *et al.* (2009) did not observe any difference in Raman spectra for the sodium niobium phosphate glass doped with 0.5 mol% of silver, as also Lima (2014) with a potassium niobium phosphate glass doped also with 0.5 mol% of silver.

VII-4 OPTICAL ANALYSIS OF GLASSES: TRANSPARENCY WINDOW AND REFRACTIVE INDEX

For transparency window determination, UV-Vis-NIR and Fourier Transform Infrared (FTIR) spectroscopy were used. Spectroscopy in the visible ultraviolet (UV-Vis-NIR) region was performed with an Agilent Cary 7000 UV-Vis-NIR spectrophotometer at LABMAT-PC, with spectra obtained between 200 nm and 2000 nm, with a resolution of 0.5 nm and a scanning speed of 150 $nm.s^{-1}$. For some samples, this measure was made at C-Labmu - UEPG, from 200 to 800 nm, using a Varian Cary 50 spectrophotometer and the same parameters. FTIR analysis was performed on an Agilent Cary 630 FTIR spectrometer at LABMAT-PC, with wavenumber ranging from 650 to 4000 cm^{-1} and resolution of 4 cm^{-1}.

Figure VII-11 show the transparency windows of potassium niobium phosphate glasses doped with silver (since the refractive index of all samples were not measured, it was not performed a correction of the α considering Fresnel reflection losses) in which all samples present a good transparency, as observed visually.

Antimony/silver-co-doped potassium niobium phosphate glasses transparency windows are shown in Figure VII-12. Cut-off of the glasses increases with co-doping, from 370 nm to 395 nm, that is due to Sb also being an element with molar mass higher than phosphorus. The infrared transparency limit is also around 6500 nm.

Figure VII-11 - Transparency window of potassium niobium phosphate glasses with addition of silver.

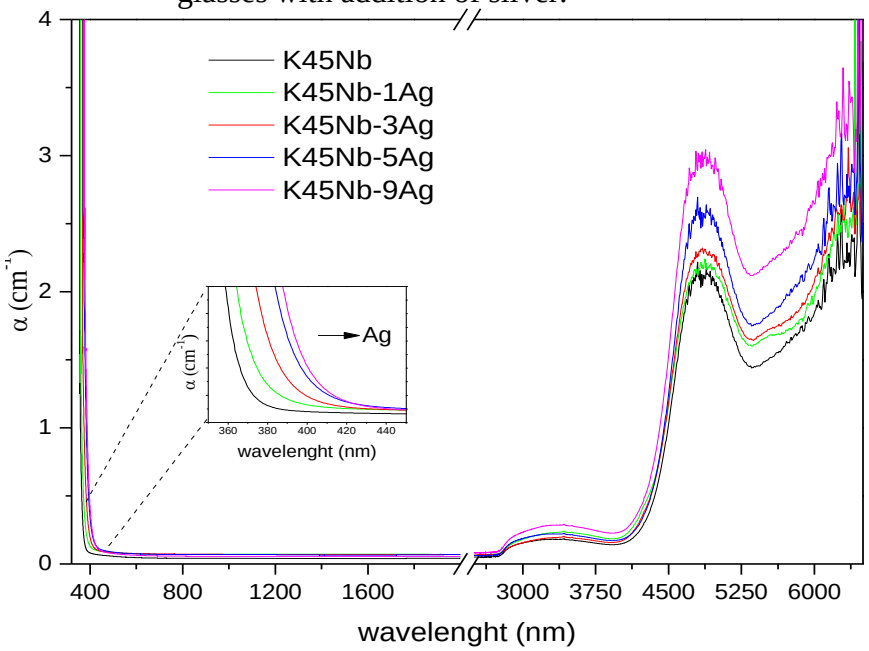

Reference: AUTHOR.

Figure VII-12 - Transparency window of potassium niobium phosphate glasses with 5 mol% of Ag.

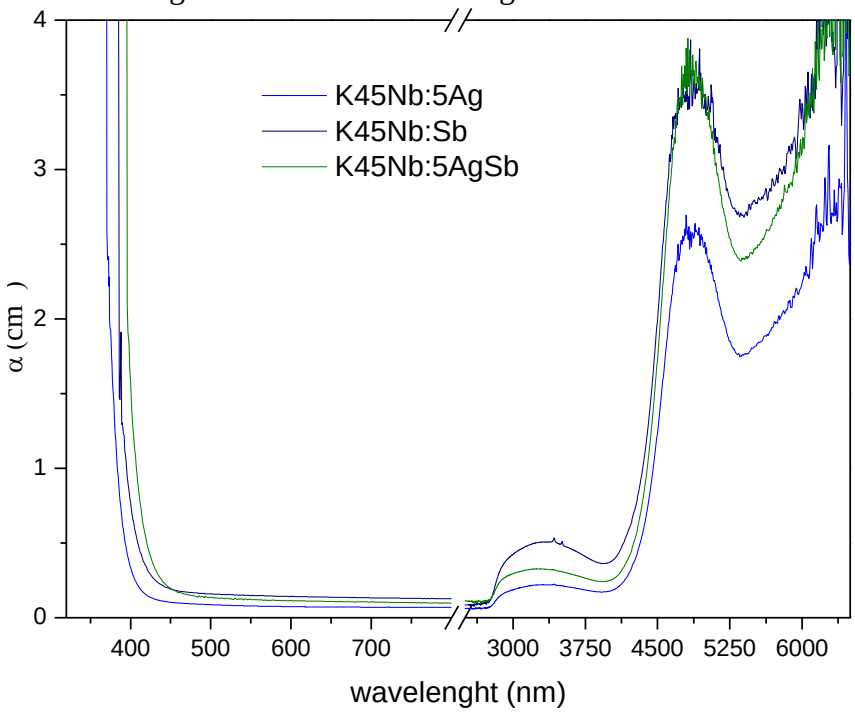

Reference: AUTHOR.

Transparency windows of sodium niobium phosphate glasses are shown in Figure VII-13, and present a similar behavior from previous glasses, with a cut-off from 360

nm[42] for silver free sample to 375 nm for Na45Nb:5Ag sample; and infrared transparency limit being around 6500 nm.

It is important to mention that for all these glasses, with both potassium or sodium, doped or co-doped, any absorption band associated to plasmon resonance is identified for glasses prepared in the described conditions. In fact, no absorption band is observed in the spectra that could be attributed to NP or NC, suggesting that silver is presented in a form of ions Ag^{+}. In general, absorption of silver ions occurs in wavelengths lower than the band gap of the studied glasses, so it cannot be observed. However, other analysis could be performed to better discussed this point.

Figure VII-13 - Transparency window of sodium niobium phosphate glasses with addition of silver.

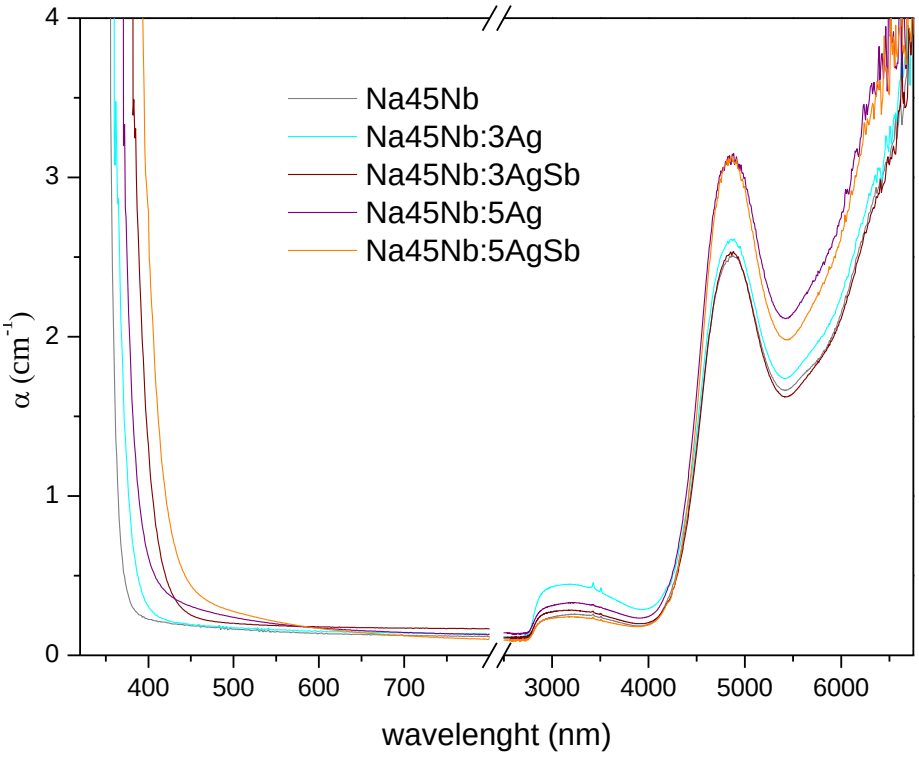

Reference: AUTHOR.

Transparency windows of sample Na45Nb:5AgSb prepared with different annealing conditions are shown in Figure VII-14. Sample annealed at Tg present a red color, and its spectra shows an absorption band centered at 495 nm. This band is attributed to plasmon resonance of silver nanoparticles Ag^{0}. In the glass $92[NaPO_3\text{-}WO_3]\text{-}4Sb_2O_3\text{-}4AgNO_3$ studied by Santos (2021), this band was centered, e.g., at 535nm. This difference is attributed to size

[42] Borophosphate glass with 42mol% Nb_2O_5 presented a cut-off of 350 nm (Fargin *et al.*, 2009).

and shape of NP and the matrix. In general, increasing the nanoparticle size, or occurring aggregation of nanoparticles, will cause a sensible broadening of the plasmonic band towards larger wavelengths.

Glass annealed at (Tg-40°C) shows a red-shift comparing to the untreated glass. And, despite its orange color, did not present any absorption band. Maybe, in this case, concentration and/or size of Ag-NP were not enough to a plasmon band be detectable, or sample still does not present silver as NP.

Figure VII-14 - Transparency window of Na45Nb:5AgSb glass samples with different annealing conditions.

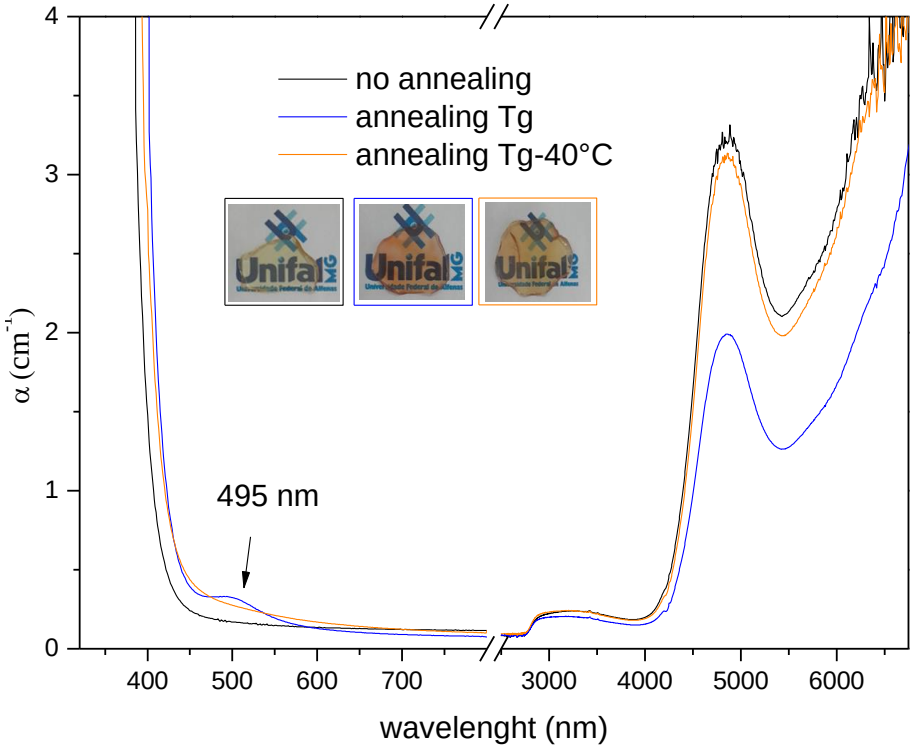

Reference: AUTHOR.

So, it is identified that annealing temperature is a key factor for the final optical properties of glass prepared with this molar composition. The reasons for the color dependence with synthesis conditions are still not well understood, but as already demonstrated for several transition metal containing glasses, redox equilibria are shifted to reduced states for higher (melt) temperatures whereas lower (melt) temperatures promote more oxidized species (MARCONDES *et al.*, 2023). In this sense, it is suggested that the quenching temperature may influence the ratio of oxidized silver species (Ag^{+}) in glass, being higher for lower temperatures of quenching and lower for higher temperatures, promoting the formation of Ag-NP responsible for the reddish color.

Refractive index measurements were performed on samples K45Nb:5Ag and K45Nb:9Ag. This measurement was made on a HORIBA Jobin Yvon Spectroscopic Ellipsometry located at State University of Maringá (UEM, *Universidade Estadual de Maringá*). The measurement was made in a range of 200 to 850 nm, using the DP2 software and the conversion of the measures with the WINELLI software.

The curves obtained are presented in Figure VII-15, in which the value of the refractive index for a wavelength of 530 nm is 1.858 for sample K45Nb:5Ag and 1.877 for K45Nb:9Ag. As observed by the curves, refractive index decreases with the increase of the wavelength due to being inversely proportional to the speed of propagation of the wave in the medium; and consequently, inversely proportional to the wavelength. These values are, for example, lower than phosphate glass containing 45 mol% of tantalum oxide presented in Chapter III-4, that was 1.908 (λ = 532 nm).

Figure VII-15 - Refractive index curves for K45Nb:5Ag and K45Nb:9Ag glasses.

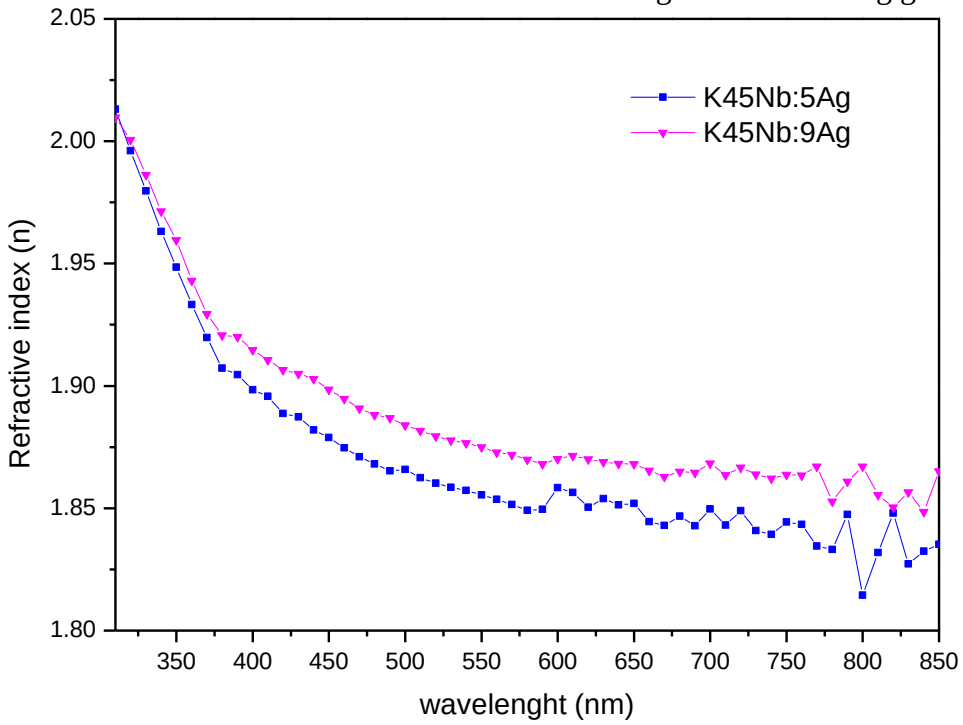

Reference: AUTHOR.

Also, refractive index increases with increment of silver, which is in accordance with the bathochromic shift observed in transparency window. Same behavior was observed by Marcondes *et al.* (2022) for glasses (100-x)[(60KPO_3-40WO_3)-xAgCl (0≤ x ≤ 20 mol%), passing from 1.643 to 1.682 (at 543 nm).

VII-5 THERMAL POLING OF NIOBIUM PHOSPHATE GLASSES

As a preliminary study, $50NaPO_3$-$45Nb_2O_5$-$5AgNO_3$ (Na45Nb:5Ag) glass was thermally poled at the LABMAT-PC in UNIFAL-MG (Brazil) in a Poling cell that was developed with *Flyever* - Figure VII-16. It consists of a hermetic enclosure with a vacuum inlet, an atmosphere control (N_2) and a pair of fan boxes. A temperature controller (with a heating limit of 400°C) is connected to the inserted heaters and a thermocouple at the base of the cell, used also as a cathode, to control the heating program and cooling during Thermal Poling treatment. A high voltage source (limit of 3 kV) is connected to the cell and a program controls the high voltage source and the current variation over time.

Figure VII-16 - Thermal Poling assembly at UNIFAL-MG (Brazil).

Reference: AUTHOR.

It was used a glass slide (0.5 x 0.5 cm) with a thin film of tin oxide and indium (ITO, 100 nm and 8 -12 Ω/sq) as anode electrode, and the sides without ITO to become conductors were metallized using a conductive silver ink. In the cathode side was used an n-doped silicon wafer with the same size as the ITO electrode, and a 130-160 μm borosilicate glass (22x22 mm) was used to prevent the sample from adhering to the cathode, impairing the optical quality; and also functioning as an open cathode. All the process occurred under 1.5 $L.min^{-1}$ N_2 flow. The

system was heated to 300°C at a rate of 10°C.min^{-1}, and after reaching the temperature, a pre-determined DC voltage - 1.5 kV or 1 kV - was applied (rate of 100 V.min^{-1}). After reaching the voltage threshold, the maximum current accomplished a maximum and then decreases since the ions migrate towards the cathode over the treatment time, and the resistivity of the anodic layer increases (that occurred only for 1.5 kV). After the current reached a value close to 0 mA, the temperature was reduced, with the electrical voltage remained until 80°C, and then the voltage was turned off and the sample removed.

Figure VII-17 presents DC applied voltage and detected current observed during Thermal Poling of sample Na45Nb:5Ag with the two different DC voltage.

Figure VII-17 - Data (DC voltage applied and detected current) from Thermal Poling experiments on Na45Nb:5Ag glass sample - 300°C: A) 1.5 kV and B) 1 kV.

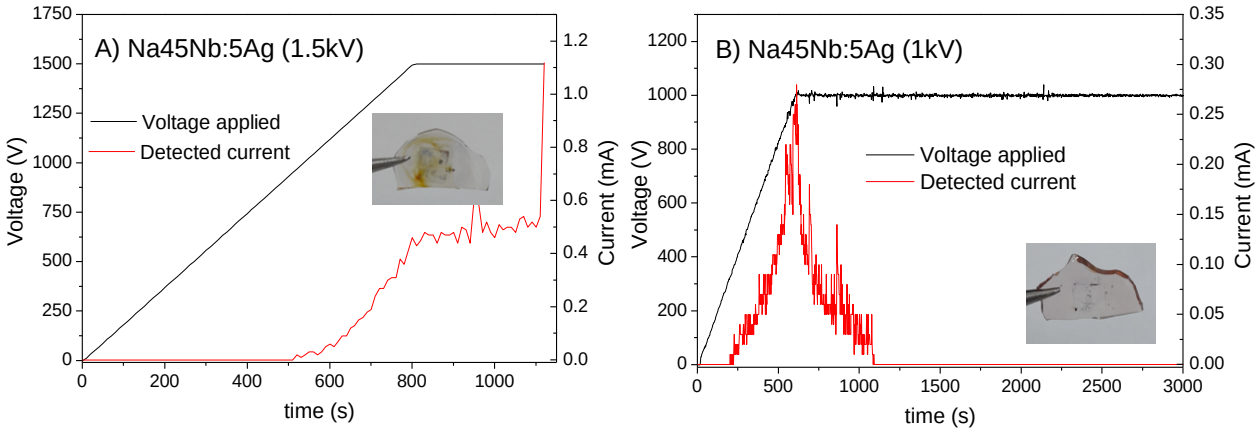

Reference: AUTHOR.

As observed in Figure VII-17A, electric current had a “jump” and so the test was interrupted. So, a second test was performed on sample keeping the same temperature and decreasing voltage, that is, 1kV. As presented in Figure VII-17B, electric current curve presented a classical behavior, with poling occurring as expected, reaching a maximum and then decreasing.

VII-6 EVALUATION OF THERMAL POLING BY EDS

As a preliminary evaluation of the effect of Thermal Poling on niobium phosphate glass containing silver, it was used Energy-Dispersive Spectroscopy (EDS) measurement that allowed the identification of the elemental composition of the studied sample. The measurement was made at Instrumental Chemical Analysis Center (CAQI, *Central de Análises Químicas Instrumentais*), University of São Paulo (USP) in São Carlos-SP, using an JSM 7200F (JEOL)

equipment. It was made in the cross-section of sample (as shown previously in Figure IV-15). Figure VII-18 presents EDS mapping for sample Na45Nb:5Ag-1kV.

Figure VII-18 - EDS mapping on cross-section of sample Na45Nb:5Ag-1kV.

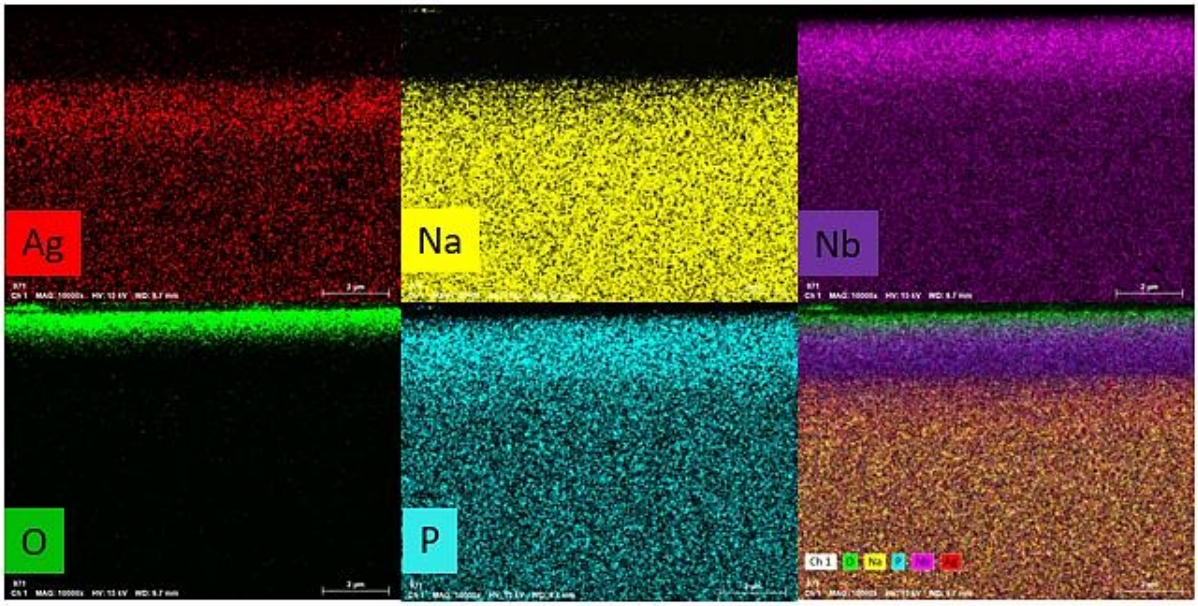

Reference: AUTHOR.

As observed by the mapping, there is a depletion layer of sodium under the anode surface after Thermal Poling. Besides sodium, silver was also depleted under the anode along approximately the same depth. For silver distribution, an interesting migration behavior is observed with three different regions (FIGURE VII-19): (1) a depleted sodium and silver layer of approximately 2.2 µm, (2) a layer of approximately 1.8 µm with a high silver content, (3) the bulk sample with a homogeneous silver content corresponding to the measured average silver concentration.

Figure VII-19 - EDS mapping of silver of sample Na45Nb:5Ag-1kV.

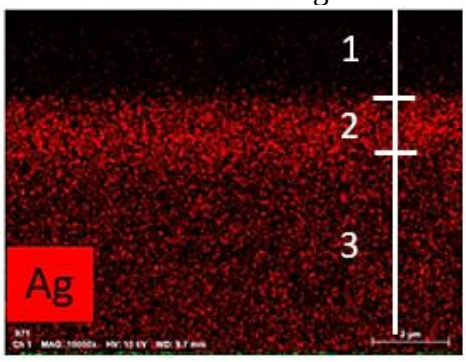

Reference: AUTHOR.

For the glass $58NaPO_3$-$42Nb_2O_5$ with 0.5% of silver thermally poled by Fargin *et al.* (2009), a silver depletion was also described, but in this case, in a smaller thickness than that of sodium. So, in the studied sample containing ~10 times more silver ions occur the opposite behavior. In this sense, the sample presents a first layer almost free of sodium and silver; and a second layer, with an apparently accumulation of silver but not of sodium. Such features, i.e., accumulation of ions along a few micrometers before bulk concentration, have already been observed, but it was not observed by just one of the two elements, so further investigations must be taken for this sample (ALLEY, BRUECK; MYERS, 1998; FARGIN *et al.*, 2009).

Furthermore, a thin layer of oxygen is observed on the anode surface. That is explained by the compensation mechanism that occurs during Thermal Poling (as explained in Chapter I-6.3). Additionally, the difference observed in niobium and phosphorus is associated to sodium/ silver depletion; which results in a greater proportion in the depletion layer comparing to the bulk glass.

Figure VII-20 presents the EDS profile of elements in a selected line from surface to bulk sample, passing through the depletion layer.

Figure VII-20 - EDS profile on cross-section of sample Na45Nb:5Ag-1kV.

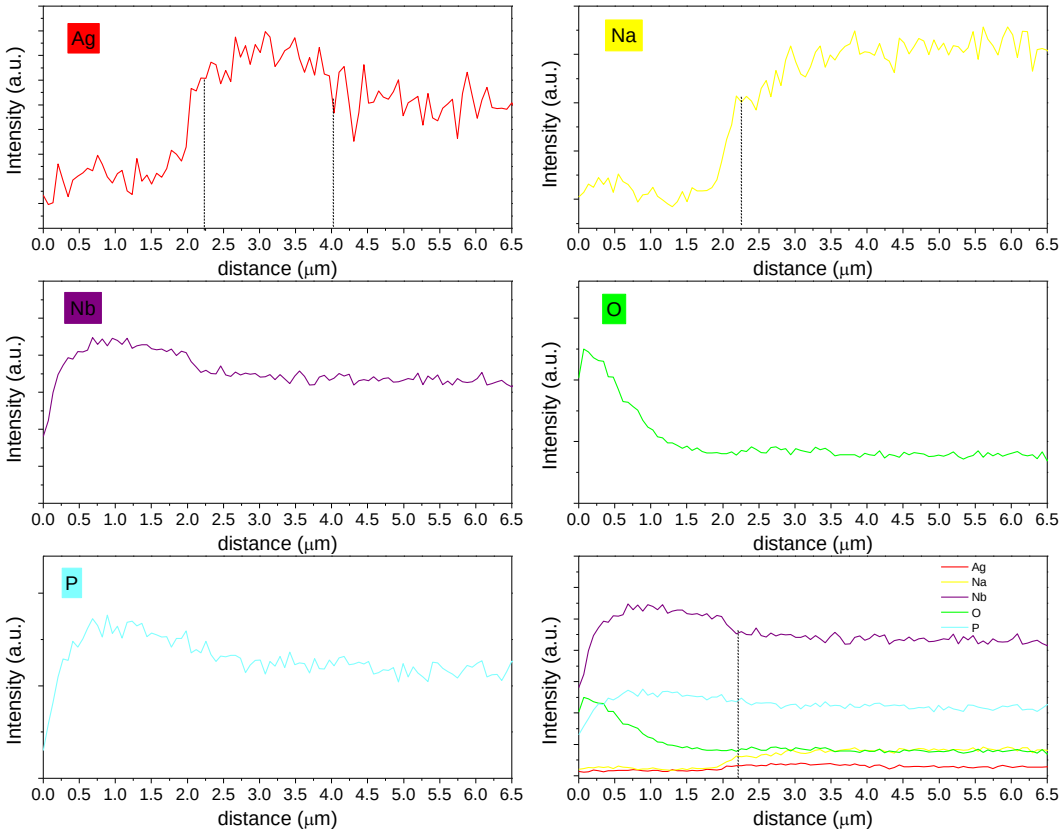

Reference: AUTHOR.
Note: The 0μm mark corresponds to the glass surface at the anode side.

It is possible with these data to infer the thickness of depletion layer, that is estimated to be around 2.2 μm for layer 1 – free of sodium and silver. For silver, as observed by the mapping, the graph presents an increase from layer 1 to 2, and a small decrease from layer 2 to 3, that occurs around 4 μm (so being ~1.8 μm thickness), corresponding to silver accumulation layer. These results are promising since refractive indices are dependent of the silver content. In this sense, further experiments using microstructured electrodes will be performed in order to control the silver content and consequently linear and nonlinear optical properties at a micrometric scale.

Chapter VII

CONCLUSIONS

According to the objectives, phosphate glasses with high niobium oxide contents (45 mol%) and doped with silver were prepared, being homogeneous and transparent. Two series of glasses were prepared: one containing potassium and other containing sodium. It was possible to incorporate high amount of silver, achieving ~9 mol% in glasses with potassium and ~5 mol% with sodium. These were confirmed by WDS, in which due to loss of phosphate in high temperature, ratio of Nb/P were even higher than determined by the nominal compositions.

The T_g temperature decreases with silver increment, that is, decreasing network connectivity. In addition, two well distinguished crystallization peaks were observed, especially, because of the high amount of niobium, made it promising for glass-ceramic crystallization of niobate crystalline phases. Also, these peaks shift to lower temperatures, decreasing the stability against crystallization as silver is introduced in the composition. In this sense, silver acts as nucleation centers.

Also, the addition of silver in the glass red-shifts the band-gap, this because silver has a higher molar mass and consequently the energy between the conduction and valence bands decreases. The glasses also showed a high percentage of transparency and relatively high refractive index values, increasing with the addition of silver.

Glasses were also co-doped with antimony, in which co-doped potassium glasses presented a yellow color, as for the Sb single doped glass. On the other hand, co-doped sodium glass presented changes for different annealing conditions, passing from yellow to red as temperature increase. In glass annealed at Tg an absorption band was observed in visible region, that is attributed to plasmon resonance of silver nanoparticles.

A preliminary thermal poling test was performed in a sodium niobium glass containing 5 mol % of silver at 1 KV. EDS measurement allowed to verify that not only occurs sodium depletion on the anode side, presenting a layer of ~2μm, but also silver is depleted and it is accumulated between the depleted layer and bulk region. Further investigation must be performed on these samples.

REFERENCES

ALLEY, T.G.; BRUECK, S.R.J.; MYERS, R.A. Space charge dynamics in thermally poled fused silica. **Journal of Non-Crystalline Solids,** [S.l.], v.242, p.165-176, 1998.

BARBOSA, J.S. **Preparação e caracterização de vidros e vitrocerâmicas luminescentes no sistema ternário TeO_2-Nb_2O_5-PbF_2** = Preparation and characterization of luminescent glasses and vitroceramics in the ternary system TeO_2-Nb_2O_5-PbF_2. 2017. 117p. Thesis (Master in Material Science and Engineering) - Universidade Federal de Alfenas, Poços de Caldas, 2017.

CASSANI, R. **Estudo de cristalização em vidros fosfatos alcalinos contendo óxido de nióbio** = Study of crystallization in alkaline phosphate glasses containing niobium oxide. 2022. 100p. Thesis (Master in Material Science and Engineering) - Universidade Federal de Alfenas, Poços de Caldas, 2022.

DMITRYUK, A.V. *et al.* The influence of glass composition on the properties of silver-doped radiophotoluminescent phosphate glasses. **Journal of Non-crystalline Solids**, [S.l.], v.202, p.173-177, 1996.

EL-SHARKAWY, E.A.; AL-SHIHRY, S.S.; YOUSSEF, A.M. Physicochemical properties of the Co_3O_4/Al_2O_3, Ag_2O/Al_2O_3 and Ag_2O-Co_3O_4/Al_2O_3 systems and their catalytic activities towards acid-base and redox reactions. **Adsorption Science & Technology**, [S.l.], v.24, p.657-672, 2006.

FARGIN, E. *et al.* Second-harmonic generation of thermally poled silver doped sodo-borophosphate glasses. **Journal of Applied Physics,** [S.l.], v.105, p.023105, 2009.

GLEBOV, L.B. Kinetics modeling in photosensitive glass. **Optical Materials,** [S.l.], v.25, p.413-418, 2004.

HSU, S.M. *et al.* Effect of silver concentration on the silver-activated phosphate glass. **Materials Chemistry and Physics**, [S.l.], v.123, p.172-176, 2010.

KARAM, L. *et al.* The effect of the sodium content on the structure and the optical properties of thermally poled sodium and niobium borophosphate glasses. **Journal of Applied Physics,** [S.l.], v.128, 043106, 2020.

LIMA, C. L. J. de. **Vidros fosfatos de metais de transição =** Transition metal phosphate glasses. 2014. 110p. Thesis (Master in Material Science and Engineering) - Universidade Federal de Alfenas, Poços de Caldas, 2014.

LO, N. T. **Second harmonic generation in germanotellurite glass ceramics doped with silver oxide.** 2016. 154p. Thesis (PhD in Chemistry) - Université de Bordeaux, Bordeaux (France), 2016.

MALAKHO, A. *et al.* Crystallization and second harmonic generation in thermally poled niobium borophosphate glasses. **Journal of Solid-State Chemistry,** [S.l.], v.178, p.1888-1897, 2005.

MARCONDES, L.M. *et al.* Structural and optical characterization of tungsten phosphate glasses containing silver and erbium. **Optical Materials**, [S.l.], v.132, p.112717, 2022.

MARCONDES, L.M. Monitoring Ag nanoparticles growth in undoped and Er^{3+}-doped glasses by in-situ UV-Vis spectroscopy and its luminescent properties. **Journal of Non-crystalline Solids**, [S.l.], v.609, p.122286, 2023.

MUÑOZ, F. *et al.* Phosphate glasses. *In:* MUSGRAVES, J.D.; HU, J.; CALVEZ, L. **Springer Handbook of Glass**. Springer International Publishing, 2019. p. 553-594.

SANTOS, F.P.de S. **Propriedades fotocromáticas dos vidros fosfatos PWSA e PZABP** = Photochromic properties of PWSA and PZABP phosphate glasses. 2021. 134p. Thesis (PhD in Physics) - Universidade Federal de Alagoas, Maceió, 2021.

SILVA, R.A. **Estudo das propriedades mecânicas e químicas de vidros fosfatos com adição de óxido de nióbio** = Study of the mechanical and chemical properties of phosphate glasses with addition of niobium oxide. 2022. 180p. Thesis (Master in Material Science and Engineering) - Universidade Federal de Alfenas, Poços de Caldas, 2022.

SMOGOR, H. *et al.* Effect of silver on phase separation and crystallization of niobium oxide containing glasses. **Journal of Solid-State Chemistry**, [S.l.], v.182, p.1351-1358, 2009.

GENERAL CONCLUSIONS

According to the general goals of this thesis, homogeneous and transparent alkali phosphate glasses with high tantalum or niobium contents were prepared and characterized. Their structural and optical properties were also investigated after being submitted to thermal poling using homogeneous and microstructured electrodes.

Tantalum addition in alkali-phosphate glasses increases network connectivity with the appearance of regions rich in [TaO_6] units that leads to the crystallization of $Na_2Ta_8O_{21}$ bronze-like perovskite crystalline phase for Ta_2O_5 contents of at least 45 mol%. Transparent and translucent Eu^{3+}-doped glass-ceramics could also be obtained with different degrees of crystallinity and transparency and it was demonstrated that the Eu^{3+} luminescent properties are strongly dependent of the crystallinity since Eu^{3+} ions are progressively inserted inside the sodium tantalate crystallites. Optical properties of glasses are also dependent on the tantalum oxide content, with red-shift of band-gap, increasing refractive index and increase in asymmetry around Eu^{3+} ions in doped glasses.

Tantalum-rich sodium phosphate glasses and glass-ceramics were submitted to thermal poling and/ or micropoling, presenting different behaviors. For glasses, samples with lower tantalum contents, that is 40 mol% of Ta_2O_5, considering the parameters tested could not be properly thermally poled that leads to electric sparks and sample damage. On the other hand, glasses with higher amounts, undoped and doped with europium, present an expected performance applying low voltages. In contrast, glass-ceramics thermally poled with same parameters of corresponding pristine glass presented a different response, in which the presence of sodium ions (Na^+) in the crystalline phase results in a lower migration kinetic of sodium ions when compared to the precursor glass as well as a lower content of depleted ions.

Both tantalum phosphate glasses and glass-ceramics presented Second Harmonic Generation (SHG) originated after Thermal Poling and associated to EFISH model ($\chi_{EFISH}^{(2)}=3\chi^{(3)}E_{int}$), indicating the break of the centrosymmetry of these glassy materials. For some of samples the value of $\chi^{(2)}$ was estimated by computational simulations, being 0.72- 1 pm/V for glasses and 0.04-0.016 pm/V for glass-ceramics. SHG has been shown to be spatially correlated with structural changes in the depleted layer, as also changes in luminescence for glasses. In the case of glass-ceramics, considering that Eu^{3+}-ions are inserted in crystals, any modifications were observed in luminescence for them.

Micro-imprinting of different patterns was also possible in tantalum phosphate glasses (that occurs concomitantly to poling), presenting changes in topology that increases with higher

applied voltages. Edge effects were also observed on micropoled samples, with SHG mainly located at the border of poled/unpoled areas, and vary accordingly with polarization. Index variation could also be demonstrated on the studied glasses. Thus, Thermal Micropoling allows a control in microscale of some optical properties on these tantalum phosphate glasses.

Sodium and potassium phosphate glasses containing high amounts of niobium were also prepared with increasing silver contents. Transparent glasses were obtained with silver contents reaching ~9 mol%, with silver decreasing network connectivity as a modifier and acting as a nucleation center, red-shifting band-gap of glasses and increasing refractive index. Co-doped glass with 5 mol% of silver and antimony exhibits different colors according to the annealing conditions, indicating modifications of silver oxidation state and agglomeration in the glass according to the temperature, in which one of them presented a plasmon resonance band.

It was also possible to perform a preliminary study of thermal poling of high niobium phosphate glasses containing a relative high amount of silver ions, in which besides sodium, silver also behaves as a mobile ion into the glass under poling conditions of 1 KV. The silver migration mechanism appears different from sodium with a depleted layer beneath the anode surface and second layer with a silver content higher than the bulk below this depleted layer.